



HAL
open science

Gouttes et billes sous grande déformation biaxiale: le rôle de la viscosité et de l'élasticité.

Carole-Ann Charles

► **To cite this version:**

Carole-Ann Charles. Gouttes et billes sous grande déformation biaxiale: le rôle de la viscosité et de l'élasticité.. Matière Molle [cond-mat.soft]. Université Montpellier, 2021. Français. NNT: 2021MONT097 . tel-03598039

HAL Id: tel-03598039

<https://tel.archives-ouvertes.fr/tel-03598039>

Submitted on 4 Mar 2022

HAL is a multi-disciplinary open access archive for the deposit and dissemination of scientific research documents, whether they are published or not. The documents may come from teaching and research institutions in France or abroad, or from public or private research centers.

L'archive ouverte pluridisciplinaire **HAL**, est destinée au dépôt et à la diffusion de documents scientifiques de niveau recherche, publiés ou non, émanant des établissements d'enseignement et de recherche français ou étrangers, des laboratoires publics ou privés.

THÈSE POUR OBTENIR LE GRADE DE DOCTEUR DE L'UNIVERSITÉ DE MONTPELLIER

En Physique

École doctorale Information Structure et Système

Unité de recherche Laboratoire Charles Coulomb

Drops and beads under large biaxial deformation: the role of viscosity and elasticity

Présentée par Carole-Ann CHARLES
le 2 décembre 2021

Sous la direction de Christian LIGOURE
et Laurence RAMOS

Devant le jury composé de

M. Christian LIGOURE, Professeur, Université de Montpellier

Mme Laurence RAMOS, Directrice de recherche, CNRS

Mme Isabelle CANTAT, Professeur, Université de Rennes 1

Mme Anne-Laure BIANCE, Directrice de recherche, CNRS

M. Yoël FORTERRE, Directeur de recherche, CNRS

M. Christian CLASEN, Professeur, KU Leuven

Directeur de thèse

Co-directrice de thèse

Présidente

Rapporteuse

Rapporteur

Examineur



UNIVERSITÉ
DE MONTPELLIER

Acknowledgments

Ce manuscrit est le résultat de presque quatre longues années de travail auquel je n'aurais pu aboutir sans les personnes citées ci-dessous. Il est donc tout naturel que la première partie de cette thèse leur soit dédiée.

Je souhaiterais remercier en tout premier lieu mes encadrants Christian Ligoure et Laurence Ramos. Merci de la confiance et de cette belle opportunité que vous m'avez offertes. J'ai énormément évolué du point de vue scientifique ces dernières années grâce à votre enthousiasme, votre rigueur et votre disponibilité lors de nos nombreuses réunions. Je garderai le souvenir de ces premières discussions scientifiques lors desquelles vous résolviez des équations dans les airs à une vitesse impressionnante sous mon regard admiratif et un peu dépassé. Grâce à votre patience, vos corrections et votre exigence, je suis fier du travail parcouru et des résultats obtenus lors de cette thèse. Ce fut un honneur et un plaisir de travailler avec vous. J'espère que nos chemins se recroiseront. Par ailleurs, je souhaiterais également vous remercier d'avoir fait en sorte que je puisse terminer le manuscrit à mon rythme et sans précipitation de dernière minute.

I would like to thank the rapporteurs of my thesis, Anne-Laure Biance and Yoël Forterre, as well as the jury members, Isabelle Cantat and Christian Clasen for the thorough reading of the manuscript and the fruitful discussion resulting from your pertinent remarks. I enjoyed very much presenting my work to you and was honored that you took the time to participate in my defense.

I would also like to thank Dimitris Vlassopoulos, Serge Mora and Lucyna Firlej for participating every year to my thesis follow up committee and for encouraging me to continue forward.

Je souhaiterais également remercier Evelyne van Ruymbeke de l'école polytechnique de Louvain-La-Neuve pour son introduction au monde fascinant de la rhéologie. Jamais je n'ai vu, lors de mes études à l'EPL, de professeur plus soucieux de partager sa passion avec ses étudiants. Merci d'avoir accepté une étudiante supplémentaire pour le mémoire et de m'avoir trouvé un sujet me permettant de continuer dans cette voie. Merci aussi de m'avoir encouragée à entreprendre un doctorat.

I would like to acknowledge the financial support of the H2020 Program (Marie Curie Actions) of the European Commission's Innovative Training Networks (ITN) (H2020-MSCA-ITN-2017) under DoDyNet REA Grant Agreement (GA) N°:76581. Thank you for the great opportunity of international exchanges and collaborations.

A Ameer, jamais je n'aurais su faire ce travail sans toi. Merci de m'avoir prise sous ton aile et de m'avoir montré les ficelles de l'impact. Je garde en souvenir ces nombreuses heures de manip dans le noir à griller nos cerveaux à coup d'azote liquide, d'éthanol et de musiques de Noël. Merci de m'avoir soutenue et poussée à avoir confiance durant ces moments difficiles qui sont inévitables lors de la thèse. Nous avons formé une "team drop impact" de choc et je serais ravie de continuer notre collaboration scientifique si l'avenir nous en donne l'occasion.

A Juliette, merci pour cette belle amitié que nous avons construite et d'avoir partagé

avec moi ta passion pour la musique, la danse et la gastronomie. Un tout grand merci pour ton soutien lors des moments difficiles et surtout pour ces innombrables relectures et suggestions. Avec toi et Ameer, j'ai touché le gros lot des équipes de soutien personnel! Encore un petit merci pour m'avoir convaincue de recommencer l'escrime après 15 années de pause.

To Jordi, my Dutch friend, thanks for sticking up with me till the end when all the others abandoned us. I hope the future brings many more adventures for us but meanwhile, I would like to thank you for all the parties, picking ups, dinners, teas, road trips, nose break, hikes (never climbs), COVID tests and vaccines,... Looking forward to make your ears bleed again on our way to Germany or Norway!

To Alice, thanks for making being a scientist look so cool! You are such an inspiration. Living with you was the best. Thanks for all the work-outs and parties. Summer of 2020 was amazing thanks to the way you bring people together.

To Matteo, my personal chef, thank you for feeding me delicious homemade Italian meals every time I was feeling discouraged, sad or just hungry. I enjoyed so much our long discussions about any subjects. Thank you for your profound generosity. I am so grateful that our paths crossed and hope to see you again many more times.

To Laura, thanks for the basic B nights after the long weeks of hard work when we needed to unwind. Thanks for stocking on herbal tea and dark chocolate at the lab for the hard times. I enjoyed our gym work-outs and sauna sessions after stretching under some cringy applauses. Talking about cringe, thanks for participating in all my crazy parties, I had so much fun.

Un tout grand merci Ty pour ta bonne humeur, ta disponibilité lors de mes nombreuses requêtes et questions, mais surtout pour m'avoir transmis "l'art de la débrouille". Merci aussi d'avoir synthétisé mes matériaux. Bonne chance avec l'instafame! Grace à Tytyc(o)uisine, je pourrai continuer à saliver devant tes petits plats sans squatter ton bureau.

Merci également aux permanents de l'équipe matière molle : Domenico, Luca, Gladys, Amélie, Julian, Pascale, Matthieu, Maurizio, Christophe, Laura, Martin, Rémi, Michel, Daniel, Anne-Caroline ainsi que Jean-Christophe, Jean-Marc, Philippe, Raymond, Edouard et Jérôme, pour vos mots d'encouragement, votre aide technique ou vos remarques et questions pertinentes lors des séminaires.

Thanks to all the non-permanents colleagues of the soft matter team with whom I had the privilege to share part of this journey: Antigoni, Kanyarat (M), Stefano, Smile, Salvatore, Dario, Myriam, Alexey, Alexandre, Haifa, Ahlem, Angelo, Abir, Alessandro, Rajam, Robin, Abdallah, Majid, Subhadarshinee, William, Pierre. I would like to thank Anthony especially for including me from the very beginning and giving me the good addresses in Montpellier.

Thank you to all the members of the DoDyNet group and in particular to the other young researcher: Consiglia, Christina, Paola, Larissa, Wendi, Rowanne, Stefania, Simone, Clément, Hongwei, Yanzhao, Bruno and Jianzhu for the sharing of knowledge and crazy adventures. I was very fortunate to share these experiences with such a kind and fun

group.

Thanks to all my Montpellier flat mates: Jake, Dylan, Solveigh, Wilko, Victor, Marie, Anouck, Tiffany, Alice, Jack, Ella and Laura. Living with you has made my experience in Montpellier much more enjoyable.

Merci à ma famille et amis qui sont venus me rendre visite à Montpellier : Maman, Papa, François, Papy, Maureen, Aurélie, Ségo, Alice, Amandine, Charlotte et Rémi. Je suis très heureuse d'avoir pu partager avec vous mon petit monde de Montpellier.

Et à Julien, merci pour tout le reste...

Contents

Introduction	1
1 State of the art on impact experiments and objectives of the thesis	3
1.1 Surfaces of impact	5
1.1.1 Extended solid surfaces	5
1.1.2 Small solid targets	7
1.1.3 Drop impact on repellent surfaces	9
1.1.3.1 Superhydrophobic surfaces	10
1.1.3.2 Superheated surfaces	11
1.1.3.3 Very cold surfaces	13
1.2 Fluids	16
1.2.1 Shear-thinning fluids	17
1.2.2 Shear-thickening fluids	19
1.2.3 Yield-stress fluids	19
1.2.4 Maxwell fluids	19
1.3 Experimental outputs and modeling	22
1.3.1 Expansion dynamics	22
1.3.2 Thickness field of the sheet	25
1.3.3 Rim bounding the sheet	27
1.4 Motivations	30
2 Materials and methods	33
2.1 Methods	33
2.1.1 Measure of surface tension	33
2.1.1.1 Pendant drop	34
2.1.1.2 Dynamical surface tension measurements	35
2.1.1.3 Spinning drop tensiometer	36
2.1.2 Rheology	37
2.1.2.1 Shear rheology	37
2.1.2.2 Extensional rheology	40
2.1.3 Set-ups for drop impact experiments	42
2.1.3.1 Impact on small solid targets	43
2.1.3.2 Cold Leidenfrost conditions	45
2.1.4 Image analysis for drop impact	49
2.1.4.1 Apparent diameter	49
2.1.4.2 Crown correction	50
2.1.4.3 Thickness field	51
2.2 Materials	57

2.2.1	Newtonian fluids	57
2.2.2	Self-assembled transient networks	58
2.2.2.1	Bridged micro-emulsions	58
2.2.2.2	Decorated wormlike micelles	62
2.2.3	PEO solutions	65
2.2.4	2, 4-bis (2-ethylhexylureido) toluene (EHUT)	67
2.2.5	Ultra soft elastic beads	70
3	Biaxial extensional viscous dissipation in sheets expansion formed by impact of drops of Newtonian and non-Newtonian fluids	73
4	Viscoelasticity and elastocapillarity effects in the impact of drops on a repellent surface	89
5	Biaxial extensional and shear viscous dissipation during the expansion of fluid sheets	101
5.1	Introduction	101
5.2	Competition between shear and biaxial extensional viscous dissipation in the expansion dynamics of Newtonian and rheo-thinning liquid sheets	102
5.3	Effect of the target size on maximal expansion	114
5.3.1	Newtonian fluids	114
5.3.2	PEO solutions	120
5.4	Conclusion	125
6	A close look at the rim of viscous sheets	127
6.1	Introduction	127
6.2	Thickness fields	128
6.3	Experimental analysis of the rim	133
6.3.1	Emergence of the rim	134
6.3.2	Thickness of the lamella at the foot of the rim	135
6.3.3	Shape of the rim	135
6.4	Theoretical considerations	142
6.4.1	Filling velocity of the rim	142
6.4.2	Filling rate of the rim	147
6.4.3	Emergence of the rim	147
6.5	Conclusion	149
7	Spinning elastic beads: a route for simultaneous measurements of the shear modulus and the interfacial energy of soft materials	151
	General conclusions and perspectives	163
	Bibliography	169

Introduction

Drop impacts are ubiquitous in our daily life, and the phenomenon of a drop deforming after impacting a substrate has fascinated scientists for centuries. With the emergence of high speed imaging, many refinements have flourished in recent years. Most studies concern drops of Newtonian fluids. However, the impacts of viscoelastic fluids, which are more relevant to most applications, have not been developed as thoroughly. Understanding the behavior of these fluids following impact and more broadly undergoing biaxial extensional deformation or mixed flow fields is crucial for applications involving drop impact (spray coating, ink-jet printing, pesticide application, ...) but also for polymer processing. When the drop, with accumulated kinetic energy, strikes the surface, it deforms into a disk-like shape and expands until reaching a maximum diameter, after which it settles or recedes. When the restituted energy is large enough, the receding is followed up by the rebound of the drop off the surface. Various instabilities like secondary drop ejections at the edge can eventually occur. The maximal diameter reached by the drop is governed by the stored surface and bulk elastic energy and by the dissipated energy.

The way one should account for the dissipation is still a matter of discussion. In this thesis, we propose two different experimental approaches to achieve this goal. One strategy is to impact the drops on a repellent surface and, this way, get rid of all shear contribution to the dissipation. The other strategy is to impact the drops on small targets of increasing sizes. In this situation, the part of the sheet in contact with the target is subjected to shear dissipation while the part extending outside the target undergoes biaxial extensional dissipation, recreating mixed flow field conditions involved in many industrial applications. These two experimental configurations are used, on one hand, with Newtonian fluids of different viscosities in order to probe the effect of viscous dissipation when no elasticity is involved. On the other hand, the combined effect of viscosity, bulk and surface elasticity is investigated with rheo-thinning viscoelastic fluids and Maxwell fluids.

The main objective of this PhD thesis is to investigate the behavior of drops of viscoelastic fluids impacting in simplified and controlled flow fields and to uncover the role of biaxial extension. The manuscript is divided in 7 chapters.

Chapter 1 is a bibliographic chapter that presents the state of the art on the topics. We report on the different types of surfaces and fluids one will come across when exploring the field of drop impact experiments. A specific section is dedicated to experimental outputs from the drop impact experiment, such as the maximal diameter reached by the sheet, its thickness field and the rim bounding the sheet. In the last part of this chapter, we present the motivations for the following work.

Chapter 2 is dedicated to the description of the experimental methods and specific fluids used in this work. For the purpose of our study, model systems, which behave as Maxwell fluids, as well as rheo-thinning viscoelastic fluids and soft elastic beads have been investigated. In this chapter, we present in details the studied fluids, their preparation and characterization methods. We also present the set-ups and characterization techniques used in this work.

In Chapter 3, the biaxial spreading dynamics of Newtonian and shear-thinning drops on a repellent surface at a fixed impact velocity is investigated. The effect of viscosity on the maximal expansion for both types of liquids is rationalized thanks to an effective biaxial extensional Ohnesorge number.

Chapter 4 expands the work from Chapter 3 by investigating more complex fluids, which behave as Maxwell fluids, and exploring the effect of the impact velocity. The experimental data for the maximal expansion and the time to reach maximal expansion are confronted to theoretical predictions obtained by solving a non-linear damping harmonic oscillator model. This model accounts for the effects of biaxial extensional viscous dissipation as well as bulk and surface elasticity.

In Chapter 5, the competition between shear and biaxial extensional dissipation underwent by a liquid sheet produced after impact of a drop on a small target is quantitatively assessed. The behavior of rheo-thinning fluids is compared to that of Newtonian fluids, and a notable difference of the mode of dissipation for the strongly shear thinning fluid (EHUT solutions) is evidenced. In a second part of this chapter, the size of the target is varied to investigate how the target size affects the maximal expansion reached by the sheet.

Chapter 6 focuses on the rim forming at the edge of an expanding Newtonian free liquid sheet. For the first time, the rim shape is measured using time resolved light absorption techniques. In this chapter, the rim filling velocity and rate are assessed experimentally and theoretically. Both showed interesting results, which were not predicted by the literature.

Chapter 7 exploits the boundary free biaxial deformation occurring in a spinning drop tensiometer to extend our study of deformation of soft materials to another setting. We independently measure the surface tension and the bulk elastic modulus of a soft elastic bead, which is not usually possible due to elasto-capillarity. Assuming a homogeneous deformation, we achieve theoretical decoupling of the contributions of the interfacial free energy and bulk elasticity at high centrifugal force, which was confirmed by the good agreement with experimental measurements and expected values. Additionally, the interfacial free energy and the interfacial tension are showed to be equal for our soft elastic beads.

We conclude by a summary of the main findings presented in this work and discuss the open perspectives.

State of the art on impact experiments and objectives of the thesis

Contents

1.1 Surfaces of impact	5
1.1.1 Extended solid surfaces	5
1.1.2 Small solid targets	7
1.1.3 Drop impact on repellent surfaces	9
1.2 Fluids	16
1.2.1 Shear-thinning fluids	17
1.2.2 Shear-thickening fluids	19
1.2.3 Yield-stress fluids	19
1.2.4 Maxwell fluids	19
1.3 Experimental outputs and modeling	22
1.3.1 Expansion dynamics	22
1.3.2 Thickness field of the sheet	25
1.3.3 Rim bounding the sheet	27
1.4 Motivations	30

After the first drawings of Leonardo da Vinci in the codex Leicester in the 16th century, methodical observations of drops impacting a surface trace back to the 18th century with the pioneer work of A.M. Worthington. He achieved the imaging of milk and mercury drop impacts thanks to an apparatus generating electric sparks synchronized with the impact [Worthington 1877, Worthington 1895] (Figure 1.1). Since then, with the emergence of high-speed imaging allowing time-resolved observations of the drop impact dynamics [Thoroddsen 2008, Josserand 2016] and pushed by environmental and industrial aspects, contributions to the field flourished.

Indeed, applications relevant to drop impact are abundant; to name a few: Ink-jet printing [Wijshoff 2018], spray cooling, spray coating [Pasandideh-Fard 2002], pesticide application [Wirth 1991] or criminal forensics [Laan 2015]. Such a wide range of applications

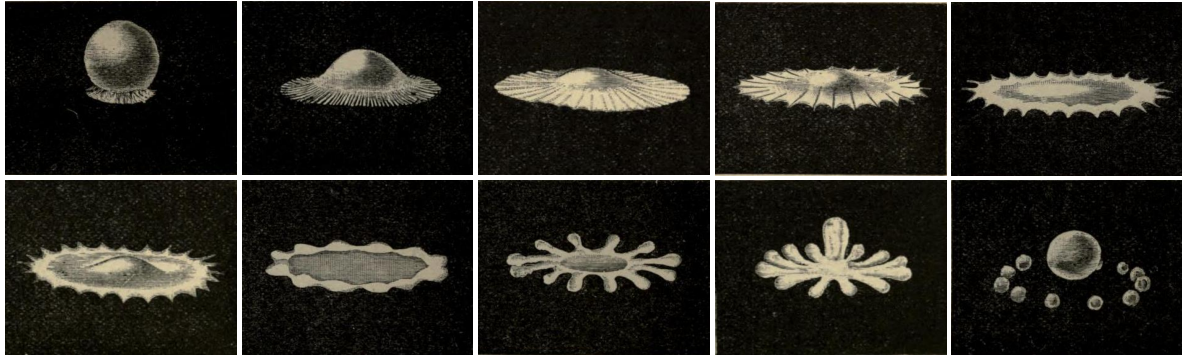


Figure 1.1: Sketches of a mercury drop during impact made by A.M. Worthington in 1895 [Worthington 1895].

pushes toward a better understanding of the underlying physics in order to optimize the related industrial processes. To this end, experimental, theoretical and numerical experiments are performed on drops impacting surfaces in various situations. The surfaces considered include thick and thin liquid films or solid surfaces of different roughness [Rioboo 2002] and wettability [Lee 2010] but also of different sizes [Rozhkov 2002, Arogeti 2019] or geometries [Josserand 2016, Wang 2017, Arogeti 2019]. Drops made of many materials have been considered, from Newtonian fluids with different viscosities [Arora 2016, Gordillo 2018], suspensions [Marston 2013, Raux 2020], shear thickening fluids [Boyer 2016] to polymer solutions [Crooks 2000] or other viscoelastic materials [Arora 2016]. Impact of soft elastic beads has also been investigated [Tanaka 2003, Tanaka 2005, Arora 2018].

When a falling drop of fluid is stopped by a surface, an internal shock wave propagates with a timescale of the order of the nanosecond. A spreading lamella is then produced at the bottom of the drop. Finally, the drop may deform into a disk-like sheet which expands radially until reaching a maximum diameter [Rioboo 2001]. The sheet settles, recedes partially or completely and sometimes rebounds depending on the nature of the fluid, the surface and dynamic parameters, such as the impact velocity, and the wettability that is usually quantified by the static contact angle between the fluid and the surface. In the drop impact context, one must consider the dynamic contact angle, which changes as the sheet expands and recedes [Rioboo 2001]. In the case of highly inertial impacts, instabilities can arise and cause the drop to break up and eject secondary droplets from the rim. This phenomenon is called splashing. These different steps can be observed in Figure 1.2 where drops are impacting a solid surface in different situations as described in section 1.1.1.

If one wants to rationalize drop impacts, one will come across several governing dimensionless numbers. Those used in this thesis are listed here [Yarin 2017]. We is the Weber number, which relates the effect of the inertial forces to the capillary forces.

$$\text{We} = \frac{\rho v_0^2 d_0}{\gamma} \quad (1.1)$$

With ρ the density, v_0 the impact velocity, d_0 , the initial diameter of the drop, γ the surface tension.

The ratio of inertial forces to viscous forces within a fluid is given by the Reynolds number, Re .

$$\text{Re} = \frac{\rho v_0 d_0}{\eta} \quad (1.2)$$

Where η is the dynamic viscosity.

Finally, the Ohnesorge number, Oh , relates the viscous forces to the surface tension and inertial forces, and can be written as a combination of We and Re .

$$\text{Oh} = \frac{\eta}{\sqrt{\rho \gamma d_0}} = \frac{\sqrt{\text{We}}}{\text{Re}} \quad (1.3)$$

Drop impact is a complex non-linear dynamical phenomenon involving three components: the drop, the substrate and the surrounding gas. When the drop hits the surface, the gas dampens the shock and a local pressure maximum under the drop creates a dimple in the fluid, which in turn promotes splashing by lifting the sheet away from the substrate [Lee 2012]. Thus, the contact area between the fluid and the solid, during expansion, is rather a ring than a disk. During the retraction of the sheet, the air film under the drop retracts in a complex manner to form a bubble. The surrounding gas is often negligible in the overall spreading dynamics [Visser 2015]. In the following, the main types of surfaces and fluids of interest for impact will be reviewed, neglecting the surrounding gas.

1.1 Surfaces of impact

As already mentioned, the surfaces on which the drops are impacted are myriad. Here we describe a few that are of interest to us.

1.1.1 Extended solid surfaces

The outcomes of a water drop after its impact on a large plane solid surface were categorized by R. Rioboo and Tropea [Rioboo 2001]. Six main categories, represented in Figure 1.2, depending on the impact velocity and the drop and surface properties, result from this classification. At low impact velocity, the stored energy after maximal expansion is not sufficient to pull back the expanded sheet and this one deposits on the

surface. Higher impact velocity may lead to splashing, either prompt or after apparition of a corona, by ejection of secondary droplets. The prompt splash only happens on rough surfaces, and the corona splash is characteristic of impacts on a liquid film [Rioboo 2001]. Instabilities during the retraction phase can lead to receding break-up, which can happen because the dynamic contact angle decreases while the sheet retracts. Finally, drop impacts with very low amount of dissipation and high initial kinetic energy can lead to partial or complete rebound in which the drops come back to its initial shape and detaches partially or completely from the substrate.

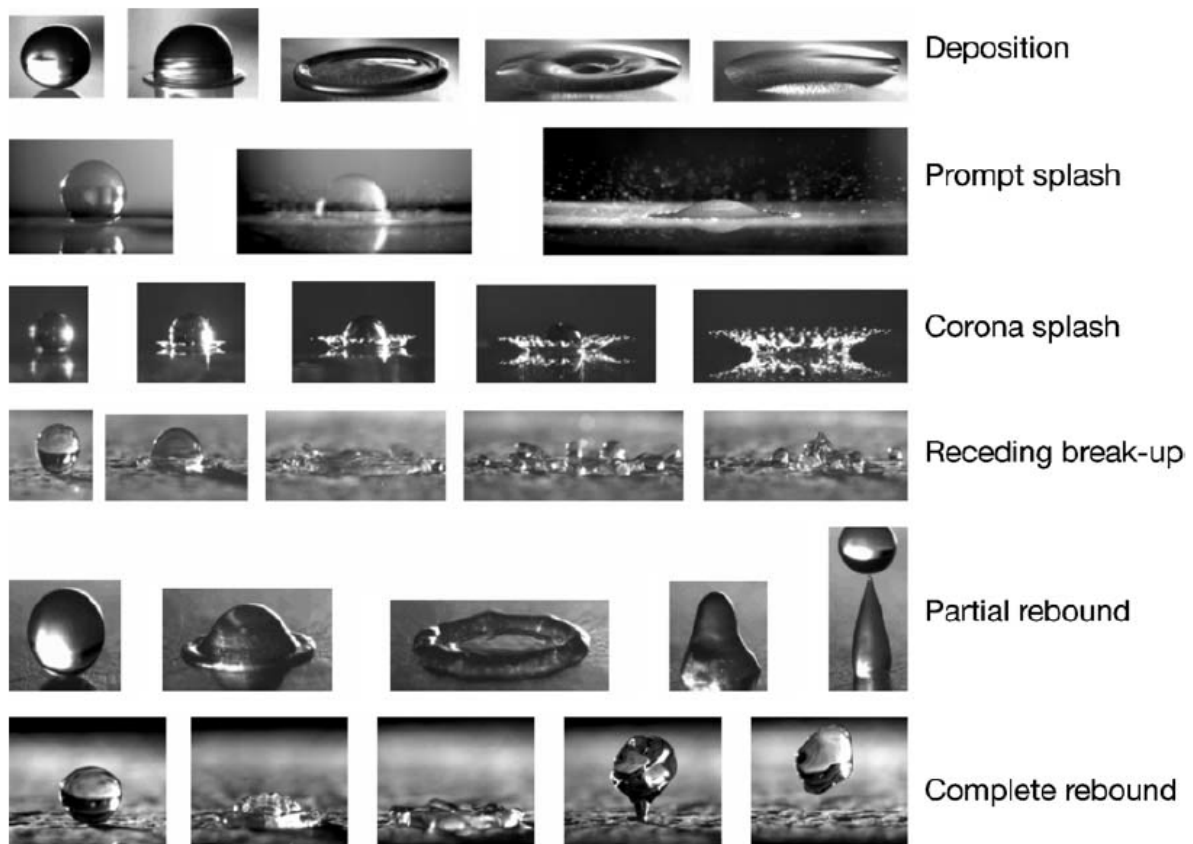


Figure 1.2: Six kinds of outcomes resulting from drop impact on a dry surface [Rioboo 2001].

Whether the sheet deposits, retracts, or rebounds depends also on the wettability of the solid surface on which the impact is performed [Josserand 2016]. A larger contact angle results in easier splashing and rebound. When impacted on a (super)hydrophobic substrate, the drop can partially or completely rebound and even form a singular jet.

1.1.2 Small solid targets

While the most studied configuration for drop impact is the infinite solid surface, the scenario of a drop impacting surfaces of various sizes and geometries is currently attracting the scientific community. For example, Lejeune et al. impacted drops on semi-infinite surfaces to study the effect of an edge on the impact outcomes (See Figure 1.3)[Lejeune 2018] and Bakshi et al. studied impacts on small spherical targets of different curvatures [Bakshi 2007]. As a matter of fact, this scenario is not only more realistic to answer industrial problems (ink droplets of size comparable to the paper roughness, pesticide droplets application or rain drops on plant leaves of different sizes, ...) but it also raises a peculiar experimental condition where a mixed flow field is generated, i.e., shear on the solid surface vs biaxial extensional in air. The part played by both flow fields in the expansion dynamic of the sheet is yet to be identified and will be an objective of this thesis.

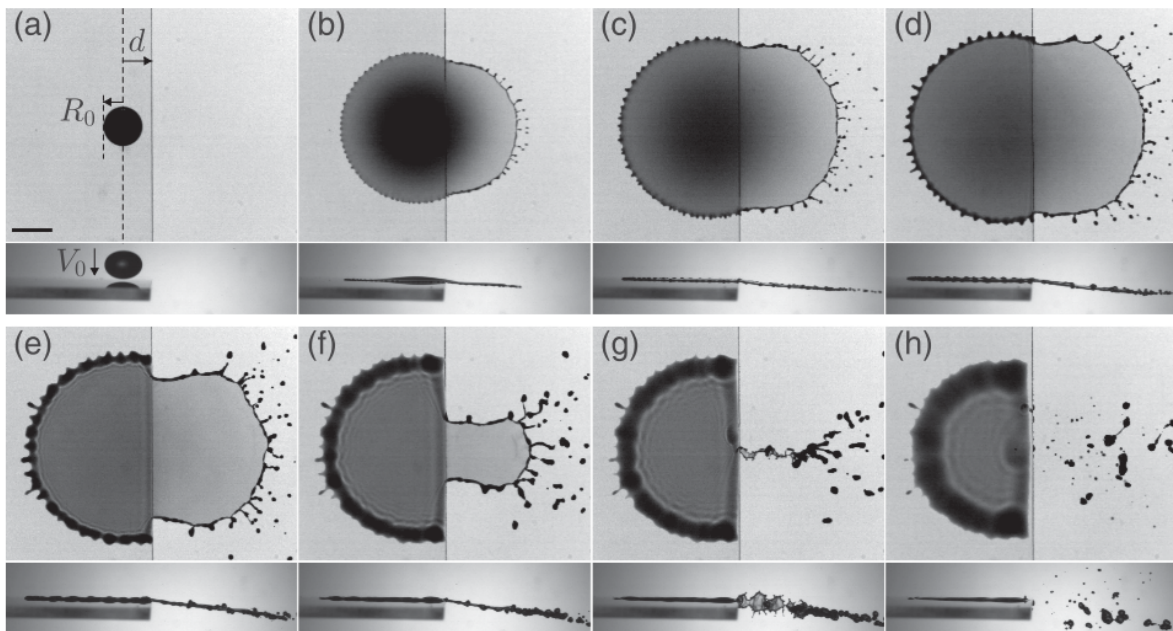


Figure 1.3: Snapshots of a drop impacting on a semi-infinite surface from top and side views at different times ((a) $t = 0$, (b) $t = 1.6$, (c) $t = 3$, (d) $t = 4.4$, (e) $t = 7$, (f) $t = 10.6$, (g) $t = 12.4$, and (h) $t = 19ms$). R_0 is the initial radius of the drop and V_0 is the impact velocity. The offset, d , is defined as the distance between the impact point and the edge. The scale bar is 5 mm. [Lejeune 2018]

The impact of drops on a small rod, or target, of cross-section comparable to that of the drop was first developed with the aim of limiting the dissipation happening during the sheet expansion on a solid surface (mainly viscous shear dissipation) [Rozhkov 2002]. In this configuration, the sheet expands freely in air beyond the target, thus avoiding strong interactions with the surface and significant shear viscous dissipation as compared

to the impact on an infinite solid surface [Rozhkov 2003, Rozhkov 2004, Villermaux 2011, Vernay 2015a, Arora 2016]. Figure 1.4.a) schematically shows the expanded sheet produced by the impact of a drop on a solid target, and time series of the expansion and retraction of the sheet is shown in Figure 1.4.b) [Ogawa 2018]. This configuration, inspired by the Savart experiment where a liquid jet hits normally a flat solid disk, was first introduced by Rozhkov et al. [Rozhkov 2002]. The flatness of the sheet was later shown to be adjustable by incorporation of a coaxial cylinder [Villermaux 2011]. Interestingly, this coaxial cylinder used to control the ejection angle of the sheet [Clanet 2002] was recently used to create waterbowls, resulting in a decrease of the contact area between the sheet and the surface [Girard 2019]. Vernay et al. and later, Wang and Bourouiba, have measured the thickness field of a water drop impacting a small cylindrical target [Vernay 2015a, Wang 2017]. They derive a self-similar solution for the full temporal and spatial profile of the expanding sheet thickness, which is in good agreement with experimental measurements. Arora et al. studied the influence of the viscosity on the maximum expansion diameter of Newtonian and viscoelastic drops impacting on a small cylindrical target [Arora 2016]. The authors provide a simple model which predicts satisfyingly the dependence of the maximal expansion of the sheet with viscosity. This model accounts for viscous dissipation in the viscous boundary layer at the interface between the surface of the target and the liquid, the part of the sheet expanding freely in air being presumed free of viscous dissipation.

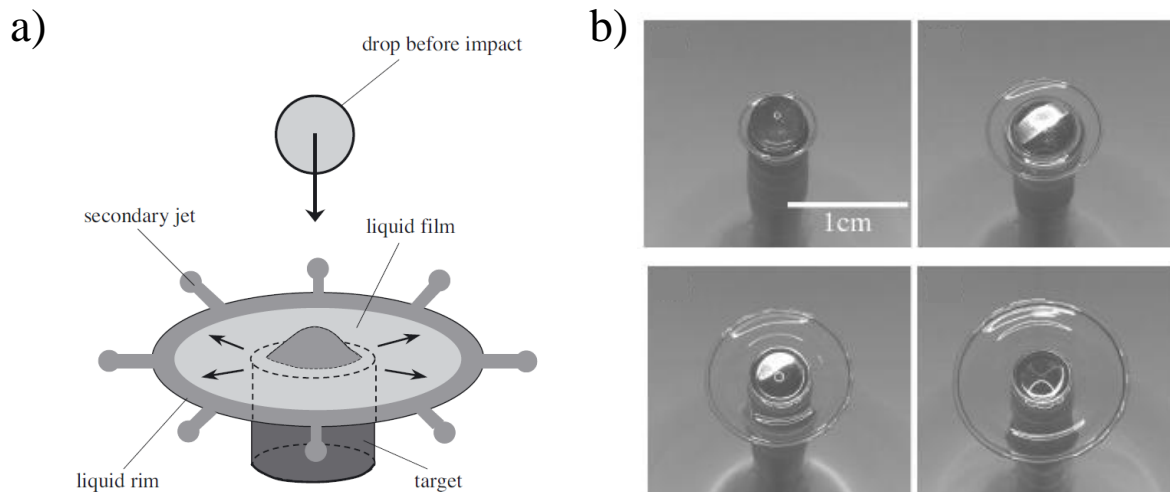


Figure 1.4: a) Schematic representation of a sheet formed by impact of a drop on a blunt cylindrical target [Rozhkov 2002]. b) Snapshot of an expanding liquid sheet resulting from the impact of a glycerin/water mixture drop of shear viscosity 240 mPa s at an impact velocity of 3.7 m/s [Ogawa 2018].

More recently, Arogeti et al. [Arogeti 2019] have impacted drops on targets of sizes

smaller than the initial diameter of the impacting drop and identified three regions of target-to-drop size ratio, β_t , for which the drop, after impact, flows radially (type A), radially and vertically (type B) and vertically (type C). The different regions are reported schematically in Figure 1.5. The other side of the target size spectrum where the size of the target increases progressively until reaching the situation of impact on a plane surface is yet to be explored.

	Type-A $1 < \beta_t \leq \beta_{max}$	Type-B $\frac{1}{2} < \beta_t \leq 1$	Type-C $\frac{1}{2} \leq \beta_t$
Initial phase			
Middle phase			
Maximal Spreading phase			

Figure 1.5: Schematic representation of the three regions identified by Arogeti et al. when impacting drops on targets with various target-to-drop size ratios, β_t [Arogeti 2019].

1.1.3 Drop impact on repellent surfaces

Investigating drop impacts on a repellent surface is of great interest to understand natural phenomena, such as the lotus effect, and for many industrial applications. Indeed, the properties of repellent surfaces can be used for self-cleaning, water droplet condensation and evaporation, anti-corrosion, resistance to rain freeze, or drag reduction. Moreover, because both the intrinsic fluid properties and the interaction between the fluid and the substrate are important for the impact dynamics, decoupling the two is crucial to better understand the fundamentals of this process. Repellent surfaces include superhydrophobic, superheated, sublimating and evaporating surfaces. For superheated,

sublimating and evaporating surfaces, a vapor layer is formed under the drop upon impact, creating shear-free boundary conditions below the expanding drop. On repellent surfaces, the dissipative processes are expected to be reduced, leading to larger maximal expansion and rebound.

1.1.3.1 Superhydrophobic surfaces

Superhydrophobic surfaces have very high water repellency. They are inspired by nature (lotus leaves, water lilies, duck feathers, butterfly wings, ...) and are usually created by patterning a substrate with a hierarchical double-scale (micro- and nano-scale) structure [de Gennes 2004]. The latest scientific findings in droplet impact on superhydrophobic surfaces have been comprehensively reviewed recently [Khojasteh 2016].

To be superhydrophobic, the surface must have a water contact angle greater than 150° , and thus offer special non-wetting properties. A rough surface with entrapped air in the cavities will behave as a superhydrophobic surface. In this situation, the drop is in the Cassie-Baxter state (the surface is chemically heterogeneous) as opposed to the Wenzel state (on a rough, but chemically homogeneous, surface) [de Gennes 2004]. Figure 1.6 shows a schematic representation of a drop in the two states.

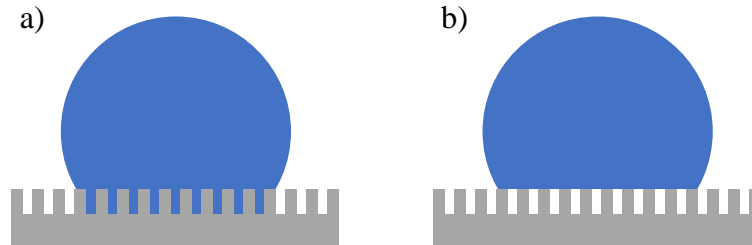


Figure 1.6: Schematic representation of a drop in a) the Wenzel state on a rough surface and b) the Cassie-Baxter state on an inhomogeneous surface.

Antonini et al. studied the effect of surface wettability on drop impact by performing experiments on different surfaces of various wettability at several impact velocities [Antonini 2012]. They found that at intermediate Weber numbers ($We < 200$) the wettability of the surface has an effect on the maximum diameter reached by the sheet, whereas wettability has no effect on the maximum diameter at $We > 200$. Superhydrophobic substrates of similar wettability but of different texture morphology also have an effect on the impact outcomes [Lv 2016]. Lv et al. studied impact on different superhydrophobic surfaces and found variations in the contact time as well as in the maximum diameter reached by the sheet. For surfaces with a hierarchical roughness, the contact time is significantly reduced, while the maximal lateral expansion is greater. Figure 1.7 shows

scanning electron microscopy (SEM) images of two superhydrophobic surfaces, along with snapshots of a drop impacting on these surfaces at different times.

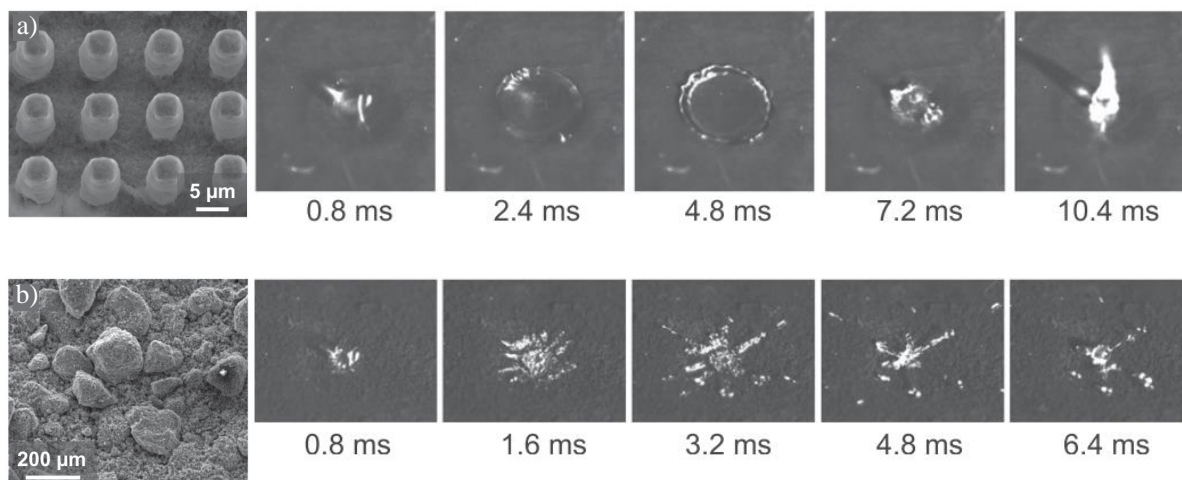


Figure 1.7: SEM images of the surfaces with a) two-tier roughness and b) hierarchical roughness, along with snapshots of a $4 \mu\text{m}$ water drop impacting them at a velocity $v_0 = 2.4 \text{ m/s}$ [Lv 2016].

Nasto et al. recently impacted drops of glycerol and water on hairy surfaces and observe different regimes of spreading and penetration of the drop: no penetration, partial penetration, penetration and capture, penetration and spreading, and penetration and drop ejection [Nasto 2019]. The authors rationalize their experimental results in terms of Reynolds and Weber numbers modified for the geometrical features of the hairs, Re^* and We^* . They obtained Re^* by balancing the kinetic energy with the viscous energy loss, and We^* by balancing the kinetic energy with the surface energy. They then delimit the different domains with a parameter, $\beta = \frac{1}{\text{Re}^*} + \frac{1}{\text{We}^*}$, given by the ratio between the energy lost by passing through the hair and the kinetic energy of the impinging drop. $\beta = 1$ corresponds to the captured state.

1.1.3.2 Superheated surfaces

The Leidenfrost effect was discovered in 1756 by Johann Gottlob Leidenfrost [Leidenfrost 1756]. He observed that a drop of water, in the vicinity of a surface above a critical temperature called the Leidenfrost temperature (around 160°C for water), does not evaporate instantaneously but rather levitates for an instant before disappearing. This phenomenon can be explained by the presence of an insulating vapor layer between the drop and the surface, which is generated from the intense evaporation of the drop. This vapor layer has a typical thickness of $100 \mu\text{m}$ as evaluated more recently [Quéré 2013]. We refer to Leidenfrost effect when this vapor layer has sufficient pressure to

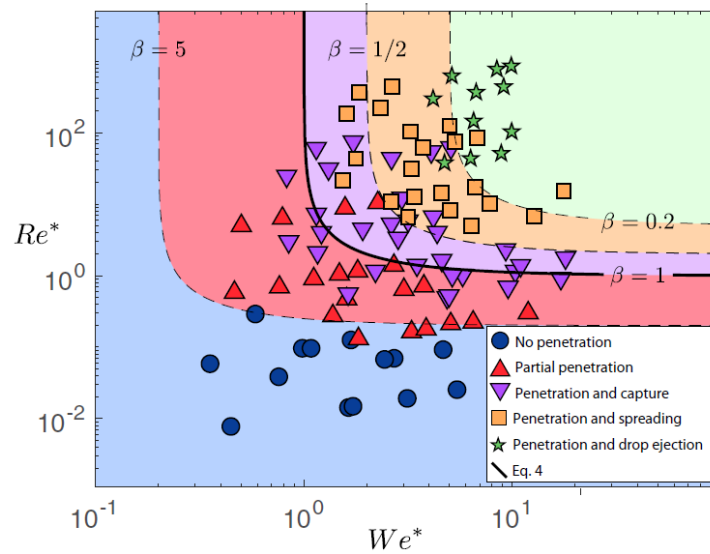


Figure 1.8: Phase diagram of the different possible states observed by Nasto et al. [Nasto 2019].

allow the drop to levitate on the hot surface while being thermally insulated from the latter.

Many authors have investigated drop impact on Leidenfrost surfaces, it was shown that the Leidenfrost temperature depends on drop impact parameters, such as the impact velocity [Moreira 2010, Yarin 2017]. If the temperature is not high enough, the fluid may touch the surface locally and other phenomenon such as evaporation, nucleate boiling or foaming will happen as depicted in Figure 1.9.

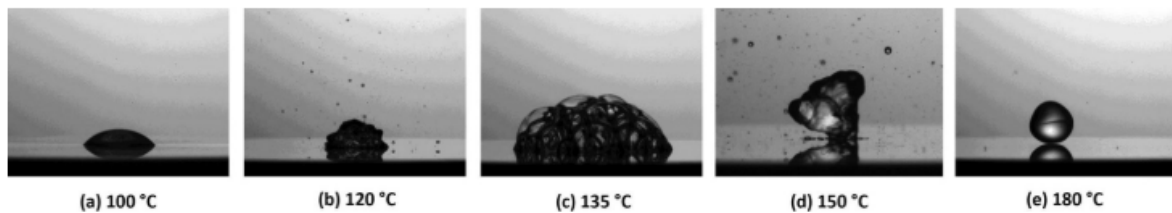


Figure 1.9: Different outcomes of drop impact onto a hot surface depending on the surface temperature. a) evaporation, b) nucleate boiling, c) foaming, d) transition, and e) film boiling (Leidenfrost effect) [Yarin 2017].

In the Leidenfrost conditions, when the temperature is high enough, the impacting drop can bounce off the surface, as a solid sphere would do [Richard 2002]. However, it is not always the case. Indeed, depending on the drop radius and velocity, different phenomenons were observed [Biance 2011]. These outcomes are depicted in Figure 1.10. In Figure 1.10 a), the drop spreads, recedes and bounces off the surface as it is expected in

the Leidenfrost conditions. This behavior happens for $We > 1$ but smaller than a critical We value, at which the edge of the sheet destabilizes into satellite droplets and splashing occurs (see Figure 1.10 b) and c)). Increasing We even more, resulted in the formation of a hole in the spreading sheet along with the splashing as shown in Figure 1.10 c). If a defect is present on the surface, the hole opening can even occur at Weber numbers for which there is no splashing (see Figure 1.10 d)). Note that a warmer substrate results in a lower impact velocity threshold for splashing [Rein 2002].

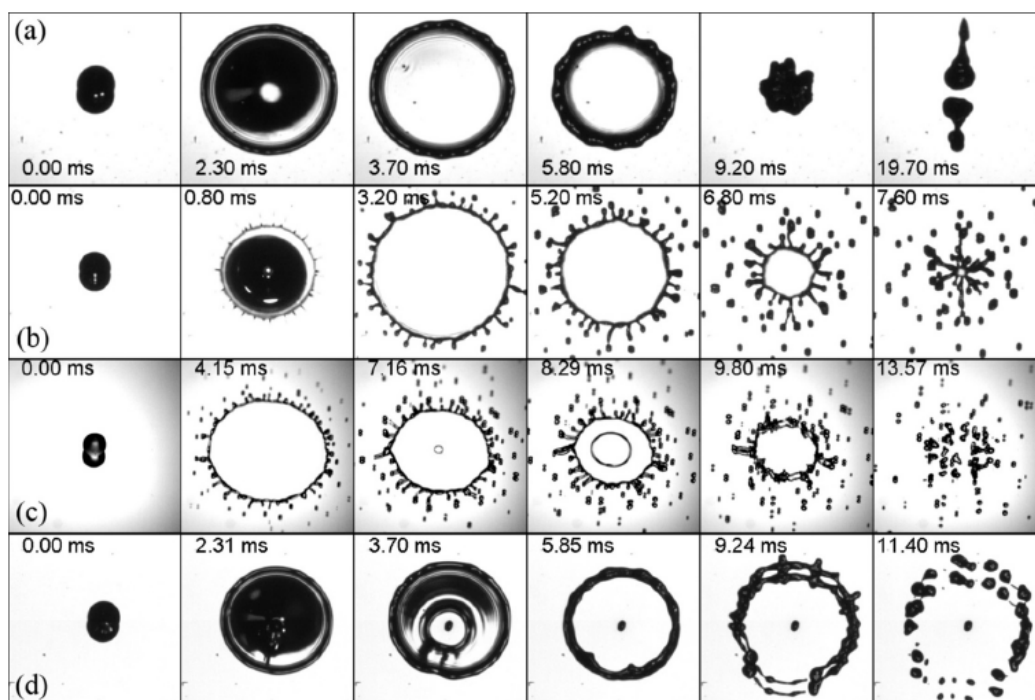


Figure 1.10: Different outcomes of a Leidenfrost drop upon impact depending on the Weber number and surface smoothness a) complete rebound, b) splash, c) splash and hole opening, d) hole opening without splash [Biance 2011].

1.1.3.3 Very cold surfaces

Sublimating surfaces The non-wetting and slip conditions produced by the dynamic Leidenfrost effect were also achieved on very cold substrates [Antonini 2013]. In the same fashion as the Leidenfrost effect, when a drop impacts dry ice, a vapor layer forms between the expanding sheet and the substrate. This vapor layer is caused by the sublimation of the outer layer of the dry ice substrate, which is nothing more than solidified carbon dioxide. The vapor layer thermally insulates the drop from the substrate and prevents interaction between the drop and the surface on which it is impacted.

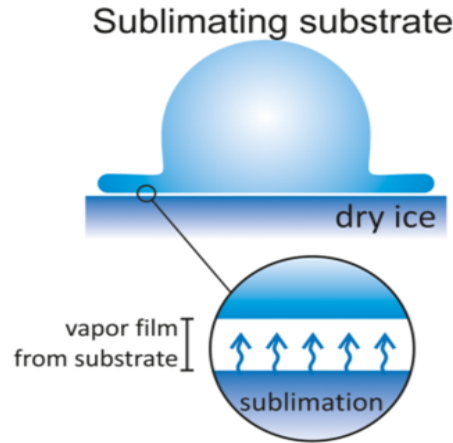


Figure 1.11: Representation of a drop on a sublimating substrate [Antonini 2013].

Antonini et al. compared the outcome of drop impact on the three previously described repellent surfaces: superhydrophobic, superheated and sublimating surfaces [Antonini 2013]. The effect of the different surfaces on the rebound time and maximum expansion are shown in Figure 1.12. Five sets of data are represented on both plots: water drops impacted on dry ice, on a hot plate and on a superhydrophobic surface, and diethylene glycol and propylene glycol drops impacted on dry ice. As a first order interpretation, the results show the same behavior for the three surfaces and the three liquids, even if the authors note and interpret that the rebound time of drops of diethylene glycol ($\eta = 35 \text{ mPa s}$) and propylene glycol ($\eta = 60 \text{ mPa s}$) is under-predicted by their rationalization. They conclude that viscosity has an effect on the drop rebound time, even for impacts on repellent surfaces. On the contrary, the maximum spread factor was not affected by viscosity in the range investigated, since all data for samples impacted in Leidenfrost conditions and on the sublimating surface collapse. The authors note that samples impacted on superhydrophobic surface expanded less and attribute this to the fact that in the case of a superhydrophobic substrate, the non-wetting and slip conditions, obtained for Leidenfrost and sublimating surfaces, are only partially reached due to partial contact between the liquid and the surface. Moreover, the author suggests that the evaporating vapor might drag the liquid along as it radially shoots outwards, leading to more important spreading.

Cold Leidenfrost Nonwetting and slip conditions were obtained by performing the impact on a thin layer of liquid nitrogen [Antonini 2013, Arora 2018]. The liquid nitrogen at a saturation temperature of 196°C evaporates when in the vicinity of a drop, at ambient temperature, causing the drop to rebound after expanding and receding in nonwetting and slip conditions. The perk of this technique is that in that case, as for sublimating surfaces, it is the substrate and not the drop that evaporates to create the insulating

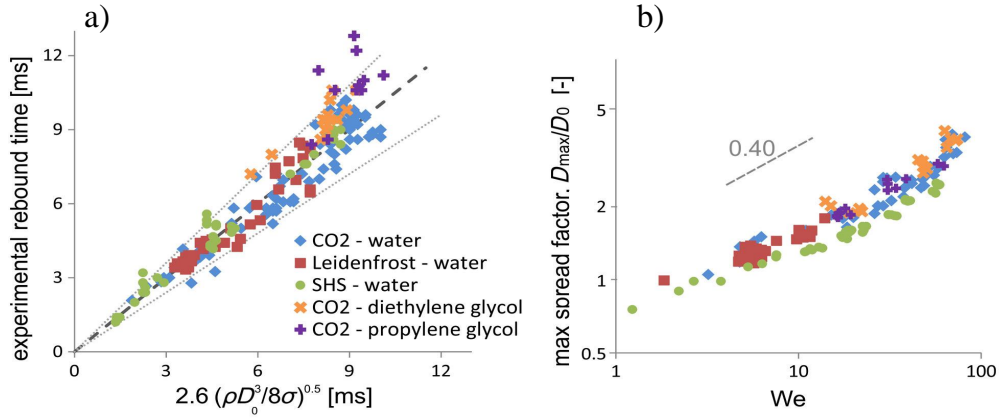


Figure 1.12: a) Rebound time of drops impacted on three different repellent surfaces as a function of $2.6(\rho D_0^3/8\sigma)^{0.5}$ with ρ , the liquid density, D_0 , the initial drop diameter, and σ , the liquid surface tension. b) Maximum spreading factor, D_{\max}/D_0 , versus the Weber number, We [Antonini 2013].

vapor layer. To produce a flat expanding sheet, the quantity of liquid nitrogen must not be too high to avoid the formation of crowns. Crown formation can happen even at relatively low drop impact velocity, due to a splash of liquid nitrogen, which has a very low surface tension (8.9 mN/m) [Antonini 2013]. Figure 1.13 shows snapshots taken from video 8 of the supplementary materials for [Antonini 2013] where a water drop impacts a metal substrate wetted by a thick liquid nitrogen film. On the thick liquid nitrogen film, the crown has a cylinder-like shape and evolves almost perpendicularly to the surface. This cylinder-like crown, which evolves almost perpendicularly to the surface, is somewhat resembling the impact of drops with high We on a thick liquid film [Wang 2000].

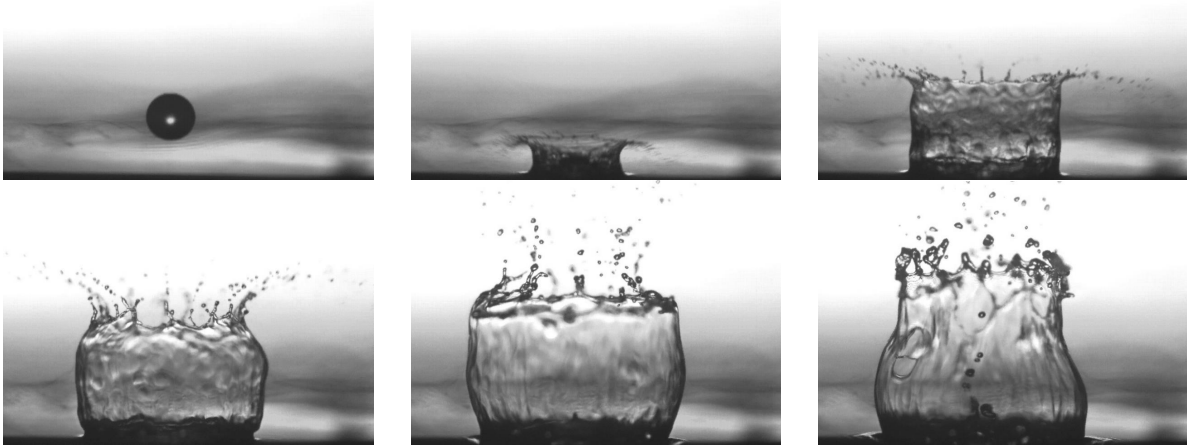


Figure 1.13: Snapshots at different times of a water drop impacting a metal substrate covered with liquid nitrogen (pictures taken from video 8 of the supplementary materials for [Antonini 2013]).

1.2 Fluids

Most studies, on both theoretical and experimental grounds, have been conducted with simple fluids, also called Newtonian fluids, which are characterized by a constant viscosity independent of the shear rate. For such fluids, an important observation is the existence of two regimes in the maximal expansion: a first regime at low viscosity for which the maximal expansion of the sheet did not depend on viscosity (capillary regime) and a second regime for which viscosity had a strong hindering effect on expansion (viscous regime) [Eggers 2010]. In the capillary regime, the expansion is expected to depend on inertia and the fluid surface tension. Additionally, it was also shown that the presence of surfactants in Newtonian fluids do not affect the maximal expansion [Pasandideh-Fard 1996]. The best results for the modeling of the experiments were obtained using the surface tension of pure water and not that of water with surfactants. The fact of considering the dynamic surface tension during drop impact was attributed to the slow diffusion of the surfactants to the surface.

The simple rheological properties of Newtonian fluids make them ideal to achieve a better understanding of the processes occurring during drop impact. On the other hand, the impacts of non-Newtonian drops was not as thoroughly explored, despite being more relevant in industrial processes. We report, here, studies on non-Newtonian fluids drop impacts. These studies are organized by the rheological behavior of the fluids of interest and are non-exhaustive.

1.2.1 Shear-thinning fluids

For non-Newtonian materials, viscosity varies with the shear rate. Fluids for which the viscosity decreases at high shear rates are called shear-thinning. Considering the thinning behavior of such fluids for impact dynamic is crucial, as the rates reached during this process can be very high. It is a complex problem because shear rate varies with space and time during drop impact and sheet expansion and receding. Polymeric fluids (homo polymer solutions or melts) belong to this class of fluids.

Adding a small amount of water-soluble polymer such as polyethylene oxide (PEO) in a drop of water can prevent its rebound when impacting a hydrophobic substrate [Bergeron 2000] or also reduce splashing (see Figure 1.14) [Crooks 2000, Bertola 2012]. Crooks et al. impacted fluids of which they had measured the transient elongational viscosity with an opposed jet rheometer [Crooks 2001]. For increasing ratios of elongational over shear viscosity, they found a decrease of the maximal diameter and the maximal height after rebound reached by drops of dilute polymer solutions after impact. The anti-rebound effect was attributed to the rise in elongational viscosity, as the shear viscosity of these fluid did not change because of the additives.

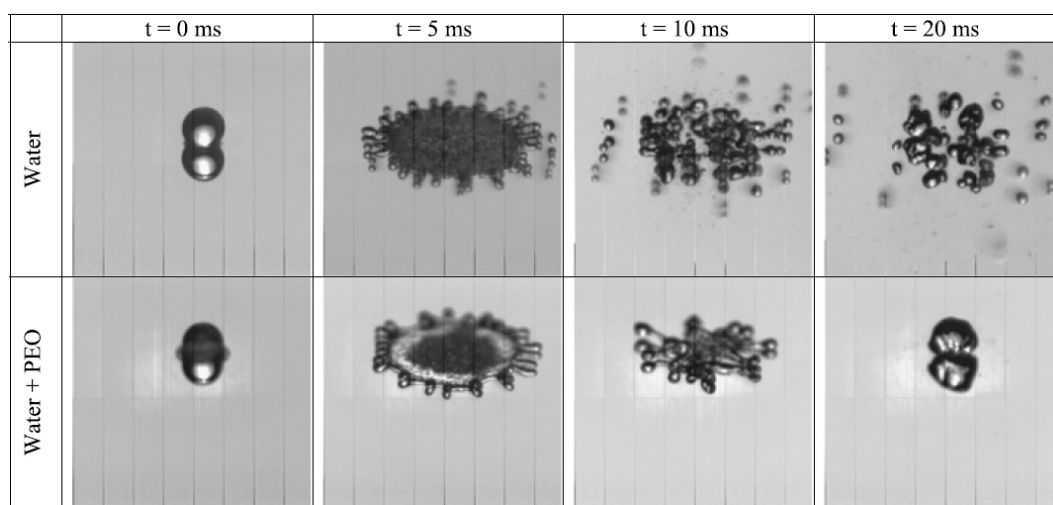


Figure 1.14: Splashing inhibition for a drop impacting onto a hot surface by addition of a minute amount of polymer of high molecular weight [Bertola 2012].

Bertola studied the impact of drops of PEO solution in the Leidenfrost conditions [Bertola 2009]. The author found that the maximal expansion is slightly smaller for the PEO solution than for water, and that the sheet is more stable at high We . He concluded that the energy distribution and dissipation must be different for the two types of fluids. In contrast to the anti-rebound effect observed in previous studies, Bertola observed an enhancement of the drop rebound for high Weber number. This result suggests that the

actual effect, that can be observed thanks to the non-wetting conditions, of elongational viscosity is not as important as it was expected from impact on hydrophobic substrates. Additionally, small concentrations of polymer additives were shown to affect only the receding phase of the impact process [Rozhkov 2003, Bartolo 2007] while larger concentrations influenced both the spreading and receding phases [Rahimi 2011].

An and Lee studied the impact of drops of xanthan solutions and quantitatively compared the impact outcomes with the ones of Newtonian fluids [An 2012]. They showed that the spreading behavior of the shear-thinning fluids can be captured by models developed for Newtonian fluids if one uses an effective shear viscosity defined as the average between the infinite-shear viscosity (viscosity at very high shear rates) and the zero-shear viscosity. Figure 1.15 shows the authors' illustration of the viscosity of a shear-thinning drop during impact.

Another well-known shear thinning fluid is blood. Studying the impact of blood droplets is also of great interest for forensic studies. De Goede et al. compared the splashing behavior of blood and Newtonian drops and found no qualitative differences in the splashing velocity even for different types of substrates [De Goede 2018]. They concluded that blood can be approximated as a Newtonian fluid during splashing.

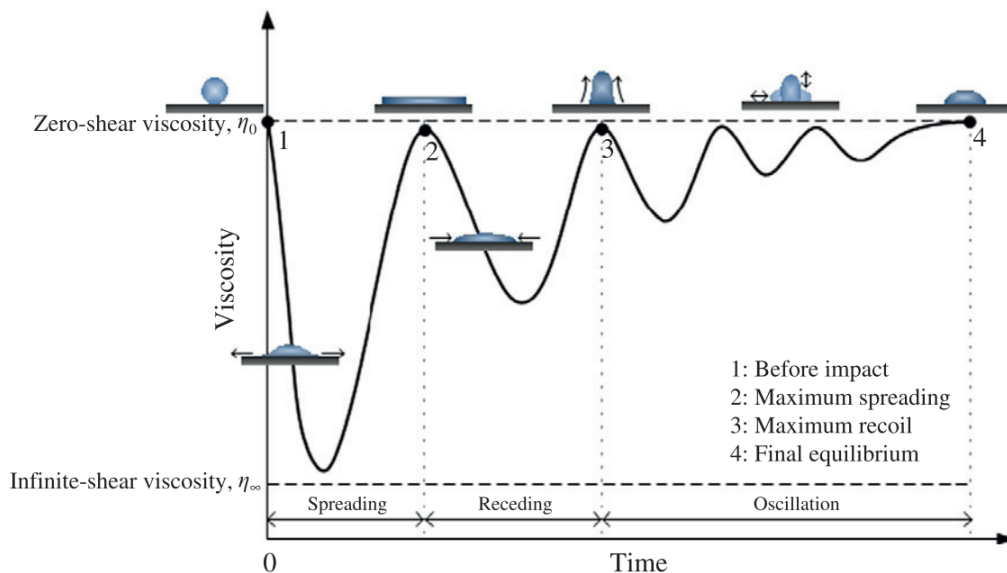


Figure 1.15: Schematic representation of the viscosity variation throughout the impact process for a shear-thinning drop [An 2012].

1.2.2 Shear-thickening fluids

Shear-thickening fluids are less common than their thinning counterparts, and typically show an increase in viscosity as the shear rate increases. The shear rates involved in the drop impact experiments can be easily controlled by increasing the velocity of the impacting drop, which allows one to probe and observe different interesting effects of the shear-thickening nature of such fluids. Bertola and Haw impacted drops of poly-methyl-methacrylate particle suspensions of high concentration over substrates of different wettability [Bertola 2015]. The drops did not exhibit inertial spreading unlike drops of Newtonian and non-Newtonian fluids. On hydrophobic surfaces, the drops relax into a spherical cap shape and stays frozen in this state for several days. This phenomenon was attributed to dilatancy and jamming occurring upon impact. Boyer et al. later impacted concentrated suspensions of cornstarch and polystyrene spheres. They observed the maximal deformation to be independent of the impact velocity and the deformation to suddenly stop during expansion [Boyer 2016]. The authors explained theoretically this phenomenon balancing kinetic energy with the energy dissipated through viscous forces, neglecting the effect of surface tension, which is dominated by the viscous forces.

1.2.3 Yield-stress fluids

Yield stress fluids are relevant for drop impact experiments, as paint belongs to that category of fluids. Yield-stress fluids flow as liquids only for a sufficiently large applied shear stress, and are otherwise predominantly solid. Thus, they behave like an elastic solid or a viscous liquid, depending on the experimental conditions [Luu 2009, Chen 2016].

Luu and Forterre compared the impact of model yield-stress fluids (Carbopol microgel solutions) on smooth and rough hydrophobic surfaces [Luu 2013]. They observed a superspreading (twice the spreading occurring on a smooth surface in the same conditions) regime on the rough hydrophobic surfaces at high Reynolds and Weber numbers, which was attributed to the surface roughness. Very recently, Sen et al. impacted yield stress fluids (Carbopol and Laponite suspensions) with and without aging and found that splashing was suppressed for the aged samples as compared to the unaged ones [Sen 2021]. After considering several hypotheses, the authors found that the most relevant explanation to the evidenced thixotropic effects is an increase in the yield stress σ_y proportional to the aged linear elastic modulus G' .

1.2.4 Maxwell fluids

Maxwell fluids are simple viscoelastic fluids characterized by an elastic modulus, G_0 , and a relaxation time, τ . This type of fluids are interesting for drop impact as their rheo-

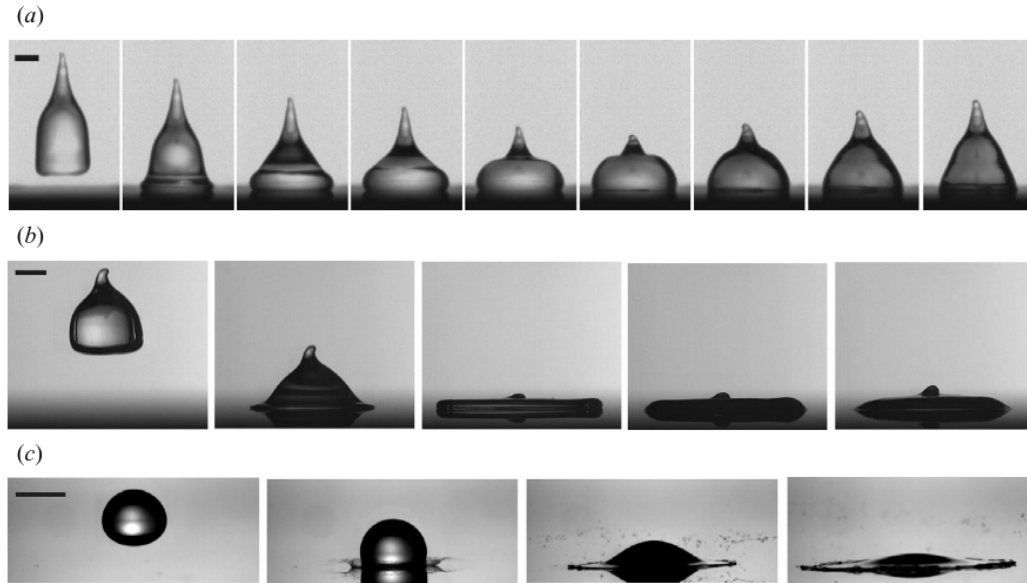


Figure 1.16: Snapshots of impacts on a glass surface of Carbopol in solution for different concentrations and impact velocities (a) 1 wt% and $v_0 = 0.5$ m/s (b) 1 wt% and $v_0 = 2.1$ m/s and (c) 0.2 wt% and $v_0 = 4.3$ m/s. The time interval between the pictures is 4 ms for (a), 5.6 ms for (b), and 0.7 ms for (c). The scale bars are 5 mm [Luu 2009].

logical properties can be tuned in order to access different visco-elasto-capillary regimes. Indeed, for large relaxation times as compared to the time of the experiment, the fluid behaves essentially as a solid and the maximal expansion is expected to be governed by the bulk elasticity. On the contrary, when the relaxation time is much lower than the time of experiment, the fluid can be assimilated to a viscous fluid. In this case, the maximal expansion is expected to be governed by capillarity or viscosity as for Newtonian fluids.

Arora and coworkers have studied the impact dynamics of viscoelastic fluids obtained by reversibly crosslinking micelles or oil droplets stabilized in water with block copolymers [Arora 2016, Arora 2018]. The linear viscoelastic behavior of these fluids can be accounted for by a Maxwell fluid model. When impacting on a small target, the authors found that for the fluids whose relaxation time is lower than the typical lifetime of the sheet (Micelles C_{12} and Microemulsions C_{12} in Figure 1.17), the maximal expansion is the same as for a Newtonian fluid with an equal zero-shear viscosity [Arora 2016]. On the other hand, they observed a deviation of the maximal expansion for samples with relaxation times larger than the typical lifetime of the sheet (Micelles C_{18} and Microemulsions C_{18} in Figure 1.17) with respect to Newtonian fluids. Indeed, the maximal expansion for these fluids was strongly enhanced as compared to Newtonian fluids and Maxwell fluids whose relaxation time is lower than the typical lifetime of the sheet. Arora et al. accounted for the samples' viscoelasticity by considering the dynamic viscosity, defined as $\eta' = \frac{G''(\omega)}{\omega}$ where $G''(\omega)$ is the loss modulus and ω , is the frequency. η' is evaluated at

$\omega = \frac{1}{t_{\max}}$, to consider relevant timescale for the impact. The experimentally acquired data collapsed when plotted as a function of this relevant dynamic viscosity (see Figure 1.17 b)).

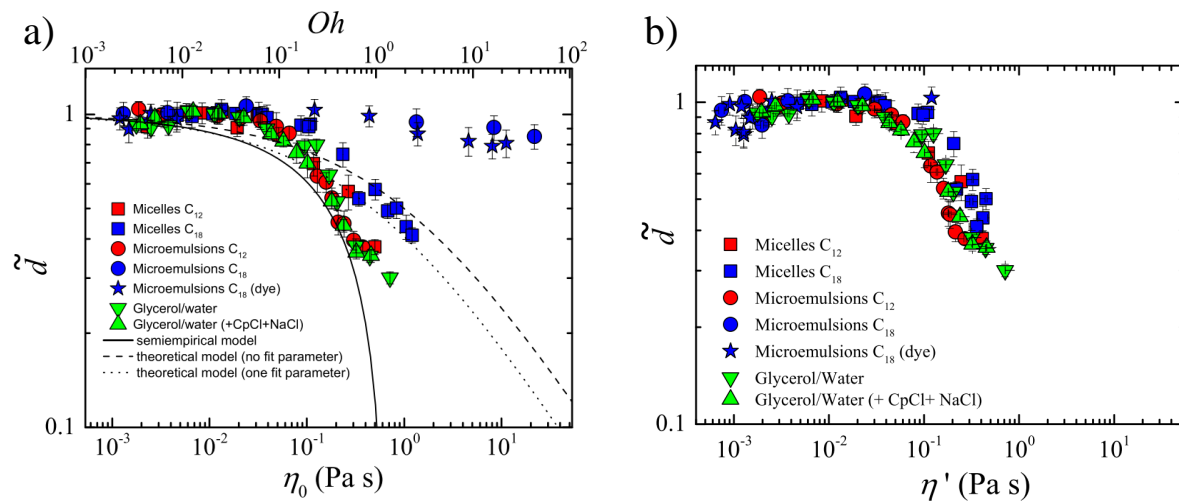


Figure 1.17: Maximum diameter (normalized by its value at low viscosity) for Newtonian and viscoelastic fluids impacted on a small target as a function of a) the zero-shear viscosity, η_0 and b) the dynamic viscosity, η' [Arora 2016].

The viscoelastic samples with relaxation times larger than the typical lifetime of the sheet, which can thus be considered as elastic beads, were also impacted in cold Leidenfrost conditions [Arora 2018]. Along with the viscoelastic samples, Newtonian liquids in the capillary regime and ultra-soft elastic beads were also impacted. For these three types of fluids and condition of impact, the viscous dissipation is assumed to be negligible. The authors provided a universal law in which the maximal spreading factor, $\frac{d_{\max}}{d_0}$, varies as the ratio of the impact velocity to a new characteristic velocity, U^* , of the material for generalized elastic deformations. $U^* = \sqrt{U_L^2 + U_S^2}$, where $U_L = \sqrt{\frac{3\gamma}{\rho d_0}}$ is the typical velocity of free oscillations of a drop and $U_S = \frac{G_0}{\rho}$ is the velocity of transverse sound waves in the elastic medium. G_0 is the shear modulus of the network. This law extends previous descriptions of the physics of impact, which rationalize the maximal extension of Newtonian fluids of low viscosity with surface tension [Biance 2006] and of soft elastic beads with bulk elasticity [Tanaka 2003, Tanaka 2005]. This unified description predicts, equally well, the maximum diameter reached by Newtonian fluids in the capillary regime, Maxwell fluids (with characteristic relaxation times much larger than the time of impact) or ultra-soft solids, but it neglects the viscous dissipation. This assumption is indeed reasonable for the fluids considered, but reaches its limit for viscoelastic fluids for which the viscous and elastic effects are of comparable magnitude and for more viscous Newtonian fluids. Developing a model to predict the maximal expansion of fluids, where both elasticity and viscosity are expected to play a role, will be the objective of a chapter of this thesis.

1.3 Experimental outputs and modeling

1.3.1 Expansion dynamics

Numerous theoretical predictions [Josserand 2016] and numerical simulations [Wang 2019, Wang 2020b, Wang 2020a] of the impact process of Newtonian fluids generally aim to predict the maximum spreading factor β_{\max} reached by the sheet as a function of combinations of characteristic dimensionless numbers (Reynolds, Weber and Ohnesorge numbers). In their table, displayed in Figure 1.18, Josserand and Thoroddsen present a few of the most commonly used formulas in the literature to fit the experimental/numerical results for β_{\max} of Newtonian drops [Josserand 2016].

Model	Expression	Comment
Scheller & Bousfield (1995)	$\beta_{\max} \sim 0.61 (Re^2 Ob)^{1/6} = 0.61 Re^{1/5} (We Re^{-2/5})^{1/6}$	Empirical law based on experimental results
Pasandideh-Fard et al. (1996)	$\beta_{\max} = \sqrt{\frac{We+12}{3(1-\cos\theta_d)+4(We/\sqrt{Re})}}$	Detailed energy balance, including contact angle (θ_d), and initial conditions
Ukiwe & Kwok (2005)	$(We+12)\beta_{\max} = 8 + \beta_{\max}^3 \left(3(1 - \cos\theta_d) + 4\frac{We}{\sqrt{Re}}\right)$	Extension of the above model, with θ_d the dynamical contact angle during spreading
Clanet et al. (2004)	$\beta_{\max} \propto We^{1/4}$	Mass balance using the impact capillary length
Roisman (2009)	$\beta_{\max} \sim 0.87 Re^{1/5} - 0.4 Re^{2/5} We^{-1/2}$	Formula obtained using a dynamical model for the spreading of the drop involving a viscous boundary layer
Eggers et al. (2010)	$\beta_{\max} = Re^{1/5} f(P)$	Similar approach to that in Roisman (2009); impact number P is defined by $P = We Re^{-2/5}$

Figure 1.18: Different models for β_{\max} as a function of the impact parameters adapted from [Josserand 2016].

Many models were developed from various approaches, and they all are very much different in the way that they are formulated. Nevertheless, they all give results in reasonably good agreement with the experimental and numerical data, making it difficult to discriminate between the different approaches. Indeed, the maximal diameter reached by the drop upon impact does not vary by many orders of magnitude and power law scaling are thus difficult to evaluate. Furthermore, at high We , splashing occurs, making these asymptotic relations unverifiable. In addition, most asymptotic models usually

neglect the initial drop radius, which should be taken into account in order to properly establish a relation between β_{\max} and the impact parameters [Josserand 2016].

Semi-empirical models based on the length scales typically encountered in drop impact experiments generally separate the problem in two regimes: a capillary regime where β_{\max} depends only on We and a viscous regime for which β_{\max} depends on Re solely [Eggers 2010]. Three modes of spreading can be considered [Yarin 2017]. In the first mode, for which We and Re are relatively small, β_{\max} is governed by the viscous and capillary forces. The second mode considers the situation in which the capillary forces govern the maximal expansion. Finally, the third mode considers the case where only the viscous effects control β_{\max} . In this third mode, We is infinite and, in this limit, Roisman estimates $\beta_{\max} \propto Re^{1/5}$. He then corrects his prediction to account for the finiteness of We by estimating the typical length scale associated with the rim motion. Fitting the experimental data acquired in different works by different groups [Roisman 2002, Pasandideh-Fard 1996, Cheng 1977], Roisman obtains the expression reported in the table in Figure 1.18 and plotted against the data in Figure 1.19.

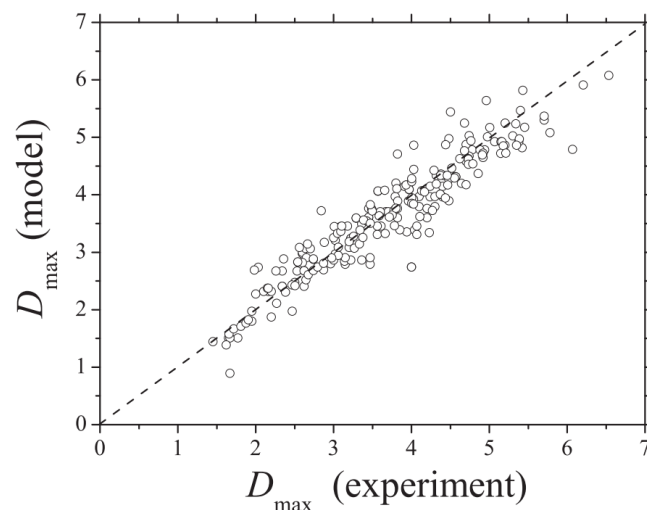


Figure 1.19: Comparison of the theoretical values obtained with the expression from Roisman for β_{\max} (see Figure 1.18) with the experimental data from [Roisman 2002, Pasandideh-Fard 1996, Cheng 1977] [Roisman 2009]. Here, the ratio of the maximal diameter of the sheet to the initial diameter of the drop (β_{\max} in the text) is D_{\max} .

Among all approaches to predict the maximal expansion of an impacting drop, the energy balance is widely used with the advantage that it can generally be easily adapted to new scenarios. During the expansion, the kinetic energy accumulated by the drop during its fall is partially stored into surface and bulk elasticity and lost by viscous dissipation. The energy balance approach considers the kinetic energy and surface energy of the drop before and during impact, as well as the energy lost throughout the expansion by viscous

dissipation. To predict the maximal spreading factor, $\beta_{\max} = \frac{d_{\max}}{d_0}$, these models consider different simplifying geometries of the sheet (see Figure 1.20), allowing to estimate the different energies at play [Attané 2007].

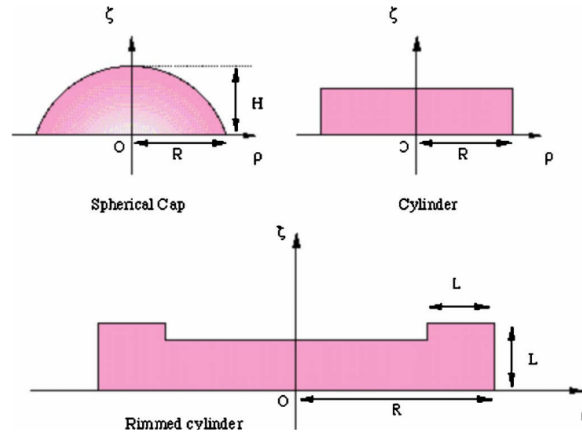


Figure 1.20: Different possible simplifying geometries used to model the expanding sheet with the energy balance considerations: spherical cap, cylinder and rimmed cylinder [Attané 2007].

A limitation of energy balance-based models is that one needs to know the velocity field to correctly estimate the dissipated energy [Yarin 2017]. Moreover, energy balance models do not usually account for the edge effects associated with the formation of the rim, which were shown to be significant [Roisman 2009]. Furthermore, several numerical and experimental studies have found that, even if friction at the solid surface is negligible, approximately half of the initial kinetic energy is lost upon impact and not converted into surface energy regardless of the properties of the liquid or impact velocity (for We between 30 and 3000) [Wildeman 2016, Padmanathan 2019]. This energy loss was attributed to internal flows in the drop. Unfortunately, such energy losses are usually not accounted for in the existing models. Despite the difficulty to account for the energy loss, the predictions obtained with models based on energy balance arguments show reasonable agreement with experiments and numerical simulations [Josserand 2016].

Harmonic oscillator model The drop impact dynamic is quite complex, which makes the following model stand out because of its notable simplicity. A harmonic spring model (as represented on Figure 1.21) was first proposed by Richard and coworkers to rationalize the contact time of a bouncing drop [Richard 2002]. This phenomenological model was later used to represent the drop expansion and bouncing by the motion of a spring-mass system of which the stiffness is proportional to the surface tension for the Newtonian drops of low viscosity impacting a super-hydrophobic substrate or in Leiden-

frost conditions [Okumura 2003, Biance 2006]. For soft elastic beads impacting a rigid surface, the stiffness is proportional to the elastic modulus [Tanaka 2003, Tanaka 2005]. In these systems, the effect of viscosity could be ignored. More recently, this model was used by Arora et al. to model the expansion of ultra-soft elastic beads and viscoelastic fluids, with long relaxation times with respect to the duration of the impact experiment, in cold Leidenfrost conditions. In this model, the spring constant includes the surface tension and the elastic modulus while neglecting the viscous dissipation [Arora 2018]. The unified description of Arora and coworkers predicts satisfyingly the maximal expansion reached by the sheet, as well as the time at maximal expansion. The spring model has been recently adapted to account for viscous dissipation in the rebound of Newtonian fluids with viscosity up to 200 mPa s by adding, to the model, a Stoke friction force calculated for the initial drop [Jha 2020]. These models, although successful in predicting the rebound time or expansion of the fluids investigated, do not hold out for very viscous fluids ($\eta > 200$ mPa s) and more complex viscoelastic fluids for which the role of bulk elasticity, surface tension and viscosity in the expansion dynamics is non-trivial.

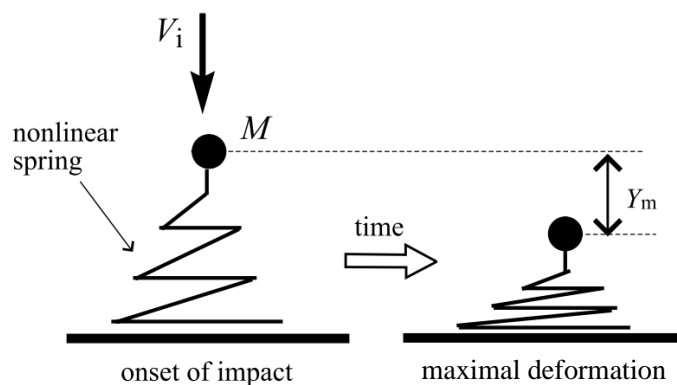


Figure 1.21: Schematic representation of the mass-nonlinear-spring model from [Tanaka 2005]. V_i is the initial velocity, M , the mass of the mass-point and Y_m , the maximum vertical displacement of the mass point.

1.3.2 Thickness field of the sheet

Beside the expansion diameter of the sheet, another very interesting parameter to follow is the thickness field of the expanding drop. The sheet morphology differs from a simple disk of uniform thickness. To comprehend this behavior, endeavors were made to obtain experimental measurements and kinematic descriptions of the time resolved thickness field of the sheet.

Using the Fourier transform profilometry technique, Lagubeau et al. measured the time resolved thickness field of drops of glycerol/water mixtures impacting on a flat hydrophobic surface [Lagubeau 2012]. Their experimental set-up and the profiles they obtained are depicted in Figure 1.22. They showed that the sheet reaches a residual minimal film thickness, of the order of $200 \mu\text{m}$, governed by the growth of a viscous boundary layer from the surface. Lagubeau et al. show that the thickness field of the sheet has a self-similar behavior, as evidenced numerically beforehand [Roisman 2009, Eggers 2010], followed by a viscous regime once the residual minimal film thickness is reached. Thus, the thickness field is partially hindered by a boundary-layer effect giving a minimal film thickness, which scales as $\text{Re}^{-2/5}d_0$.

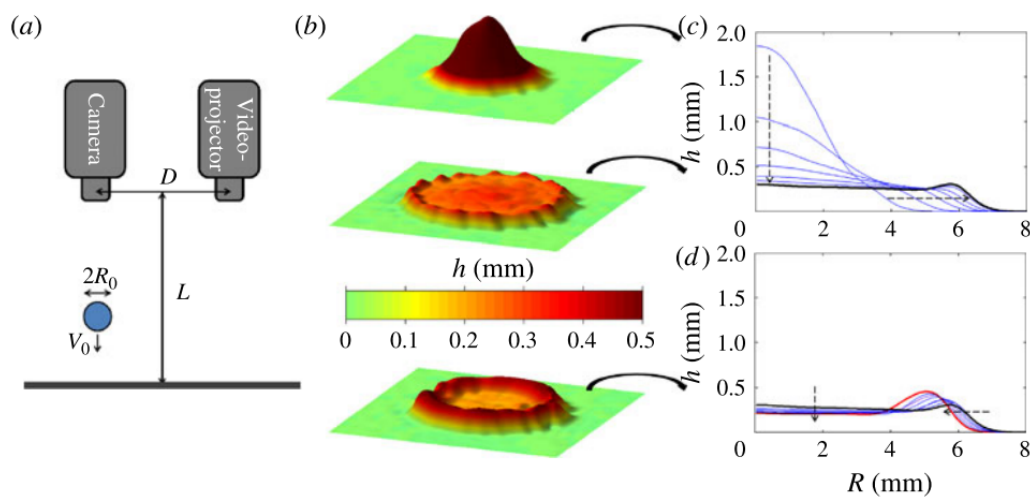


Figure 1.22: (a) Experimental set-up for thickness field measurement by profilometry. (b) Height mapping of the drop at different times. (c) and (d) Successive thickness profiles in function of the radial position [Lagubeau 2012].

Lastakowski et al. measured the thickness field of impacting drops of different liquids (ethanol, isopropanol–glycerol mixtures) onto superheated and room temperature surfaces using dye adsorption [Lastakowski 2014]. The local thickness field was used alongside the local flow velocity to model the global behavior of drop expansion. An interesting result is that the time evolution of the thickness of the center part of the sheet follows a power-law decay in good agreement with theoretical predictions and with an exponent -1.7 for Leidenfrost impacts. Lastakowski et al. deduce analytically the evolution of the lamella thickness and obtain a self-similar profile analogously to [Roisman 2009, Eggers 2010, Lagubeau 2012] with almost no viscous coupling between the drop and the substrate and when a viscous boundary layer can develop from the liquid-solid interactions at the surface. In the situation where a viscous boundary layer can develop, the authors found that a saturation thickness, h_f , is reached at the coalescence of the viscous boundary layer and the sheet thickness in the inviscid case, giving the

dependence $h_f \simeq Re^{-2/5}$.

Vernay et al. measured the thickness field of a drop of water with erioglaucine disodium salt, a dye which allows visualization of the thickness field variation by transmittance [Vernay 2015a]. The authors evidence two asymptotic regimes at short and long times, which are delineated by the time, t^* , at which they observe a maximum of the film thickness for a given radial position. At $t < t^*$, the thickness of the sheet, h , is proportional to t/r^3 , with r , the radial position, as predicted theoretically by [Rozhkov 2004] and at $t > t^*$, $h \propto 1/rt$ as theoretically predicted by [Villermaux 2011].

Later, Wang and Bourouiba unified the two predictions from [Rozhkov 2004] and [Villermaux 2011] into a self-similar solution for the thickness profile of a liquid sheet expanding in air [Wang 2017]. They found a good agreement of their unified self-similar solution with their impact experiments performed on a range of surface-to-drop size ratios and with the experiments of [Vernay 2015a].

1.3.3 Rim bounding the sheet

At the free edges of a liquid sheet, the capillary forces, opposing the inertia of the liquid, are responsible for the emergence of a thicker rim propagating, with a finite velocity, toward the sheet [Yarin 2017]. The thicker rim surrounding the sheet is often assimilated to a toroid of circular cross-section (see Figure 1.23). Instabilities in this rim are known to be driven by both the Rayleigh-Taylor and Rayleigh-Plateau mechanisms. They lead to splashing [Krechtnikov 2010]. Understanding the mechanism of rim destabilization into smaller droplets during impact is important for a wide range of industrial processes such as paint, coating, and combustion, but also to understand the propagation mechanism of diseases in the air. Indeed, the secondary droplets resulting from the fragmentation of the rim can travel on over long distances to convey plant diseases in the air due to rain droplets impacting the leaves [Gilet 2015].

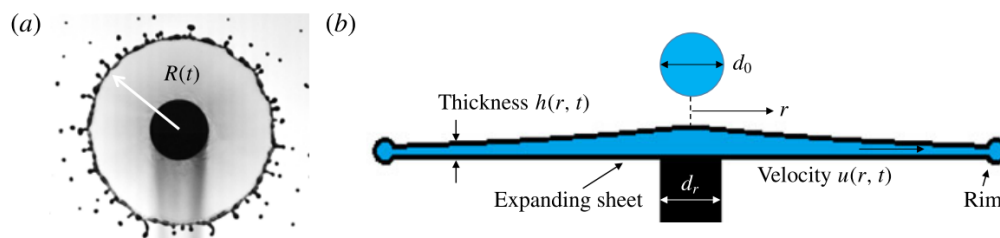


Figure 1.23: (a) Dyed water sheet expanding after impact on a small target. (b) Schematic representation of the expanding sheet cross-section. [Wang 2017]

The rim is the critical link between the sheet and droplets, and its destabilization has been extensively investigated. For example, Villermaux and Bossa discussed the reasons of rim destabilization and reported experimentally the evolution of the radius of the sheet, its stability and the resulting fragment drop size distribution [Villermaux 2011]. Later, Wang et al. have come up with a criterion predicting the unsteady fragmentation of the sheet where the thickness is governed by a local instantaneous Bond number equal to unity and calculated with the instantaneous local rim acceleration [Wang 2018]. Very recently, Wang and Bourouiba have physically explained the birth, growth and breakup of filaments from the rim [Wang 2021a].

On the other hand, very little research have taking interest in the growth dynamics and shape of the rim during the expansion of a liquid sheet without destabilization. In their paper about water spreading on glass, Roux and Cooper-White reported the rim thickness (which they call foot thickness) from side view imaging for several impact velocities [Roux 2004]. As it can be seen in Figure 1.24, the thickness grows approximately linearly with time until reaching a maximum value. This maximum value was found to decrease as the impact velocity increased. Additionally, they found that the rate at which the rim thickness grows also decreases when the impact velocity increases.

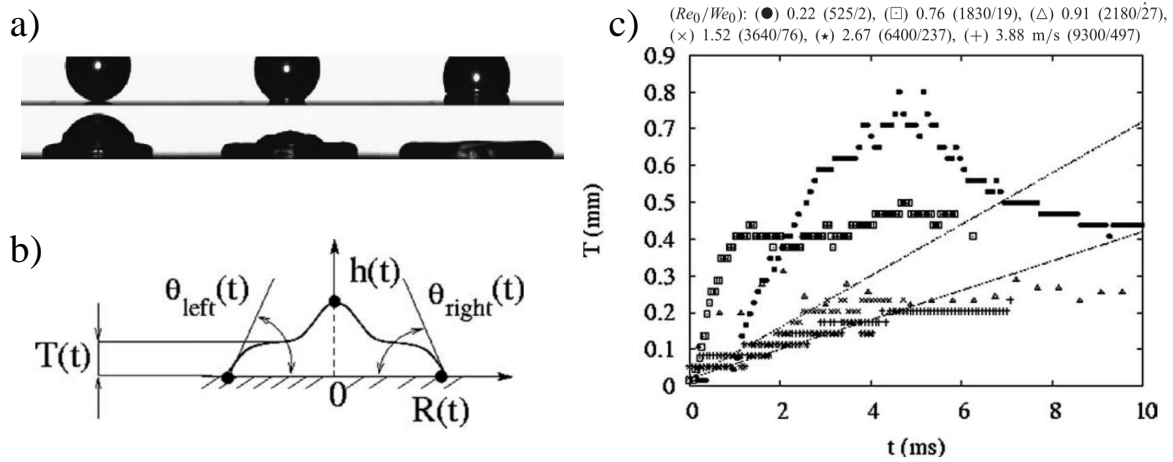


Figure 1.24: a) Snapshot of a water drop impacting a glass surface at $v_0 = 0.76$ m/s. b) Schematic representation of the side view of an expanding drop with the expanding radius, $R(t)$, the height, $h(t)$, the foot thickness, $T(t)$, and the apparent contact angles $\theta_{\text{left}}(t)$ and $\theta_{\text{right}}(t)$. c) Time evolution of the foot thickness for different impact velocities [Roux 2004].

Later, de Ruiter et al. also measured the height of the rim from side view imaging but at early times ($t < t_{\text{col}} = \frac{d_0}{v_0}$ with d_0 , the initial diameter of the drop, and v_0 , the impact velocity) for methanol, ethanol, and isopropanol drops impacting a mirror at different impact velocity [de Ruiter 2010]. They observed, at low impact velocity (0.9, 1 and 1.2

m/s), the same monotonic increase of the thickness with time and decrease with increasing impact velocity. At higher impact velocity (1.4, 1.5 and 1.6 m/s), however, a plateau is observed in the time evolution of the thickness.

Eggers et al. developed a model for the rim dynamics by writing the mass and momentum balance at the rim [Eggers 2010]. They evaluated the volume, considering the rim as a torus. Their model predicts the rim size and mass to grow only during the receding regime of the sheet.

Ogawa et al. measured the time evolution of the cross-sectional radius of the rim from a sheet formed by the impact of a glycerol/water mixture on a small target [Ogawa 2018]. This cross-sectional radius was obtained by averaging the rim width over each angular position from 0 to π . The authors show a deviation of the experimental measurements of the cross-sectional radius with half of the capillary length as expected from the prediction of [Wang 2018]. Indeed, the latter claim that the cross-sectional diameter of the rim corresponds to the capillary length based on the edge deceleration only for a local rim Reynolds number of 8.5, which is not the local rim Reynolds number obtained by [Ogawa 2018]. Additionally, they derive an expression for the radial velocity of the liquid entering the rim from the sheet and for the sheet thickness in contact with the rim from the volumetric flow rate of the fluid entering the rim. This volumetric flow rate is calculated using the measured cross-sectional radius of the rim and the sheet radius, considering the rim to be a torus.

Very recently, Wang used their "Advanced Image Processing" algorithm to measure the width, height and volume of the rim and fingers during unsteady fragmentation of dyed water drops impacted on a small target [Wang 2021b]. Their algorithm separates the ligaments from the rim and measures the rim thickness for each angular position. The width of the ligament is averaged along its length, which is given by the curvilinear distance from root to tip. Finally, the volumes of the rim and of the ligaments are calculated assuming an axisymmetric circular cross-section. The rim is thus assimilated to a torus. They found that the thickness of the sheet at the rim scales with We^{-1} and show that the volume of fluid shed from the rim, at all time, is of the same order of magnitude as the rim volume itself. Wang and Bourouiba theoretically predict the rate of volume injection into the rim, Q_{in} , as well as the cumulative volume fraction entering the rim, Ω_{in}/Ω_0 . They confront the theory with their experimental data for water drops impacted at different Weber numbers and show good agreement as well as no dependence of Q_{in} and Ω_{in}/Ω_0 with We . Figure 1.25 shows a schematic drawing of the sheet with b , the width of the rim, q_{out} and q_{in} , the rate of fluid volume leaving and entering the rim respectively, r the radial axis, r_0 , the initial radius of the drop and r_s , the radius of the sheet along with experimental measurements confronted to theoretical rationalizations.

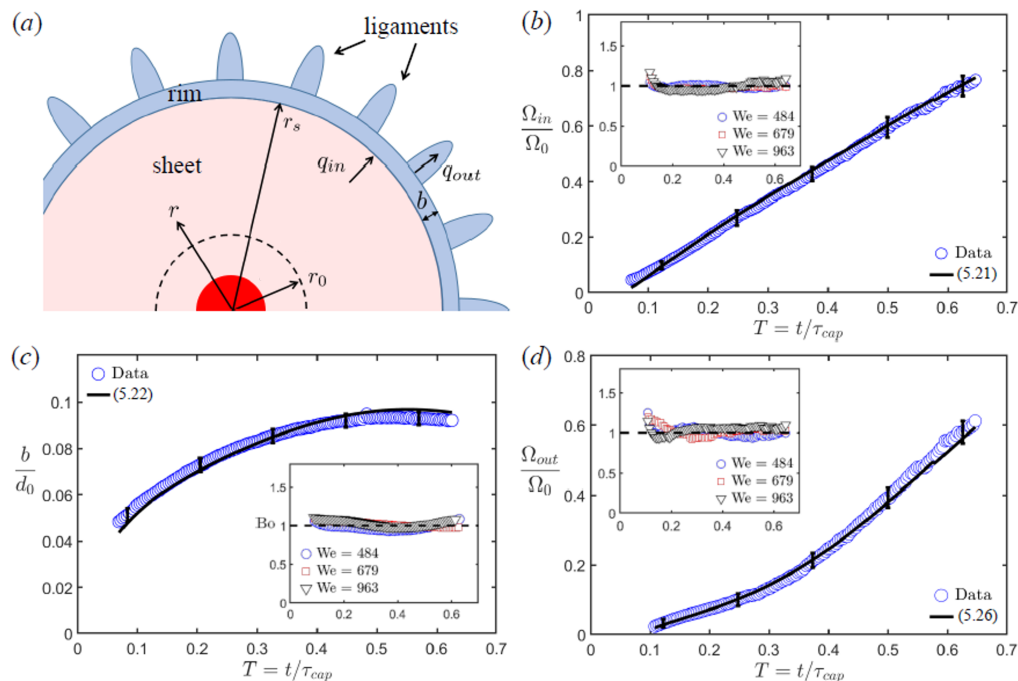


Figure 1.25: (a) Schematic representation of the sheet. (b) The cumulative fluid volume, Ω_{in} , entering the rim from the sheet normalized by the initial volume of the drop, Ω_0 , (c) the rim thickness, b , normalized by the initial drop diameter, d_0 , and (d) the cumulative volume, Ω_{out} , shed from the rim normalized by Ω_0 as a function of time normalized by the capillary time, τ_{cap} . The solid lines are the theoretical predictions for $We = 679$. In the insets, the experimental values are normalized by their theoretical predictions. [Wang 2021b]

1.4 Motivations

We have seen that many experimental configurations have been developed to study various outcomes of the impact of Newtonian and viscoelastic drops, as well as elastic beads. The field is, in fact, not exhaustive and allows for much development. The dynamics of water drop impact is very well documented and understood, allowing researchers to go further in the understanding of complex fluids dynamics upon impact. Yet, the way we should account for dissipation and elasticity in the expansion dynamics of Newtonian and viscoelastic fluids is still unclear. In this thesis, we will try to answer remaining open questions in the field by selecting the experimental set-ups and fluids to be in the optimal conditions.

An objective of this thesis is to provide deeper understanding of the dissipation process during drop impact not only for Newtonian fluids but also for viscoelastic fluids. We impact rheo-thinning fluids, which are the most important class of complex fluids, and Newtonian fluids with viscosities spanning over three orders of magnitude, first,

in simplified, repellent conditions to evaluate the dissipation due to biaxial extensional deformation. Thereafter, the same fluids are impacted on small solid targets of increasing sizes, playing with the mixed flow field which combines biaxial extensional and shear dissipation. This competition between shear and biaxial extensional viscous dissipation within the framework of impact dynamics is investigated for the first time, to the best of our knowledge, in this thesis.

Complex fluids are further investigated and reveal the effect of a non-trivial combination of viscosity, capillarity and bulk elasticity on the expansion dynamics. The fluids considered in this part of the thesis are model Maxwell fluids, which have been carefully home-synthesized in order to finely tune the relaxation time and elastic modulus, thus giving access to different visco-elasto-capillary regimes. They are characterized by low elastic moduli, and relaxation times varying over almost two orders of magnitude. The impacts are performed on a repellent surface to simplify as far as possible the experimental conditions and thus obtain a better understanding of the effect of the fluid properties on the expansion dynamics.

Moreover, the rim was not thoroughly studied and measurements of the rim shape are still missing to fully understand the rim dynamics during sheet expansion after drop impact. We thus take the opportunity provided by the configuration of our experimental set-up for drop impact in cold Leidenfrost conditions to improve knowledge about the rim dynamics.

Beside being relevant to numerous industrial processes, drop impact experiments is a great tool to probe the mechanical properties of viscoelastic fluids and ultra-soft solids under equibiaxial extensional deformation. Despite being ubiquitous in the processing of polymeric materials, measurements of rheological properties of viscoelastic fluids and ultra-soft solids under equibiaxial extensional deformation are limited. Indeed, obtaining well-controlled equibiaxial elongational deformations in the laboratory is challenging. Several solutions exist such as bubble inflation [Joye 1972, Maerker 1974, Johnson 2016], lubricated squeezing flow [Huang 1993, Venerus 2010, Venerus 2019], opposite nozzle flow [Cathey 1988, Walker 1996] or spinning drop apparatus [Joseph 1992, Pieper 1998, Xie 2017] but they all have their drawbacks. The work in this thesis will also be considered with this in mind. This is why the deformation of soft polyacrylamide beads in a spinning drop apparatus is investigated, deepening our comprehension over the biaxial extensional deformation obtained during drop impact.

Materials and methods

Contents

2.1	Methods	33
2.1.1	Measure of surface tension	33
2.1.2	Rheology	37
2.1.3	Set-ups for drop impact experiments	42
2.1.4	Image analysis for drop impact	49
2.2	Materials	57
2.2.1	Newtonian fluids	57
2.2.2	Self-assembled transient networks	58
2.2.3	PEO solutions	65
2.2.4	2, 4-bis (2-ethylhexylureido) toluene (EHUT)	67
2.2.5	Ultra soft elastic beads	70

The first part of this chapter is dedicated to the description of the different methods and set-ups employed to characterize the samples. The second part of the chapter gives a complete description of the chemical systems studied in this thesis.

2.1 Methods

2.1.1 Measure of surface tension

Interfacial tension is a phenomenon that, at the molecular level, results from the difference in energy between molecules at a fluid interface when compared to their bulk counterparts. It is equally correctly described as a measure of how much energy is required to make a unit area of interface between two immiscible liquids. Knowing the surface tension of our systems is crucial for the rationalization of our experimental results because when the drop expands following its impact on a surface, the material surface increases, resulting in enhanced surface energy. Here, we present different techniques used to measure the steady and dynamic surface tension of the air/sample interface.

2.1.1.1 Pendant drop

Measurements of the surface tension at equilibrium are performed optically using the profile analysis tensiometer, PAT1M, from Sinterface. This equipment analyzes the shape of a drop hanging from a needle. This shape is determined by the balance of forces, particularly surface tension and gravity. The surface tension aims to minimize the surface area by conferring a spherical shape to the drop, while gravity elongates the latter. The analysis of the drop shape is based on the Young-Laplace equation which relates the pressure difference, ΔP , between the inside, P_{in} , and outside, P_{ext} , to the curvature of the interface.

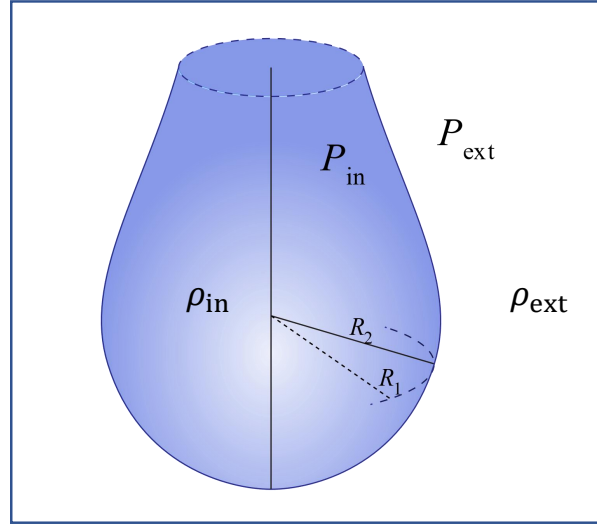


Figure 2.1: Schematic representation of a pendant drop.

$$\Delta P = P_{\text{int}} - P_{\text{ext}} = \gamma \left(\frac{1}{R_1} + \frac{1}{R_2} \right) \quad (2.1)$$

with γ , the surface tension and R_1 and R_2 the principal curvature radii of the drop (Figure 2.1). After numerical resolution of the Young-Laplace equation, the surface tension can be related to the drop shape by the equation

$$\gamma = \frac{\Delta \rho g R_0^2}{\beta} \quad (2.2)$$

with $\Delta \rho = \rho_{\text{in}} - \rho_{\text{out}}$, the density difference between the inside and outside of the drop, g , the gravitational force, R_0 , the drop radius of curvature at the apex and $\beta = \frac{\Delta \rho g R_0^2}{\gamma}$, the bond number introduced in 1883 by Bashforth and Adams [Berry 2015]. It is important for this technique to have no elasticity in the fluid as the resulting complex inertial flow fields might inhibit analysis using the equilibrium Young-Laplace equation [Berry 2015].

For this reason, the surface tension of the viscoelastic fluids in this thesis are measured on samples in the very dilute regime.

2.1.1.2 Dynamical surface tension measurements

In the case of drop impact experiments, the relevant surface tension quantity should be taken from the dynamic measurement of surface tension as the impact event lasts around 10 ms. For surfactant-based samples, this dynamic value of surface tension is different from its equilibrium value [Zhang 1997]. Here, we measure the dynamic surface tension with the bubble pressure method and compare the time corresponding to drop impact dynamics to the surface age of the bubble in the maximum bubble pressure measurements.

In the maximum bubble pressure method, a capillary is partially immersed in a bath of the liquid of interest. Air is then expelled from the capillary into the liquid, creating a bubble. The pressure inside of the bubble is measured by a manometer at the tip of the capillary and depends on the bubble curvature radius, r_B . As the air is blown inside the bubble, the curvature radius decreases until reaching a minimum which corresponds to the radius of the capillary, R_{Kap} . At this point, the pressure in the bubble is maximum, as depicted in Figure 2.2, and the surface tension can be evaluated using the Young–Laplace equation for spherical bubble shape within the liquid:

$$\gamma = \frac{R_{\text{Kap}}}{2} (P_{\text{max}} - P_{\text{min}}) \quad (2.3)$$

After this, the bubble quickly increases in size before detaching from the capillary tip allowing a new bubble to take its place.

At a newly created interface with a liquid containing surfactants molecules, the interfacial surface tension gradually decreases as the surfactant molecules move towards the interface until the interfacial surface tension reaches its equilibrium value. The time to reach the equilibrium surface tension depends on the bulk surfactant concentration and the mobility of the surfactants in the liquid. By varying the bubble lifetime, we have access to a dynamic measurement of the surface tension since r_B will reach R_{Kap} after more or less time. The resulting variation of the surface tension with time can be fitted with the equation [Xi Yuan Hua 1988]

$$\gamma - \gamma_{\text{inf}} = \frac{\gamma_0 - \gamma_{\text{inf}}}{1 + \left(\frac{t}{t^*}\right)^n} \quad (2.4)$$

With γ_{inf} , the equilibrium value of the surface tension, γ_0 , the surface tension of the solvent, t^* , a fitting parameter with units of time and n , a fitting exponent.

The dynamic surface tensions measurements were performed using a maximum bubble pressure tensiometer from Sita (with a resolution of 0.1 mN/m for the surface tension and 1 ms for the bubble lifetime) as part of an industrial secondment at DSM, in The Netherlands.

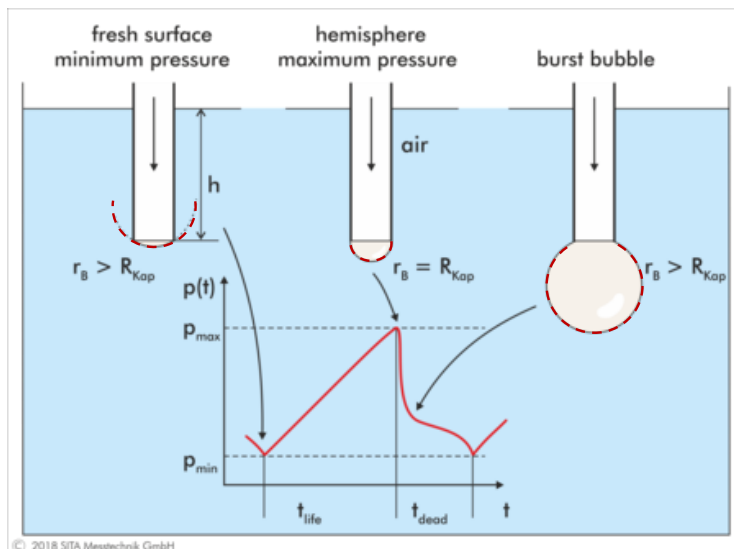


Figure 2.2: Schematic representation of the maximum bubble pressure method [GmbH-Internetagentur 2020]. r_B is the curvature radius of the bubble and R_{Kap} , the capillary radius.

2.1.1.3 Spinning drop tensiometer

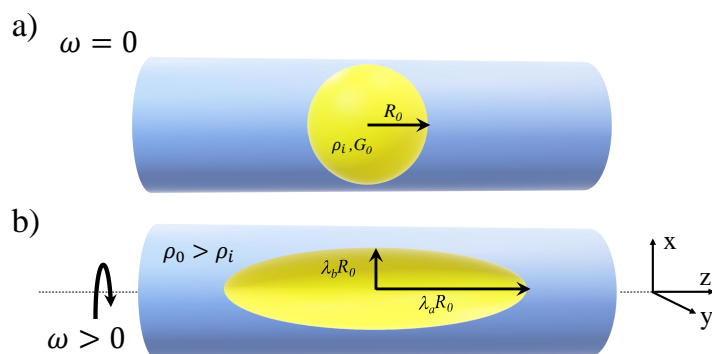


Figure 2.3: Schematic representation of a) a spherical drop at rest immersed in a liquid of higher mass density and b) deformed by centrifugal forcing while rotating with and angular velocity, $\omega > 0$. The drops are contained in a cylindrical capillary.

A spinning drop tensiometer drives a drop immersed in a denser immiscible fluid in rotation by spinning the capillary in which they are placed. The equilibrium shape of the drop under rotation is related to the interfacial tension between the drop and the surrounding fluid by Vonnegut's equation.

$$\gamma = \frac{\Delta\rho\omega^2}{4}R_0^3 \quad (2.5)$$

with $\Delta\rho$, the difference between the densities of the drop and of the surrounding fluid

and R_0 , the initial radius of the drop.

Though this type of tensiometers are usually used to measure low liquid-liquid interfacial free energies [Vonnegut 1942, Bamberger 1984, Liu 2012], it has been also used to characterize the mechanical properties of thin elastic capsules [Pieper 1998] and viscoelastic properties of polymer melts [Joseph 1992, Patterson 2007].

We investigate the biaxial deformation of soft elastic beads immersed in a denser immiscible fluid by spinning them in the capillary of the KRÜSS spinning drop tensiometer (SDT). A soft bead of polyacrylamide is placed in a capillary filled with a denser immiscible fluid (a fluorinated oil under the commercial name *Fomblin Y, LVAC25/6* with a density $\rho = 1.9$ g/mL). The capillary is put under rotation at a given angular velocity, ω , ranging from 6000 to 15000 rpm and the bead starts to stretch along the axis of rotation because of the centrifugal forces (see Figure 2.3). The rotation forces the bead to take an ellipsoidal shape with axes $X = \lambda_b R_0$, $Y = \lambda_b R_0$ and $Z = \lambda_a R_0$. Where λ_a and λ_b , the stretch ratios, are two strictly positive constants. The equilibrium shapes of the elastic bead is analyzed for each angular velocity.

2.1.2 Rheology

Rheology is the discipline that studies the deformation and flow of matter when submitted to an external stress. Its name was inspired by "Panta rhei", the aphorism of Heraclitus meaning "everything flows". Newtonian fluids such as air or water can be characterized by a coefficient of viscosity independent on the strain rate, which is not the case for most fluids. These fluids whose coefficient of viscosity varies with the rate of deformation are called non-Newtonian fluids, and they can be characterized by rheology.

2.1.2.1 Shear rheology

Principle of shear rheology A shear flow consists of the relative motion of adjacent fluid layers when subjected to an external force. A simple example of a shear flow is the planar Couette flow, in which shear is generated between a moving and a fixed solid surface as depicted in Figure 2.4. The top plate is put into motion at a velocity, v , by a force, F . The shear strain is given by $\gamma = \frac{d}{h}$ where d is the displacement and h , the distance between the plates. The shear rate is given by $\dot{\gamma} = \frac{v}{h}$. The resulting shear stress, $\sigma = \frac{F}{S}$, is given by the force applied on the moving plate by the materials divided by the area of the plates, S . The shear viscosity, η , is given by Newton's law and relates the shear stress to the shear rate, $\eta = \frac{\sigma}{\dot{\gamma}}$. The elastic modulus, G , is given by Hooke's law and relates the shear stress to the shear strain, $G = \frac{\sigma}{\gamma}$.

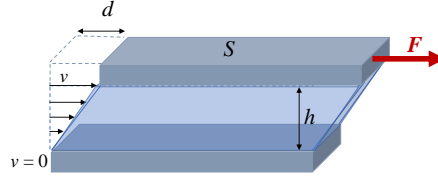


Figure 2.4: Schematic representation of a planar Couette flow.

To measure these quantities, we use rotational rheometers. Maurice Couette built in 1890 the first practical rotational rheometer [Macosko 1994]. Such instrument establishes a relationship between the shear stress, σ , and the shear strain, γ , by measuring the stress relaxation for an applied strain (strain controlled rheometer) or the strain response to an applied stress (stress controlled rheometer).

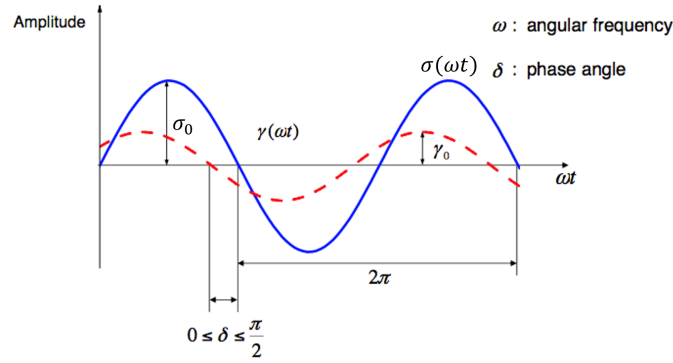


Figure 2.5: Oscillatory shear response in blue to an applied sinusoidal strain in red.

When conducting oscillatory shear measurements, that can be performed with a rotational rheometer, the applied strain is sinusoidal and the resulting stress oscillates sinusoidally at the same oscillation frequency, ω , but with a shifted phase angle, δ , comprised between 0 and $\frac{\pi}{2}$ as seen in Figure 2.5. The applied deformation is given by equation 2.6 and the response by equation 2.7. The stress wave (Eq. 2.6) can be decomposed into two waves of the same frequency leading to two dynamic moduli: G' , the storage or elastic modulus in phase with the applied strain wave, and G'' , the loss or viscous modulus out of phase with the applied strain rate.

$$\gamma(t) = \gamma_0 \sin(\omega t) \quad (2.6)$$

$$\sigma(t) = \sigma_0 \sin(\omega t + \delta(\omega)) \quad (2.7)$$

$$\sigma(t) = \sigma_0 \cos(\delta(\omega)) \sin(\omega t) + \sigma_0 \sin(\delta(\omega)) \cos(\omega t) \quad (2.8)$$

$$\sigma(t) = \gamma_0 G' \sin(\omega t) + \gamma_0 G'' \cos(\omega t) \quad (2.9)$$

From equations 2.8 and 2.9, the relationship of $G'(\omega)$ and $G''(\omega)$ can be retrieved.

$$G'(\omega) = \frac{\sigma_0}{\gamma_0} \cos(\delta(\omega)) \quad (2.10)$$

$$G''(\omega) = \frac{\sigma_0}{\gamma_0} \sin(\delta(\omega)) \quad (2.11)$$

Models for common complex fluids

Maxwell fluid One mode Maxwell model describes the behavior of the simplest viscoelastic liquid using a spring, to account for the elastic nature of the sample, and a dashpot, to account for its viscous nature as shown in Figure 2.6. The spring deforms instantaneously and relaxes immediately upon stress release, and the dashpot extends with time as long as the stress is applied. The constitutive equation of the one mode Maxwell model is given by:

$$\sigma + \frac{\eta}{G_0} \dot{\sigma} = \eta \dot{\gamma} \quad (2.12)$$

With η , the viscosity, G_0 , the characteristic elastic modulus and τ , the characteristic relaxation time. In this model, the storage and the loss moduli respectively read

$$G'(\omega) = \frac{G_0(\omega\tau)^2}{1 + (\omega\tau)^2} \quad (2.13)$$

$$G''(\omega) = \frac{G_0(\omega\tau)}{1 + (\omega\tau)^2} \quad (2.14)$$

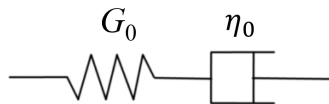


Figure 2.6: Representation of the one mode Maxwell model.

Shear thinning fluids We can also measure the dependence of the viscosity on the shear rate, $\dot{\gamma}$, by applying a shear rate ramp and measuring the steady state viscosity. This kind of experiment may highlight shear thickening (η increasing with increasing $\dot{\gamma}$) or thinning (η decreasing with increasing $\dot{\gamma}$) behavior. The latter is more commonly observed as compared to the previous one, which explains the multitude of phenomenological models developed to describe the shear thinning phenomenon. Among these models, the Cross model, given by Equation 2.15 [Cross 1965], is widely used to provide a good description of the shear-thinning behavior.

$$\eta_S(\dot{\gamma}) = \eta_\infty + \frac{\eta_0 - \eta_\infty}{1 + (k\dot{\gamma})^n} \quad (2.15)$$

With η_∞ , the viscosity at very large shear rate that is often comparable to the solvent viscosity, η_0 , the zero-shear-rate viscosity, n , the shear-thinning exponent and k , a parameter corresponding to the inverse of a critical shear rate that differentiates a Newtonian regime from a shear-thinning regime.

Experimental protocol To perform our shear rheological measurements, we use two rotational rheometers: the Anton Paar MRC302 or the Ares RFS 1KFRT rheometers, equipped with stainless steel cone and plate geometries of diameter 50 mm, cone angle of 1° and truncation of $101 \mu\text{m}$ or a stainless steel cylindrical Couette geometry for very dilute samples. Dynamic strain sweeps with strain amplitude from 0.1% to 100% are conducted at frequencies of 10 and 50 rad/s to define the linear viscoelastic regime. Dynamic frequency sweeps are performed in the linear regime, for an oscillation frequency, ω , varying from 100 to 0.01 rad/s. Temperature control is ensured by a Peltier element (accuracy of 0.2°C).

2.1.2.2 Extensional rheology

Extensional deformations are present in many industrial processes such as fiber spinning, thermoforming, film blowing, blow molding, and foam production [Macosko 1994]. This type of flow has been less investigated for soft viscoelastic samples, as it is difficult to generate a homogeneous extensional flow for such materials. Three types of extensional flow exist: uniaxial (Figure 2.7.a)), planar (Figure 2.7.b)), and biaxial (Figure 2.7.c)). For uniaxial extensional deformation, the sample is stretched in one direction and compressed equally in the two others. In planar extension, the deformation in one of the directions is prohibited and the sample reduces only from one direction while it is being stretched in the third direction. For biaxial extension, the material is equally stretched in two directions while it is compressed in the third direction. Biaxial extensional flow is usually thought of as a flow which produces a radial tensile stress [Steffe 1996]. The biaxial extensional flow is of interest for our drop impact and spinning drop experiments. For this reason, this

flow will be described more extensively below.

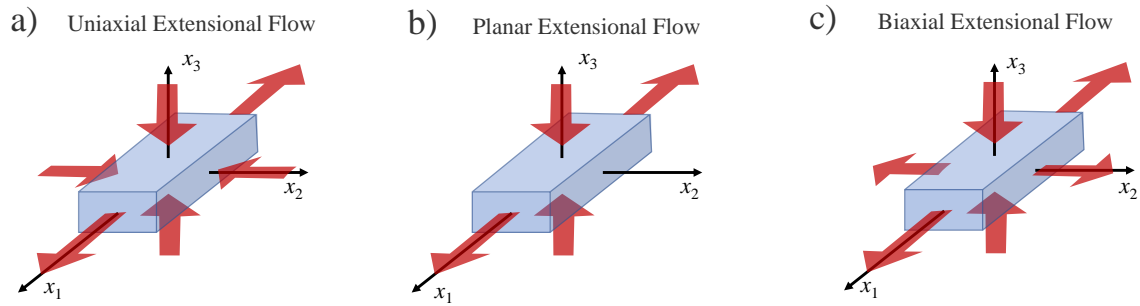


Figure 2.7: Schematic representation of a material under a) uniaxial b) planar and c) biaxial extension.

Biaxial extensional rheology Let us consider a material in Cartesian coordinates undergoing biaxial extension as in Figure 2.7.c). The velocity distribution in the biaxial extensional flow produced by this deformation reads

$$\begin{cases} u_1 = \dot{\epsilon}x_1 \\ u_2 = \dot{\epsilon}x_2 \\ u_3 = -2\dot{\epsilon}x_3 \end{cases}$$

where $\dot{\epsilon} > 0$ is the biaxial extensional rate. For the flows considered in this work, axial symmetry leads to the more convenient choice of cylindrical coordinates, which gives the velocity distribution

$$\begin{cases} u_r = \dot{\epsilon}r \\ u_\theta = 0 \\ u_z = -2\dot{\epsilon}z \end{cases}$$

Because there is no shear involved in the pure biaxial extensional flow, the stress tensor components $\sigma_{rz} = \sigma_{r\theta} = \sigma_{z\theta} = 0$. The strain tensor, \mathbf{D} , reads

$$\mathbf{D} = \begin{bmatrix} \dot{\epsilon} & 0 & 0 \\ 0 & \dot{\epsilon} & 0 \\ 0 & 0 & -2\dot{\epsilon} \end{bmatrix} \quad (2.16)$$

The normal stress difference that drives the biaxial flow is

$$\sigma_B = \sigma_{rr} - \sigma_{zz} \quad (2.17)$$

For a viscous fluid, the stress tensor is

$$\boldsymbol{\sigma} = 2\eta\mathbf{D} \quad (2.18)$$

with η , the shear viscosity.

From equations 2.16, 2.17 and 2.18,

$$\sigma_B = \eta_B \dot{\epsilon}_B \quad (2.19)$$

where the biaxial extensional viscosity is defined in terms of shear viscosity as $\eta_B = 6\eta$.

This relationship between biaxial extensional and shear viscosities holds for Newtonian fluids and in the limiting case, $\lim_{\dot{\epsilon}_B \rightarrow 0} \eta_B(\dot{\epsilon}_B) = 6 \lim_{\dot{\gamma} \rightarrow 0} \eta(\dot{\gamma})$, for non-Newtonian fluids at small strains [Steffe 1996]. At high strains, a reliable relationship between shear and extensional viscosities is still to be established.

2.1.3 Set-ups for drop impact experiments

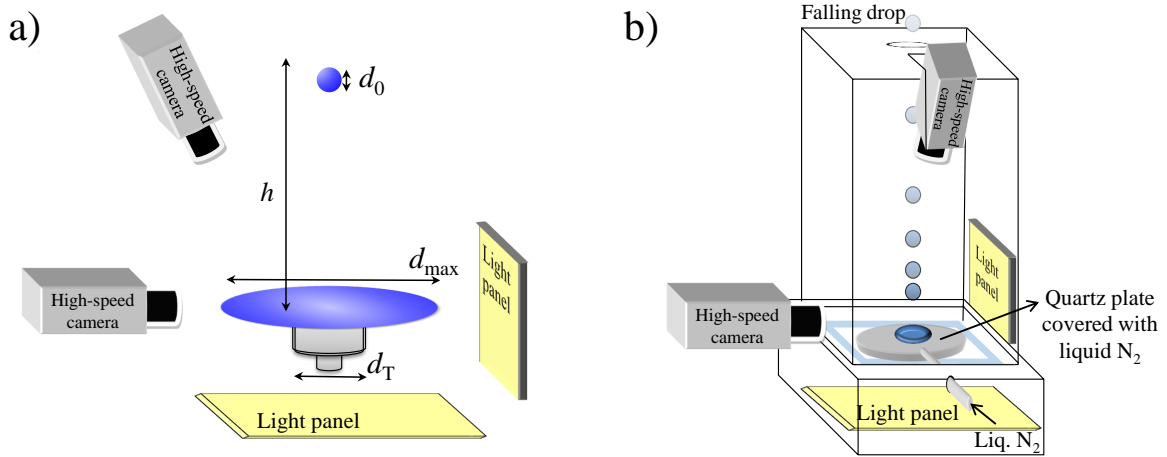


Figure 2.8: Schematic illustrations of the set-up for drop impact on targets a) and on a quartz plate covered with a thin layer of liquid nitrogen b). The impact is simultaneously recorded from the side and the top by two high-speed cameras.

To perform the drop impact experiments, we use two set-ups presented in Figure 2.8 for which drops are impacted on a) a target or b) a thin layer of liquid nitrogen. In both cases, drops of fluid are formed with the help of a syringe pump running at 1 ml/min and connected, through a flexible Teflon tube, to a needle (with an internal diameter of 2 mm) centered and placed vertically above the zone of impact. Because the internal diameter of the needle is fixed, small variation in the initial diameter, d_0 , of the drops will occur because of the different surface tensions of the samples. In our experiments, d_0 , varies between 3.1 and 3.8 mm as measured from $d_0 = \sqrt{4A_0/\pi}$ with A_0 , the surface of the drop right before

impact. The distance from which the drop is released dictates its velocity upon impact, which is given by a free fall law with a zero initial velocity and neglecting air friction: $v_0 = \sqrt{2gH}$ with H the height from which the drop is released and g the acceleration due to gravity. Vernay et al. showed that this approximation is quite reasonable [Vernay 2016].

The drop falls from the needle on the target or on the cold quartz plate covered with the liquid nitrogen layer. Upon impact, the drop is stopped in its fall and violently deformed into a liquid sheet which expands radially. The latter expands until reaching a maximal diameter and then retracts owing to the surface tension and stored elastic energy. The sheet is bounded by a thicker border called rim that can destabilize into ligaments and can lead to secondary drops ejections depending on the fluid viscosity, the impact velocity and the amount of dissipation occurring during the event. When the dissipated energy is very low, the drop can rebound after the retraction phase[Rioboo 2001].

The impact events are filmed by a high speed camera, Phantom V 7:3, operating at 6700 fps with a resolution of 800×600 pixels² from the top. The camera forms an angle of approximately 10° with the vertical plane. For most experiments, a simultaneous recording of the expansion is captured from the side by a Phantom miro M310 operating at 3200 fps with a resolution of 1280×800 pixels². The illumination enabling proper acquisition is provided by high-intensity backlights; Phlox HSC with a luminance of 98 cd/m² and Phlox LLUB with a luminance of 20 cd/m². To ensure reproducibility, the impact of each sample is repeated at least thrice. The temperature (20°C on average) and humidity ($\sim 40\%$) level of the room is systematically measured before each impact experiment to control the experimental conditions.

2.1.3.1 Impact on small solid targets

The impact of drops on a small target as represented on Figure 2.8.a was originally introduced by Rozhkov et al. [Rozhkov 2002].

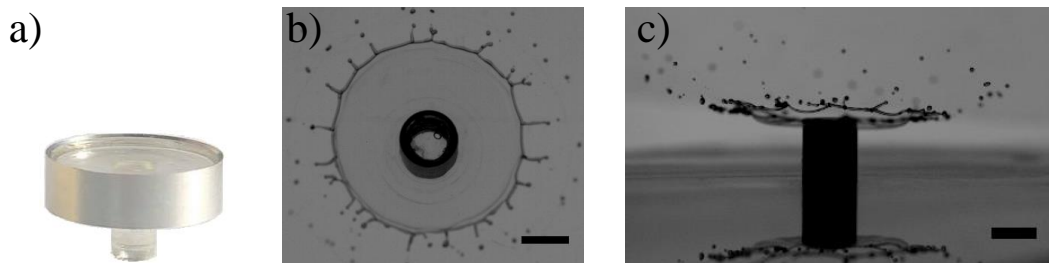


Figure 2.9: a) Picture of a translucent target with $d_T = 17$ mm. (b,c) Snapshots of a viscous sheet of 52% of glycerol in water impacted at $v_0 = 3.7$ m/s on a target of 6 mm from the top (b) and from the side(c). Scale bars are 5 mm.

Impact of fluid drops were first conducted on a small aluminum target of diameter, $d_T=6.5$ mm with an impact velocity, v_0 of 4.2 m/s. To avoid dewetting, the target is covered by a thin glass lamella that is treated with a plasma gun (Corona Surface Treater from Electro-Technic products) to ensure hydrophilicity [Vernay 2015a]. After rationalization of the experimental data obtained with this target, the influence of the target diameter on the expansion of the drops was investigated using, this time, translucent targets with diameters from 5 to 30 mm (as seen in Figure 2.9.a). The translucent targets are made from cured Norland optical adhesive, which has hydrophilic properties. Molds for the targets are made in aluminum to allow layer by layer curing of the adhesive. For a few samples, the impact velocity was varied between 1.5 and 4.2 m/s when impacting the translucent targets of different sizes. For the rest, the impact velocity was fixed at $v_0 = 3.7$ m/s. Both opaque and transparent targets are set in a coaxial cylinder made from aluminum to ensure good planarity of the ejected sheet [Villermaux 2011]. The flatness of the sheet during the expansion which can be compromised by an off-centered drop or a maladjustment of the coaxial cylinder is ensured by the side view imaging. The targets are fixed on a Plexiglas plate placed over a high-intensity backlight (Phlox LLUB) with a luminance of 20 cd/m². Images resulting from the impact of two fluids on a target at different times are shown in Figure 2.10.

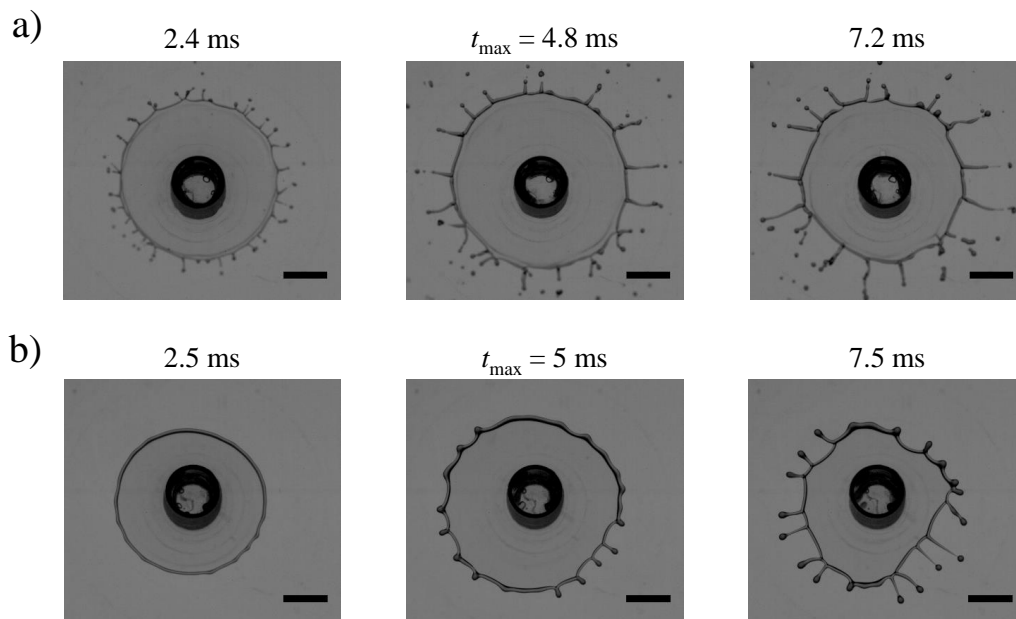


Figure 2.10: Snapshot of drops of a) 52% and b) 80% glycerol-water impacted at $v_0 = 3.72$ m/s on a translucent target of diameter, $d_T = 6$ mm at different times. Scale bars are 5 mm. As indicated, $t_{\max} = 4.8$ ms (a) and 5 ms (b), correspond to the maximal expansion of the sheet.

2.1.3.2 Cold Leidenfrost conditions

To suppress the shear viscous dissipation that arises from the interaction between the fluid and the substrate, drop impact experiments are also performed using the cold Leidenfrost effect (Figure 2.11)[Antonini 2013, Arora 2018].

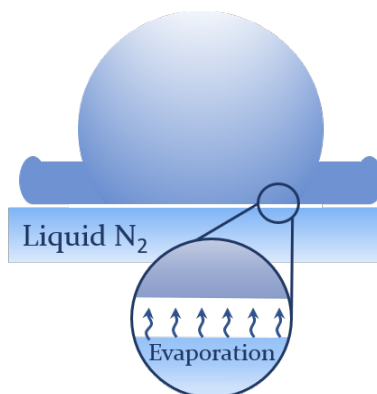


Figure 2.11: Representation of the cold Leidenfrost effect on the early stage of a drop impacting on a thin layer of liquid nitrogen (adapted from [Antonini 2013]).

We coat a quartz plate with a thin layer of liquid nitrogen which has a boiling point of $T_s = -196.15^\circ\text{C}$. The drop which is at ambient temperature will cause the liquid nitrogen to evaporate when in its vicinity, thus creating a vapor layer that thermally insulates the expanding sheet from the substrate and confers nonwetting and slip conditions for the expansion [Antonini 2013]. Figures 2.12.a,b show top and side views of the maximal expansion of the sheet formed by the impact of a viscoelastic sample at $v_0 = 4.7$ m/s. The snapshots show that the sheet at maximal expansion has a near circular shape and lays almost flat on the nitrogen gas. Snapshots from the top of a sheet formed by the impact of another viscoelastic sample with $v_0 = 4.22$ m/s at different times are shown in Figure 2.13. To ensure reproducibility, each impact is repeated until each sample has at least three acceptable experimental results at each impact velocity (ranging from 1.5 to 5 m/s).

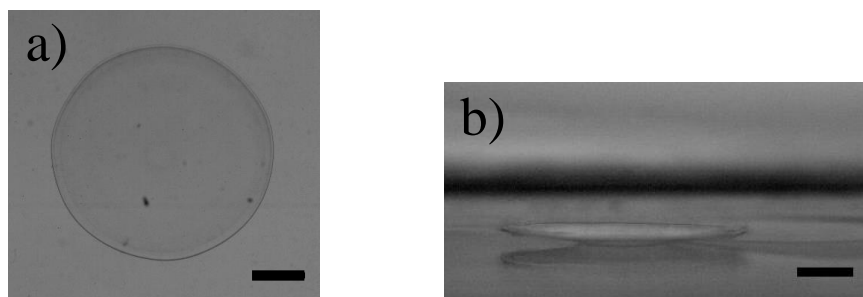


Figure 2.12: Snapshots of a viscoelastic sheet (sample M14 ϕ 10r6) taken at maximal expansion from the top (a) and from the side (b). The impact velocity is $v_0 = 4.7$ m/s. The scale bars represent 5 mm.

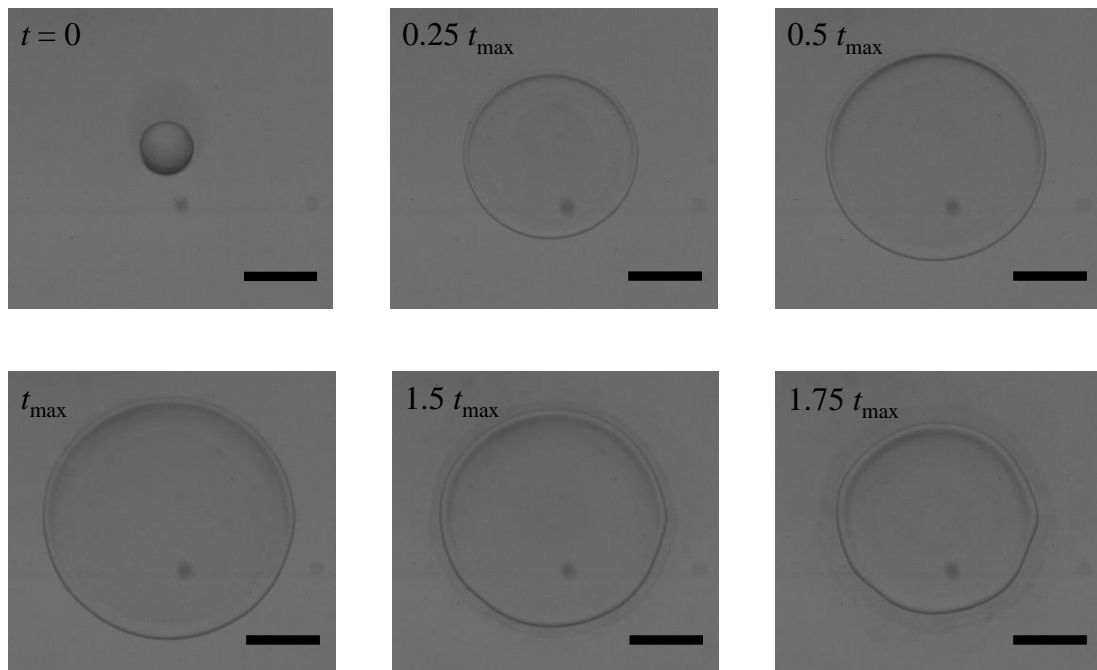


Figure 2.13: Snapshot of a drop of viscoelastic sample (WM ϕ 7 α 1.8) impacted at $v_0 = 4.22$ m/s in cold Leidenfrost conditions at $t=0$, $0.25 t_{\max}$, $0.5 t_{\max}$, t_{\max} , $1.5 t_{\max}$ and $1.75 t_{\max}$. where $t_{\max} = 5.7$ ms is the time at maximal expansion. Scale bars are 5 mm.

For an impact to be accepted, the drop should be supported by the nitrogen gas all through its expansion. This can be quantified by a simple heat transfer (see section 2.1.3.2) but can also be assessed experimentally. Indeed, as seen in Figure 2.14, if the amount of liquid nitrogen on the quartz is not sufficient, the sheet will freeze. On the contrary, if there is too much liquid nitrogen, crown formation, where the outer part of the sheet is deviated upward during expansion, occurs. To avoid these situations, the impact is performed at the onset of liquid nitrogen evaporation. This can be achieved by cooling down the quartz plate sufficiently so that the evaporation is slowed down and the front of evaporation becomes visible, allowing us to release the drop at the right time and perform the impact in good conditions. In some cases, crown formation cannot be avoided (See section 2.1.4.2). In these cases, side imaging is used to apply a correction to the maximal diameter reached by the sheet.

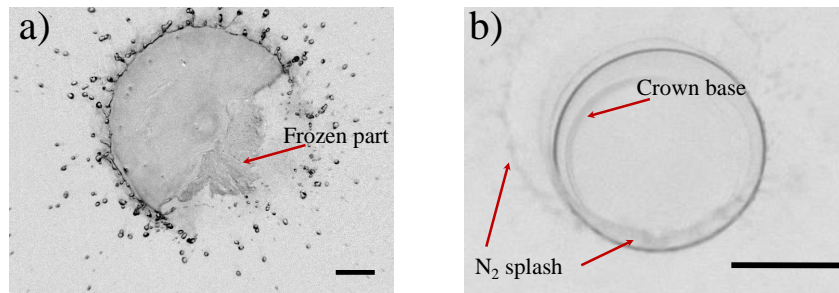


Figure 2.14: Images from impact with too little a) or too much b) liquid nitrogen. The fluid impacted in a) is water and in b) is silicone oil with a viscosity of 397 mPa s. Both fluids are impacted at 4.22 m/s. Scale bars are 5 mm.

Heat transfer In the cold Leidenfrost conditions, the drop is impacted on a cold quartz plate covered with liquid nitrogen at a temperature of $T_s = -196.15^\circ\text{C}$, the liquid nitrogen boiling point. The question of a possible temperature change of the drop arises. We can already see from the impact videos if the drop freezes on the surface or not. To ensure that its temperature remains constant throughout the expansion, we estimate the heat transfer when a drop at room temperature impacts a thin layer of liquid nitrogen at T_s . The heat transfers from the warm drop to the liquid nitrogen, thus inducing its evaporation. The nitrogen vapor is supported by the liquid nitrogen layer underneath until this latter is completely evaporated (see Figure SM1). From this situation, two questions arise: how long does it take for the liquid nitrogen layer to completely evaporate once in the vicinity of the drop, and what is the temperature of the drop at maximal expansion?

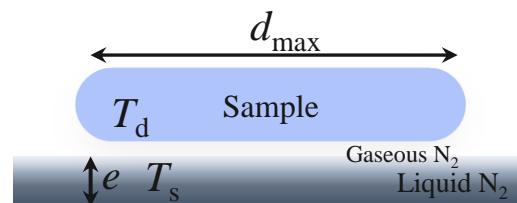


Figure 2.15: Schematic representation of the drop in the vicinity of the liquid nitrogen after impact. T_d is the drop temperature, e is the thickness of the liquid nitrogen film and T_s its boiling point. Before impact, $e \approx 50$ nm [Arora 2018].

- Time to evaporate the liquid N_2

Heat transfer processes that involve change of phase of a fluid are dominated by convection because of the fluid motion induced during the process [Cengel 2002]. Thus, the rate of heat change between the vapor and the liquid N_2 is given by:

$$hS\Delta T = L \frac{dm_{\text{N}_2}}{dt} \quad (2.20)$$

Here, m_{N_2} is the mass of liquid nitrogen to evaporate, $\frac{dm_{N_2}}{dt}$ is its vaporization rate, $L = 199$ kJ/kg [Cengel 2001] is the latent heat of vaporization, h is the convection heat transfer coefficient, S , the area of contact and $\Delta T = T_v - T_s$ where T_v is the N_2 vapor temperature and T_s , the temperature of the liquid nitrogen. We assume the temperature of the N_2 vapor to be homogeneous and equal to the mean between the temperatures of the drop and liquid N_2 ($T_v = \frac{T_d + T_s}{2}$) with $T_s = -196.15^\circ\text{C}$, and $T_d = 20^\circ\text{C}$, the initial drop temperature.

The time for the liquid nitrogen under the drop to evaporate is

$$t_{\text{evap}} \approx \frac{m_{N_2}}{\frac{dm_{N_2}}{dt}} = \frac{m_{N_2} L}{h S \Delta T} \quad (2.21)$$

with $m_{N_2} = \frac{1}{4} \pi e d_{\text{max}}^2 \rho_{N_2}$. ρ_{N_2} is the liquid N_2 density. The thickness of the liquid nitrogen film, e , is approximately 50 nm as measured by ellipsometry [Arora 2018]. The diameters used for the estimation of the surface of contact, S , are $d_{\text{max}} = 20, 25,$ and 30 mm. Using $\rho_{N_2} = 809$ kg/m³ [Cengel 2001], the mass of liquid nitrogen to evaporate are $1.3 \cdot 10^{-8}, 2 \cdot 10^{-8},$ and $2.8 \cdot 10^{-8}$ kg.

The convection heat transfer coefficient, h , is not an intrinsic property of the fluid but is a parameter determined experimentally and which depends on variables influencing convection (surface geometry, the nature of fluid motion, the properties of the fluid, and the bulk fluid velocity). Nonetheless, it can be derived from the natural convection Nusselt number, Nu, for the upper surface of a cold plate [Cengel 2002].

$$h = \frac{k \text{Nu}}{l} \quad (2.22)$$

with $k = 18.3 \cdot 10^{-3}$ W/mK, the thermal conductivity of the bulk fluid measured at $-73.15^\circ\text{C} \approx T_v = -87.85^\circ\text{C}$ [Bergman 2011] and l , the characteristic length of the contact area (Surface/Perimeter). The Nusselt number reads [Cengel 2002]

$$\text{Nu} = 0.27 \text{Ra}_L^{1/4} \quad (2.23)$$

with Ra_L , the Rayleigh number [Cengel 2002]

$$\text{Ra}_L = \frac{g \beta \Delta T l^3}{\nu^2} \text{Pr} \quad (2.24)$$

with $g = 9.81$ m/s, the acceleration due to gravity, $\beta = \frac{1}{T_v}$, the thermal expansion coefficient, $\nu = 7.65 \cdot 10^{-6}$ m²/s, the kinematic viscosity of nitrogen vapor at -73.15°C [Bergman 2011] and $\text{Pr} = 0.736$, the Prandtl number at -73.15°C [Bergman 2011]. The Prandtl number is the ratio between the momentum diffusivity over the thermal diffusivity.

We finally obtain $h = 9.6, 9.1$ and 8.7 W/m²K which gives respectively $t_{\text{evap}} = 7.7, 8.2,$ and 8.6 ms for the three different maximum diameters. The drop will therefore

be supported by evaporating liquid nitrogen during the whole expansion process as $t_{\text{evap}} \geq t_{\text{max}}$ since t_{max} ranges between 1.5 and 8 ms in our experiments.

- Temperature of the drop at t_{max}

Now that we made sure the drop is supported by the evaporating N₂ layer during the expansion, we solve the equation for the heat exchange between the drop and the N₂ vapor. As a first-order approximation, we consider Newtons law of cooling, for which we assume no thermal gradient in the sample. [Hendricks 1971, Kim 2011, Bergman 2011]

In this case, the main mode of heat transport is conduction as its contribution is one order of magnitude higher than the contribution from convection and two orders of magnitude higher than the contribution from radiation. Thus, the heat exchange between the drop and the N₂ vapor is given by

$$-m_{\text{drop}}C_p \frac{dT}{dt} = k \frac{S}{e} (T - T_s) \quad (2.25)$$

with $C_p = 4.18$ kJ/kgK, the specific heat of water, m_{drop} , the mass of the drop with $\rho_{\text{drop}} \approx \rho_{\text{water}}$, $k = 18.3 \cdot 10^{-3}$ W/mK, the thermal conductivity of the N₂ vapor measured at $-73.15^\circ\text{C} \approx T_v = -87.85^\circ\text{C}$ [Bergman 2011], S , the surface of contact, e , the thickness of the vapor layer, T , the temperature of the sample and T_s , the temperature of the liquid N₂. After integration from T_d to T_{max} , equation 2.25 reads

$$T_{\text{max}} = (T_d - T_s) \exp\left(\frac{-kt_{\text{max}}S}{m_{\text{drop}}C_p e}\right) + T_s \quad (2.26)$$

with T_{max} , the temperature of the drop at maximal expansion (at $t = t_{\text{max}}$).

Using a surface S calculated from the mean diameter from d_0 to d_{max} , d_{mean} , we estimate the temperature at maximal extension for three viscoelastic samples impacted at $v_0 = 4.2$ m/s: M14 ϕ 8r9 ($t_{\text{max}} = 1.5$ ms and $d_{\text{mean}} = 6.57$ mm), M14 ϕ 8r8 ($t_{\text{max}} = 3$ ms and $d_{\text{mean}} = 10.98$ mm) and WM ϕ 9 α 4 ($t_{\text{max}} = 6.4$ ms and $d_{\text{mean}} = 14.85$ mm). The estimated temperature of the sheet at maximal expansion for samples M14 ϕ 8r9, M14 ϕ 8r8 and WM ϕ 9 α 4 are respectively 19.96°C, 19.80°C and 19.21°C.

This simple heat transfer model shows that even though the temperature gradient between the drop and the liquid nitrogen is important, the N₂ vapor layer between the two successfully insulates the drop from thermal variation during the expansion process.

2.1.4 Image analysis for drop impact

This section details the different methods used for the analysis of drop impact.

2.1.4.1 Apparent diameter

The time evolution of the diameter for the experiments of drop impact using the set-ups described in sections 2.1.3.1 and 2.1.3.2 is computed with the ImageJ software.

The recording from the top of the sheet expansion and retraction gives a frame every 0.149 ms. The frames are saved as a stack in TIFF (tagged image file format) format. The background is first removed by dividing each frame by the first image taken before the drop enters the field of vision of the camera. The sheet can then easily be delimited by adjusting the binary threshold (see Figure 2.16 b)) allowing the measure of the sheet area A with the "analyze particle" command. From the sheet area, A , we deduce an apparent diameter, $d = \sqrt{\frac{4A}{\pi}}$. Using this approach, the fingers are taken into account. Nevertheless, the latter are negligible in the calculation of the surface area and thus do not induce important error for the diameter. In the following, for each impact velocity and sample, the reported time evolution of the sheet diameter corresponds to an average over three different experiments. The origin of time is chosen at the time just before the drop hits the target or comes into contact with the nitrogen layer and starts to deform in such a way that the diameter at $t = 0$ is d_0 , the initial drop diameter.

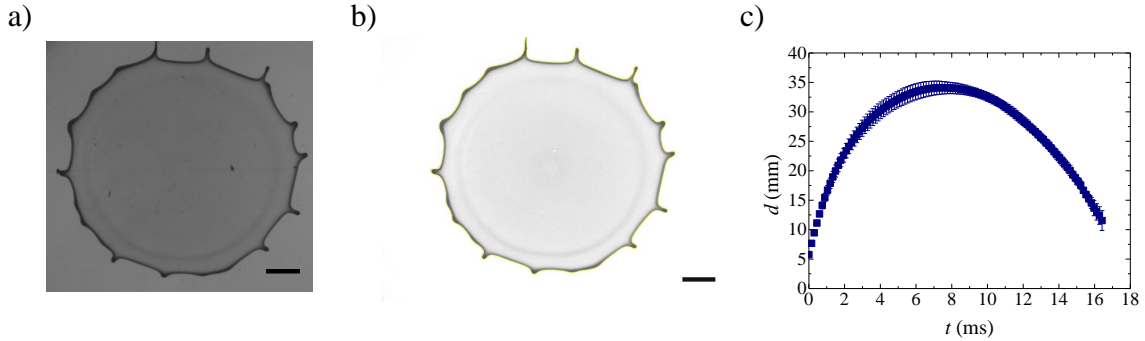


Figure 2.16: a) Sheet at maximal expansion for a Newtonian sample (87% glycerol in water) [$\eta = 145$ mPa s] impacted at $v_0 = 4.22$ m/s. Scale bar is 5 mm. b) Selection (in yellow) of the sheet area after dividing the image of the sheet by the first image taken before the drop enters the field of vision of the camera. c) Time evolution of the sheet diameter obtained from measurements of the area for the same sample. The error bars come from the average of three distinct experiments.

2.1.4.2 Crown correction

For Newtonian fluids with shear viscosities lower than ~ 100 mPa s impacted on liquid nitrogen, the expanding sheet exhibits a corona shape as shown on Figure 2.17.b, even without an excess of liquid nitrogen. This crown formation results in an underestimation of the actual diameter when using the method described in section 2.1.4.1 to analyze the top view images [Louhichi 2020]. The underestimated d_{\max} is corrected for all Newtonian samples with shear viscosities below 100 mPa s by using ℓ_{\max} , the correct diameter of the sheet measured from the side images, instead of d_{\max} . ℓ_{\max} is obtained by adding the

lengths of the raised part to the length of the flat part of the sheet as shown in Figure 2.17.b. We measure that the deviation from d_{\max} , $(\ell_{\max} - d_{\max})/d_{\max}$, follows more or less a logarithmic dependence from 0 % to 14% with the viscosity, η , for η from 1.7 to 209 mPa s. The impacts that were not recorded from the side are corrected by multiplying d_{\max} by a correcting factor found using the simple linear relation shown in Figure 2.17.c. We check, on the other hand, that for all investigated viscoelastic samples, the sheets remain flat and no correction is necessary.

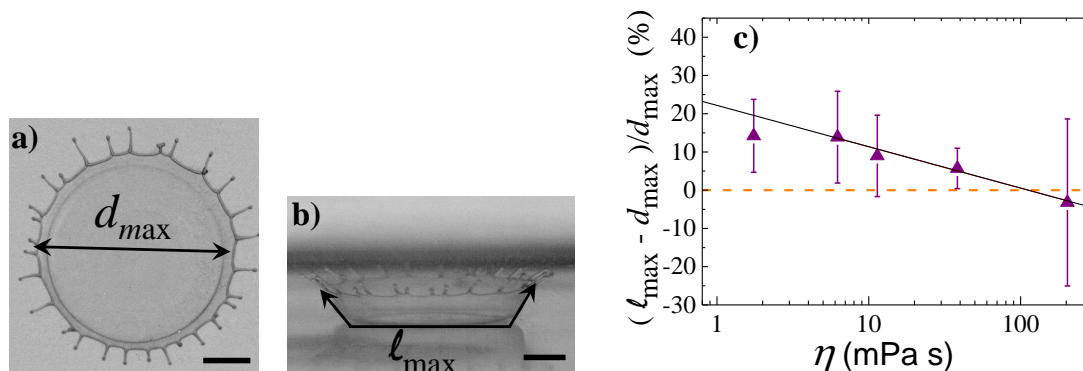


Figure 2.17: a) top and b) side views of a sheet at maximum expansion of a low viscous Newtonian sample ($\eta = 1.5$ mPa s). The figure shows that the effective maximal diameter, d_{\max} , from the top view underestimates the maximum expansion of the sheet ℓ_{\max} due to a corona effect that is observed only for low viscosity samples. c) Relative side view correction effect (in %) as a function of the zero-shear viscosity for glycerol/water mixtures. The continuous line is an empirical fit of the data points given by $y = 0.2 - 0.1 \log(x)$.

2.1.4.3 Thickness field

The variation of the thickness field of the expanding liquid sheets in cold Leidenfrost conditions, $h(r, t)$, with t , the time, and r , the radial position, is determined using the absorption of light by a dyed solution. The same method was used previously [Lastakowski 2014, Vernay 2015a, Wang 2017]. We dissolve 1.19 g/L of water-soluble Nigrosin purchased from Sigma Aldrich in glycerol-water solutions. The viscosities of these solutions are measured after addition of the dye at 20°C and range from 1 (for pure water) to 813 mPa s.

Calibration curve A calibration curve is built by correlating a gray level measured with the software ImageJ to a known thickness. To do so, a controlled volume of liquid, V_{liq} , is placed between two microscope coverslips of area, $A = 22 \times 22$ mm², with a micropipette giving liquid films of controlled thickness, $h = \frac{V_{\text{liq}}}{A}$. The thickness is varied from 5 to 500 μm . The samples are placed on the quartz plate of the experimental set-up

described in section 2.1.3.2. Images are captured with slight variations of the incident light intensity and for several concentrations of glycerol in water (from 0 to 97.5 wt% of glycerol) to ensure that a slight change in the illumination condition and the addition of glycerol does not impact the numerical values for the intensity. The calibration curve in Figure 2.18 is obtained by at least three repetitive measurements of the intensity over the whole surface for each film thickness and viscosity. In the case of more viscous fluids, time is given to allow the homogenization of the film thickness. The thickness is plotted against the logarithm of the gray level of the corresponding liquid film, I , divided by the gray level of two coverslips on top of each other, I_0 . $h = 0$ thus corresponds to the two coverslips without sample.

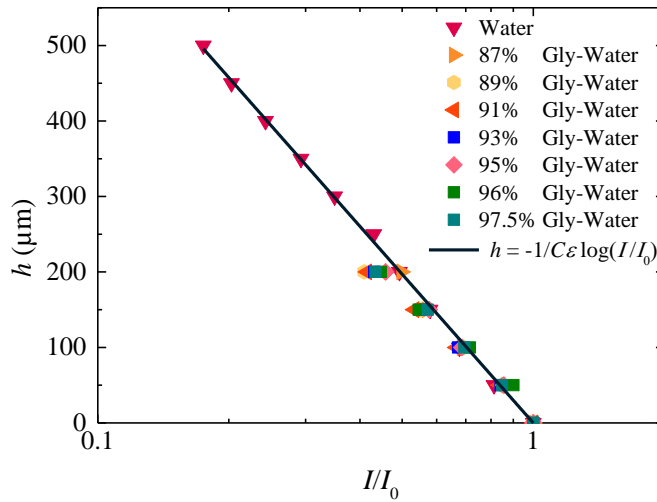


Figure 2.18: Calibration curve showing the thickness against I/I_0 in (log,lin) scale for glycerol/water mixtures of different concentrations with 1.19 g/L of Nigrosin. The line is the fit with the Beer-Lambert law and gives the prefactor $\frac{1}{C\varepsilon} = 284\text{m}$.

The calibration curve follows the exponential decrease of the intensity with the thickness predicted by the Beer-Lambert law:

$$h = -\frac{1}{\varepsilon C} \log\left(\frac{I}{I_0}\right) \quad (2.27)$$

with ε , the molar extinction coefficient and C , the concentration of dye. This calibration curve is used to correlate the intensity of the expanding sheet to its corresponding thickness and is valid up to, at least, $h = 500\mu\text{m}$.

Thickness field To measure the thickness field of the sheet, first, the intensity is normalized by the intensity of an image taken just before the drop enters the field of vision of the camera by dividing each frame by the first using ImageJ. The resulting images are

saved as TIFF files and analyzed with Matlab. Our Matlab code measures for each frame, i.e. time, the normalized intensity for each pixel of polar coordinates (r, θ) and takes the average value over all azimuthal angles, θ . The origin of r is taken for each experiment at the center of a circle containing the sheet. Hence, the normalized intensity field depends on the radial distance, r , and time, t . This averaged normalized intensity field, $\frac{I}{I_0}(r, t)$ is converted into thickness field, $h(r, t)$, using the Beer-Lambert law. The origin of time is taken at the time at which the drop comes into contact with the liquid nitrogen layer, and the origin of the radial distance is taken at the center of the sheet. The maximum noise measured outside of the sheet is of $10 \mu\text{m}$. We thus have a range of validity between $10 \mu\text{m}$ and $500 \mu\text{m}$.

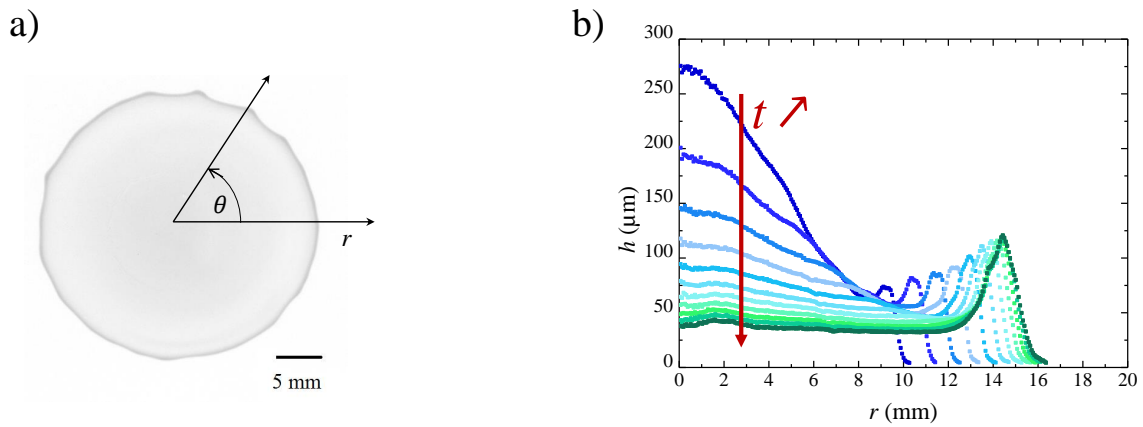


Figure 2.19: a) Image of 93 wt% glycerol water mixture ($\eta = 365 \text{ mPa s}$) at d_{max} divided by the initial intensity. b) Thickness profile of 93 wt% glycerol water mixture along r for different times after impact. The impact velocity is $v_0 = 4.2 \text{ m/s}$.

Limitations of the method The thickness measurement method has some limitations at short times ($t < 1.79$ ms). Indeed, we see that the thickness first increases before decreasing (see Figure 2.20.a)), which is not physically possible, and that, when computing the volume of the sheet from the thickness profiles, the volume is not well-defined at short times even for a sample of high viscosity, for which there is no secondary droplet ejection (see Figure 2.20.b)). Two causes were identified. Extending the calibration to higher thicknesses in Figure 2.21, a deviation from the Beer Lambert law is observed. We could have used another expression for the calibration at thicknesses above $500 \mu\text{m}$. However, this deviation is not the only problem. Indeed, in Figure 2.22, we observed a saturation of the gray level at the center of the sheet, which shows that the error at short times does not come only from the conversion from intensity to thickness but comes partly from the saturation of the intensity for larger thickness. The reason for this saturation remains unexplained. For this reason, we will focus, in our study related to the sheet profiles, on the times after 1.79 ms.

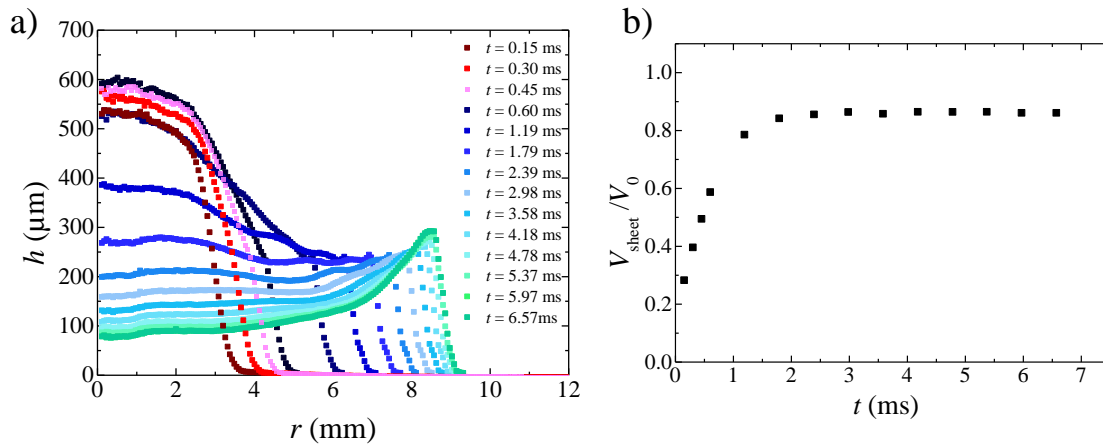


Figure 2.20: a) Thickness profiles in function of the radial position at different times, including the short times ($t < 1.79$ ms) and b) volume of the sheet normalized by the initial volume of the drop as a function of time for a glycerol/water sample of viscosity 813 mPa s.

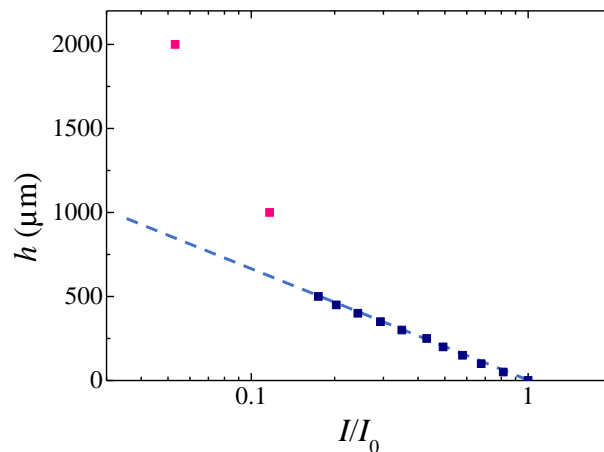


Figure 2.21: Calibration curve extended to thickness above $500 \mu\text{m}$ for water.

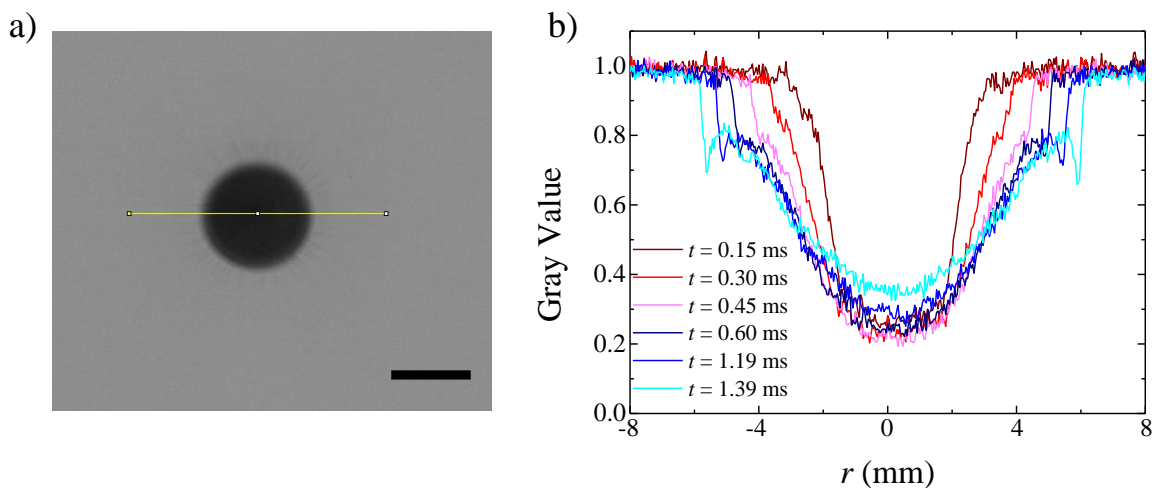


Figure 2.22: a) Snapshot of the glycerol/water with $\eta = 813 \text{ mPa s}$ sheet at $t = 0.3 \text{ ms}$. The scale bar is 5 mm . b) Gray value of the straight horizontal line across the sheet (in yellow) at different times.

Rim detection method The instantaneous thickness profile displays a non-monotonic evolution, with the radial distance, r . The continuous decrease of h as r increases is followed by a sharp increase related to the thicker rim, before going to values fluctuating from maximum $\pm 10 \mu\text{m}$ around 0 corresponding to the edge of the liquid sheet. In Chapter 6, we study the evolution of the rim with time for Newtonian fluids of different viscosities. This analysis is done with Matlab. The code analyses $h(r, t)$ for each time and selects the outer and inner sides as well as the peak of the rim to return the volume of the rim and

the position of the peak at each time. The outer side, R_{out} , (in magenta in Figure 2.23) is found by removing the noise and taking the first non-zero value. For the peak of the rim, R_{peak} (in light orange in Figure 2.23) or the inner side, R_{in} , (in green in Figure 2.23) the code uses the derivative of h with respect to r divided by h , h'/h (dark orange curve in Figure 2.23) and finds respectively the value closest to zero, for the peak value, or 0.15 mm^{-1} , for the inner side of the rim, when starting from R_{out} . The criterion to find R_{in} is arbitrary and was varied from 0.10 to 0.20 mm^{-1} to ensure the robustness of our findings. The results were not sensitive to the criterion as it is shown in Chapter 6. The volume of the rim, V_{rim} is computed using $V_{\text{rim}}(t) = \int_{R_{\text{in}}(t)}^{R_{\text{out}}(t)} 2\pi r h(r, t) dr$.

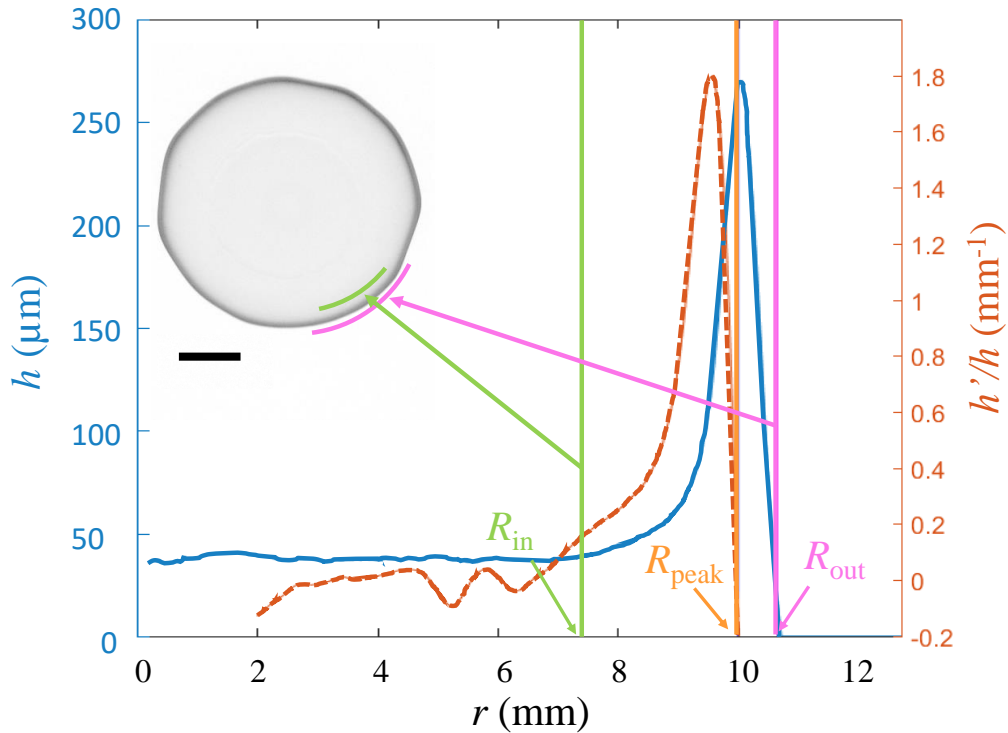


Figure 2.23: h (blue line) and h'/h (orange dashed line) in function of r for 91 wt% glycerol water mixture ($\eta = 270 \text{ mPa s}$) impacted at $v_0 = 4.2 \text{ m/s}$. The left side of the rim, R_{in} (green), and the right side of the rim, R_{out} (magenta), are shown with arrows on the corresponding image of the sheet. The scale bar is 5 mm.

2.2 Materials

2.2.1 Newtonian fluids

For the purposes of comparison, we use two types of Newtonian fluids for the drop impact experiments: Silicone oils and glycerol/water mixtures.

Silicone oils ($[-\text{Si}(\text{CH}_3)_2\text{O}-]_n$) of viscosity 5, 96, 339, 485 and 970 mPa s, purchased from Sigma Aldrich, were blended to obtain zero-shear viscosities ranging from 5 to 970 mPa s at 20°C. The surface tension of silicone oils of various viscosity was measured in the literature and was found not to vary significantly around 20 mN/m [Crisp 1987]. The density of these blends was calculated from the densities of the purchased oils and varies from 0.913 to 0.97 g/ml.

Glycerol ($\text{C}_3\text{H}_8\text{O}_3$) purchased from Sigma Aldrich and Milli-Q water mixtures were prepared with concentrations in weight percent of glycerol varying between 0 and 97.5. To allow the measurement of the sheet thickness field, 1.19 g/L of Nigrosin ($\text{C}_{22}\text{H}_{16}\text{N}_6\text{Na}_2\text{O}_9\text{S}_2$) purchased from Sigma Aldrich, also known as Acid black 2, was added to the mixtures. The shear viscosities measured at 20°C by rheometry for these samples were found to lie between 1 mPa s (for pure water) and 813 mPa s. The densities were calculated from the densities of pure glycerol and water and range from 1.05 g/ml to 1.25 g/ml. The surface tension varies between 72 mN/m (for pure water) and 64 mN/m (for 97.5 % of glycerol) [Takamura 2012].

For Newtonian samples, the shear viscosity, η , is measured by applying a ramp of steady shear rate varying from $\dot{\gamma} = 0.01 \text{ s}^{-1}$ to 1000 s^{-1} . As by definition for Newtonian fluids, $\eta(\dot{\gamma})$ is constant as seen in Figure 2.24.a. η ranges between 5 and 970 mPa s for the silicone oils and between 1 and 813 mPa s for the glycerol and water mixtures at 20°C as seen in Figure 2.24.b.

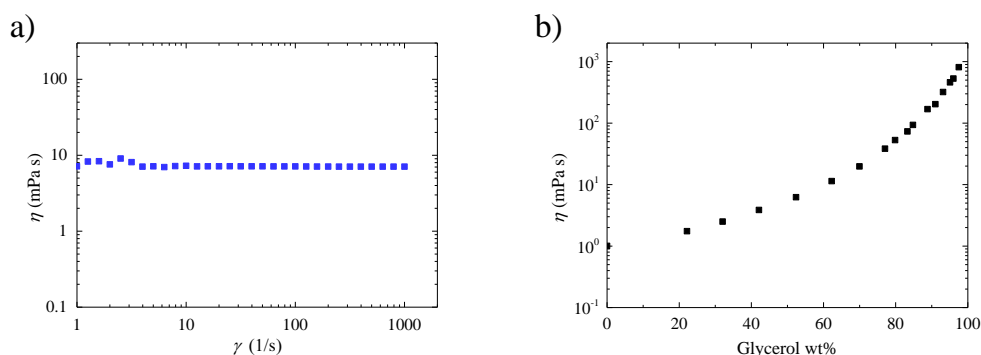


Figure 2.24: a) $\eta(\dot{\gamma})$ for 52% of glycerol in water. b) Values of η for the different mixtures of glycerol and water.

2.2.2 Self-assembled transient networks

To understand how viscoelasticity affects the expansion dynamic of impacted drops, several viscoelastic networks were produced and investigated.

2.2.2.1 Bridged micro-emulsions

The first class of viscoelastic systems are oil droplets stabilized in brine ($[\text{NaCl}]=0.2 \text{ M}$), also called micro-emulsions, reversibly linked by telechelic polymers. Telechelic polymers are triblock copolymers home-synthesized by Dr. Ty Phou (L2C) and consist of water-soluble poly-(ethylene oxide), PEO, backbones of $35,000 \text{ gmol}^{-1}$ onto which aliphatic chains, $\text{C}_n\text{H}_{2n+1}$, were grafted at both ends. The end chains, also called stickers, are hydrophobic and will thus enter the core of the oil droplet to minimize their interactions with the aqueous solvent. By doing so, the triblock copolymer will either form a loop and decorate a droplet or, if the concentration is sufficiently high, the two stickers on the chain can enter different droplets and create a reversible bridge between the latter (Figure 2.25.a). The multiplication of these links forms a three-dimensional network (Figure 2.25.b) able to carry elastic forces transiently at the macroscopic scale.

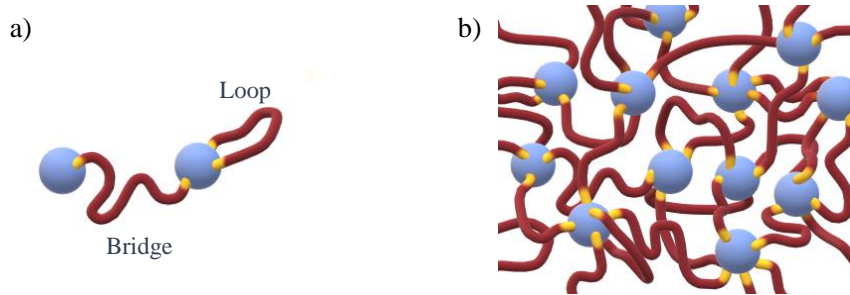


Figure 2.25: Schematic illustration of a) a bridge and loop and b) the bridged micro-emulsions network.

The macroscopic properties of this system can be tailored to meet one's needs by changing the mass fraction of oil droplets, the number of stickers per droplet and the length of the stickers or the PEO backbone. Here, to achieve the desired material properties, we keep the size of the oil droplets and the length of the polymer backbone constant as we vary the mass fraction of oil droplets, ϕ , the number of stickers per droplet, r , and their length. The micro-emulsion droplets are monodisperse when diluted over the range of 1-20 wt % [Filali 1999]. Their size is controlled by the addition of surfactant, cetylpyridinium chloride (CpCl) and cosurfactant, n-octanol, to the brine. The CpCl and n-octanol form a surfactant film around the oil, decane. This film exhibits a spontaneous curvature radius dictated by two parameters Ω and Γ :

$$\Omega = \frac{m_{\text{cosurfactant}}}{m_{\text{surfactant}}} \quad \text{and} \quad \Gamma = \frac{m_{\text{oil}}}{m_{\text{surfactant}} + m_{\text{cosurfactant}}}$$

with $m_{\text{surfactant}}$, $m_{\text{cosurfactant}}$ and m_{oil} the mass of CpCl, n-octanol and decane [Filali 1999]. For $\Omega = 0.25$ and $\Gamma = 0.56$, the radius of the drop, which corresponds to the spontaneous curvature radius of the surfactant film, was measured by small angle neutron scattering and found to be $62 \pm 1 \text{ \AA}$ [Filali 2001]. This radius remains constant upon addition of the triblock copolymers up to $r \approx 80$ [Filali 1999]. r is the number of stickers per droplet defined as

$$r = \frac{\text{number of aliphatic chains}}{\text{number of oil droplets}}$$

The aliphatic chains have lengths C₁₂, C₁₄ or C₁₈. The number and size of the stickers, along with the mass fraction of oil droplets, ϕ , control the phase diagram of the micro-emulsions (see figure 2.26). ϕ is defined by

$$\phi = \frac{m_{\text{hydrophobic}} + m_{\text{oil}}}{m_{\text{total}}}$$

with $m_{\text{hydrophobic}}$, m_{oil} and m_{total} the mass of all hydrophobic parts of the surfactant, cosurfactant and telechelic polymer, the mass of oil and the total mass respectively.

The samples were prepared by adding the surfactant, CpCl, to a solution of 0.2 M of NaCl in Milli-Q water. CpCl was previously purified in house by consecutive recrystallizations in water and in acetone. After dissolution of the CpCl, the cosurfactant, n-octanol, was added to form micelles before the addition of decane to swell the latters. After gentle stirring, the mixture is filtered with a syringe filter unit with 0.22 μm pore size. Telechelic polymers are then added to form the gel by bridging the oil droplets. This final mixture is swirled until a homogeneous, transparent gel is obtained. This last step can take up to a few days. The resulting samples are kept away from light at a controlled temperature of 30°C. Figure 2.26 shows phase diagrams for micro-emulsions linked by a) PEO-C₁₂, b) PEO-C₁₈ and c) PEO-C₁₄. For low values of ϕ and r , the samples are liquid (sol state) and flow easily. As we increase the values of ϕ and r , the telechelic polymers start connecting oil droplets together until eventually forming a transient network corresponding to the gel phase of the diagram. On the diagrams, these two phases are separated by a dashed line representing the percolation line [Filali 2001]. For the micro-emulsions linked by PEO-C₁₂, the change in rheological properties between the sol and gel phases is very smooth and a percolation line is difficult to define [Filali 2001]. In the two-phases region, phase-separation is observed and a very dilute sol phase coexists with a concentrated gel phase [Filali 2001].

The samples used here have a number of stickers per droplet, r , between 4 and 9 and hydrophobic mass fractions, ϕ , of 8 or 10%. The micro-emulsions are named $Mn\phi XrY$ with n , the number of carbon per sticker for the telechelic polymers, X the value in weight % for ϕ , the hydrophobic mass fraction and Y, the value of r , the average number of stickers per oil droplet.

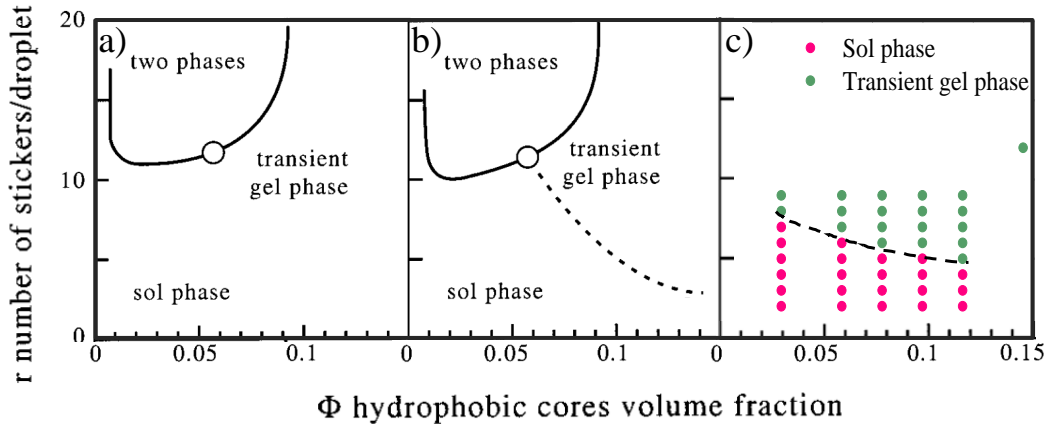


Figure 2.26: Phase diagrams of micro-emulsions connected by a) PEO-C₁₂, b) PEO-C₁₈ and c) PEO-C₁₄. The dashed lines in b),c) delimit the sol and transient gel phases. c) was measured for purposes of this thesis, and a-b) were adapted from [Filali 2001].

Surface tension An equilibrium value of 28 mN/m for the surface tension is measured by the pendant drop method for non bridged micro-emulsions. As explained in section 2.1.1.2, in the case of drop impact experiments, the relevant surface tension quantity should be taken from the dynamic measurement of surface tension. The dynamic surface tension of micro-emulsions is measured for three different samples (M14 ϕ 8r8, M14 ϕ 10r6 and M14 ϕ 8r6) and the average of these three measurements is shown in Figure 2.27 and fitted by Equation 2.4. The fitting parameters are $t^* = 0.27$ s and $n = 0.99$. In the following, the surface tension considered for the micro-emulsions is the dynamic surface tension at the time needed for the sheet to reach its maximal expansion, t_{\max} (between 1.2 and 6.5 ms), which happens to be equal to the surface tension of the solvent, 72 mN/m.

Linear rheology The linear response of micro-emulsions to oscillatory shear is measured with a strain amplitude of $\gamma = 1\%$ at 20°C. The resulting curves for the loss, G'' , and storage, G' , moduli in function of the angular frequency of three representative micro-emulsions (M18 ϕ 10r4, M14 ϕ 8r9 and M12 ϕ 10r8) are shown on Figure 2.28. The relaxation times, τ , of micro-emulsions with PEO-C₁₄ and PEO-C₁₂ are very short and cannot be obtained by the crossover of G'' and G' . To obtain values for τ and for the elastic modulus, G_0 , the loss, G'' , and storage, G' , moduli in function of the angular frequency are fitted (dashed lines in Figure 2.28) by the Maxwell model (equations 2.14 and 2.13). The elastic modulus, G_0 , the relaxation time, τ , and the zero-shear viscosity, $\eta_0 = G_0\tau$, for all investigated micro-emulsions are reported in table 2.1.

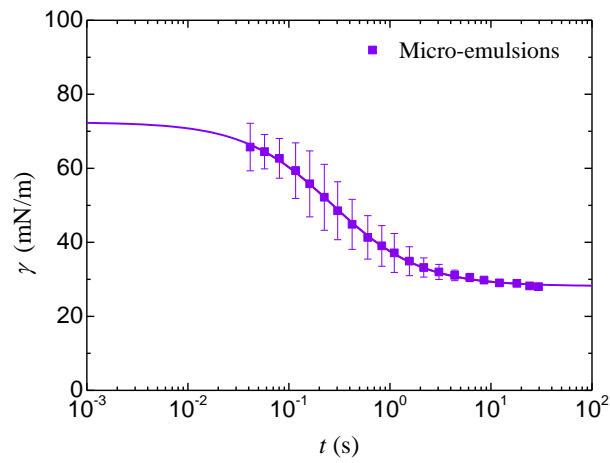


Figure 2.27: Dynamic surface tension measurements for micro-emulsions (M14 ϕ 8r8, M14 ϕ 10r6 and M14 ϕ 8r6). Error bars come from the average of three experiments. The line is the fit obtained with equation 2.4 and the fitting parameters are $t^* = 0.27$ s and $n = 0.99$.

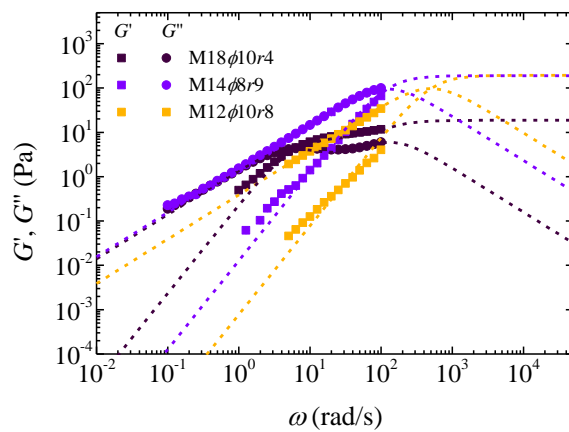


Figure 2.28: Storage, $G'(\omega)$ (squares), and loss, $G''(\omega)$ (circles), moduli as a function of the oscillation frequency, ω for three micro-emulsion samples (M18 ϕ 10r4, M14 ϕ 8r9 and M12 ϕ 10r8). Symbols are experimental data and the dashed lines are Maxwell model fits.

Table 2.1: Rheological properties of micro-emulsions. G_0 is the elastic modulus, τ , the relaxation time and η_0 , the zero-shear viscosity

Micro-emulsions			
Name	G_0 [Pa]	τ [ms]	η_0 [Pas]
M18 ϕ 10r4	10	178	1.78
M14 ϕ 8r9	189	8	1.5
M14 ϕ 8r8	128	6	0.77
M14 ϕ 10r6	48	5	0.23
M14 ϕ 8r6	31	4	0.12
M12 ϕ 10r8	194	2	0.39

2.2.2.2 Decorated wormlike micelles

The second class of viscoelastic systems consist of entangled wormlike micelles [Rehage 1988, Rehage 1991] formed by sodium salicylate (NaSal) and cetylpyridinium chloride (CpCl), that self-assemble in brine ([NaCl]=0.5 M). When these molecules, consisting of a hydrophilic head and a hydrophobic tail, are added to the brine, they self-assemble to minimize the interaction of the hydrophobic parts with water. For a sufficiently large surfactant molecule concentration, above the critical micellar concentration, the molecules form micelles. Micelles are aggregates where the hydrophilic heads form an outer shell inside which the hydrophobic tails can segregate, expelling most of the water. The shape and size of these entities can vary with the nature and size of the surfactant molecules, the temperature, the type and concentration of salt in the aqueous media and the addition of a cosurfactant. It was shown that controlling the surfactant to cosurfactant molar ratio allows one to produce elongated micelles (see figure 2.29). Consequently, the spherical micelles change into rod shaped micelles that in turn evolve into wormlike tubes. These wormlike micelles are able to create entanglements, but also to break and recombine in response to external stimuli [Rehage 1988, Rehage 1991]. Such entangled wormlike micelles are able to transmit elastic force in a transient way. Here, the molar ratio [NaSal]/[CpCl] is fixed at 0.5.

The micelles are decorated by triblock copolymers purchased from Serva (*Synperonic* F-108). These copolymers are known as poloxamers. They have an average molar mass of 14 kg/mol and are constituted of a short poly-(propylene oxide), PPO, central backbone of 48 monomers and two poly-(ethylene oxide), PEO, end chains of 127 monomers [Massiera 2002b]. The hydrophobic PPO anchors onto the surfactant micelles, leaving the hydrophilic ends swollen in the solvent. The decorated wormlike micelles are characterized by ϕ , the weight fraction of surfactant and α , the ratio between the number of POE chains and the number of surfactant molecules.

$$\phi = \frac{m_{\text{surfactant}} + m_{\text{cosurfactant}}}{m_{\text{total}}} \quad \text{and} \quad \alpha = \frac{\text{number of PEO chains}}{\text{number of surfactant molecules}}$$

It can be observed from measurements of the elastic modulus, G_0 , and the relaxation

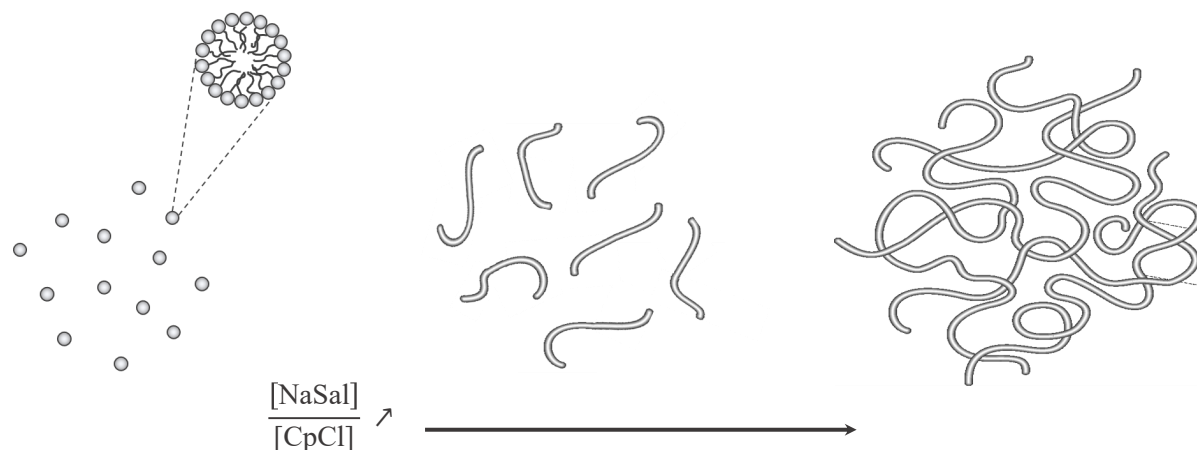


Figure 2.29: Evolution, with the molar ratio of NaSal to CpCl, of micelles in solution, from spheres to wormlike micelles.

time, τ , as a function of ϕ performed for wormlike micelle samples with different concentrations of F-108 triblock copolymer [Massiera 2002a] that changing α and ϕ allows one to easily tune the values of G_0 and τ . We chose values of α and ϕ in order to obtain similar elastic moduli with various relaxation times.

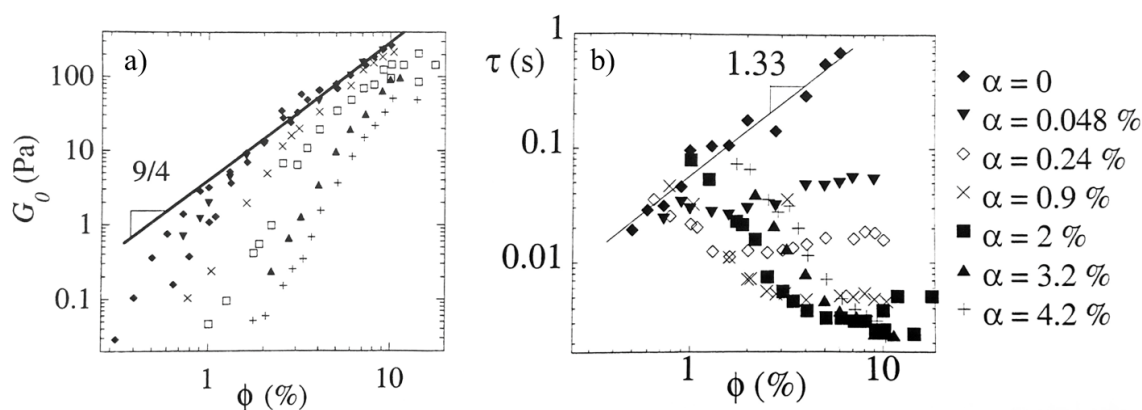


Figure 2.30: a) Elastic modulus, G_0 , and b) relaxation time, τ , as a function of ϕ for wormlike micelle samples with different concentrations of F-108 triblock copolymer. [Massiera 2002a]

The samples were prepared by weight. The poloxamers were first added to a solution of 0.5 M of NaCl in Milli-Q water. The previously purified CpCl is then incorporated to the solution and after its dissolution, the cosurfactant, NaSal, was finally added. This final mixture is swirled several times before being kept away from light at a controlled temperature of 30°C. We used samples with ϕ in the range from 5 to 9% and α from 0.48 to 4%. The name of wormlike micelles follows the following nomenclature WM ϕ X α Y with

X the value in weight % for ϕ and Y the value in % for α , the mole fraction of amphiphilic polymer.

Surface tension An equilibrium value of 34 mN/m for the surface tension is measured by the pendant drop method. As the relevant surface tension quantity for the drop impact experiments is the dynamic surface tension, we measure the latter for three different samples (WM ϕ 9 α 4, WM ϕ 7 α 1.8 and WM ϕ 5 α 0.48) and the average of these three measurements is shown in Figure 2.31 and fitted by Equation 2.4. The fitting parameters are $t^* = 0.36$ s and $n = 1.34$. In the following, the surface tension considered for the wormlike micelles is the dynamic surface tension at the time needed for the sheet to reach its maximal expansion, t_{\max} (between 1.2 and 6.5 ms), which happens to be equal to the surface tension of the solvent, 72 mN/m.

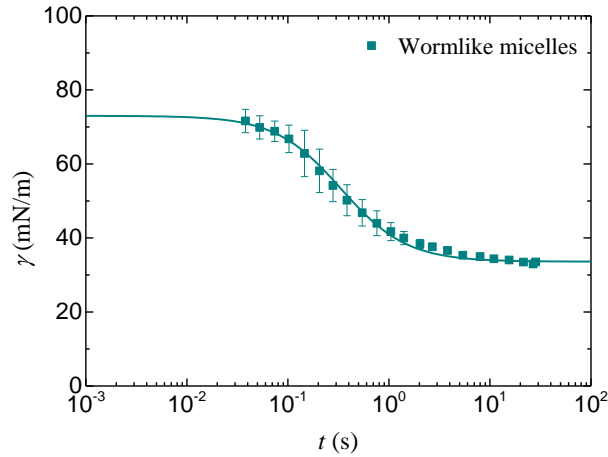


Figure 2.31: Dynamic surface tension measurements for wormlike micelles (WM ϕ 9 α 4, WM ϕ 7 α 1.8 and WM ϕ 5 α 0.48). Error bars come from the average of three experiments. The line is the fit obtained with equation 2.4 and the fitting parameters are $t^* = 0.36$ s and $n = 1.34$.

Linear rheology The linear response of wormlike micelles to oscillatory shear is measured with a strain amplitude $\gamma = 1\%$ at 20°C. The resulting curves for the loss, G'' , and storage, G' , moduli in function of the angular frequency of samples WM ϕ 9 α 4, WM ϕ 7 α 1.8 and WM ϕ 5 α 0.48 are shown on Figure 2.32.a. The stress relaxation behavior of such polymer was first explained by Cates in 1987 [Cates 1987] by adding to the reptation model from de Gennes [De Gennes 1971] reversible breaking and reformation of the chains as an additional relaxation mode. When the breaking and reformation process is faster than the reptation time, the stress relaxes following a monoexponential decay and the solutions rheological behavior is accurately described by the one mode Maxwell model

[Fischer 1997]. Fitting the experimentally measured loss and storage moduli for the worm-like micelles by equations 2.14 and 2.13 (dashed lines in Figure 2.32.a) gives the elastic modulus, G_0 , the relaxation time, τ , and the zero-shear viscosity, $\eta_0 = G_0\tau$, reported in table 2.2.

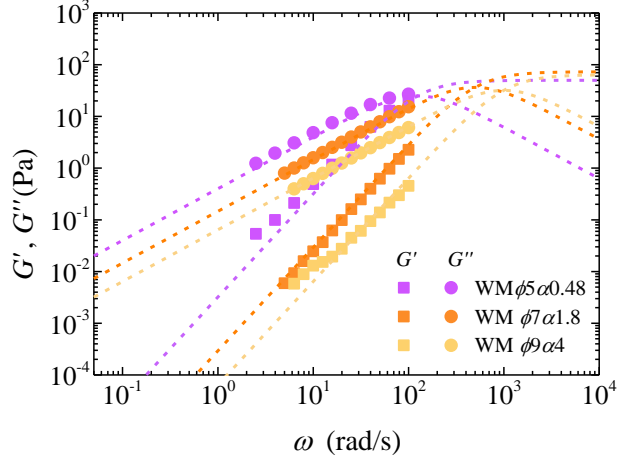


Figure 2.32: a) Storage, $G'(\omega)$ (squares), and loss, $G''(\omega)$ (circles), moduli as a function of the oscillation frequency, ω . The dashed lines are one mode Maxwell fits.

Table 2.2: List of wormlike micelles samples and their rheological properties. G_0 is the elastic modulus, τ , the relaxation time and η_0 , the zero-shear viscosity

Wormlike micelles			
Name	G_0 [Pa]	τ [ms]	η_0 [Pas]
WM $\phi 5\alpha 0.48$	50	8	0.4
WM $\phi 7\alpha 1.8$	73	2	0.146
WM $\phi 9\alpha 4$	64	1	0.031

2.2.3 PEO solutions

Solutions of high molecular weight poly-(ethylene oxide) (8000 kg/mol) are also investigated. The PEO is purchased from Sigma Aldrich and diluted as received in Milli-Q water with concentrations, C , varying between 10^{-3} wt% and 2 wt%. The solution is then stirred at ambient temperature for at least 24 h in the dark. To enhance contrast for analysis, 0.25 g/L of Nigrosin is added to the solutions after homogenization. The surface tension of high molecular weight PEO solutions is independent of polymer concentration and is $\gamma_{PEO} = 62 \text{ mNm}^{-1}$ [Louhichi 2020]. The density of the PEO solutions is assumed to be equal to the density of the solvent, $\rho = 1 \text{ g/mL}$.

Dynamic frequency sweeps are performed with an applied sinusoidal strain of amplitude of $\gamma = 10\%$ with ω varying from 100 to 0.01 rad/s. Figure 2.33.a shows the loss, G'' , and storage, G' , moduli as a function of the oscillatory frequency, ω , for some representative concentrations of PEO in water. The relaxation time, τ , is obtained, for most samples, by the crossover of G' and G'' . The relaxation time of samples for which the crossover cannot be measured experimentally are obtained by extrapolation of the relation between τ and the polymer concentration as shown in Figure 2.33.c. The zero-shear viscosity η_0 is plotted in Figure 2.33.d and one can observe the existence of two regimes. For $C < 0.27\%$, the viscosity increases slowly with the polymer concentration, which corresponds to the unentangled solution regime. At concentrations, $C > 0.27\%$, the viscosity increases strongly ($\eta_0 \propto C^{4.7}$) with the polymer concentration, which is the signature of entanglements, as predicted by scaling arguments based on the tube model [Rubinstein 2003]. The zero-shear viscosity varies by more than 5 orders of magnitude from 1 mPa s to 10^5 mPa s. The elastic modulus, $G_0 = \eta_0/\tau$, the relaxation time, τ , and the zero-shear viscosity, η_0 , for all investigated PEO solutions are reported in table 2.3. Solutions in the unentangled regime ($C < 0.27\%$) are liquid and cannot be modeled by a Maxwell fluid.

Table 2.3: List of all PEO solutions and their rheological properties. G_0 is the elastic modulus, τ , the relaxation time and η_0 , the zero-shear viscosity

PEO solutions			
C [%]	G_0 [Pa]	τ [s]	η_0 [mPa s]
2	18	9.14	$1.6 \cdot 10^5$
1.5	31	2.1	$6.3 \cdot 10^4$
1	13.6	0.48	$6.5 \cdot 10^3$
0.8	17	0.18	$3.1 \cdot 10^3$
0.6	12.6	0.05	$6.3 \cdot 10^2$
0.5	13.6	0.02	$2.7 \cdot 10^2$
0.2	-	-	8
0.13	-	-	4
0.08	-	-	2.5
0.06	-	-	2.4
0.0312	-	-	1.8
0.016	-	-	1.6
0.004	-	-	1.2
0.001	-	-	1.1

Figure 2.33.b depicts the complex viscosity calculated from the linear viscoelastic spectra as, $|\eta^*(\omega)| = \frac{\sqrt{G'(\omega)^2 + G''(\omega)^2}}{\omega}$ in function of frequency, along with the steady shear viscosity, $\eta(\dot{\gamma})$ as a function of shear rate. The nice collapse of the dynamic and steady data validates the Cox-Merz rule [Cox 1958]. We find that all samples are strongly shear-thinning and can be fitted satisfyingly by the Cross model (Eq.2.15) [Cross 1965].

The fitting exponent, n , increasing from 0.59 to 0.85 when the concentration increases. Moreover, for all concentrations the fitting parameter k increases monotonically with the polymer concentration, as does the characteristic relaxation time τ_0 , marking the onset of shear-thinning.

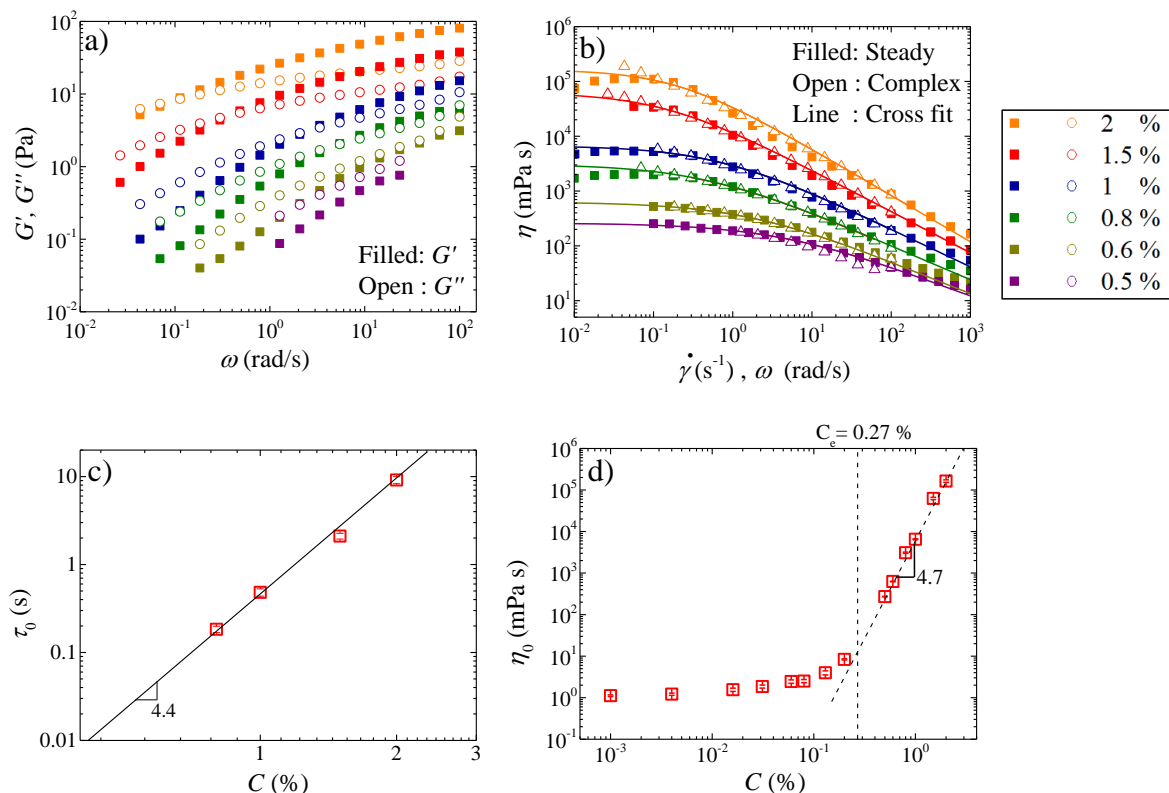


Figure 2.33: a) Storage, $G'(\omega)$ (squares), and loss, $G''(\omega)$ (circles), moduli as a function of the oscillation frequency, ω . b) Complex viscosity as a function of the oscillation frequency, $\eta^*(\omega)$ (closed symbols) and steady shear viscosity as a function of the shear rate, $\eta_s(\dot{\gamma})$, (open symbols), and fits (lines) using the Cross equation (Eq 2.15). c) Evolution with C of the terminal relaxation time, τ_0 , and d) of the zero-shear viscosity, η_0 .

2.2.4 2, 4-bis (2-ethylhexylureido) toluene (EHUT)

Wormlike micellar solutions made of 2, 4-bis (2-ethylhexylureido) toluene, which abbreviates as EHUT, were synthesized according to [Lortie 2002]. The EHUT monomer ($C_{25}H_{44}N_4O_2$) forms hydrogen bonds in an apolar solvent resulting in self-associated small and long rod-like structures with a temperature- and solvent-dependent diameter. Figure 2.34, shows a phase diagram for EHUT molecules in solution with toluene (C_7H_8). The structure of the EHUT monomer is shown, along with a schematic illustration of the

various aggregates formed (out of scale), i.e., filaments and tubes. Hydrogen bonds are represented by dotted lines connecting the urea functions (black circles). At concentrations above the critical micellar concentration and high temperatures, the monomers form thin filaments with diameters comparable to the size of one EHUT monomer (1.3 nm). At lower temperatures, EHUT molecules form thick tubes with cross-section of approximately three EHUT monomers in size. In Chapter 5, the EHUT molecules are dispersed in dodecane ($C_{12}H_{26}$). For the concentrations investigated ($C=0.37$ g/L to $C=3$ g/L), they form tubes at temperatures lying between 20°C and 25°C . This was confirmed by Fourier transform infrared spectroscopy (FTIR), small angle neutron scattering (SANS) and rheology measurements. These tubes are long enough to entangle and create viscoelastic networks.

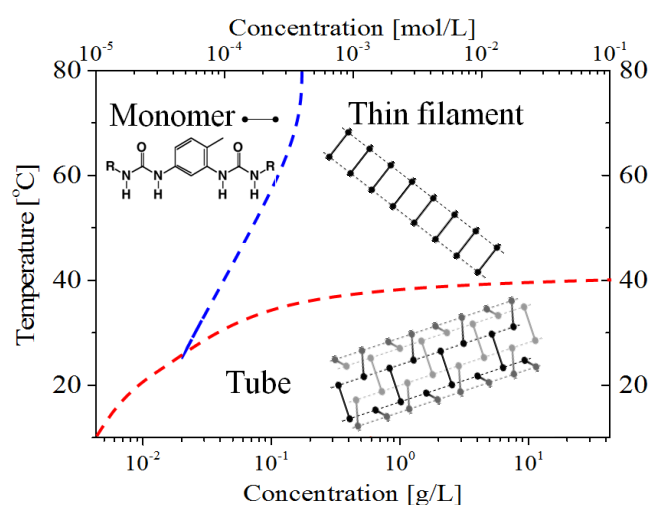


Figure 2.34: Phase diagram for EHUT solutions in toluene [Bouteiller 2005] showing the transition between monomers and supramolecular filaments. The chemical structure of the EHUT monomer is shown, along with a schematic illustration of the various aggregates formed (out of scale), i.e., filaments and tubes. Hydrogen bonds are represented by dotted lines connecting the urea functions (black circles).

EHUT powder was added to dodecane accordingly to the targeted concentration and left under stirring at 80°C for 48 hours. The resulting solution is completely transparent and thermodynamically stable at room temperature (25°C). Rheological measurements of EHUT solutions are performed immediately after the end of the preparation protocol and in the same conditions as for the impact experiments.

The surface tension of the EHUT solutions is assumed to be independent of concentration. The value $\gamma = 25 \pm 2$ mNm⁻¹ is measured for a dilute sample ($C = 0.37$ g/L) with the pendant drop method. The density of the EHUT solutions is assumed to be equal to the density of the solvent, $\rho = 0.75$ g/mL.

Dynamic frequency sweeps are performed with an applied sinusoidal strain of amplitude of $\gamma = 10\%$ with ω varying from 100 to 0.01 rad/s. The resulting storage, $G'(\omega)$, and loss, $G''(\omega)$, moduli measurements are shown for some representative solutions in Figure 2.35.a and fitted with the one mode Maxwell model (Equations 2.13 and 2.14) which works well to describe the viscoelastic behavior at lower frequencies. Figure 2.35.b shows the complex viscosity, $|\eta^*(\omega)|$ as a function of frequency, along with the steady shear viscosity, $\eta(\dot{\gamma})$ as a function of shear rate for some representative solutions of EHUT. The nice collapse of the dynamic and steady data validates the Cox-Merz rule [Cox 1958]. These solutions are strongly shear-thinning as $\eta(\dot{\gamma})$ decrease strongly with increasing shear rate, $\dot{\gamma}$. The Cross model (Equation 2.15) provides a good description of the shear-thinning behavior of EHUT solutions with shear-thinning exponent $n = 0.97 \pm 0.05$. All measurements are performed under the same temperature and humidity conditions as for the drop impact experiments.

Table 2.4: List of all EHUT solutions and their rheological properties. G_0 is the elastic modulus, τ , the relaxation time and η_0 , the zero-shear viscosity

EHUT solutions			
C [g/L]	G_0 [Pa]	τ [s]	η_0 [Pas]
3	8.5	8.6	73
2.85	6.5	12.7	75.5
2.6	5.8	9.4	55.8
2.33	4.5	7.3	31.4
2	3.1	6.7	19.2
1.5	1.8	6.3	12.2
1	0.7	5	2.6
0.37	0.15	2.5	0.5

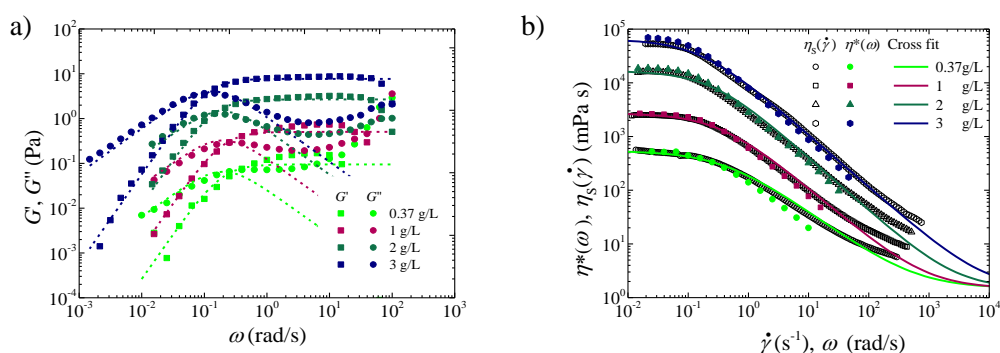


Figure 2.35: a) Storage, $G'(\omega)$ (squares), and loss, $G''(\omega)$ (circles), moduli as a function of the oscillation frequency, ω . b) Complex viscosity as a function of the oscillation frequency, $\eta^*(\omega)$ (closed symbols) and steady shear viscosity as a function of the shear rate, $\eta_s(\dot{\gamma})$, (open symbols), and fits (lines) using the Cross equation (Eq 2.15).

2.2.5 Ultra soft elastic beads

Polyacrylamide beads are prepared in our lab by Dr. Ty Phou through a redox activated free radical copolymerization of acrylamide and N,N'-methylenebis-acrylamide in water in the presence of Tetramethylethylenediamine (TEMED) and sodium persulfate as initiators. TEMED is used to accelerate the formation of sodium persulfate radicals by primary radical formation in redox initiation, which will serve as catalysts for the reaction. The resulting sodium persulfate free radicals trigger the radicalization of acrylamide monomers. Acrylamide radicals react with the monomers in solution to begin the polymerization chain reaction. Poly-acrylamide chains, while growing, are randomly cross-linked by the N,N'-methylenebis-acrylamide to form a network. The resulting gel properties depend on the polymerization conditions, such as temperature and surrounding gas, as well as on the monomer concentrations [Chen 1979, Menter 2000]. The reaction is represented on Figure 2.36. Because polymerization can be inhibited by the presence of oxygen and impurities, the reaction takes place in an inert atmosphere. Before mixing, reagent solutions are saturated with nitrogen gas, which is an inert gas.

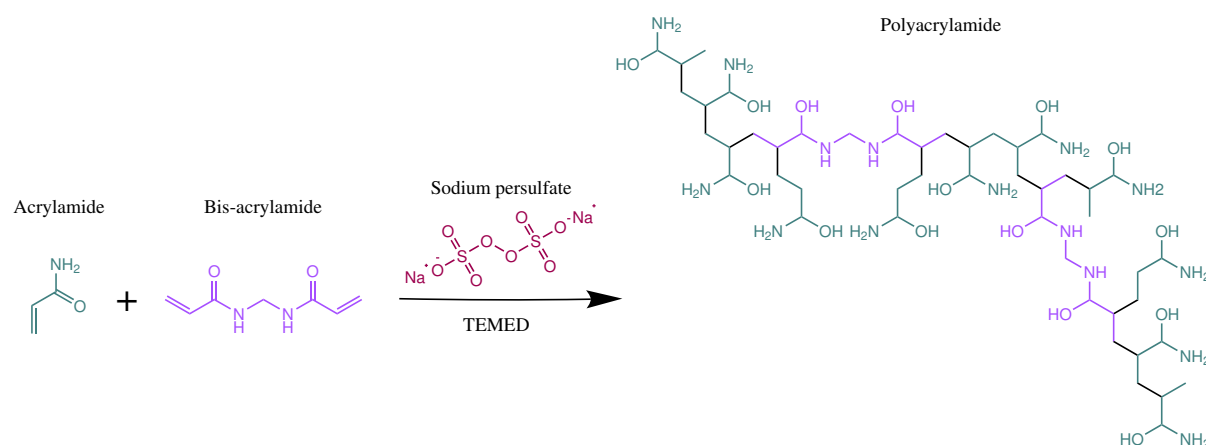


Figure 2.36: Copolymerization reaction of acrylamide and bis-acrylamide.

The elastic beads are synthesized in the background fluid used for the spinning drop experiments. This background fluid should not be miscible with water and must have a density higher than the element to be set in spinning motion. We used a fluorinated oil, *FomblinY* LVAC 25/6, $(CF_3O[-CF(CF_3)CF_2O-]_x(-CF_2O-)_yCF_3)$ ($x = 25$ and $y = 6$) of average molar weight 3,300 g/mol with a density of 1.9 g cm^{-3} at 25°C as purchased from Sigma-Aldrich. The mass density of the beads is considered equal to the density of water at $T = 25^\circ\text{C}$, $\rho = 0.997 \text{ g cm}^{-3}$ because of the low mass fractions of acrylamide employed to reach the targeted low elastic moduli.

The monomer and co-monomer solutions are mixed before adding the TEMED and sodium persulfate. Appropriate volumes ($\sim 1\mu\text{L}$), yielding to drops of 1 mm, are quickly

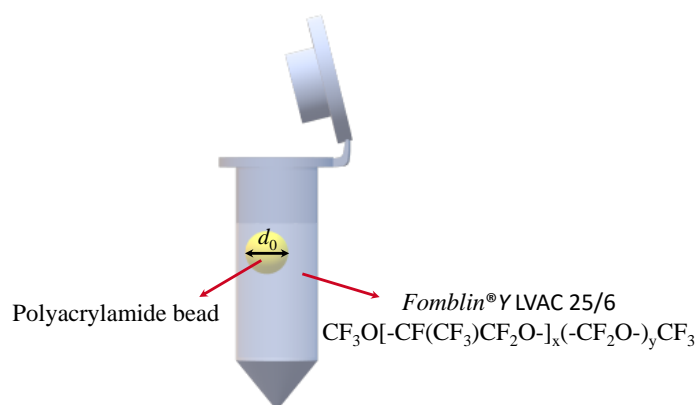


Figure 2.37: Representation of an elastic bead floating in fluorinated oil.

transferred to Eppendorf tubes filled with fluorinated oil where polymerization will take place. Because the size of the droplets are small enough, the interfacial energy between the aqueous drops and the oil is able to give the drops a spherical shape. This interfacial energy was measured for the solution in absence of initiators using a spinning drop tensiometer and found to be $33 \pm 3 \text{ mN m}^{-1}$. Concentrations of bis-acrylamide and acrylamide were fixed respectively to 0.00119 ± 0.0006 and $0.45 \pm 0.01 \text{ mol/L}$. For the concentrations of initiator used, the time for polymerization to be complete is of approximately two hours.

The refractive index of the fluorinated oil ($n_b = 1.299$) is close to that of water. For this reason, a small amount of fluorescein was added to the monomer and co-monomer solution to increase the contrast between the water-based beads and the background fluid and facilitate the tracking of the bead deformation in the spinning drop tensiometer.

Biaxial extensional viscous dissipation in sheets expansion formed by impact of drops of Newtonian and non-Newtonian fluids

In this chapter, we report the publication *Biaxial extensional viscous dissipation in sheets expansion formed by impact of drops of Newtonian and non-Newtonian fluids* A. Louhichi, C.-A. Charles, T. Phou, D. Vlassopoulos, L. Ramos and C. Ligoure, *Physical Review Fluids*, 5 (5), 053602, 2020, in which we investigate the expansion of free liquid sheets produced by impact of Newtonian and shear-thinning polymer solutions on a thin layer of liquid nitrogen. This work has been carried out mostly by Ameer Louhichi. My contribution to this work concerns (i) the conduction of the experiments on impact of the Newtonian fluids and PEO solutions with A. Louhichi, (ii) the analysis of the data for Newtonian fluids, (iii) the improvements on the set-up (including the use of a quartz plate, less liquid nitrogen, simultaneous top and side views), and (iv) the contribution to the discussions on the results.

Biaxial extensional viscous dissipation in sheets expansion formed by impact of drops of Newtonian and non-Newtonian fluids

Ameur Louhichi ^{1,2}, Carole-Ann Charles,¹ Ty Phou,¹ Dimitris Vlassopoulos ²,
Laurence Ramos ^{1,*} and Christian Ligoure ^{1,†}

¹Laboratoire Charles Coulomb (L2C), Université de Montpellier, CNRS, Montpellier, France

²Institute of Electronic Structure and Laser, FORTH, Heraklion 70013, Crete, Greece
and Department of Materials Science and Technology, University of Crete, Heraklion 70013, Crete, Greece



(Received 17 July 2019; accepted 7 April 2020; published 6 May 2020)

We investigate freely expanding liquid sheets made of either simple Newtonian fluids or solutions of high molecular water-soluble polymer chains. A sheet is produced by the impact of a drop on a quartz plate covered with a thin layer of liquid nitrogen that suppresses shear viscous dissipation due to an inverse Leidenfrost effect. The sheet expands radially until reaching a maximum diameter and subsequently recedes. Experiments indicate the presence of two expansion regimes: the capillary regime, where the maximum expansion is controlled by surface tension forces and does not depend on the viscosity, and the viscous regime, where the expansion is reduced with increasing viscosity. In the viscous regime, the sheet expansion for polymeric samples is strongly enhanced as compared to that of Newtonian samples with comparable zero-shear viscosity. We show that data for Newtonian and non-Newtonian fluids collapse on a unique master curve where the maximum expansion factor is plotted against the relevant effective *biaxial extensional* Ohnesorge number that depends on fluid density, surface tension, and the biaxial extensional viscosity. For Newtonian fluids, this biaxial extensional viscosity is six times the shear viscosity. By contrast, for the non-Newtonian fluids, a characteristic *Weissenberg number*-dependent biaxial extensional viscosity is identified, which is in quantitative agreement with experimental and theoretical results reported in the literature for biaxial extensional flows of polymeric liquids.

DOI: [10.1103/PhysRevFluids.5.053602](https://doi.org/10.1103/PhysRevFluids.5.053602)

I. INTRODUCTION

Over the last 15 years, the understanding of drop impact on solid targets has progressed considerably due to high-speed imaging methods [1], allowing one to observe in real time the fate of a drop upon impact under various experimental conditions and to probe a rich variety of phenomena, including dynamics of sheets in the expansion and receding regimes, spatiotemporal evolution of the thickness of the sheets [2,3], fingering instabilities [4–6], and fractures and production of satellite droplets [7–9]. Concerning the nature of the impacting drops, mainly Newtonian fluids of different viscosities have been investigated, although a few relevant studies with shear-thickening fluids [10], shear-thinning fluids [11–17], yield stress fluids [18], or Maxwell fluids without shear thinning [19,20]. Most studies have been performed on drops impacting a flat surface that can be smooth or rough [21], horizontal or tilted [22], hydrophobic or hydrophilic [23]. Often, surfaces have a

*laurence.ramos@umontpellier.fr

†christian.ligoure@umontpellier.fr

very large size compared to that of the drop such that the entire spreading event occurs on the target [8,14,15,24–27], but targets of size comparable to that of the drops [2,3,16,28,29] or drops impacting only partially a small target [30] have also been studied.

The complex interaction of a drop with a solid surface during drop collision may be removed or at least significantly reduced by using repellent surfaces, which avoid a direct contact between the liquid sheet and the solid target. Repellent surfaces include superhydrophobic surfaces [31], hot plates above the Leidenfrost temperature [32,33] or sublimating surfaces [20,34]. Nevertheless, the fact that shear viscous dissipation can be neglected during the expansion of the sheet after impact does not mean that there is no viscous dissipation process. Indeed, *biaxial extensional* viscous dissipation is dominant in freely expanding sheets. Surprisingly this has never been documented to the best of our knowledge, except in a very recent paper [35], where the authors have attributed an inhibition of a drop-substrate contact during drop impact to a large increase of the extensional viscosity.

A possible reason for ignoring the biaxial extensional viscous dissipation is that for sheets expanding completely on a solid surface, viscous dissipation should be dominated by shear. For small targets however, both shear and biaxial extensional viscous dissipation processes may be relevant: this is the goal of a future publication. In the present paper, only biaxial extensional viscous dissipation is relevant as the sheet expands freely due to the inverse Leidenfrost effect discussed below. In this work, we investigate the expansion dynamics of free sheets of a viscoelastic thinning fluid produced upon impacting a single drop on a repellent surface in inverse Leidenfrost conditions, and compare it to the respective response of Newtonian fluids. We demonstrate that accounting for the viscous dissipation due to biaxial extensional viscosity during the expansion of the sheet is crucially important. We provide a simple approach to evaluate the biaxial extensional viscosity of thinning viscoelastic fluids, and finally propose a model to quantitatively account for the viscosity dependence of the maximum expansion of sheets.

The paper is organized as follows. We first describe the materials and methods. We then show the shear rheological properties of the viscoelastic fluids of interest and their behavior upon impact on a repellent surface. Subsequently, we rationalize the results by accounting for the biaxial extensional viscosity and by means of a simple scaling model. The main conclusions are summarized in the last section.

II. MATERIALS AND METHODS

A. Materials

We investigate solutions of polyethylene-oxide (PEO) of high molecular weight ($M_v = 8000$ kDa) from Sigma-Aldrich. Several samples with concentration C between 10^{-3} wt% and 2 wt% are prepared by adding PEO powder, as received, to the appropriate volume of deionized pure water, or mixtures of water and glycerol (20 wt%, 35 wt%, and 41.66 wt% glycerol), and leave the solution under stirring at $T = 25$ °C for 24 h at least in the dark, until complete dissolution. Note that, in order to enhance the visualization contrast, all PEO solutions are colored using a Nigrosin dye (from Sigma-Aldrich) at concentration 0.025 wt%. The surface tension of high molecular weight PEO solutions is independent of polymer concentration ($\gamma = 62$ mNm $^{-1}$) [36]. Pendant drop experiments confirm that the addition of dye does not affect the surface tension of the final solutions. In addition, in order to compare the behavior of viscoelastic polymer solutions with that of simple fluids, we use two classes of Newtonian fluids, mixtures of water and glycerol and silicon oils. Silicon oils, with shear viscosities from 5.2 to 1075 mPa s and an average surface tension of 20 mN/m [37], were purchased from Sigma Aldrich and used as received. Mixtures of water and glycerol with concentrations ranging from 22 to 97.5 wt% glycerol are prepared, yielding shear viscosities from 1.7 to 1910 mPa s (depending on the glycerol weight fraction and temperature), densities from 1.05 to 1.25 g/ml, and an average surface tension of 65 mN/m (as measured with a pendant drop setup).

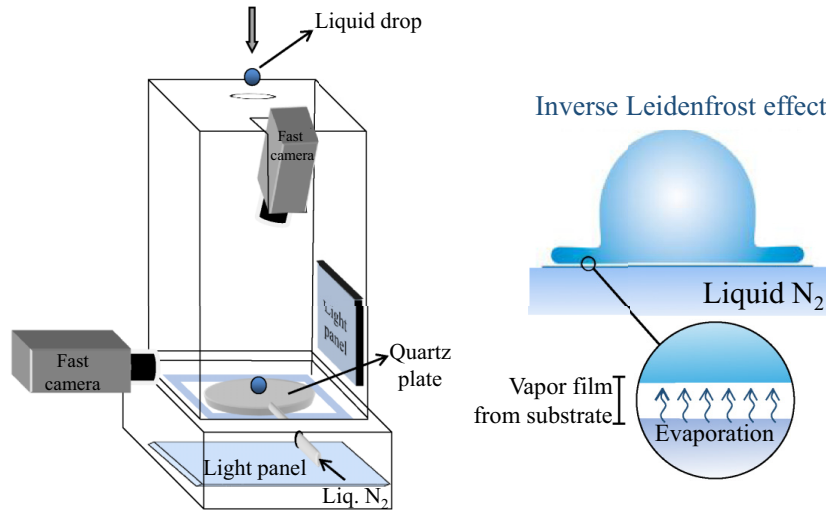


FIG. 1. Left: Schematic illustration of the impact experiments setup showing a drop falling on a liquid nitrogen thin layer. The expansion event is recorded using two fast cameras allowing concomitant top and side visualizations. Right: Adapted from Ref. [34], schematic of the inverse Leidenfrost effect at the origin of the shear free expansion.

B. Methods

1. Drop impact experiments

To substantially eliminate the role of friction or adhesion with the solid surface on the impact dynamics, we work under inverse Leidenfrost conditions. This is achieved by impacting a drop at ambient temperature T (between 18.5 and 22.5 °C) on a polished quartz slide covered with a thin layer of liquid nitrogen (N_2) at $T = -196$ °C (see Fig. 1). The setup is described elsewhere [20]. Upon impact of the drop, a vapor cushion forms at the liquid interface due to the evaporation of N_2 , providing a unique scenario of nonwetting slip conditions that eliminates shear viscous dissipation [34,38]. The rare cases where the impacting drop comes in direct contact with the surface with instantaneous freezing are eliminated, so the nitrogen vapor film keeps the liquid drop separated from the surface for all the reported experiments. Before each impact, the quartz slide is first cleaned by blowing N_2 gas, and then a thin layer (typical thickness 50 nm as measured by ellipsometry) of liquid N_2 is deposited on the slide. The liquid is injected from a syringe pump with a flow rate of 1 ml/min through a needle placed above the target, from the side as shown in Fig. 1. The diameter of the falling drop is constant, $d_0 = 3.9 \pm 0.2$ mm, as measured by image analysis and confirmed from the drop mass. The drop falls from a height $h = 91$ cm, yielding an impact velocity $v_0 = \sqrt{2gh} = 4.2$ ms⁻¹ (g is the acceleration of gravity). The drop impact is recorded from the top [Fig. 2(a)] using a high-speed camera (Phantom V 7:3) operated at 6700 frames/s with a resolution of 800×600 pixels². The angle between the camera axis and the horizontal plane is fixed to about 10°. A second high-speed camera (Phantom miro M310), operated at 3200 frames/s with a resolution of 1280×800 pixels², is eventually used simultaneously to record a side view [Fig. 2(b)].

2. Image analysis

The time evolution of the sheet size is measured with ImageJ software by analyzing top-view images. We first subtract the background image from the expansion movie and highlight the rim by a binary thresholding. This allows us to determine the sheets contour and measure its area A . Note that A does not include the fingers emanating from the rim of the expanding film; they may appear for low viscous samples (Fig. 2) but do not develop for more viscous ones (see Fig. 4 below). An apparent sheet diameter is simply deduced: $d = \sqrt{\frac{4A}{\pi}}$. The results are obtained by averaging for each sample the time evolution of the sheet diameter from three different experiments. Note, however,

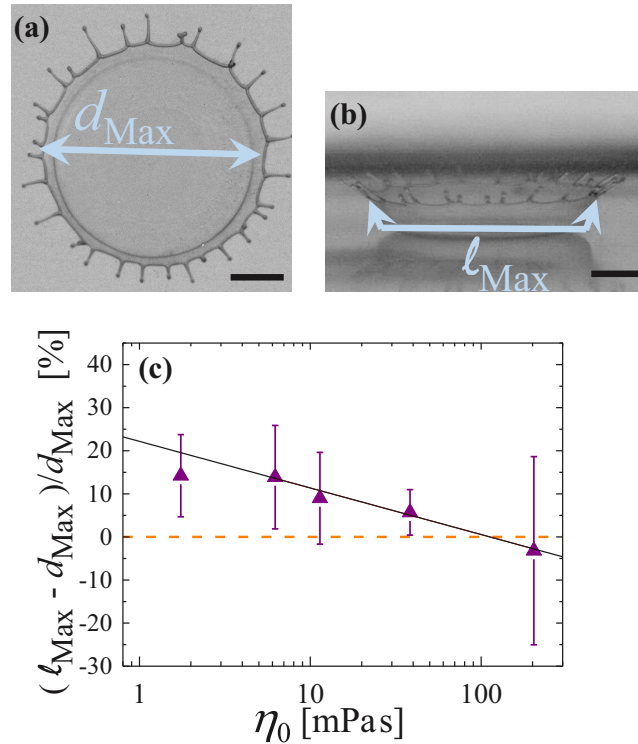


FIG. 2. (a) Top-view and (b) side-view snapshots of the maximum expansion of a low viscous Newtonian sample (22wt% glycerol-water mixture), revealing that the effective diameter d_{Max} from the top view underestimates the maximum expansion of the sheet l_{Max} . (c) Relative side-view correction effect (in %) as a function of shear viscosity of Newtonian glycerol-water. The line is an empirical fit of the data points (symbols).

that corrections have to be performed for low-viscosity samples. Indeed, side-view images reveal the occurrence of a so-called corona splash [Fig. 2(b)] [8], for low viscous Newtonian samples. This implies that the routine standard analysis using top-view images would underestimate the maximum expansion diameter. The side view allows one to evaluate the actual diameter of the sheet [see l_{Max} in Fig. 2(b)]. The fractional underestimation, defined as $\frac{l_{Max} - d_{Max}}{d_{Max}}$, with d_{Max} the maximum diameter measured from top-view images, is plotted as a function of the samples zero-shear viscosity, η_0 , in Fig. 2(c). We find that the fractional underestimation decreases logarithmically with η_0 , from about 22wt% for the lowest viscosity sample and vanishes for $\eta_0 \geq 100$ mPa s. Hence, in the following, quantitative corrections are made for the maximum expansion diameter based on the empirical logarithmic law. For samples with a shear viscosity larger than 100 mPa, the sheet remains flat and no correction is needed.

3. Rheology

Linear viscoelastic and steady shear viscosity measurements are performed with a MCR302 stress-controlled rheometer (Anton Paar, Austria), operating in the strain-control mode and equipped with a stainless steel cone and plate geometry with a diameter of 50 mm, cone angle of 1° and truncation of $101 \mu\text{m}$. Temperature control ($\pm 0.2^\circ\text{C}$) is achieved by means of a Peltier element. The linear viscoelastic spectra are obtained by applying a small amplitude sinusoidal strain, such that data are obtained in the linear regime ($\gamma = 10\%$), varying the angular frequency, ω , from 100 to 0.01 rad/s, and measuring the storage, $G'(\omega)$, and loss, $G''(\omega)$, moduli. The complex viscosity is calculated from the linear viscoelastic spectra as $|\eta^*(\omega)| = \frac{\sqrt{[G'(\omega)^2 + G''(\omega)^2]}}{\omega}$. The steady shear viscosity, $\eta(\dot{\gamma})$ is measured by applying a ramp of steady shear rate varying from 0.01 to 1000 s^{-1} .

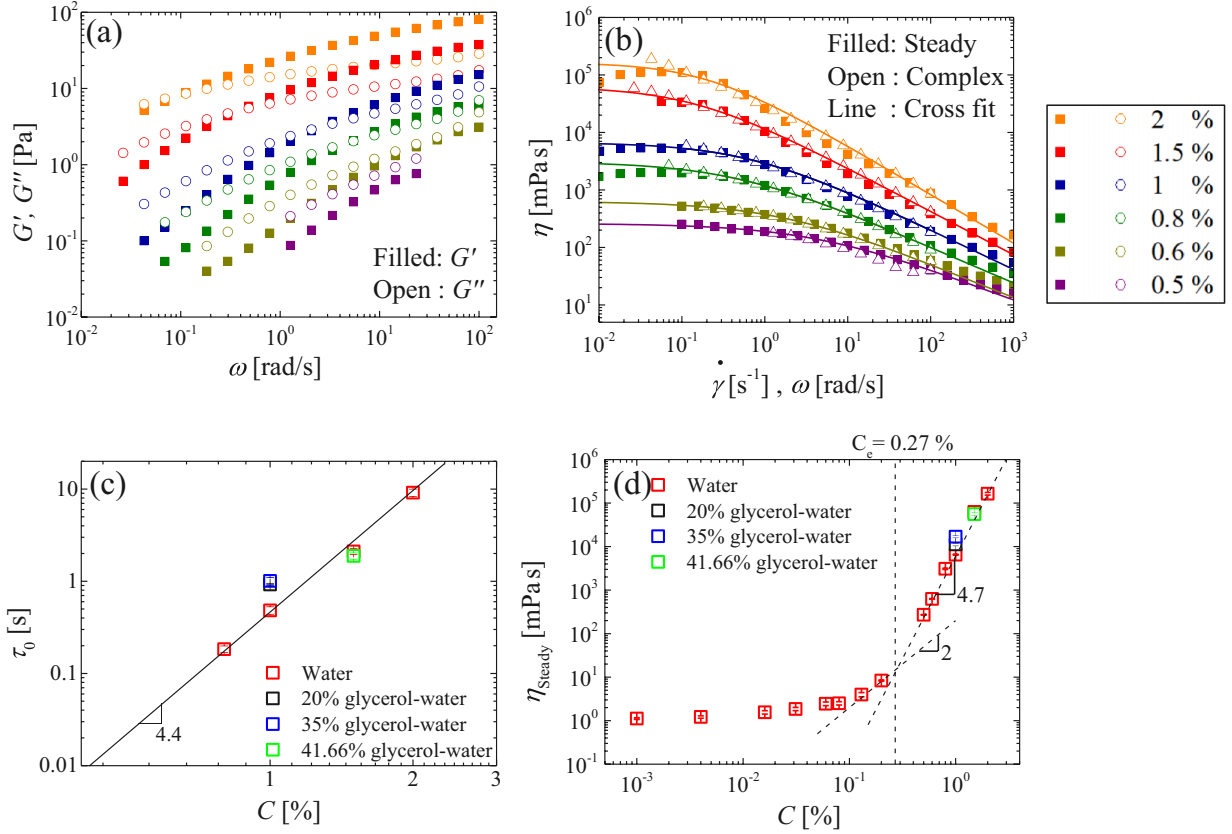


FIG. 3. (a) Frequency dependence of the storage (G') and loss (G'') moduli, and (b) complex viscosity as a function of frequency (open symbols) and steady shear viscosity as a function of shear rate (filled samples), and fits (lines) using the Cross equation [Eq. (1)], for samples with different PEO concentrations C as indicated in the legend. (c) Evolution with C of the terminal relaxation time and (d) of the zero shear viscosity.

III. RESULTS

A. Shear rheology

Figure 3(a) shows the dynamic moduli as a function of oscillatory frequency for aqueous polymer solutions with various concentrations. For $C > 0.6$ wt%, the crossover of G' and G'' marks a characteristic relaxation time τ_0 , which is the best estimate for the onset of the terminal regime. Figure 3(c) shows that $\tau_0 \sim C^{0.44}$ s. This scaling exponent is in the range that have been reported for high molecular weight PEO aqueous solutions [39]. Results for samples prepared with mixtures of water and glycerol are consistent with those obtained for pure water samples [Fig. 3(c)].

The zero shear viscosity, η_0 , varies by more than 5 orders of magnitude from 1 to 10^5 mPa s for the samples investigated. The variation of η_0 with polymer concentration, C , reveals the two expected regimes [Fig. 3(d)]: an unentangled regime for $C < 0.27\%$, where the viscosity increases slowly with the polymer concentration, and an entangled regime at larger concentration, where $\eta_0 \propto C^{4.7}$, in agreement with predictions by scaling arguments based on the tube model [40].

Figure 3(b) depicts the complex viscosity, $|\eta^*(\omega)|$ as a function of frequency, along with the steady shear viscosity, $\eta(\dot{\gamma})$ as a function of shear rate, $\dot{\gamma}$. The nice collapse of the dynamic and steady data validates the Cox-Merz rule [41]. We find that all samples are strongly shear thinning and that an empirical fit by means of the Cross model provides a good description of the shear-thinning behavior of PEO solutions [continuous lines in Fig. 3(b)] [42]:

$$\eta_s(\dot{\gamma}) = \eta_\infty + \frac{\eta_0 - \eta_\infty}{1 + (k\dot{\gamma})^n}. \quad (1)$$

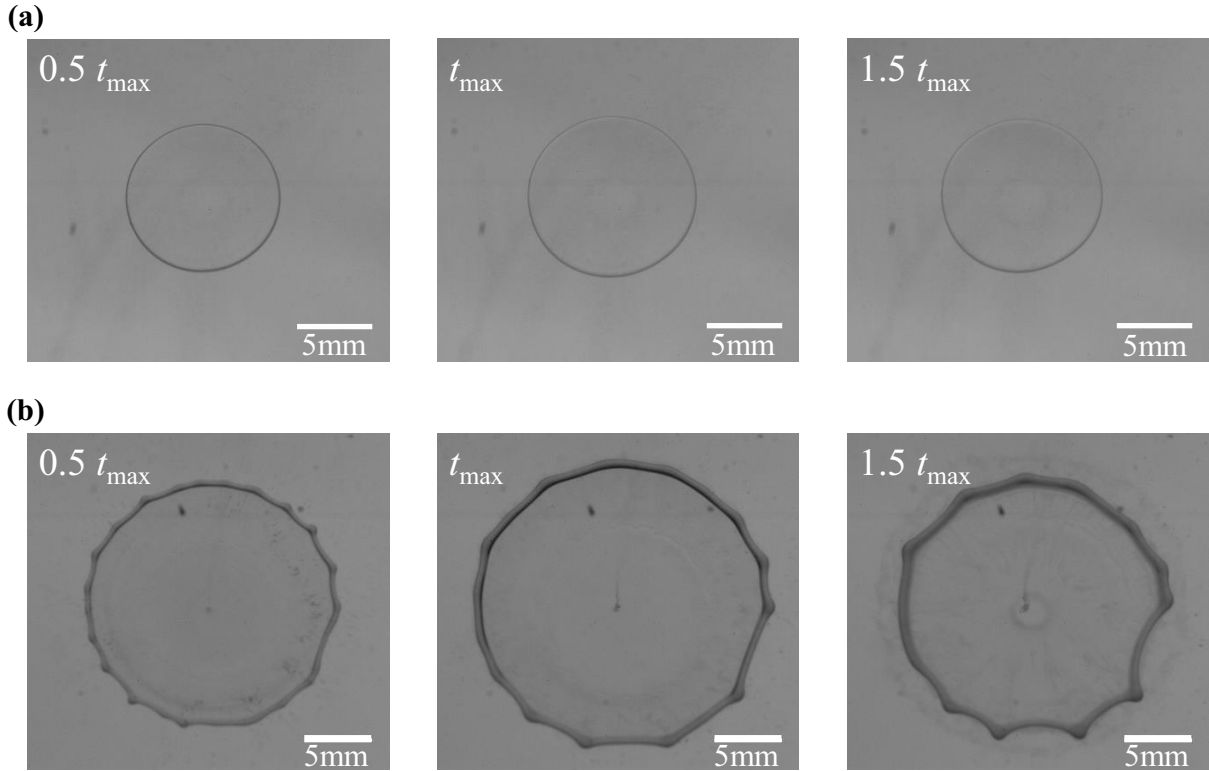


FIG. 4. Snapshots taken at different times, as indicated, during the expansion and retraction of the sheet for (a) a Newtonian silicon oil with shear viscosity $\eta_0 = 658$ mPa s; maximum expansion reached at time $t_{max} = 5.22$ ms and (b) a PEO solution with $C = 0.6\text{wt}\%$ and $\eta_0 = 628$ mPa s; maximum expansion reached at time $t_{max} = 5.02$ ms. The bar sets the scale.

Here η_∞ is the viscosity at very large shear rate that we set equal to the solvent viscosity (water or water-glycerol mixture), η_0 is the zero-shear viscosity [plotted in Fig. 3(d)], n is the shear-thinning exponent, and the parameter k is the inverse of a critical shear rate that delimitates a Newtonian regime from a shear-thinning regime. We find that the shear-thinning exponent n increases with increasing C from 0.59 to 0.85. Moreover, for all concentrations the fitting parameter k is monotonically increasing with C , similarly to the characteristic relaxation time τ_0 , and it marks the onset of shear thinning.

B. Drop impact experiments

Once hitting the repellent surface, the drop expands freely in air until reaching a maximum expansion. It then retracts because of surface tension. This corresponds to an axisymmetric biaxial extensional flow. The overall behavior is illustrated in Fig. 4, which depicts snapshots of the drop after its impact for a PEO solution with $C = 0.6\%$ ($\eta_0 = 628$ mPa s) and for a Newtonian sample of comparable zero-shear viscosity ($\eta_0 = 658$ mPa s). The two samples display strikingly different behavior: the viscoelastic fluid drop expands much more than the Newtonian drop and moreover forms a thicker rim. More quantitatively, we show [Figs. 5(a) and 5(b)] selective raw data for the time evolution of the effective sheet diameter normalized by the original drop, $\frac{d}{d_0}$, for PEO solutions at different concentrations and Newtonian liquids (here silicon oils, but water-glycerol mixtures exhibit the same behavior) with different viscosities. The origin of time is chosen at the time when the drop hits the liquid nitrogen layer. Expansion and retraction regimes are shown, yielding a bell shape for the curves. We note that the curves for the viscoelastic fluids are very symmetric as opposed to the ones for the more viscous Newtonian fluids, where a very long

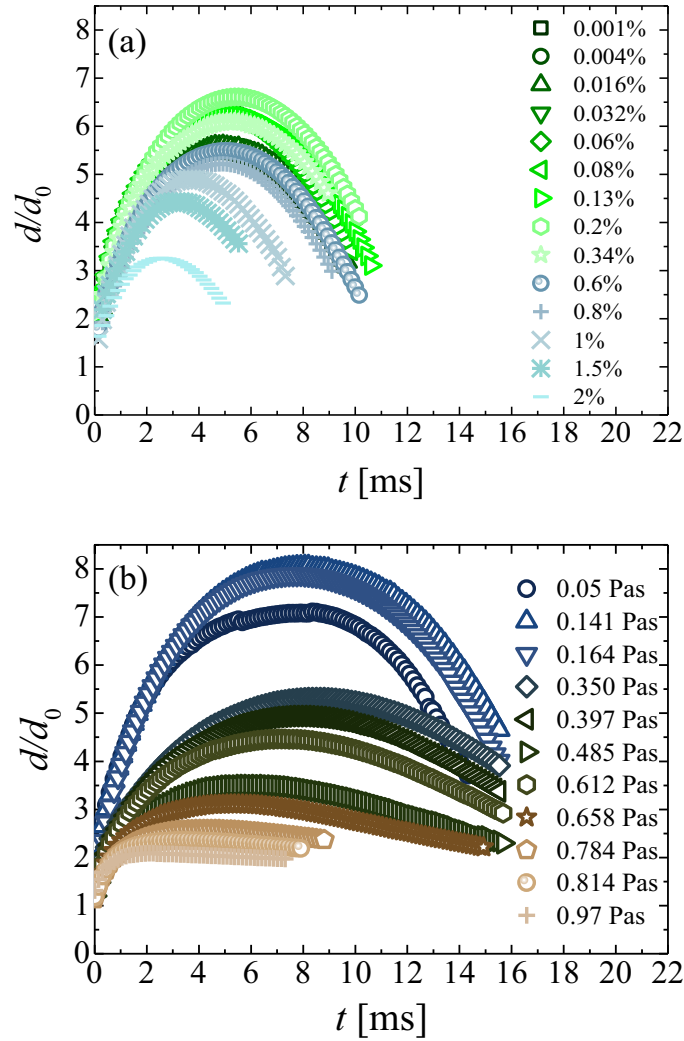


FIG. 5. Time evolution of the sheet diameter normalized by the initial drop diameter for (a) PEO solutions with different concentrations and (b) silicon oils with different shear viscosities, as indicated in the legends. The origin of the time is taken at the drop impact.

retraction regime is measured. These findings deserve deeper investigations in the future, but in the following, we focus on the maximum expansion diameter d_{Max} .

For a biaxial extensional flow, during the expansion of free liquid sheets after impact on a repellent surface, the relevant viscosity is the biaxial extensional viscosity defined as $\eta_B = \frac{\sigma_{rr} - \sigma_{zz}}{\dot{\epsilon}}$, where $\dot{\epsilon}$ is the strain rate, and σ_{rr} and σ_{zz} are the stress tensor components in cylindrical coordinates.

For a Newtonian fluid the constant biaxial extensional viscosity $\eta_B = \eta_B^0 = 6\eta_0$, where η_0 is the zero-shear viscosity and 6 is the Trouton ratio [43]. As a first-order analysis aiming at rationalizing the expansion dynamics of sheets of Newtonian and thinning fluids, we consider the maximum expansion factor, d_{Max}/d_0 , with d_0 the initial drop diameter and plot [Fig. 6(a)] this quantity as a function of the biaxial extensional viscosity η_B^0 . Note that the shear viscosity is measured at the room temperature of the impact experiment; this is of particular importance for water-glycerol mixtures which exhibit a strong temperature dependant viscosity [44]. Similarly to findings for Newtonian fluids impacting a small solid target [19], two regimes are observed for both polymer solutions and Newtonian fluids. At low η_B^0 a capillary regime prevails, where the maximum expansion is mainly driven by a balance between surface tension forces and inertial forces, with viscous dissipation being negligible. Hence, this regime is characterized by a plateau. By contrast, in the viscous regime at higher η_B^0 , d_{Max} decreases monotonically with increasing viscosity.

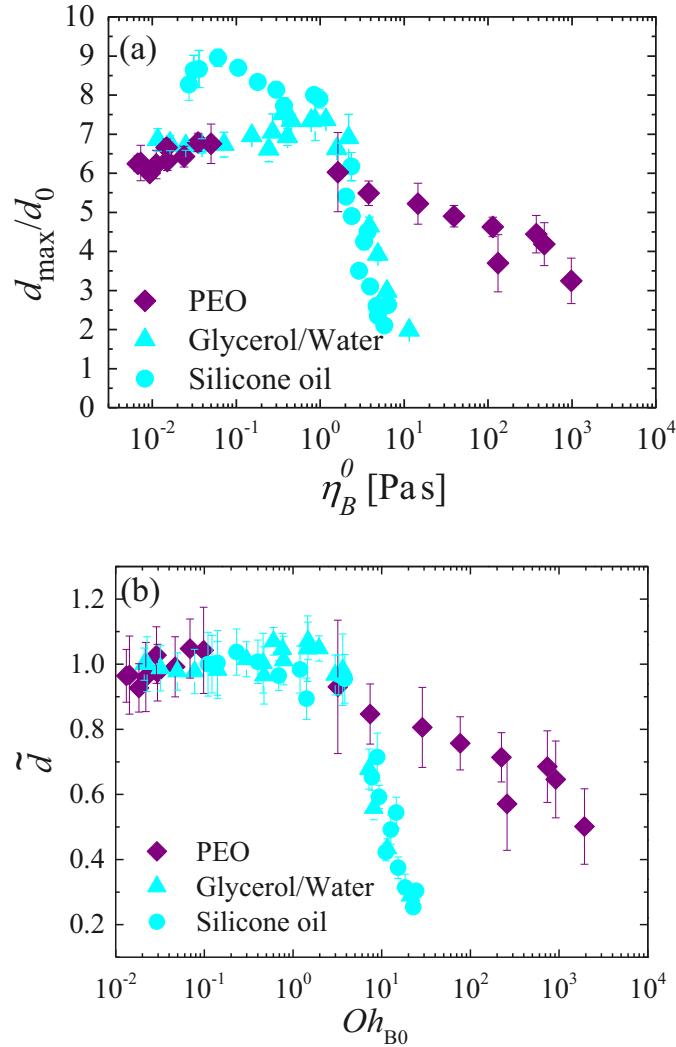


FIG. 6. (a) Maximum diameter of the sheet normalized by the initial drop diameter as a function of the biaxial extensional viscosity, and (b) normalized maximum expansion factor as a function of the biaxial extensional Ohnesorge number, for PEO solutions and for Newtonian liquids.

To get further insight into the observed behavior, we use the normalized maximum expansion factor, \tilde{d} , adopting the same definition as in Refs. [12,19]:

$$\tilde{d} = \frac{d_{\text{Max}}}{d_{\text{Max}}^{\text{cap}}}, \quad (2)$$

where $d_{\text{Max}}^{\text{cap}}$ is the maximum expansion diameter in the capillary regime (at low viscosity). This normalized quantity allows us to compare drops with different initial sizes and different surface tensions. In addition, to account for different surface tensions for different samples, data are plotted against the biaxial extensional Ohnesorge number, $[Oh_{B0}]$, the ratio of biaxial extensional viscous forces to inertial and surface tension forces:

$$Oh_{B0} = \frac{\eta_B^0}{\sqrt{\rho\gamma d_0}} \quad (3)$$

with ρ the sample density and γ the surface tension. Figure 6(b) shows the evolution of \tilde{d} with Oh_{B0} for both polymer solutions and Newtonian fluids. The data for the two types of Newtonian samples overlap nicely onto a master curve and exhibit a capillary regime (for $Oh_{B0} \lesssim Oh_{B0}^c = 2$) characterized by a plateau, followed by a biaxial extensional viscous dissipation regime. We find

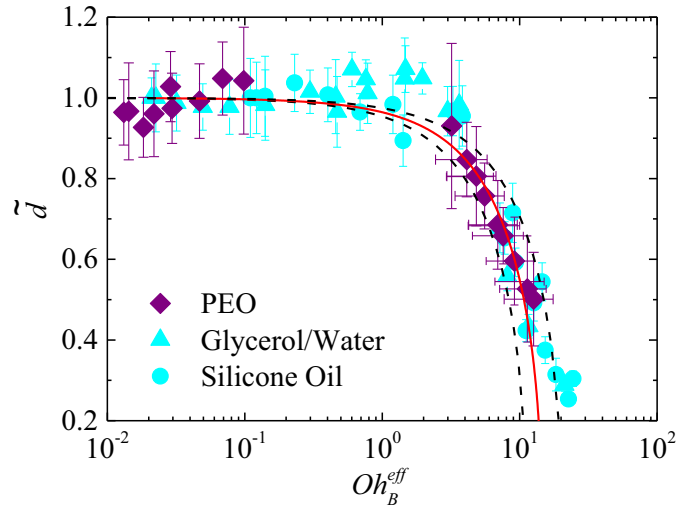


FIG. 7. Normalized maximum expansion factor as a function of the effective biaxial extensional Ohnesorge number for polymer solutions and for the two classes of Newtonian samples. The thin continuous line is the best fit with Eq. (11), and the dashed lines are used to evaluate error bars on the fit parameter.

that for the thinning fluids, the onset of the viscous regime takes place at approximately the same critical biaxial extensional Ohnesorge number Oh_{B0}^c as for Newtonian liquids. Interestingly, however, \tilde{d} decreases much more gradually with Oh_{B0} as compared to Newtonian fluids in the viscous regime. This clearly suggests the importance of a biaxial extensional thinning of the polymer solutions in the viscous dissipation regime. In the next section, we provide a rationalization for the biaxial extensional expansion dynamics of sheets produced with Newtonian and non-Newtonian fluids.

IV. DISCUSSION

A. Rationalization of biaxial extensional thinning

From the data of Fig. 6(b), one can easily define an effective biaxial extensional thinning viscosity η_B^{shift} for polymer samples belonging to the viscous regime ($Oh_{B0} > Oh_{B0}^c$) by shifting horizontally the experimental data point so that they fall on the master curve found for Newtonian samples. The shifted values are discussed in Fig. 9 below. No shift is performed in the capillary regime ($Oh_{B0} < Oh_{B0}^c$) since viscous dissipation is not relevant. Doing so we build a master curve (Fig. 7) for the maximum expansion \tilde{d} as a function of Oh_B^{Thin} for all types of samples, where the effective biaxial extensional Ohnesorge number $Oh_B^{Thin} = Oh_{B0}$ for Newtonian samples and viscoelastic thinning samples in the capillary regime and $Oh_B^{Thin} = \frac{\eta_B^{shift}}{\eta_B} Oh_{B0}$ for viscoelastic thinning samples in the viscous regime. Below we rationalize the shifting of Fig. 7 and the use of biaxial extensional viscosity of non-Newtonian fluids.

1. Determination of the pertinent strain rate

Experimentally, measuring properly the biaxial extensional viscosity is a challenging task, especially for relatively low viscosity fluids such as the present polymers [45–51]. In order to rationalize η_B^{shift} , the first step is to properly account for the deformation rate experienced by sheets during their expansion in air. Here we provide an estimate.

The effective strain rate, defined as $\dot{\epsilon} = \frac{1}{d} \frac{\partial d}{\partial t}$, is not constant in the expansion regime, but decreases with time and vanishes at maximum expansion (Fig. 8). Note that the film expansion is a time-dependent problem, but here we focus on the maximum diameter (end of expansion process) and measure the average rate experienced by the sheet during the expansion. The average value for

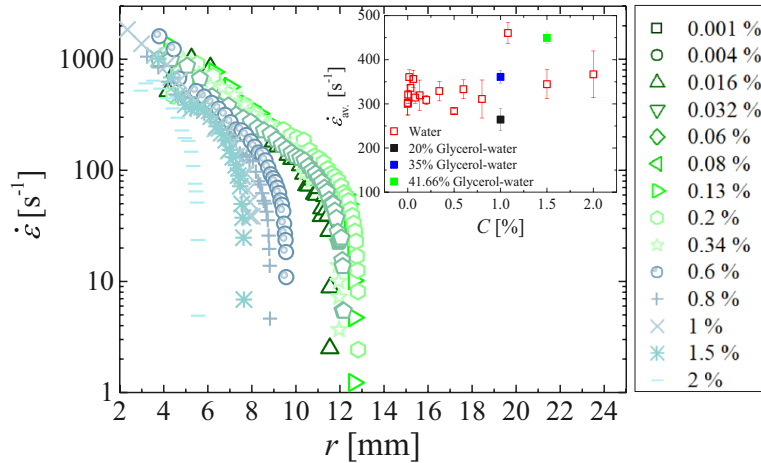


FIG. 8. Evolution of the expansion strain rate as a function of the sheet radius during its expansion for aqueous PEO solutions at different concentrations, as indicated in the legend. Inset: Average strain rate calculated according to Eq. (4) as a function of concentration. Error bars represent the standard deviation from three different experiments.

the strain rate in the expansion regime is then calculated as

$$\dot{\epsilon}_{av} = \frac{\int_0^{r_{Max}} r \dot{\epsilon} dr}{\int_0^{r_{Max}} r dr}. \quad (4)$$

Here $r_{Max} = \frac{d_{Max}}{2}$ is the radius of the sheet at its maximum expansion. We get an average strain rate for each solution that it is used for the rest of the analysis. Note, however, that within experimental errors ($\simeq 15\%$ as shown in the inset of Fig. 8), the effective strain rate does not vary significantly with concentration. Indeed, we obtain a value of $338 \pm 49 \text{ s}^{-1}$ by averaging over all samples, including the PEO solutions prepared in glycerol-water mixtures.

2. Biaxial extensional viscosity

Given the difficulty in obtaining reliable experimental data for the biaxial extensional viscosity $\eta_B(\dot{\epsilon})$ with our samples, we attempt at providing reasonable estimations. To this end, we rely on two pioneering experimental works for the measurements of the biaxial extensional viscosity of viscoelastic solutions [52,53], where similar scaling have been found in spite of using different techniques and different samples: wormlike micelles in Ref. [52] and concentrated polymer solutions in Ref. [53]. At low Weissenberg numbers ($Wi = \dot{\epsilon}\tau_0 < 1$), i.e., for rates lower than the inverse of the terminal relaxation time, τ_0 , the biaxial extensional viscosity is independent of the rate and follows the expectation for a Newtonian fluid: $\eta_B = \eta_B^0 = 6\eta_0$ with η_0 the zero-shear viscosity. By contrast, when $Wi > 1$, the biaxial extensional viscosity decreases with rate, $\eta_B \sim \dot{\epsilon}^{-p}$ with a thinning exponent $p = 0.5$ [53]. This scaling has been also predicted by Marrucci and Ianniruberto [54] using a tube-based model for polymer melts hence, pointing out the universality of the biaxial extensional thinning behavior.

Based on the similar linear viscoelastic response for the PEO solutions and those investigated in Refs. [52,53], we expect our samples to exhibit a similar behavior for the biaxial extensional viscosity as a function of expansion rate. Thus, for each impact experiment in the viscous regime, we define an effective Weissenberg number as $Wi^{eff} = \tau_0 \dot{\epsilon}_{av}$, where τ_0 is given by linear shear rheology measurements for the data showing crossover between G' and G'' and extrapolated, according to the power law presented in Fig. 3(c), for data without the crossover (0.5wt% and 0.6wt%); $\dot{\epsilon}_{av}$ is measured from experiments [Fig. 8(b)]. The effective biaxial extensional thinning is characterized by the experimental data points $(Wi^{eff}, \eta_B^{shift})$, where η_B^{shift} are obtained from Fig. 7. We show in Fig. 9

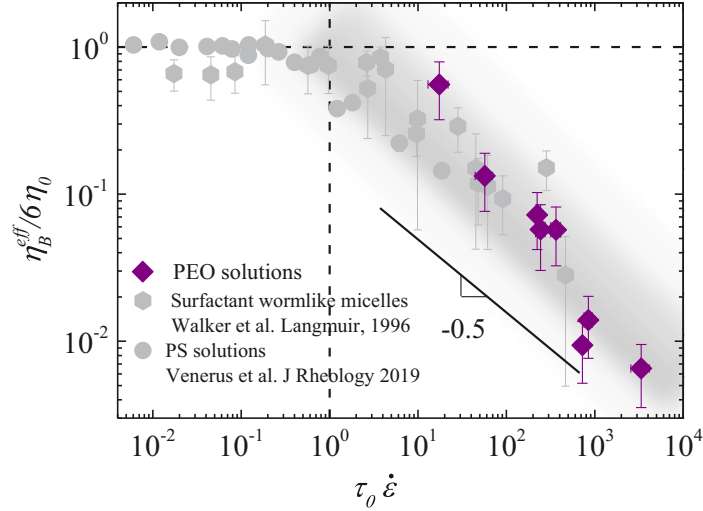


FIG. 9. Effective biaxial extensional viscosity of PEO solutions, extracted from the manual shift of the data in Fig. 7, normalized by the plateau biaxial extensional viscosity as a function of the Weissenberg number, plotted together with literature data as indicated in the legend. A unique master biaxial extensional flow curve is obtained with a thinning exponent of -0.5 in agreement with theoretical predictions (see text). The gray zone highlights the -0.5 slope.

the variation of the normalized effective biaxial extensional viscosity of PEO solutions $\eta_B^{\text{shift}}/(6\eta_0)$ as a function of the effective Weissenberg number Wi^{eff} obtained from drop impact experiments in the viscous regime. On the same plot, we report the experimental data of Refs. [52,53]. We find a remarkable agreement between our shifted values and those from the literature, even though the expansion sheet dynamics that result from the impact of drops are nonstationary, supporting our simple approach.

B. Rationalization of the maximal expansion by considering the biaxial deformation

To go one step further, we provide below scaling laws to account semiquantitatively for the dependence of the maximum expansion on the biaxial extensional viscosity (Fig. 7). We restrict our analysis to Newtonian samples. Indeed, for the normalized maximum expansion factor, each non-Newtonian sample in the viscous regime can be replaced by a Newtonian sample exhibiting the same normalized maximum expansion factor as shown before.

We adopt an energy conservation balance and first consider the capillary regime, for which the initial kinetic energy is assumed to be fully converted into surface energy at the maximum expansion of the sheet:

$$\frac{1}{2}mv_0^2 \simeq 2\pi\gamma(d_{\text{Max}}^{\text{cap}})^2, \quad (5)$$

where $m = \rho\pi d_0^3/6$ is the mass of the drop and $d_{\text{Max}}^{\text{cap}}$ is the diameter at maximum expansion of the sheet in the capillary regime where viscous dissipation is negligible. In the viscous regime, we need to add to the right-hand side of Eq. (5) a term accounting for the viscous dissipation, which here is assumed to result only from the biaxial extensional deformation:

$$\frac{1}{2}mv_0^2 \simeq 2\pi\gamma d_{\text{Max}}^2 + E_B. \quad (6)$$

Combining Eqs. (5) and (6), we obtain for the normalized maximum expansion factor, \tilde{d} ,

$$\tilde{d} = \frac{d_{\text{Max}}}{d_{\text{Max}}^{\text{cap}}} = \sqrt{1 - \frac{2E_B}{mv_0^2}}, \quad (7)$$

with E_B the biaxial extensional energy dissipated during the process of sheet expansion. To a first approximation, E_B can be written as

$$E_B \approx \int_0^{t_{\text{Max}}} dt \int_V \sigma_B(\dot{\epsilon}) \dot{\epsilon} dV, \quad (8)$$

where $V = \frac{\pi d_0^3}{6}$ is the volume of the drop, $\sigma_B(\dot{\epsilon}) = \eta_B \dot{\epsilon}$, and t_{Max} is the time to reach maximum expansion. Hence, assuming also a volume conservation with a uniform thickness sheet, Eq. (8) can be rewritten as

$$E_B \approx \eta_B \frac{\pi d_0^3}{6} \int_0^{t_{\text{Max}}} \left(\frac{1}{d} \frac{\partial d}{\partial t} \right)^2 dt. \quad (9)$$

Using a simple first-order scaling approach to calculate the strain rate, we consider $\frac{\partial d}{\partial t} \approx \frac{d_{\text{Max}} - d_0}{t_{\text{Max}}}$ and a geometric average between the initial and final values of the sheet diameter, $d \approx \sqrt{d_0 d_{\text{Max}}}$, Eq. (9) reads

$$E_B \approx \eta_B \frac{\pi d_0^2}{6} \frac{(d_{\text{Max}} - d_0)^2}{d_{\text{Max}} t_{\text{Max}}}. \quad (10)$$

Here $\frac{(d_{\text{Max}} - d_0)^2}{d_{\text{Max}} t_{\text{Max}}}$ can be considered as an apparent velocity, v_{app} , close to the initial expansion speed of the drop upon impact. Combining Eqs. (7) and (10) together with the definition of the biaxial extensional Ohnesorge number, one predicts

$$\tilde{d} = \sqrt{1 - \alpha \text{Oh}_B} \quad (11)$$

with $\alpha = \frac{2v_L v_{\text{app}}}{v_0^2}$ and $v_L = \sqrt{\frac{\gamma}{\rho d_0}}$ is the typical velocity of free oscillations of the drop [55]. We find that the functional form of Eq. (11) reproduces very nicely the experimental data (Fig. 7), which implies that v_{app} is approximatively constant. The best fit of the data (continuous red line) yields, for all concentrations, $\alpha = 0.06 \pm 0.02$, where the error bars are used to obtain the two envelopes of the data (dashed black lines). This value is compared to the theoretical expectations for the parameter α . For Newtonian fluids, $v_{\text{app}} = 2.3 \pm 1.2$ m/s, thus $\alpha = 0.25 \pm 0.02$. Overall, the fit parameter of the master curve is thus found in reasonable agreement with the ones calculated using the different experimental quantities, thus justifying the relevance of our approach.

V. CONCLUSION

Drop impact experiments on repellent surfaces have been performed with Newtonian fluids and shear-thinning polymer solutions. Two regimes for the maximum expansion diameter of freely expanding sheets have been identified: a capillary regime, where the maximum expansion does not depend on viscosity, and a viscous regime, where the maximum expansion is reduced with increasing viscosity. We have demonstrated that the dominant source of viscous dissipation is the biaxial extensional deformation during sheet expansion, which consequently controls the maximum expansion of the sheets in the viscous regime. We have provided a scaling prediction of the sheet maximum expansion as a function of the biaxial extensional Ohnesorge number, in good quantitative agreement with our experimental results. For viscoelastic thinning fluids, we have proposed a simple approach to measure the biaxial extensional thinning viscosity based on the maximum expansion factor of a freely expanding sheet: the relevant characteristic thinning viscosity is simply given by the viscosity of a Newtonian fluid with the same normalized expansion factor; it obeys the behavior of the biaxial extensional viscosity of polymeric samples as a function of the Weissenberg number in stationary conditions, providing one considers the mean biaxial extensional rate of the sheet during the expansion regime, as the relevant strain rate for the Weissenberg number. Our approach constitutes a first and crucial step toward the development of a new class of biaxial extensional

rheometry tools based on drop impact experiments but needs further investigations (in current progress) including drops of different diameters and different impact heights.

ACKNOWLEDGMENTS

This work was financially supported by People Programme (Marie Curie Actions) of the European Union's Seventh Framework Programme (FP7/2007-2013) under Supolen REA Grant Agreement No. 607937, the labex NUMEV (ANR-10-LAB-20), and the H2020 Program (Marie Curie Actions) of the European Commission's Innovative Training Networks (ITN) (H2020-MSCA-ITN-2017) under DoDyNet REA Grant Agreement No. 765811. We acknowledge Dr. Sara Lindeblad Wingstrand (DTU) for discussions concerning extensional rheology, Dr Srishti Arora (Northwestern University) for her help in impact experiments, and Dr. Benoit Loppinet (IESL-FORTH) for fruitful discussions.

-
- [1] S. T. Thoroddsen, T. G. Etoh, and K. Takehara, High-speed imaging of drops and bubbles, *Annu. Rev. Fluid Mech.* **40**, 257 (2008).
 - [2] C. Vernay, L. Ramos, and C. Ligoure, Free radially expanding liquid sheet in air: Time- and space-resolved measurement of the thickness field, *J. Fluid Mech.* **764**, 428 (2015).
 - [3] Y. Wang and L. Bourouiba, Drop impact on small surfaces: Thickness and velocity profiles of the expanding sheet in the air, *J. Fluid Mech.* **814**, 510 (2017).
 - [4] S. S. Yoon, R. A. Jepsen, M. R. Nissen, and T. J. O'Hern, Experimental investigation on splashing and nonlinear fingerlike instability of large water drops, *J. Fluids Struct.* **23**, 101 (2007).
 - [5] T. S. T and J. Sakakibara, Evolution of the fingering pattern of an impacting drop, *Phys. Fluids* **10**, 1359 (1998).
 - [6] H. Marmanis and S. T. Thoroddsen, Scaling of the fingering pattern of an impacting drop, *Phys. Fluids* **8**, 1344 (1996).
 - [7] D. van der Meer, Impact on granular beds, *Annu. Rev. Fluid Mech.* **49**, 463 (2017).
 - [8] C. Josserand and S. T. Thoroddsen, Drop impact on a solid surface, *Annu. Rev. Fluid Mech.* **48**, 365 (2016).
 - [9] D. Bonn, J. Eggers, J. Indekeu, J. Meunier, and E. Rolley, Wetting and spreading, *Rev. Mod. Phys.* **81**, 739 (2009).
 - [10] F. Boyer, E. Sandoval-Nava, J. H. Snoeijer, J. F. Dijksman, and D. Lohse, Drop impact of shear thickening liquids, *Phys. Rev. Fluids* **1**, 013901 (2016).
 - [11] N. Laan, K. G. de Bruin, D. Bartolo, C. Josserand, and D. Bonn, Maximum Diameter of Impacting Liquid Droplets, *Phys. Rev. Appl.* **2**, 863 (2014).
 - [12] S. M. An and S. Y. Lee, Maximum spreading of a shear-thinning liquid drop impacting on dry solid surfaces, *Exp. Thermal Fluid Sci.* **38**, 140 (2012).
 - [13] J. J. Cooper-White, R. C. Crooks, and D. V. Boger, A drop impact study of worm-like viscoelastic surfactant solutions, *Colloids Surf. A* **210**, 105 (2002).
 - [14] R. Crooks and D. V. Boger, Influence of fluid elasticity on drops impacting on dry surfaces, *J. Rheol.* **44**, 973 (2000).
 - [15] D. Izbassarov and M. Muradoglu, Effects of viscoelasticity on drop impact and spreading on a solid surface, *Phys. Rev. Fluids* **1**, 023302 (2016).
 - [16] A. Rozhkov, B. Prunet-Foch, and M. Vignes-Adler, Dynamics and disintegration of drops of polymeric liquids, *J. Non-Newtonian Fluid Mech.* **134**, 44 (2006).
 - [17] H. K. Huh, S. Jung, K. W. Seo, and S. J. Lee, Role of polymer concentration and molecular weight on the rebounding behaviors of polymer solution droplet impacting on hydrophobic surfaces, *Microfluid. Nanofluid.*, **18**, 1221 (2015).
 - [18] L.-H. Luu and Y. Forterre, Drop impact of yield-stress fluids, *J. Fluid Mech.* **632**, 301 (2009).

- [19] S. Arora, C. Ligoure, and L. Ramos, Interplay between viscosity and elasticity in freely expanding liquid sheets, *Phys. Rev. Fluids* **1**, 083302 (2016).
- [20] S. Arora, J. M. Fromental, S. Mora, T. Y. Phou, L. Ramos, and C. Ligoure, Impact of Beads and Drops on a Repellent Solid Surface: A Unified Description, *Phys. Rev. Lett.* **120**, 148003 (2018).
- [21] R. Rioboo, M. Marengo, and C. Tropea, Time evolution of liquid drop impact onto solid, dry surfaces, *Exp. Fluids* **33**, 112 (2002).
- [22] A. L. N. Moreira, A. S. Moita, E. Cossali, M. Marengo, and M. Santini, Secondary atomization of water and isooctane drops impinging on tilted heated surfaces, *Exp. Fluids* **43**, 297 (2007).
- [23] M. Lee, Y. S. Chang, and H.-Y. Kim, Drop impact on microwetting patterned surfaces, *Phys. Fluids* **22**, 072101 (2010).
- [24] G. German and V. Bertola, Impact of shear-thinning and yield-stress drops on solid substrates, *J. Phys.: Condens. Matter* **21**, 375111 (2009).
- [25] J. B. Lee, D. Derome, R. Guyer, and J. Carmeliet, Modeling the maximum spreading of liquid droplets impacting wetting and nonwetting surfaces, *Langmuir* **32**, 1299 (2016).
- [26] C. Ukiwe and D. Y. Kwok, On the maximum spreading diameter of impacting droplets on well-prepared solid surfaces, *Langmuir* **21**, 666 (2005).
- [27] D. C. D. Roux and J. J. Cooper-White, Dynamics of water spreading on a glass surface, *J. Colloid Interface Sci.* **277**, 424 (2004).
- [28] A. Rozhkov, B. Prunet-Foch, and M. Vignes-Adler, Dynamics of a liquid lamella resulting from the impact of a water drop on a small target, *Proc. R. Soc. London* **460**, 2681 (2004).
- [29] E. Villermaux and B. Bossa, Drop fragmentation on impact, *J. Fluid Mech.* **668**, 412 (2011).
- [30] S. Lejeune, T. Gilet, and L. Bourouiba, Edge effect: Liquid sheet and droplets formed by drop impact close to an edge, *Phys. Rev. Fluids* **3**, 083601 (2018).
- [31] D. Richard, C. Clanet, and D. Quéré, Surface phenomena: Contact time of a bouncing drop, *Nature (London)* **417**, 811 (2002).
- [32] L. H. J. Wachters, L. Smulders, J. R. Vermeulen, and H. C. Kleiweg, The heat transfer from a hot wall to impinging mist droplets in the spheroidal state, *Chem. Eng. Sci.* **21**, 1231 (1966).
- [33] A.-L. Biance, C. Clanet, and D. Quéré, Leidenfrost drops, *Phys. Fluids* **15**, 1632 (2003).
- [34] C. Antonini, I. Bernagozzi, S. Jung, D. Poulikakos, and M. Marengo, Water Drops Dancing on Ice: How Sublimation Leads to Drop Rebound, *Phys. Rev. Lett.* **111**, 014501 (2013).
- [35] M. Y. Pack, A. Yang, A. Perazzo, B. Qin, and H. A. Stone, Role of extensional rheology on droplet bouncing, *Phys. Rev. Fluids* **4**, 123603 (2019).
- [36] B. H. Cao and M. W. Kim, Molecular weight dependence of the surface tension of aqueous poly(ethylene oxide) solutions, *Faraday Discuss.* **98**, 245 (1994).
- [37] A. Crisp, E. de Juan Jr., and J. Tiedeman, Effect of silicone oil viscosity on emulsification, *Arch. Ophthalmol.* **105**, 546 (1987).
- [38] S. Chen and V. Bertola, The impact of viscoplastic drops on a heated surface in the Leidenfrost regime, *Soft Matter* **12**, 7624 (2016).
- [39] M. Ortiz, D. De Kee, and P. J. Carreau, Rheology of concentrated polyethylene oxide solutions, *J. Rheol.* **38**, 519 (1994).
- [40] M. Rubinstein and R. H. Colby, *Polymer Physics* (Oxford University Press, Oxford, 2003).
- [41] W. P. Cox and E. H. Merz, Correlation of dynamic and steady flow viscosities, *J. Polym. Sci.* **28**, 619 (1958).
- [42] M. M. Cross, Rheology of non-Newtonian fluids: A new flow equation for pseudoplastic systems, *J. Colloid Sci.* **30**, 417 (1965).
- [43] C. W. Macosko, *Rheology: Principles, Measurements and Applications* (Wiley-VCH, New York, 1994).
- [44] J. B. Segur and H. E. Oberstar, Viscosity of glycerol and its aqueous solutions, *Ind. Eng. Chem.* **43**, 2117 (1951).
- [45] J. M. Maerker and W. R. Schowalter, Biaxial extension of an elastic liquid, *Rheologica Acta* **13**, 627 (1974).
- [46] D. D. Joye and G. W. Poehlein, A bubble inflation technique for the measurement of viscoelastic properties in equal biaxial extensional flow, *Trans. Soc. Rheol.* **16**, 421 (1972).

- [47] D. C. Venerus, T. Y. Shiu, T. Kashyap, and J. Hosttetter, Continuous lubricated squeezing flow: A novel technique for equibiaxial elongational viscosity measurements on polymer melts, *J. Rheol.* **54**, 1083 (2010).
- [48] M. Johnson, N. Murphy, R. Ekins, J. Hanley, and S. Jerrams, Equi-biaxial fatigue testing of EPM utilising bubble inflation, *Polymer Testing* **53**, 122 (2016).
- [49] H. M. Huang and J. L. Kokini, Measurement of biaxial extensional viscosity of wheat-flour doughs, *J. Rheol.* **37**, 879 (1993).
- [50] P. Hachmann and J. Meissner, Rheometer for equibiaxial and planar elongations of polymer melts, *J. Rheol.* **47**, 989 (2003).
- [51] C. A. Cathey and G. G. Fuller, Uniaxial and biaxial extensional viscosity measurements of dilute and semi-dilute solutions of rigid rod polymers, *J. Non-Newtonian Fluid Mech.* **30**, 303 (1988).
- [52] L. M. Walker, P. Moldenaers, and J. F. Berret, Macroscopic response of wormlike micelles to elongational flow, *Langmuir* **12**, 6309 (1996).
- [53] D. C. Venerus, R. M. Mick, and T. Kashyap, Equibiaxial elongational rheology of entangled polystyrene melts, *J. Rheol.* **63**, 157 (2019).
- [54] G. Marrucci and G. Ianniruberto, Interchain pressure effect in extensional flows of entangled polymer melts, *Macromolecules* **37**, 3934 (2004).
- [55] F. R. S Rayleigh, On the capillary phenomena of jets, *Proc. R. Soc. London* **29**, 71 (1879).

Viscoelasticity and elastocapillarity effects in the impact of drops on a repellent surface

In this chapter, we report the paper *Viscoelasticity and elastocapillarity effects in the impact of drops on a repellent surface*, C.-A. Charles, A. Louhichi, L. Ramos and C. Ligoure, *Soft Matter*, 17, 5829-5837, 2021, where we present a non-linear damped harmonic oscillator model to predict the maximal expansion and the time to reach it of a free liquid sheet. The impacting drops are Newtonian fluids with biaxial extensional viscosities varying over three order of magnitude and viscoelastic samples spanning a large range of elastic moduli, characteristic relaxation times and viscosities.

Cite this: *Soft Matter*, 2021,
17, 5829

Viscoelasticity and elastocapillarity effects in the impact of drops on a repellent surface†

Carole-Ann Charles,  Ameur Louhichi,  Laurence Ramos  and
Christian Ligoure *

We investigate freely expanding viscoelastic sheets. The sheets are produced by the impact of drops on a quartz plate covered with a thin layer of liquid nitrogen that suppresses shear viscous dissipation as a result of the cold Leidenfrost effect. The time evolution of the sheet is simultaneously recorded from top and side views using high-speed cameras. The investigated viscoelastic fluids are Maxwell fluids, which are characterized by low elastic moduli, and relaxation times that vary over almost two orders of magnitude, thus giving access to a large spectrum of viscoelastic and elastocapillary effects. For the purposes of comparison, Newtonian fluids, with viscosity varying over three orders of magnitude, are also investigated. In this study, d_{\max} , the maximal expansion of the sheets, and t_{\max} the time to reach this maximal expansion from the time at impact, are measured as a function of the impact velocity. By using a generalized damped harmonic oscillator model, we rationalize the role of capillarity, bulk elasticity and viscous dissipation in the expansion dynamics of all investigated samples. In the model, the spring constant is a combination of the surface tension and the bulk dynamic elastic modulus. The time-varying damping coefficient is associated to biaxial extensional viscous dissipation and is proportional to the dynamic loss modulus. For all samples, we find that the model reproduces accurately the experimental data for d_{\max} and t_{\max} .

Received 22nd March 2021,
Accepted 19th May 2021

DOI: 10.1039/d1sm00438g

rsc.li/soft-matter-journal

1 Introduction

When a drop with a high level of kinetic energy hits a surface, it expands radially into a transient sheet, until reaching a maximum diameter before, in some cases, receding partially or completely depending on the nature of the drop and the surface. Predicting the maximum diameter and the time needed for the sheet to reach the latter is crucial for many industrial applications such as spray coating,¹ pesticide application,² forensic science³ or ink-jet printing.⁴ As a matter of fact, the dynamics of drop impact has been extensively studied over the years and has been greatly aided by the emergence of high speed imaging.^{5,6} The impact of a drop can now be observed in real time for various systems such as Newtonian fluids with different viscosities,^{7,8} suspensions of particles,^{9,10} shear thickening fluids,¹¹ polymer solutions¹² or other viscoelastic materials¹³ as well as soft elastic beads.¹⁴ These materials are impacted on many different surfaces such as thick and thin liquid films or solid surfaces of different roughness¹⁵ and wettability¹⁶ but also of different sizes, geometries^{6,7,17} or inclinations.¹⁸

Numerous rationalizations⁶ and simulations^{19–21} of the impact process have provided great insight into the expansion dynamics

of Newtonian fluids. These models are generally based on a balance of energy and aim to predict the maximum diameter reached by the sheet as a function of characteristic adimensional numbers (Reynolds, Weber and Ohnesorge numbers). In the case of viscoelastic fluids, rationalization is however more complex and was not as extensively studied.^{22,23} Though, because most industrial impact phenomenon involve viscoelastic fluids, understanding the behavior of impacted viscoelastic drops is of great interest.

Impact dynamics of viscoelastic fluids is more complex than for Newtonian fluids. For this reason, we simplify the contribution of dissipation by impacting drops on a repellent surface. Such surfaces include superhydrophobic surfaces,²⁴ hot plates above the Leidenfrost temperature^{25,26} or cold plates used in cold Leidenfrost conditions.^{14,27} Repellent surfaces avoid a direct contact between the liquid sheet and the solid surface hence it suppresses the contact between the drop and the solid surface during drop collision and sheet expansion. Viscous dissipation due to shear is therefore suppressed. However, the use of repellent surfaces does not suppress all viscous dissipation. We have recently shown that biaxial extensional viscosity is the relevant source of viscous dissipation involved in the impact dynamics of drops in cold Leidenfrost conditions for which the shear dissipation is suppressed.²⁸

In this work, we investigate the expansion dynamics of freely expanding sheets formed by the impact of drops of viscoelastic

Laboratoire Charles Coulomb (L2C), Université de Montpellier, CNRS, Montpellier, France. E-mail: christian.ligoure@umontpellier.fr

† Electronic supplementary information (ESI) available. See DOI: 10.1039/d1sm00438g

Paper

fluids for which the effects of bulk elasticity, capillarity and viscosity combine in a non-trivial way. Drops are impacted in cold Leidenfrost conditions at several impact velocities. A simple model of 1D harmonic oscillator was used to provide a quantitative estimate of the expansion dynamics of sheets without viscous dissipation for drops of inviscid fluids,^{29,30} for elastic beads³¹ and for ultra-soft elastic beads and viscoelastic drops with long relaxation times with respect to the duration of the impact experiment.¹⁴ Viscous damping has also been recently included in the 1D oscillator model to account for viscous dissipation in the rebound of Newtonian fluids³² or droplet oscillation after impact.³³ Here, we show that taking into account the viscoelastic nature of the samples is crucial to capture into a generalized damped oscillator model, beyond the scaling arguments, the non-trivial combination of bulk elasticity, surface tension and viscosity in the expansion dynamics of viscoelastic drops following impact. The model successfully describes the expansion of sheets made from viscoelastic fluids as well as Newtonian liquids with a wide range of viscosities allowing one to extend investigations further than the capillary regime.

2 Methods and materials

2.1 Experimental set-up

With the aim of weeding out the shear dissipation, drop impact experiments are performed under cold Leidenfrost conditions using a set-up described previously.^{14,28} The drop at ambient temperature impacts a quartz plate covered by a thin layer of liquid nitrogen (boiling point $T_s = -196.15$ °C). As the temperature of the drop is higher than T_s , the liquid nitrogen evaporates partially upon impact, creating a vapor layer under the expanding drop of typical thickness 100 μm .³⁴ The drop is supported by the evaporating nitrogen throughout the whole expansion process and is left to expand free of shear viscous dissipation.^{27,35}

The experimental set-up is schematically shown in Fig. 1a. The drops are released from a needle (internal diameter 2 mm) placed vertically above the quartz surface and connected, through a flexible Teflon tube, to a syringe pump set at a flow rate of 1 ml min^{-1} . The initial diameter of the drop, d_0 , varies between 3.1 and 3.8 mm depending on the fluids surface tension. The height, H , from which the drop is released into a free fall is varied between 11 cm and 131 cm in order to obtain impact velocities ranging between 1.5 and 5 m s^{-1} . Drops accumulate inertial energy throughout their fall until reaching the surface covered with the thin liquid nitrogen layer where they expand and reach a maximal expansion before retracting due to surface tension and stored elastic energy. During retraction, some droplets are eventually expelled from the rim. The whole process is captured from the top, at an angle of approximately 10° with the vertical plane, by a high speed camera, Phantom V 7:3, operating at 6700 fps with a resolution of 800×600 pixels² and, for most experiments, simultaneously from the side by a Phantom miro M310 operating at 3200 fps with a resolution of 1280×800 pixels². We use the side imaging to check that the sheets are flat during the whole duration of the expansion. The top

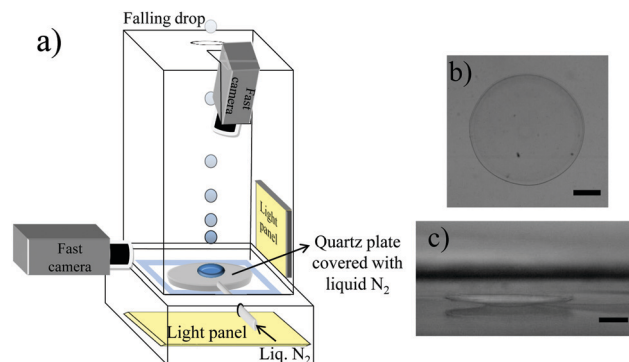


Fig. 1 (a) Schematic illustration of the set-up where a drop falls onto a quartz plate covered with a thin layer of liquid nitrogen. The impact is simultaneously recorded from the top and the side by two fast cameras. (b and c) Snapshots of a viscoelastic sheet (sample M14 ϕ 10r6) taken at maximal expansion from the top (b) and from the side (c). The impact velocity is $v_0 = 4.7$ m s^{-1} . The scale bars represent 5 mm.

view imaging is used to quantify the expansion dynamic. Proper illumination for acquisition is provided by high-intensity backlights; Phlox HSC with a luminance of 98 cd m^{-2} in the bottom and Phlox LLUB with a luminance of 20 cd m^{-2} on the side. The temperature (20 °C on average) of the room is systematically measured before each impact experiment to control the experimental conditions. Between each impact, the substrate is cleaned with ethanol. Fig. 1b and c show top and side views of a viscoelastic sheet taken at its maximal expansion. The snapshots show that the sheet at maximal expansion has a near circular shape and lays almost flat on the nitrogen gas.

As the temperature of the fluid on which the drop is impacted is very low ($T_s = -196.15$ °C, the boiling point of liquid nitrogen) as compared to the initial temperature of the drop (about 20 °C), one should ensure that the drop does not freeze upon impact and that its temperature remains constant throughout the expansion. We thus quantify the typical time for the heat to transfer from the drop to the quartz plate and compare this time to the typical time of an experiment (typically of the order of a few ms). The principal heat transfer mode between the sample and the vapor layer is conduction.^{36–38} The calculation is reported in the ESI.† It shows that the temperature of the sheet decreases by less than 0.8 °C when the sheet reaches maximal expansion. Hence, it is reasonable to assume that the temperature of the sheet does not vary considerably until maximum expansion. Thus, in the following the rationalization of the experimental results will be done using the fluids properties measured at 20 °C, close to the temperature of the drop impact experiments.

2.2 Image analysis

The stacks of frames obtained from top view imaging are analyzed using ImageJ software. The sheet is delimited by adjusting the threshold and its area, A , is measured for each frame using the analyze particle command. We have checked that corrections in the measured area, due to the camera angle, can be safely neglected. An apparent diameter, d , is extracted using $d = \sqrt{\frac{4A}{\pi}}$.

For Newtonian fluids with zero shear viscosities lower than 100 mPa s, the maximal diameter is corrected in accordance with observations made in ref. 28. Indeed, for these low viscosity samples side view imaging shows that the sheet exhibits a corona shape, resulting in an underestimation of the actual diameter if simply estimated from top imaging.²⁸ We check that for all investigated viscoelastic samples, the sheets remain flat and no correction is necessary. In the following, for each impact velocity and sample, the reported time evolution of the sheet diameter corresponds to an average over three different experiments.

2.3 Shear rheology

All samples are characterized rheologically using either Anton Paar MRC302 or ARES RFS 1KFRT rheometers, equipped with stainless steel cone and plate geometries of diameter 50 mm with an angle of 1° and a truncation of 101 μm. Dynamic strain sweeps with strain amplitude from 0.1% to 100% are conducted at frequencies of 10 and 50 rad s⁻¹ to define the linear viscoelastic regime. Dynamic frequency sweeps are performed at a strain amplitude $\gamma = 1\%$, well in the linear regime, for an angular frequency varying from 100 to 0.01 rad s⁻¹. Temperature is set at 20 °C for all measurements and controlled using a Peltier element (accuracy of 0.2 °C).

2.4 Systems

Two classes of fluids are investigated: two types of Newtonian liquids and two types of viscoelastic fluids.

The Newtonian liquids consist of silicone oil blends (SO) and glycerol–water mixtures (G–W). Silicone oils are purchased from Sigma Aldrich and blended to give mixtures of different viscosities. The zero shear viscosities of the blends vary from 5 mPa s to 970 mPa s as measured at 20 °C, their average surface tension is 20 mN m⁻¹³⁹ and their density varies between 0.913 and 0.97 g ml⁻¹ (as calculated from the densities of the purchased silicone oils). The composition of glycerol–water mixtures varies from 0 to 97.5% w/w glycerol, yielding zero shear viscosities from 1 mPa s (for pure water (W)) to 813 mPa s (for 97.5% w/w glycerol), densities from 1.05 g ml⁻¹ to 1.25 g ml⁻¹, and an average surface tension of 65 mN m⁻¹, as measured with a pendant drop set-up.

The first viscoelastic system consists of bridged micro-emulsions composed of decane droplets of radius 6 nm^{14,40} stabilized in brine (0.2 M NaCl) by cetylpyridinium chloride (CpCl) as surfactant, and *n*-octanol as co-surfactant, with a molar ratio of *n*-octanol over CpCl of 0.65. The droplets are reversibly linked by polymer chains of poly(ethylene oxide) (PEO) of molar mass 35 kg mol⁻¹ with hydrophobic stickers grafted at both ends, resulting in the formation of a transient network. The micro-emulsions are characterized by the number of carbon atoms in each sticker, *n* (*n* = 12, 14 or 18), the average number of stickers per droplet, *r*, comprised between 4 and 9, and ϕ , the mass fraction of oil droplets ($\phi = 8$ and 10%). The sample preparation is described elsewhere.¹³

The second viscoelastic system consists of entangled wormlike micelles^{41,42} produced by self-organization, in 0.5 M brine, of surfactant molecules, sodium salicylate (NaSal) and CpCl, with a

fixed molar ratio [NaSal]/[CpCl] of 0.5. Micelles are decorated by an amphiphilic polymer (Synperonic F-108), purchased from Serva, a PEO–PPO–PEO (with PPO being polypropylene oxide) triblock copolymer with an average molar mass of 14 kg mol⁻¹. The addition of amphiphilic polymer allows to easily tune the relaxation time.⁴³ The micelles preparation is described in ref. 44. Micelles are characterized by ϕ , the mass fraction of surfactant (between 5 and 9%) and α the molar ratio of amphiphilic polymer over surfactant (from 0.48 to 4%).

For both classes of viscoelastic samples, the linear rheological behavior can be well described in the frequency range of interest by a one mode Maxwell model in which the viscoelasticity is characterized by a single relaxation time, τ and a plateau modulus, G_0 . In this model, the storage and the loss moduli respectively read $G'(\omega) = \frac{G_0(\omega\tau)^2}{1 + (\omega\tau)^2}$ and $G''(\omega) = \frac{G_0(\omega\tau)}{1 + (\omega\tau)^2}$ with ω , the oscillation frequency. In reduced units, the storage and the loss moduli respectively read $\tilde{G}' = G'/G_0 = \frac{\tilde{\omega}^2}{1 + \tilde{\omega}^2}$ and $\tilde{G}'' = G''/G_0 = \frac{\tilde{\omega}}{1 + \tilde{\omega}^2}$ with $\tilde{\omega} = \omega\tau$. Fitting the frequency-dependent linear viscoelastic response of the samples with a Maxwell model allows one to determine the elastic plateau, G_0 and the characteristic time, τ . These characteristic parameters are reported in Table 1 along with the dynamic viscosity, $\eta_0 = G_0\tau$ for all viscoelastic samples. The plateau modulus, G_0 , ranges from 10 to 194 Pa and the relaxation time, τ , from 1 ms to 178 ms, yielding dynamic viscosities, $G_0\tau$, between 0.031 and 1.78 Pa s. The samples are made to have relaxation times smaller than, comparable to, or larger than the characteristic time of the experiment, typically 6 ms, with the aim to probe viscous and elastic effects. We find (Fig. 2) that the experimental data (symbols) for all viscoelastic samples collapse on one master curve which conforms to the one-mode Maxwell model (lines), showing that the samples viscoelasticity can indeed be satisfyingly described by this model.

Table 1 List of viscoelastic samples and their rheological properties. Micro-emulsion samples are named $Mn\phi XrY$ with *n*, the number of carbon per sticker for the telechelic polymers, *X* the value in % g/g for ϕ , the hydrophobic weight fraction and *Y*, the value of *r*, the average number of stickers per oil droplet. The name of wormlike micelle samples follows the nomenclature: $WM\phi X\alpha Y$ with *X* the value in % g/g for ϕ , the mass fraction of surfactant, and *Y* the value in % for α , the mole fraction of amphiphilic polymer. G_0 is the elastic modulus, τ , the relaxation time and $\eta_0 = G_0\tau$, the zero shear viscosity

Name	G_0 [Pa]	τ [ms]	η_0 [Pa s]
Micro-emulsions			
M18 ϕ 10r4	10	178	1.78
M14 ϕ 8r9	189	8	1.5
M14 ϕ 8r8	128	6	0.77
M14 ϕ 10r6	48	5	0.23
M14 ϕ 8r6	31	4	0.12
M12 ϕ 10r8	194	2	0.39
Wormlike micelles			
WM ϕ 5 α 0.48	50	8	0.4
WM ϕ 7 α 1.8	73	2	0.146
WM ϕ 9 α 4	64	1	0.031

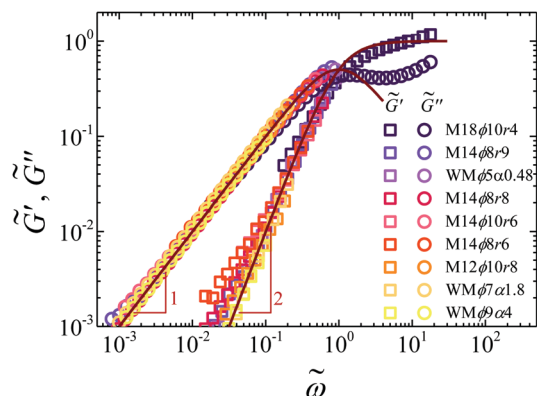


Fig. 2 (Symbols) reduced storage, \tilde{G} (squares), and loss, \tilde{G}'' (circles), moduli as a function of the reduced oscillatory frequency, $\tilde{\omega}$, for the viscoelastic samples, as indicated in the legend. Moduli, G' and G'' , are normalized by the sample shear modulus, G_0 , and the frequency, ω , is multiplied by the sample characteristic relaxation time, τ . (Lines) Theoretical expectations for a one-mode Maxwell fluid.

3 Experimental results

After its release, the drop reaches the surface covered with a thin liquid nitrogen layer and expands with a disk-like shape on a gaseous nitrogen cushion. After reaching a maximal expansion, the sheet retracts due to surface tension and bulk elastic energy. A series of snapshots showing the whole process, from the impact of the drop to the expansion of the sheet and subsequently its retraction is displayed in Fig. 3. The expansion and retraction events result in bell shaped curves for the time evolution of the diameter of the sheet. During the retraction regime, axisymmetry is lost due to non-reversible instabilities and the sheet cannot be reasonably assimilated to a disk anymore. For this reason, this regime will not be further investigated. We define $\beta = \frac{d}{d_0}$, the stretching ratio with d , the apparent diameter of the sheet and d_0 , the initial diameter of the drop. The origin of time is chosen at the time at which the drop comes into contact with the nitrogen vapor layer in such a way that the diameter at $t = 0$ is d_0 , and hence $\beta = 1$. Fig. 4a shows the time evolution of β for sample M14 ϕ 8r9 at different impact velocities, v_0 ,

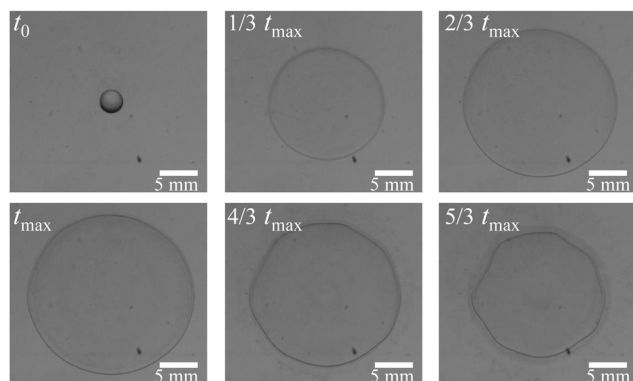


Fig. 3 Snapshots taken at different times, as indicated, during the expansion and retraction of a sheet produced with sample M14 ϕ 10r6 impacted at a velocity of 4.7 m s⁻¹. The bar sets the scale.

from 1.5 to 5 m s⁻¹ as indicated in the legend. The normalized diameter at maximum expansion, β_{\max} , increases monotonically with the impact velocity while the time to reach maximal expansion, t_{\max} , slightly increases with v_0 . Fig. 4b shows the time evolution of β for all viscoelastic samples and three Newtonian samples with viscosity of 1, 216 and 658 mPa s, for a same impact velocity $v_0 = 4.2$ m s⁻¹. Overall, the curves follow the same general behavior but the key parameters, β_{\max} and t_{\max} vary strongly from one sample to another (between 3.1 and 6.7 for β_{\max} and between 1.4 and 6.3 ms for t_{\max} at $v_0 = 4.2$ m s⁻¹) with no straightforward dependence on the rheological parameters, G_0 , τ or η_0 .

From the evolution of the diameter with time, we extract β_{\max} and t_{\max} . The viscoelastic fluids are impacted at different impact velocities and the dependence of β_{\max} and t_{\max} with the impact velocity is shown in Fig. 5a and b. Additionally, the effect of v_0 on β_{\max} and t_{\max} for two Newtonian samples: water and a mixture with 91% g/g of glycerol in water ($\eta_0 = 216$ mPa s) is also shown in Fig. 5a and b. The other Newtonian samples (star symbols) are all impacted at one velocity ($v_0 = 4.2$ m s⁻¹) with β_{\max} and t_{\max} decreasing for increasing viscosity (symbols of increasing darkness). The dependence of β_{\max} with the impact velocity follows $\beta_{\max} \propto v_0$ with prefactors which are sample-dependent. One could not infer simple correlations

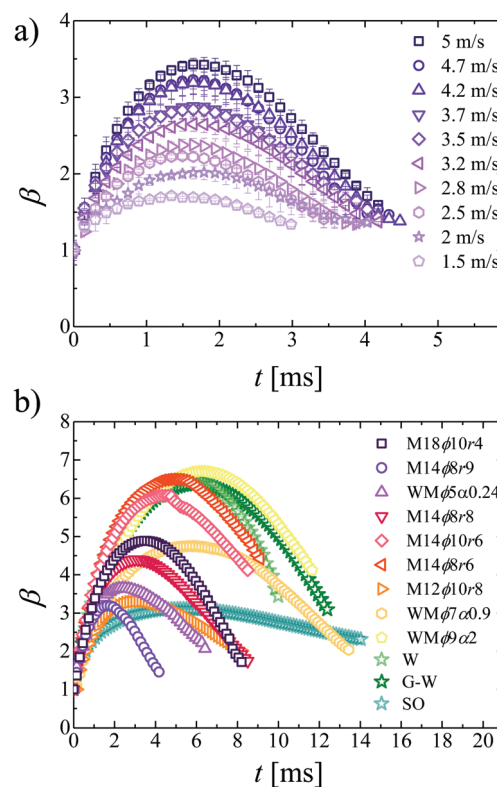


Fig. 4 Time evolution of the sheet diameter upon impact normalized by the initial drop diameter for (a) sample M14 ϕ 8r9 at different impact velocities as indicated in the legend (b) all viscoelastic samples and selected Newtonian fluids: pure water (W, $\eta_0 = 1$ mPa s), glycerol water mixture (G-W, $\eta_0 = 216$ mPa s) and silicone oil (SO, $\eta_0 = 658$ mPa s) impacted at $v_0 = 4.2$ m s⁻¹. The error bars in (a) represent the standard deviation of three different experiments. Error bars have been removed from (b) for more clarity.

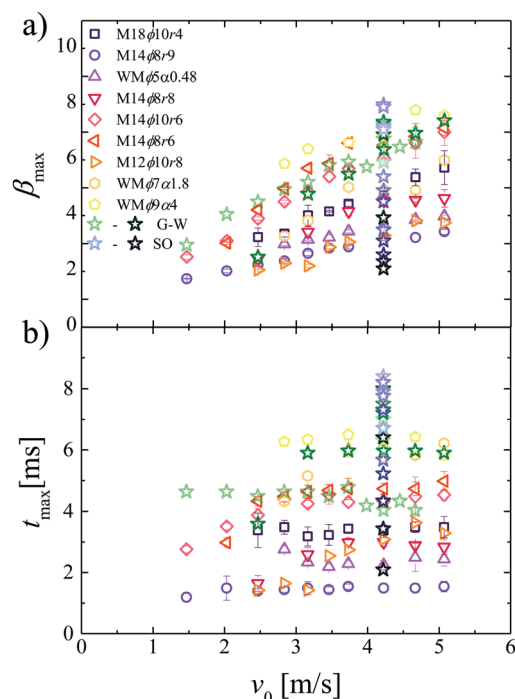


Fig. 5 Normalized maximal expansion (a) and time at maximal expansion (b) as a function of the impact velocity for all Newtonian and viscoelastic samples, as indicated in the legend. The increasing viscosity of the two classes of Newtonian samples are represented by shades of increasing darkness. The error bars represent the standard deviation of three different experiments.

between the prefactors and the samples viscosity, bulk elasticity or relaxation time. On the other hand, t_{\max} is roughly constant with the impact velocity but varies from one sample to another. We observe a small decrease at low impact velocity for samples with relaxation time lower than the time of the experiment (M14 ϕ 8r8, M14 ϕ 10r6, M14 ϕ 8r6, M12 ϕ 10r8 and WM ϕ 7 α 1.8).

The next section of the paper aims to predict the experimental values obtained for d_{\max} and t_{\max} by rationalizing the interplay between viscosity, and surface and bulk elasticity, for the expansion dynamic.

4 Damped oscillator model

4.1 Equation of motion

A common method to correlate the maximal stretching ratio, β_{\max} , to the impact parameters is to balance inertia with the energy contributions arising either from surface tension,^{24,29,30} bulk elasticity^{45,46} or both surface and bulk elasticity.¹⁴ Below, we show that viscosity, surface tension and bulk elasticity are all crucial to quantitatively account for our experimental data. We write an energy balance equation for the expanding sheet after impact that includes at all times the contributions of the kinetic energy, E_K , the surface energy, E_γ , the bulk elastic energy, E_{bulk} , and the biaxial extensional viscous dissipation energy, E_B .

$$E_K + E_\gamma + E_{\text{bulk}} + E_B = \text{Constant} \quad (1)$$

All energy terms are computed below considering the limit of large deformations ($d \gg d_0$) and assuming that the sheet, at

all times, is a disk of diameter, d , and of uniform thickness, h_s .^{47,48} From volume conservation, $h_s = \frac{2d_0^3}{3d^2}$.

The kinetic energy, E_K , reads

$$E_K = \int_0^{d/2} \frac{1}{2} v_r^2 \rho 2\pi h_s r dr = \frac{m v^2}{4} \quad (2)$$

with m , the mass of the drop, d , the diameter of the sheet at a time t and $v_r = \frac{2vr}{d}$, the Eulerian velocity field in the material along r , the radial coordinate, where v is the velocity of the expansion front. This velocity field has been found to describe accurately the expansion dynamics of Newtonian fluids.^{10,49}

The surface energy, E_γ reads

$$E_\gamma = \frac{1}{2} \pi \gamma d^2 \quad (3)$$

The contribution of the disk edge to the surface energy is neglected due to the large deformation limit considered here.

The bulk elastic energy, E_{bulk} , is approximated by the biaxial extensional linear elastic deformation energy of a soft solid in the limit of large deformation:^{14,45}

$$E_{\text{bulk}} \approx V_{\text{drop}} G_{\text{eff}} \left(\frac{d}{d_0} \right)^2 \quad (4)$$

with $V_{\text{drop}} = \frac{\pi d_0^3}{6}$, the volume of the drop and G_{eff} , the relevant shear elastic modulus of the sample, to be discussed in Section 4.2.

We assume that the unique source of dissipation is viscous and originates from the biaxial extensional deformation of the sheet.²⁸ Indeed, dissipation due to shear is eliminated thanks to the non-wetting and slip conditions achieved with the cold Leidenfrost effect leaving biaxial extensional viscous dissipation as the only remaining viscous contribution. The biaxial extensional viscous dissipation energy, E_B , reads: $E_B = \int_0^{t_{\max}} \int_V \varphi dV dt$. Here, φ is the dissipation function which reads $\varphi \approx \eta_{B,\text{eff}} \dot{\epsilon}^2$ with $\dot{\epsilon} = \frac{1}{d} \frac{\partial d}{\partial t}$, the Hencky strain rate and $\eta_{B,\text{eff}}$, the relevant biaxial extensional viscosity of the sample. In the following, we assume $\eta_{B,\text{eff}}$ to be constant with time for one given impact experiment (*i.e.* one given sample and one given impact velocity)²⁸ as discussed in Section 4.2.

$$E_B \approx \eta_{B,\text{eff}} \pi \frac{d_0^3}{6} \int_0^{t_{\max}} \left(\frac{1}{d} \frac{\partial d}{\partial t} \right)^2 dt \quad (5)$$

Inserting eqn (2)–(5) in the energy balance (eqn (1)) and deriving the latter with respect to time, one obtains the equation of motion for a free expanding sheet:

$$\ddot{d} + \frac{c(d)}{m} \dot{d} + \omega_0^2 d = 0 \quad (6)$$

Eqn (6) is a nonlinear second order differential equation that can be viewed as the equation of motion of a damped harmonic oscillator with an angular frequency:

$$\omega_0 = \sqrt{\frac{8\pi}{m} \left(\gamma + \frac{d_0 G_{\text{eff}}}{3} \right)} \quad (7)$$

Paper

and a non-constant viscous damping coefficient which decreases through the expansion, as d increases.

$$c(d) = \frac{4\pi d_0^3 \eta_{B,\text{eff}}}{3} \frac{1}{d^2} \quad (8)$$

In the absence of viscous dissipation ($c = 0$) we retrieve the 1D undamped harmonic oscillator equation successfully used to model the expansion dynamics of sheets produced with various materials, with $\omega_0^2 = \frac{8\pi\gamma}{m}$ for Newtonian fluids of low viscosity²⁶ (in that case $G_{\text{eff}} = 0$), $\omega_0^2 = \frac{8\pi d_0 G_{\text{eff}}}{3m}$ for elastic beads⁴⁵ and $\omega_0^2 = \frac{8\pi}{m} \left(\gamma + \frac{d_0 G_{\text{eff}}}{3} \right)$ for ultrasoft elastic beads.¹⁴ When viscous dissipation is not negligible, the relevant rheological parameters to consider are less straightforward, and are discussed below.

4.2 Discussion on the relevant rheological parameters

When viscous dissipation is not negligible, $c \neq 0$ is proportional to the biaxial extensional viscosity $\eta_{B,\text{eff}}$. In the case of Newtonian fluids ($G_{\text{eff}} = 0$), $\eta_{B,\text{eff}} = 6\eta_0$, the zero-shear viscosity multiplied by the Trouton ratio.^{28,50} The Newtonian sample biaxial extensional viscosities thus range from 6 to 4880 mPa s for mixtures of glycerol and water and from 30 to 5820 mPa s for silicone oil blends. For the Maxwell fluids, the approach is less straightforward as the biaxial extensional viscosity, but also the elastic modulus, are expected to be time-dependent to account for the samples viscoelasticity.¹³ Hence, we need to estimate G_{eff} and $\eta_{B,\text{eff}}$ at the relevant frequency. As a first order approach, the relevant frequency can be estimated as the Hencky strain rate, $\dot{\epsilon}$, undergone by the sheet during its expansion. The Hencky strain rate is non-stationary and vanishes at maximal expansion as illustrated in Fig. 6a for one sample (M14 ϕ 8r9) impacted at different velocities. We choose as characteristic frequency the mean value of $\dot{\epsilon}$ averaged over the duration of the expansion regime: $\bar{\dot{\epsilon}} = \frac{\int_0^{t_{\text{max}}} \dot{\epsilon} dt}{t_{\text{max}}}$. The mean values are plotted in Fig. 6b as a function of the impact velocity for all viscoelastic samples. We measure that $\bar{\dot{\epsilon}}$ ranges between 194 and 516 s⁻¹ corresponding to Weissenberg number, $Wi = \bar{\dot{\epsilon}}\tau$, values from 0.3 to 68.9. We find that $\bar{\dot{\epsilon}}$ varies almost linearly with v_0 , with a sample-dependent proportionality constant. In the following, for Maxwell fluids, the relevant shear elastic modulus, G_{eff} , is taken as the elastic part, G' , of the complex modulus, G^* , at the relevant frequency:

$$G_{\text{eff}} = G'(\bar{\dot{\epsilon}}) = G_0 \frac{(\tau \bar{\dot{\epsilon}})^2}{1 + (\tau \bar{\dot{\epsilon}})^2} \quad (9)$$

Similarly, the biaxial extensional viscosity for viscoelastic fluids at the relevant strain rate is evaluated using the viscous part, G'' , of the complex modulus, G^* , and assuming the same Trouton ratio as for the Newtonian fluids:

$$\eta_{B,\text{eff}} = 6 \frac{G''(\bar{\dot{\epsilon}})}{\bar{\dot{\epsilon}}} = 6G_0 \frac{\tau}{1 + (\tau \bar{\dot{\epsilon}})^2} \quad (10)$$

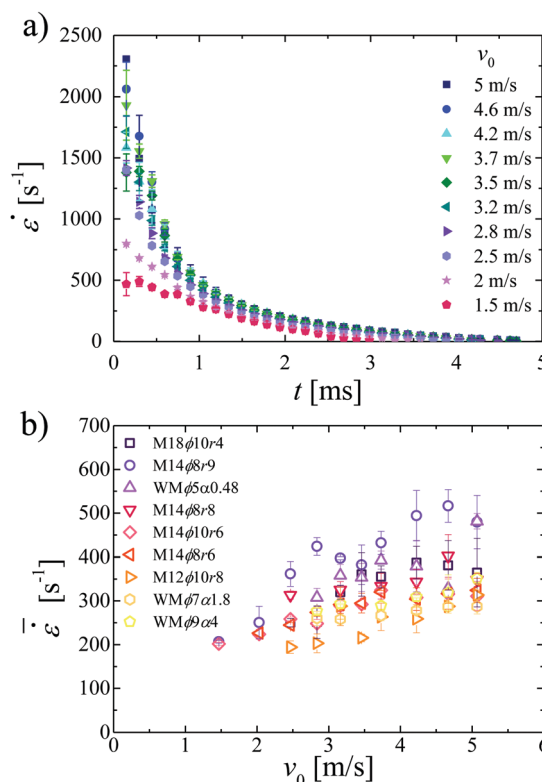


Fig. 6 (a) Time evolution of the Hencky strain rate during the sheet expansion for the sample M14 ϕ 8r9 at different impact velocities, v_0 , as indicated in the legend. (b) Strain rate averaged over time as a function of v_0 for all viscoelastic samples. Error bars represent the standard deviation of three different experiments.

4.3 Approximate analytical solution and comparison with experiments

Eqn (6) is not analytically solvable. Therefore, we propose to solve the problem analytically for two limits of the damping coefficient: (i) $c \approx c_{\text{min}} = c(d_{\text{max}}) = \frac{4\eta_B \pi d_0^3}{3d_{\text{max}}^2}$ and (ii) $c \approx c_{\text{max}} = c(d_0) = \frac{4\eta_B \pi d_0}{3}$. In these two cases, the equation of motion of the free sheet (eqn (6)) reduces to a simple damped harmonic oscillator model with a constant damping factor. Using c_{max} , we overestimate the effect of the viscous drag and using c_{min} , we underestimate it. We check that all our samples verify the condition $\frac{c}{2m} < \omega_0^2$ which corresponds to the underdamped regime of the harmonic oscillator. In this regime, the solution of eqn (6) is

$$d(t) = C e^{-\frac{c}{2m}t} \cos(\omega_d t - \Phi) \quad (11)$$

The parameters $\omega_d = \sqrt{\omega_0^2 - \left(\frac{c}{2m}\right)^2}$, $C = d_0 \sqrt{\left(\frac{2v_0}{d_0 \omega_d} + \frac{c}{2m \omega_d}\right)^2 + 1}$ and $\Phi = \tan^{-1}\left(\frac{2v_0}{d_0 \omega_d} + \frac{c}{2m \omega_d}\right)$ are obtained from the initial conditions, $d(0) = d_0$ and $\dot{d}(0) = 2v_0$ (see ESI†).

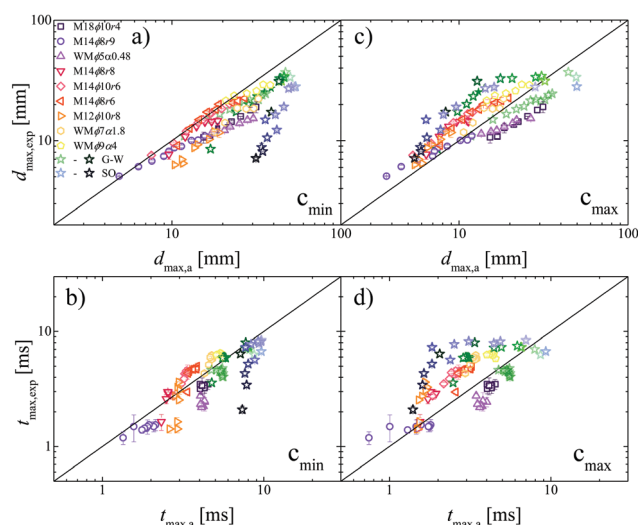


Fig. 7 Experimental d_{\max} (a and c) and t_{\max} (b and d) as a function of their respective theoretical predictions using the damped harmonic oscillator assumption with an underestimation (c_{\min} , a and b) or overestimation (c_{\max} , c and d) of the damping coefficient for all samples. The lines represent $x = y$.

The maximum of d gives the theoretical time at maximal expansion which allows one to obtain the analytic equations, $t_{\max,a}$ and $d_{\max,a}$.

$$t_{\max,a} = \frac{1}{\omega_d} \arctan \left(\frac{2v_0\omega_d}{d_0\omega_d^2 + \frac{cv_0}{m} + d_0c^2} \right) \quad (12)$$

$$d_{\max,a} = Ae^{-\frac{c}{2m}t_{\max,a}} \cos(\omega_d t_{\max,a} - \Phi) \quad (13)$$

In order to validate the present model, the analytical approximate predictions of the maximal diameter, $d_{\max,a}$ and the time at maximal expansion, $t_{\max,a}$ are compared with the experimental results. Fig. 7 shows the experimental values for d_{\max} and t_{\max} plotted against the theoretical ones when using the relevant parameters of the drops in the underdamped harmonic oscillator model approximation (eqn (12) and (13)). In Fig. 7(a and b) the dissipation is evaluated with $c = c_{\min}$ and in Fig. 7(c and d) with $c = c_{\max}$. Lines representing $x = y$ allow one to judge more easily the quality of the analytical approximation of the model. The agreement between the underdamped harmonic oscillator model and the experimental data is good (relative error of approximately 30%). As expected, when the viscous dissipation is underestimated ($c = c_{\min}$), respectively overestimated ($c = c_{\max}$), overall the analytical predictions are larger (respectively smaller) than the experimental values and the data points are all below (respectively above) the lines $d_{\max,a} = d_{\max,exp}$ and $t_{\max,a} = t_{\max,exp}$.

4.4 Numerical resolution and comparison with experiments

To refine the prediction and better account for the competition between non-stationary elasticity, viscous dissipation and capillarity, we solve eqn (6) numerically. Fig. 8 shows the

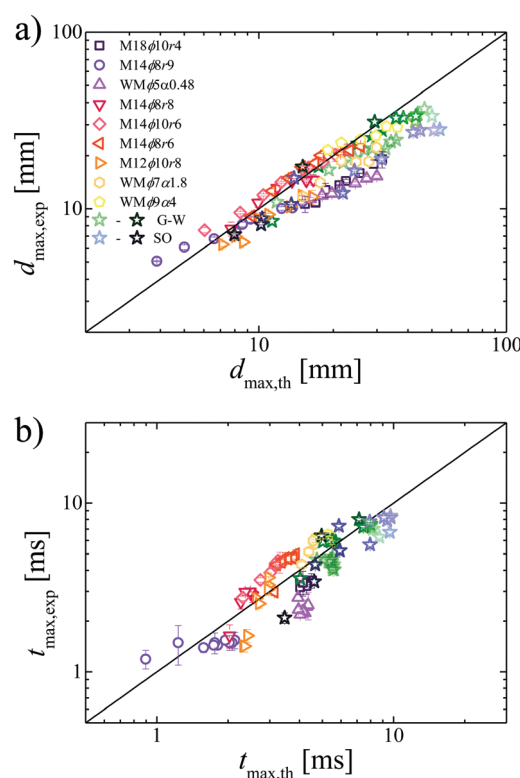


Fig. 8 Experimental (a) d_{\max} , and (b) t_{\max} as a function of their respective theoretical predictions using numerical resolution of eqn (6) for all samples. The lines represent $x = y$.

experimental data against the theoretical predictions after numerical resolution. The results agree well with the prediction for d_{\max} as well as for t_{\max} considering that no adjustable parameters are used to determine theoretical predictions. We can predict d_{\max} and t_{\max} with a relative error of approximately 25% for Newtonian fluids with biaxial extensional viscosities varying over three order of magnitude and viscoelastic samples spanning a large range of elastic moduli, characteristic relaxation times and viscosities. Despite the fact that we investigate Newtonian samples of high viscosity and viscoelastic fluids, we find comparable relative error as previous works focusing on low viscosities Newtonian fluids impacted in similar conditions. Indeed, a relative error of 20%, at best, has been found when comparing experimental maximal expansion of Newtonian fluids of low viscosities impacted on a repellent surface⁵¹ to theoretical predictions using analytical, empirical, and scale relations^{52,53} as well as dynamical models.^{54–56}

Furthermore, the dynamics of expansion of the sheets can be relatively well described from only two parameters, t_{\max} and d_{\max} . Fig. 9 shows, for four representative samples, the evolution of the experimental diameter (symbols) along with its numerical prediction using eqn (6) (lines) normalized by their maximal values, as a function of the time normalized by t_{\max} . In the expansion regime, a maximal error of 5% is found between the normalized experimental data and the corresponding normalized theoretical predictions. Much larger deviations can be observed in the receding regime as different complex phenomena such as

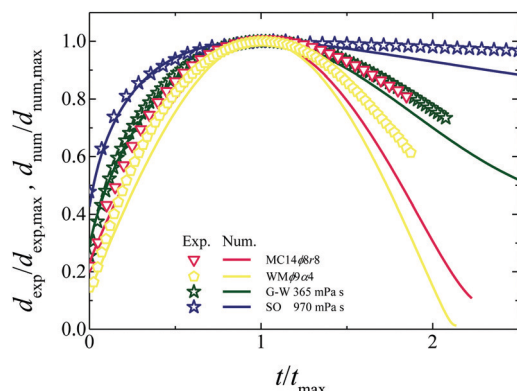


Fig. 9 Experimental (symbols) and theoretical (eqn (6)) (lines) evolution of the diameter of the sheet normalized by its value at maximal expansion as a function of the time normalized by the time at maximal expansion for samples M14 ϕ 8r8 and WM ϕ 9z4, a glycerol water mixture (G-W, $\eta_0 = 365$ mPa s) and a silicone oil (SO, $\eta_0 = 970$ mPa s) impacted at $v_0 = 4.2$ m s $^{-1}$.

the loss of axisymmetry, expulsion of secondary droplets or pinning due to the cold surface, which are not taken into account in our rationalization, could occur.

5 Conclusion

Drop impact experiments on repellent surfaces have been performed with Newtonian and Maxwell fluids. Maxwell fluids have been carefully chosen to display a wide range of relaxation times, shorter, comparable or much larger than the typical experimental time, allowing us to investigate the roles of viscosity, bulk elasticity and capillarity in the expansion dynamics of fluid sheets. We have used a cold Leidenfrost effect-based set-up so that the dominant source of viscous dissipation is the biaxial extensional deformation of the sheet. We have provided a systematic study of the effect of the impact velocity on the maximum diameter of the expanding sheet, and the time at which maximum expansion is reached. The expansion dynamics could be successfully modeled by a nonlinear damped harmonic oscillator model, where the damping coefficient decreases during the expansion and is proportional to the biaxial extensional dynamic viscosity, and the undamped angular frequency of the oscillator results from a simple combination of the surface tension and the dynamic modulus of the sample. For the viscoelastic samples, we have proposed to take as dynamic viscosity and dynamic modulus the viscosity and elastic modulus at a characteristic rate equal to the mean Hencky strain rate of the sheet in the expansion regime. The numerical prediction for the maximal expansion diameter, d_{\max} , and the time to reach maximal expansion, t_{\max} , agree quantitatively well with the experimental results, without adjustable parameters. Our approach is simple but quite general and we believe it could successfully be applied to more complex viscoelastic materials, of relevance for applications.

Conflicts of interest

There are no conflicts to declare.

Acknowledgements

This work was financially supported by the H2020 Program (Marie Curie Actions) of the European Commission's Innovative Training Networks (ITN) (H2020-MSCA-ITN-2017) under DoDyNet REA Grant Agreement (GA) No. 765811. We thank Pr. Daniel Read (University of Leeds) and Pr. Dimitris Vlassopoulos (IESL-FORTH) for fruitful discussions and Dr Ty Phou (L2C, Montpellier) for his technical assistance.

Notes and references

- M. Pasandideh-Fard, V. Pershin, S. Chandra and J. Mostaghimi, *J. Therm. Spray Technol.*, 2002, **11**, 206–217.
- W. Wirth, S. Storp and W. Jacobsen, *Pest. Sci.*, 1991, **33**, 411–420.
- N. Laan, K. G. De Bruin, D. Slenker, J. Wilhelm, M. Jermy and D. Bonn, *Sci. Rep.*, 2015, **5**, 11461.
- H. Wijshoff, *Curr. Opin. Colloid Interface Sci.*, 2018, **36**, 20–27.
- S. T. Thoroddsen, T. G. Etoh and K. Takehara, *Annu. Rev. Fluid Mech.*, 2008, **40**, 257–285.
- C. Josserand and S. Thoroddsen, *Annu. Rev. Fluid Mech.*, 2016, **48**, 365–391.
- Y. Wang and L. Bourouiba, *J. Fluid Mech.*, 2017, **814**, 510–534.
- L. Gordillo, T. P. Sun and X. Cheng, *J. Fluid Mech.*, 2018, **840**, 190–214.
- J. O. Marston, M. M. Mansoor and S. T. Thoroddsen, *Phys. Rev. E: Stat., Nonlinear, Soft Matter Phys.*, 2013, **88**, 1–4.
- P. S. Raux, A. Troger, P. Jop and A. Sauret, *Phys. Rev. Fluids*, 2020, **5**, 1–11.
- F. Boyer, E. Sandoval-Nava, J. H. Snoeijer, J. F. Dijksman and D. Lohse, *Phys. Rev. Fluids*, 2016, **1**, 1–9.
- R. Crooks and D. V. Boger, *J. Rheol.*, 2000, **44**, 973–996.
- S. Arora, C. Ligoure and L. Ramos, *Phys. Rev. Fluids*, 2016, **1**, 1–15.
- S. Arora, J. M. Fromental, S. Mora, T. Phou, L. Ramos and C. Ligoure, *Phys. Rev. Lett.*, 2018, **120**, 148003.
- R. Rioboo, M. Marengo and C. Tropea, *Exp. Fluids*, 2002, **33**, 112–124.
- M. Lee, Y. S. Chang and H.-Y. Kim, *Phys. Fluids*, 2010, **22**, 72101–72108.
- M. Arogeti, E. Sher and T. Bar-Kohany, *Chem. Eng. Sci.*, 2019, **193**, 89–101.
- A. L. N. Moreira, A. S. Moita, E. Cossali, M. Marengo and M. Santini, *Exp. Fluids*, 2007, **43**, 297–313.
- Y. B. Wang, X. D. Wang, Y. R. Yang and M. Chen, *J. Phys. Chem. C*, 2019, **123**, 12841–12850.
- Y. B. Wang, Y. F. Wang, S. R. Gao, Y. R. Yang, X. D. Wang and M. Chen, *Langmuir*, 2020, **36**, 9306–9316.
- X. Wang, D. J. Lin, Y. B. Wang, S. R. Gao, Y. R. Yang and X. D. Wang, *AIChE J.*, 2020, **66**, e16647.
- V. Bertola, *Adv. Colloid Interface Sci.*, 2013, **193–194**, 1–11.
- P. Shah and M. M. Driscoll, preprint arXiv:2012.10433, 2020.
- D. Richard, C. Clanet and D. Quéré, *Nature*, 2002, **417**, 811.

- 25 L. H. J. Wachters, L. Smulders, J. R. Vermeulen and K. Hc, *Chem. Eng. Sci.*, 1966, **21**, 1231–1238.
- 26 A.-L. Biance, C. Clanet and D. Quéré, *Phys. Fluids*, 2003, **15**, 1632–1637.
- 27 C. Antonini, I. Bernagozzi, S. Jung, D. Poulidakos and M. Marengo, *Phys. Rev. Lett.*, 2013, **111**, 14501.
- 28 A. Louhichi, C.-A. Charles, T. Phou, D. Vlassopoulos, L. Ramos and C. Ligoure, *Phys. Rev. Fluids*, 2020, **5**, 053602.
- 29 A.-L. Biance, F. Chevy, C. Clanet, G. Lagubeau and D. Quéré, *J. Fluid Mech.*, 2006, **554**, 47–66.
- 30 M. Andrew, J. M. Yeomans and D. O. Pushkin, *Soft Matter*, 2017, **13**, 985–994.
- 31 Y. Tanaka, *Phys. Rev. E: Stat., Nonlinear, Soft Matter Phys.*, 2006, **73**, 31403–31406.
- 32 A. Jha, P. Chantelot, C. Clanet and D. Quéré, *Soft Matter*, 2020, **16**, 7270–7273.
- 33 S. Lin, B. Zhao, S. Zou, J. Guo, Z. Wei and L. Chen, *J. Colloid Interface Sci.*, 2018, **516**, 86–97.
- 34 D. Quéré, *Annu. Rev. Fluid Mech.*, 2013, **45**, 197–215.
- 35 S. Chen and V. Bertola, *Soft Matter*, 2016, **12**, 7624–7631.
- 36 K. J. Hendricks and R. C. Baumeister, *NASA Technical Reports Server*, NASA, Washington, DC, 1970.
- 37 K. J. Hendricks and R. C. Baumeister, *Advances in Cryogenic Engineering*, Springer, 1971, **16**, 455–466.
- 38 H. Kim, Y. H. Lee and H. Cho, *J. Korean Phys. Soc.*, 2011, **58**, 1628–1632.
- 39 A. Crisp, E. de Juan and J. Tiedeman, *Arch. Ophthalmol.*, 1987, **105**, 546–550.
- 40 M. Filali, M. J. Ouazzani, E. Michel, R. Aznar, G. Porte and J. Appell, *J. Phys. Chem. B*, 2001, **105**, 10528–10535.
- 41 H. Rehage and H. Hoffmann, *J. Phys. Chem.*, 1988, **92**, 4712–4719.
- 42 H. Rehage and H. Hoffmann, *Mol. Phys.*, 1991, **74**, 933–973.
- 43 G. Massiera, PhD thesis, Université de Montpellier 2, 2002.
- 44 G. Massiera, L. Ramos and C. Ligoure, *Langmuir*, 2002, **18**, 5687–5694.
- 45 Y. Tanaka, Y. Yamazaki and K. Okumura, *Europhys. Lett.*, 2003, **63**, 146–152.
- 46 Y. Tanaka, *Eur. Phys. J. E: Soft Matter Biol. Phys.*, 2005, **18**, 95–103.
- 47 P. Attané, F. Girard and V. Morin, *Phys. Fluids*, 2007, **19**, 012101.
- 48 J. Eggers, M. A. Fontelos, C. Josserand and S. Zaleski, *Phys. Fluids*, 2010, **22**, 1–13.
- 49 C. Vernay, L. Ramos and C. Ligoure, *Phys. Rev. Lett.*, 2015, **115**, 198302.
- 50 C. W. Macosko, *Rheology: Principles, Measurements and Applications*, Wiley-VCH, 1994.
- 51 J. T. Pearson, D. Maynes and B. W. Webb, *Exp. Fluids*, 2012, **53**, 603–618.
- 52 C. Clanet, C. Béguin, D. Richard and D. Quéré, *J. Fluid Mech.*, 2004, **517**, 199–208.
- 53 I. V. Roisman, *Phys. Fluids*, 2009, **21**, 052104.
- 54 M. Pasandideh-Fard, Y. M. Qiao, S. Chandra and J. Mostaghimi, *Phys. Fluids*, 1996, **8**, 650–659.
- 55 I. V. Roisman, R. Rioboo and C. Tropea, *Proc. R. Soc. London, Ser. A*, 2002, **458**, 1411–1430.
- 56 C. Ukiwe and D. Y. Kwok, *Langmuir*, 2005, **21**, 666–673.

Additional considerations on the relevant rheological parameters

In this section, we discuss the relevance of the rheological parameters considered in section 4.2 of the previous paper by solving the equation of motion for a free expanding sheet (equation 6 of the paper) for four different cases.

- Dynamic elastic modulus with viscous dissipation : $G_{\text{eff}} = G'(\bar{\dot{\epsilon}})$ and $\eta_{\text{B,eff}} = 6 \frac{G''(\bar{\dot{\epsilon}})}{\bar{\dot{\epsilon}}}$
- Dynamic elastic modulus no viscous dissipation : $G_{\text{eff}} = G'(\bar{\dot{\epsilon}})$ and $\eta_{\text{B,eff}} = 0$
- Static elastic modulus with viscous dissipation : $G_{\text{eff}} = G_0$ and $\eta_{\text{B,eff}} = 6\eta_0$
- Static elastic modulus no viscous dissipation : $G_{\text{eff}} = G_0$ and $\eta_{\text{B,eff}} = 0$

The first case is the situation adopted in the paper. In the dynamic cases, we take into account the fact that the sheet expansion is a dynamic process and thus the rheological parameters of viscoelastic fluids must be assessed at the relevant frequency, $\bar{\dot{\epsilon}}$. In the static cases, the dynamic character of the experiment is overlooked, and the rheological parameters are taken as a biaxial viscosity equal to 6 times the zero-shear viscosity, η_0 , and an elastic modulus equal to the plateau modulus, G_0 . Additionally, in both the dynamic and static cases, we consider the repercussion of neglecting the biaxial extensional dissipation.

The experimental values against the theoretical expectations for the maximal diameter, d_{max} and for the time at maximal expansion t_{max} for the different cases are represented in Figures 4.1 and 4.2, respectively.

Comparing Figures 4.1.a) and 4.2.a) with Figures 4.1.b) and 4.2.b) shows that not taking the dissipation into account in the dynamic case, does not drastically change the predictions for d_{max} and t_{max} for the viscoelastic fluids. By contrast, the behavior of very viscous Newtonian fluids is not well described anymore.

On the other hand, using the static value for elasticity, G_0 , while neglecting the viscous dissipation does not change much the predictions for d_{max} and worsens the predictions for t_{max} , as it can be deduced from comparing Figures 4.1.b) and 4.2.b) with Figures 4.1.d) and 4.2.d).

In Figures 4.1.c) and 4.2.c), using $6\eta_0$ to account for the viscous dissipation, while using G_0 for the elasticity, gives very poor predictions for the viscoelastic samples for which the relaxation times are larger than or comparable to the characteristic time of the experiment.

To conclude, we have shown here that taking into account both the dissipation and the dynamic nature of the sheet expansion resulting from the drop impact in our damped harmonic oscillator model is crucial to accurately predict d_{max} and t_{max} for Maxwell fluids with a large range of elastic moduli and relaxation times, and very viscous Newtonian fluids.

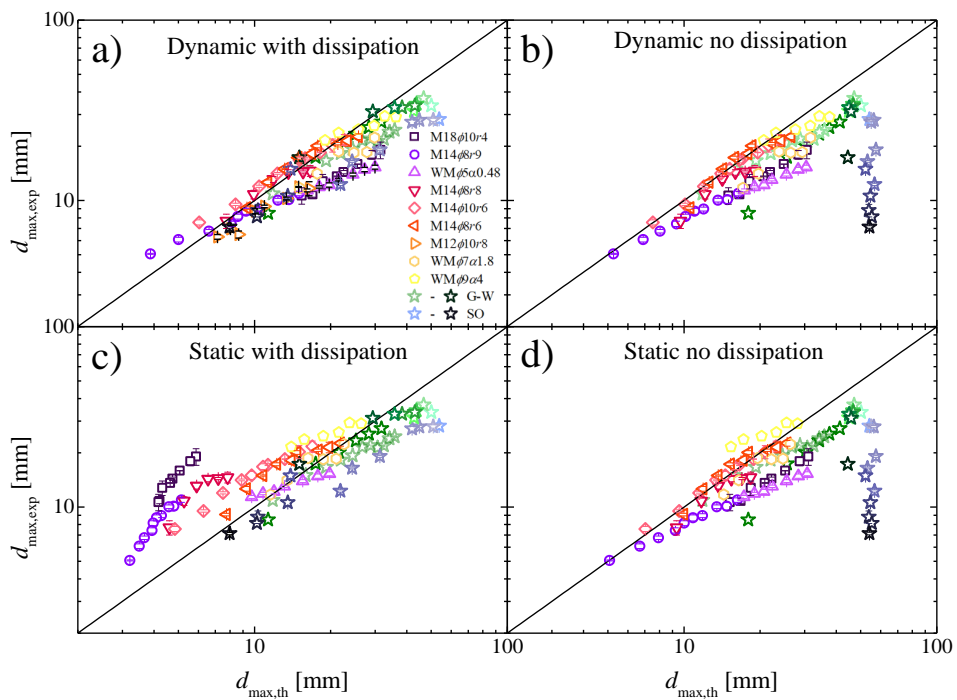


Figure 4.1: Experimental d_{\max} as a function of the theoretical prediction for the different cases as indicated on the graphs.

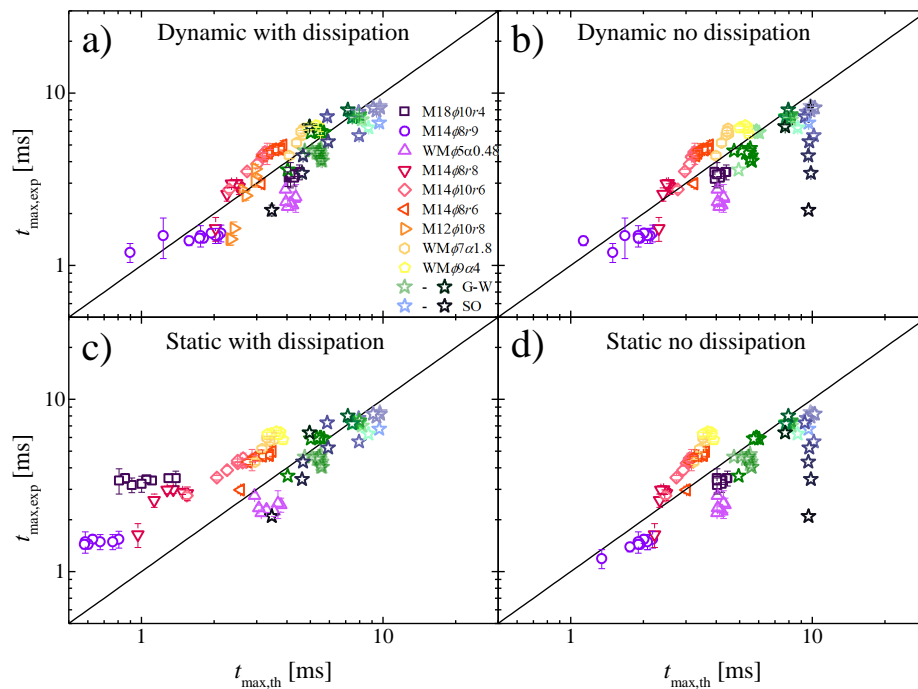


Figure 4.2: Experimental t_{\max} as a function of the theoretical prediction for the different cases as indicated on the graphs.

Biaxial extensional and shear viscous dissipation during the expansion of fluid sheets

Contents

5.1 Introduction	101
5.2 Competition between shear and biaxial extensional viscous dissipation in the expansion dynamics of Newtonian and rheo-thinning liquid sheets	102
5.3 Effect of the target size on maximal expansion	114
5.3.1 Newtonian fluids	114
5.3.2 PEO solutions	120
5.4 Conclusion	125

In this chapter, the dynamics of expanding sheets produced by the impact of drops of Newtonian and rheo-thinning fluids on targets of different sizes is investigated. We assess the competition between biaxial extensional and shear viscous dissipation on the targets by measuring the maximum expansion diameter of the sheet as a function of the relevant viscosity. Additionally, we show that the rheo-thinning nature of the samples must be taken into account to successfully predict the maximal expansion of the sheet.

5.1 Introduction

The non-wetting and slip conditions provided by the cold Leidenfrost phenomenon in Chapter 4 are rarely achieved in real life situations, yielding more complex dissipation processes. A more realistic configuration is obtained by performing the impact on plane solid surfaces. Drop impact on solid surface with size much larger than the sheet's maximal diameter was extensively studied [Jossierand 2016]. Here, we perform instead impacts on a target with a size comparable to the size of the drop [Rozhkov 2002]. This situation, for instance, mimics the process of ink jet printing, which projects ink drops whose diameters compare to the typical roughness size of the paper. When the drop impacts the target,

the sheet expanding in the air is free from the viscous no-slip boundary condition at the solid substrate and undergoes biaxial extensional viscous dissipation as in the previous cold Leidenfrost conditions. The part of the sheet remaining on the target, however, must satisfy the no-slip condition and thus is also subjected to shear-induced dissipation. The competition between shear and biaxial extensional viscous dissipation in the expansion dynamics of Newtonian and rheo-thinning liquid sheets is the subject of this chapter. We investigate both Newtonian and rheo-thinning fluids. Rheo-thinning fluids are fluids whose viscosity decreases at higher deformation rates. They are used in many applications as their thinning behavior facilitates their processability. In section 5.2, the competition between shear and biaxial extensional viscous dissipation is evaluated for a fixed target to drop ratio. Section 5.3 explores the situation in which the shear dissipation is continuously tuned by varying the target to drop ratio.

5.2 Competition between shear and biaxial extensional viscous dissipation in the expansion dynamics of Newtonian and rheo-thinning liquid sheets

In this section, we report the paper *Competition between shear and biaxial extensional viscous dissipation in the expansion dynamics of Newtonian and rheo-thinning liquid sheets*, A. Louhichi*, C-A. Charles*, S. Arora, L. Bouteiller, D. Vlassopoulos, L. Ramos and C. Ligoure, *Physics of Fluids*, 33 (7), 073109, 2021, in which the dissipation mechanisms emerging from the impact of drops of Newtonian and rheo-thinning fluids on a small cylindrical target are identified and quantitatively evaluated.

* These two authors contributed equally to this work.

Competition between shear and biaxial extensional viscous dissipation in the expansion dynamics of Newtonian and rheo-thinning liquid sheets

Cite as: Phys. Fluids **33**, 073109 (2021); doi: [10.1063/5.0057316](https://doi.org/10.1063/5.0057316)

Submitted: 19 May 2021 · Accepted: 30 June 2021 ·

Published Online: 21 July 2021



View Online



Export Citation



CrossMark

Ameur Louhichi,^{1,2}  Carole-Ann Charles,¹  Srishti Arora,¹ Laurent Bouteiller,³  Dimitris Vlassopoulos,² 
Laurence Ramos,^{1,a)}  and Christian Ligoure^{1,b)} 

AFFILIATIONS

¹Laboratoire Charles Coulomb (L2C), Université de Montpellier, CNRS, Montpellier, France

²Institute of Electronic Structure and Laser, FORTH, Heraklion 70013, Crete, Greece and Department of Materials Science and Technology, University of Crete, Heraklion 70013, Crete, Greece

³Sorbonne Université, CNRS, IPCM, Equipe Chimie des Polymères, Paris, 75005, France

^{a)}Electronic mail: laurence.ramos@umontpellier.fr

^{b)}Author to whom correspondence should be addressed: christian.ligoure@umontpellier.fr

ABSTRACT

When a drop of fluid hits a small solid target of comparable size, it expands radially until reaching a maximum diameter and subsequently recedes. In this work, we show that the expansion process of liquid sheets is controlled by a combination of shear (on the target) and biaxial extensional (in the air) deformations. We propose an approach toward a rational description of the phenomenon for Newtonian and viscoelastic fluids by evaluating the viscous dissipation due to shear and extensional deformations, yielding a prediction of the maximum expansion factor of the sheet as a function of the relevant viscosity. For Newtonian systems, biaxial extensional and shear viscous dissipation are of the same order of magnitude. On the contrary, for thinning solutions of supramolecular polymers, shear dissipation is negligible compared to biaxial extensional dissipation and the biaxial thinning extensional viscosity is the appropriate quantity to describe the maximum expansion of the sheets. Moreover, we show that the rate-dependent biaxial extensional viscosities deduced from drop impact experiments are in good quantitative agreement with previous experimental data and theoretical predictions for various viscoelastic liquids.

Published under an exclusive license by AIP Publishing. <https://doi.org/10.1063/5.0057316>

I. INTRODUCTION

Drop impact process on solid surfaces is an extremely active research area because of the development of high-speed imaging technology,¹ and its implication in many industrial applications, such as the impact of pesticide drops on plant leaves² or in inkjet printing.³

We can distinguish two main experimental configurations. On the one hand, drops are impacted on a flat solid surface with a size much larger than the drop size, in a way that the whole expansion event occurs on the target.^{4–10} The sheet spreads thus in intimate contact with a uniform surface. Hence, viscous dissipation is mainly shear-induced. In that case, it has been reported that the shear rate-dependent viscosity is the pertinent parameter to describe the dissipation process in the expansion dynamics of non-Newtonian fluids.^{8,10–14} Note, however, that the retraction dynamics was suggested

to be dominated by the nonlinear extensional viscosity for a drop of fluid containing polymer additives.¹⁵

The other distinguishable configuration, albeit sparsely studied, involved impacting drops on repellent surfaces where there is no contact with the surface, hence eliminating shear dissipation. Such surfaces may include superhydrophobic surfaces,^{16–19} hot plates above the Leidenfrost temperature,^{20,21} and, more recently, cold plates covered with liquid nitrogen to exploit the cold Leidenfrost effect.^{22–25} We have demonstrated elsewhere²⁴ that, in the so-called viscous regime, biaxial extensional dissipation dominates the sheet dynamics produced using the cold Leidenfrost effect.

Nature and pertinent industrial problems are more complex than the above two extreme cases. Hence, we may consider a third scenario, where drops impact a solid target of size comparable to that of the

drop. In this case, a part of the expanding sheet is in contact with the target surface and the other part is expanding freely in the air, which, depending on the sample viscosity, may be the largest part of the sheet.^{26–36} Although the situation of impacting drops on small targets was originally conceived to reduce the friction dissipation,²⁶ it turns out that it actually highlights the competition between shear dissipation (on the target) and biaxial extensional dissipation (in the air). In this work, we assess this competition by evaluating both dissipations (shear and biaxial extensional) for Newtonian and rheologically thinning non-Newtonian fluids. We show that, for Newtonian fluids, the shear and biaxial extensional dissipations are of the same order of magnitude. However, for the non-Newtonian thinning samples, the biaxial extensional dissipation is found to control the sheet expansion dynamics. We compare our data with experimental measurements of biaxial extensional viscosity of thinning fluids^{24,37,38} and model semi-quantitatively the sheet expansion dynamics using a biaxial extensional thinning viscosity.

II. MATERIALS AND METHODS

A. Materials

1. Newtonian fluids

We investigate two classes of Newtonian fluids, silicone oils, and mixtures of water and glycerol. Silicone oils, with zero-shear-rate viscosities from 4.5 to 339 mPa s, an average surface tension of 20 mN/m,³⁹ and densities ranging from 0.913 to 0.97 g/mL, are purchased from Sigma-Aldrich and used as received. Glycerol/water mixtures with concentrations ranging from 22 to 100% g/g glycerol are used, yielding zero-shear rate viscosities from 1.7 to 1910 mPa s, densities from 1.05 to 1.25 g/mL,⁴⁰ and an average surface tension of 65 mN/m (as measured with a pendant drop setup).

2. Non-Newtonian fluids

As non-Newtonian system, we choose wormlike micellar solutions (WLM) made of 2,4-bis(2-ethylhexylureido)toluene, abbreviated as EHUT, dispersed in dodecane. This monomer has the ability to self-associate by means of hydrogen bonding in an apolar solvent (dodecane) forming supramolecular polymers.^{41–47} As schematically shown in Fig. 1, EHUT molecules self-assemble into small and long rod-like structures whose cross section is solvent- and temperature-dependent. Above critical concentration and temperature, the monomers self-assemble into thin filaments with a diameter (1.3 nm) comparable to the size of one EHUT monomer. At lower temperatures, thick tubes with a cross section equivalent to about three EHUT monomers form. In this work, we investigate samples in the tube region of the phase diagram, in the temperature range between 20 °C and 25 °C, and concentration range from $C = 0.37$ to $C = 3$ g/L, where the tubes are long enough to entangle, allowing us, hence, to explore a wide range of viscoelastic properties. Although this phase diagram is made for EHUT supramolecular assemblies formed in toluene, Fourier transform infrared spectroscopy (FTIR), small-angle neutron scattering (SANS), and rheology studies confirm that the range of temperatures and concentrations investigated here also corresponds to the tube region of the EHUT assemblies formed in dodecane.^{43–45} The surface tension for EHUT solutions is assumed to be independent of concentration. We take $\Gamma = 25 \pm 2$ mN m⁻¹ as measured with a pendant drop experiment for a dilute sample ($C = 0.37$ g/L). The density

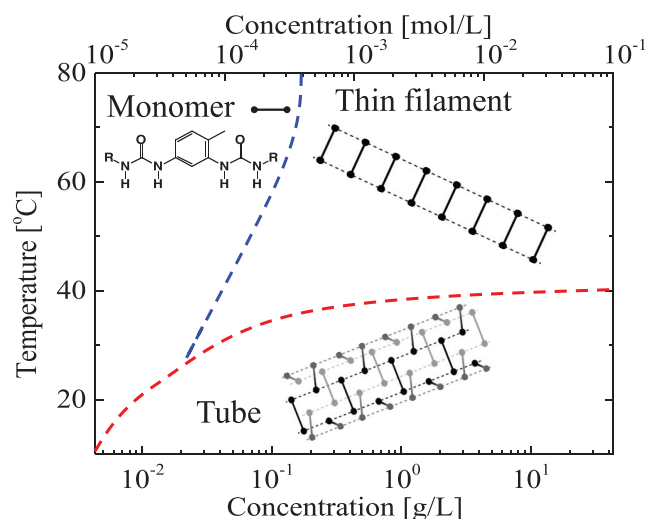


FIG. 1. Phase diagram for EHUT solutions in toluene⁴³ showing the transition between monomers and supramolecular filaments. The structure of the EHUT monomer is shown, along with a schematic illustration of the various aggregates formed (out of scale), that is, filaments and tubes. Hydrogen bonds are represented by dotted lines connecting the urea functions (black and gray circles).

of the EHUT solutions is assumed to be equal to the density of the solvent, $\rho = 0.75$ g/mL.

B. Methods

1. Solution rheology

Linear and nonlinear shear rheology measurements are performed with an MCR501 stress-controlled rheometer (Anton Paar, Austria), operating in the strain control mode and equipped with a stainless-steel cylindrical Couette geometry. Temperature control (± 0.2 °C) is achieved by means of a Peltier element.

For Newtonian and non-Newtonian samples, the zero-shear-rate viscosity, η_0 , is measured by applying a ramp of steady shear rate varying from 0.01 to 1000 s⁻¹.

For EHUT solutions, the linear viscoelastic spectra are obtained by applying a small-amplitude sinusoidal strain ($\gamma = 10\%$) with varying angular frequency, ω , from 100 to 0.01 rad/s, and measuring the storage, $G'(\omega)$, and loss, $G''(\omega)$, moduli. The complex viscosity is also calculated from the linear viscoelastic spectra as $|\eta^*(\omega)| = \frac{\sqrt{(G'(\omega))^2 + (G''(\omega))^2}}{\omega}$. All experiments are performed in open air without any particular humidity precaution (the relative humidity is about 40%). Since hydrogen bonding systems such as EHUT self-assemblies are very sensitive to humidity,^{48,49} and because we do not control the drop impact environmental conditions, we ensure that both bulk rheology and drop impact experiments are conducted under the same temperature and humidity conditions.

2. Drop impact experiment

To study the competition between shear and biaxial extensional viscous dissipations, two drop impact experimental setups are used.

The main setup based on the impact on a small cylindrical target was originally designed by Vignes-Adler *et al.*²⁶ and subsequently modified by several groups.^{30,31,50} We use the same setup as in,^{31,32} schematically shown in Fig. 2(a). In brief, a hydrophilic glass target of diameter $d_T = 6.5$ mm is fixed on top of an aluminum rod with the same diameter. The liquid is injected from a syringe pump with a flow rate of 1 ml/min through a needle placed vertically above the target. The initial diameter of the falling drop is constant, $d_0 = 3.9 \pm 0.2$ mm, as measured by image analysis and by weighting the drops. Note that, considering the difference in fluids' surface tensions, we have adapted the needle diameter to produce a constant drop diameter (a needle with a diameter of 2 mm for fluids with a surface tension of 65 mN/m and a needle diameter of 4 mm for fluids with $\Gamma = 20$ –25 mN/m). The drop falls from a height $h = 91$ cm, yielding an impact velocity $v_0 = \sqrt{2gh} = 4.2$ m s⁻¹ (g is the acceleration of gravity). The corresponding Weber numbers, $We = \frac{v_0 \rho d_0}{\Gamma}$, are $We \sim 1200$ for glycerol/water mixtures, $We \sim 3400$ for silicone oils, and $We \sim 2400$ for EHUT-based samples. The target is mounted on a transparent Plexiglas plate, illuminated from below by a high-luminosity backlight (Phlox LLUB, luminance of 20 cd/m²). The drop impact is recorded from the top using a high-speed camera (Phantom V 7:3) operating at 6700 frames/s with a resolution of 800×600 pixels². The angle between the camera axis and the horizontal plane is fixed at about 10°.

Additional experiments are performed with Newtonian fluids under cold Leidenfrost conditions.²² The relevant setup is described elsewhere²⁴ and schematized in Fig. 2(b). In brief, the drop maintained at room temperature impacts a smooth surface (polished silicon wafer or quartz slide with a diameter larger than the maximum sheet diameter) covered with a thin layer of liquid nitrogen (temperature $T = -196$ °C). Upon impact, a vapor cushion forms at the liquid interface due to the evaporation of N₂, providing a unique scenario of non-wetting and slip conditions that eliminates shear viscous dissipation.^{22,51} Details on the heat transfer involved in the impact of drops in cold Leidenfrost conditions have been reported elsewhere,²⁵ and it does not change significantly the temperature of the drops during the expansion phase of the sheet.

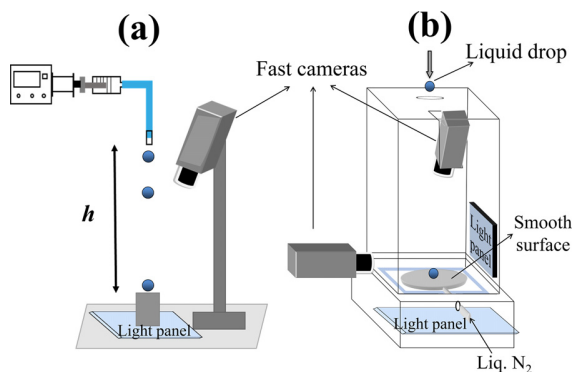


FIG. 2. (a) Schematic illustration of the main experimental setup configuration, consisting of a drop impacting a small solid target as described in the text. (b) Schematic illustration of the second experimental setup showing a drop falling on a liquid nitrogen thin layer. The expansion event is recorded using two fast cameras allowing concomitant top and side visualizations.

3. Image analysis

The time evolution of the diameter of the sheet is measured with ImageJ software. We first subtract the background image from the expansion movie and highlight the rim by a binary thresholding. This allows us to determine the contour of the sheet and measure its area A . An apparent sheet diameter is simply deduced as: $d = \sqrt{\frac{4A}{\pi}}$. The results are obtained by averaging for each sample the time evolution of the sheet diameter from three different experiments. Note that for the small target setup, the dark black central disk is the target and precludes to study the expansion of sheets that do not cross the edge of the target. For the cold Leidenfrost setup, in addition to the top view images, systematic side view images are also collected, though not shown here, to correct the maximum expansion diameter for the corona effect observed for the low viscosity samples (viscosity smaller than 100 mPa s), as detailed in Ref. 24.

III. RESULTS AND DISCUSSION

A. Newtonian fluids

1. Drop impact experiments

Once hitting the target, the drop spreads first on the target and then expands freely in the air until reaching a maximum expansion. It then retracts because of surface tension and eventually bulk elasticity for non-Newtonian fluids (representative videos of the impact process are available in the multimedia). This general phenomenology has been observed for many types of fluids impacting a small solid target.^{26,30–32,34,50,52} The overall behavior is illustrated in Fig. 3

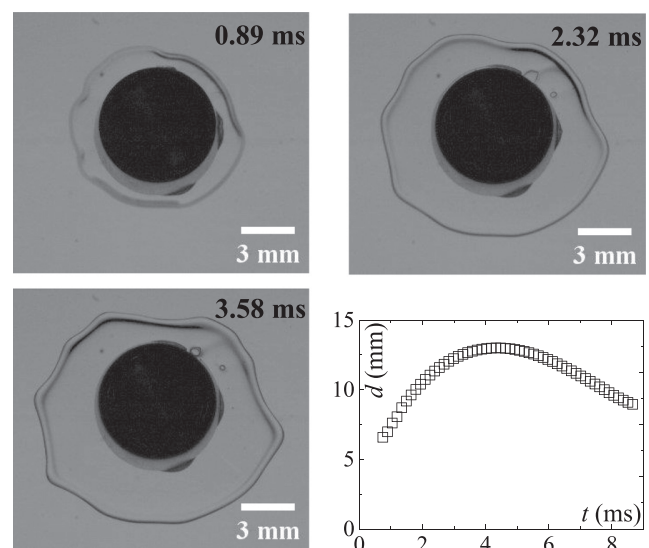


FIG. 3. Snapshots taken at different times (as indicated on each image) during the expansion of the sheet for a glycerol/water mixture with a viscosity $\eta_0 = 160$ mPa s produced upon impact on a solid target with a diameter $d_T = 6.5$ mm. The maximum expansion occurs at $t_{Max} = 3.58$ ms. The black area represents the surface of the target. Video of a drop of glycerol and water mixture (160 mPa s) impacting on a target of diameter 6.5 mm at an impact velocity of 4.2 m/s. The impact was filmed with a high-speed camera operating at 6700 fps and has been slowed down 200 times for the videos. Multimedia view: <https://doi.org/10.1063/5.0057316.1>

(Multimedia view) that depicts snapshots of the drop after its impact for a Newtonian sample (glycerol/water) with $\eta_0 = 160 \pm 10$ mPa s at different times. In the bottom right of Fig. 3, we show the corresponding time evolution of the effective sheet diameter, d , where the expansion and retraction regimes can be clearly determined (we choose for the origin of time, the time when the drop hits the target). Similarly, in Fig. 4 (Multimedia view), we present snapshots for the same Newtonian sample at different times, when it expands and retracts under cold Leidenfrost conditions obtained by impacting a drop on a thin layer of liquid N₂. The origin of time is set when the droplet starts expanding on the nitrogen vapor cushion.

Despite qualitatively similar behavior, we find that, for a same sample and a same impact velocity, the maximum expansion diameter of the sheet, d_{Max} , is significantly larger under cold Leidenfrost conditions ($d_{\text{Max}} = 34.6$ mm) than with the small target ($d_{\text{Max}} = 12.9$ mm). When the expansion results from the impact on the target, only the inner portion of the sheet is at intimate contact with the target surface, while its outer part is free in the air, resulting in a combination of two potential sources of viscous dissipation: shear on the target and biaxial extensional everywhere but predominantly in air. The situation is less complex when the sheet is produced under cold Leidenfrost conditions because the sheet is expanding on the liquid nitrogen vapor, ensuring biaxial extensional deformation as the unique source of viscous dissipation.²⁴

The cold Leidenfrost conditions allow also the observation of the sheet central region, usually obscured by the target. It is worth noting

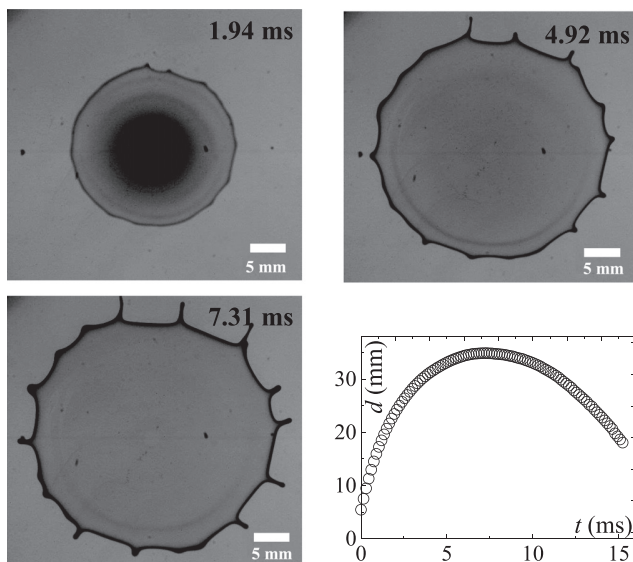


FIG. 4. Snapshots taken at different times (as indicated on each image) during the expansion of the sheet for a glycerol/water mixture with a viscosity $\eta_0 = 160$ mPa s produced upon impact under cold Leidenfrost conditions. The maximum expansion occurs at $t_{\text{Max}} = 7.31$ ms. Video of a drop of glycerol and water mixture (160 mPa s) impacting on liquid nitrogen at an impact velocity of 4.2 m/s and video of a drop of EHUT solution ($C = 0.37$ g/L) impacting a target of diameter 6.5 mm at an impact velocity of 4.2 m/s. The impact was filmed with a high-speed camera operating at 6700 fps and has been slowed down 200 times for the videos. Multimedia view: <https://doi.org/10.1063/5.0057316.2>

the occurrence of a thicker rim for the sheet when impacted on the target and, on the other hand, the appearance of a larger number of better defined fingers instabilities under cold Leidenfrost conditions. However, we will not discuss further these two interesting features, which are out of the scope of this work. Moreover, in the rest of the paper, we will focus on the sheets expansion dynamics up to their maximum expansion and not consider the retraction regime.

In order to follow the expansion dynamics of different samples, we focus on the maximum expansion diameter d_{Max} . We use a normalized maximum expansion diameter, \tilde{d} , adopting the same definition as in Refs. 24 and 32:

$$\tilde{d} = \frac{d_{\text{Max}}}{d_{\text{Max}}^{\text{cap}}}. \quad (1)$$

Here, d_{Max} is the maximum diameter of the sheet and $d_{\text{Max}}^{\text{cap}}$ is the maximum expansion diameter in the capillary regime (at low viscosity), where viscous dissipation does not reduce significantly the maximum expansion diameter. This normalized quantity allows us to compare drops with different initial diameters d_0 and different surface tensions. In addition, to account for the variation of surface tensions among samples, the data are plotted against the dimensionless zero-shear-rate Ohnesorge number, which expresses the ratio of viscous forces to inertial and surface tension forces: $\text{Oh}_0 = \frac{\eta_0}{\sqrt{\rho\Gamma d_0}}$, with ρ the sample density, Γ the surface tension, and η_0 the zero-shear-rate viscosity. Results for different Newtonian fluids obtained using two experimental conditions (target and cold Leidenfrost) are presented in Fig. 5. Note that, for the more viscous glycerol/water mixtures ($\eta_0 > 200$ mPa s), experiments on the solid target are not shown because the maximum expansion diameter is smaller than the target diameter itself. We find two regimes for both experimental configurations. The capillary regime where the dynamics is independent of viscosity resulting in a constant $\tilde{d} \approx 1$, and the viscous regime, where

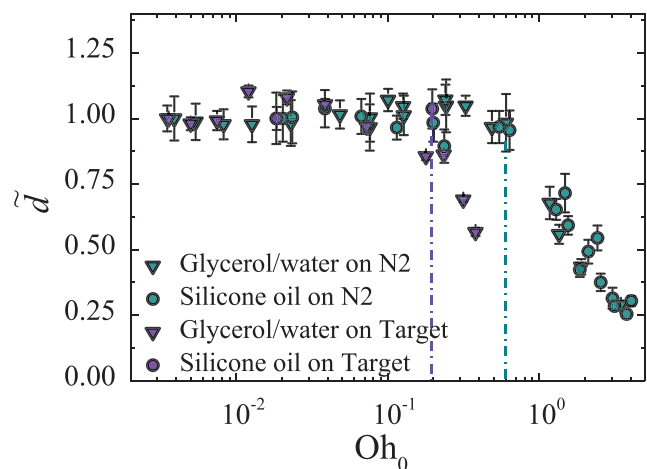


FIG. 5. Normalized maximum expansion as a function of the zero-shear-rate Ohnesorge number, Oh_0 , for the two classes of Newtonian samples, as indicated in the legend, and for the two experimental configurations: small solid target (purple symbols) and cold Leidenfrost conditions (green symbols). Dotted lines indicate the onset of the viscous regime for each configuration. For the Newtonian samples (glycerol/water) presented in Figs. 3 and 4, $\text{Oh}_0 = 0.31$.

\tilde{d} decreases with increasing viscosity. Importantly, the transition from capillary to viscous regime occurs at a larger Oh_0 number (higher viscosity) for the sheets produced under cold Leidenfrost conditions ($Oh_0 \approx 0.6$) compared to those produced by the impact on a target ($Oh_0 \approx 0.2$). This implies that viscous dissipation is more important with the target setup than with the cold Leidenfrost setup, as exemplified by comparing the expansion dynamics of the Newtonian sample presented in Figs. 3 and 4.

In addition, Fig. 5 confirms the fact that even in the absence of friction on a solid surface, a dissipation regime exists resulting in the decrease in \tilde{d} with Oh_0 . In this configuration, the deformation of the sheet is biaxial extensional.²⁴ The dissipation on a small solid target is by contrast more complex because it results from the contact with a solid surface and from free expansion in the air (similar to that under cold Leidenfrost conditions). Thus, in Sec. III A 2, we will analyze the contribution of each dissipation mechanism to the expansion dynamics of a Newtonian drop impacting a small solid surface.

2. Viscous dissipation processes

a. Shear dissipation energy. To estimate the shear dissipation energy, we first define the shear rate experienced by the sheet during its expansion on the small solid target. We approximate the expanding sheet by a disk. The shear flow velocity field on the target^{53,54} reads

$$\begin{cases} v_r = \frac{2}{RH} \frac{dR}{dt} rz & \text{(radial),} \\ v_z = \frac{-2}{RH} \frac{dR}{dt} z^2 & \text{(axial),} \end{cases} \quad (2)$$

where $R(t) = \frac{d(t)}{2}$ is the radius of the expanding sheet, r denotes the radial direction, z denotes the axial direction, and $H(t) = \frac{d_0^3}{6R(t)^2}$ is the mean thickness of the expanding sheet in the disk shape approximation with d_0 the drop diameter. The instantaneous shear rate reads

$$\dot{\gamma} = \frac{1}{2} \left(\frac{\partial v_r}{\partial z} + \frac{\partial v_z}{\partial r} \right) = \frac{1}{RH} \frac{dR}{dt} r. \quad (3)$$

The viscous shear energy dissipated, E_S , during the sheet expansion process can be written as

$$E_S \approx \int_0^{t_{\max}} \int_V \sigma_S \dot{\gamma} dV dt, \quad (4)$$

where V denotes the sheared volume and σ_S is the shear stress. During the expansion of the drop sheet, the viscous boundary layer thickness, $\delta(t) = \alpha \sqrt{\frac{\eta_S t}{\rho}}$ (α is an unknown prefactor and $\eta_S = \eta_0$ is the shear viscosity), which quantifies the thickness of the sheet that is actually sheared.^{32,55,56} At a short time, $\delta < H$, but the viscous boundary layer grows with time, while the film thickness, $H(t)$, decreases. Hence, at some time δ exceeds H and the relevant thickness to be considered is H and not δ anymore.

For simplicity, here, we consider the two limits for the viscous shear energy: (i) $E_{S,H}$, where the relevant thickness for the sheared volume is $H(t)$; and (ii) $E_{S,\delta}$, where the relevant thickness for the sheared volume is $\delta(t)$. $E_{S,H}$ reads

$$\begin{aligned} E_{S,H} &= \int_0^{t_{\max}} dt \int_0^{d(t)/2} \eta_S \dot{\gamma}^2 2\pi r H dr \\ &= \frac{3\pi\eta_S d_T^4}{16d_0^3} \int_0^{t_{\max}} \left(\frac{dR}{dt} \right)^2 dt. \end{aligned} \quad (5)$$

With the approximations $\int_0^{t_{\max}} \left(\frac{dR}{dt} \right)^2 dt \approx t_{\max} \left\langle \left(\frac{dR}{dt} \right)^2 \right\rangle$, $t_{\max} \approx \frac{d_{\max}}{v_0}$, and $d_{\max} \gg d_0$, $E_{S,H}$ reads

$$E_{S,H} \approx \frac{3\pi\eta_S d_T^4 v_0}{64d_0^3} d_{\max}. \quad (6)$$

On the other hand, $E_{S,\delta}$ reads

$$\begin{aligned} E_{S,\delta} &= \int_0^{t_{\max}} dt \int_0^{d(t)/2} \eta_S \dot{\gamma}^2 2\pi r \delta dr \\ &= \frac{9\pi\alpha\eta_S^{3/2} d_T^4}{8\sqrt{\rho} d_0^6} \int_0^{t_{\max}} R^2 \left(\frac{dR}{dt} \right)^2 t^{1/2} dt. \end{aligned} \quad (7)$$

With the approximations $\int_0^{t_{\max}} R^2 \left(\frac{dR}{dt} \right)^2 t^{1/2} dt \approx t_{\max} \left\langle \frac{1}{4} \left(\frac{dR}{dt} \right)^2 \right\rangle \left\langle t^{1/2} \right\rangle$, $t_{\max} \approx \frac{d_{\max}}{v_0}$, and $d_{\max} \gg d_0$, $E_{S,\delta}$ reads

$$E_{S,\delta} \approx \frac{3\pi\alpha\eta_S^{3/2} d_T^4 v_0^{1/2}}{256\sqrt{\rho} d_0^5} \left(\frac{d_{\max}}{d_0} \right)^{7/2}. \quad (8)$$

b. Biaxial extensional dissipation energy. A typical example of a biaxial extensional flow is the compression of a sample sandwiched between two (continuously) lubricated surfaces.⁵⁷ The biaxial viscosity is defined as $\eta_B = \frac{\sigma_{rr} - \sigma_{zz}}{\dot{\epsilon}}$, where $\dot{\epsilon}$ is the strain rate, and σ_{rr} and σ_{zz} are the stress tensor components in cylindrical coordinates.⁵⁷ The stress tensor difference $\sigma_{rr} - \sigma_{zz}$ is commonly expressed as the biaxial stress σ_B . Hence, the biaxial viscosity reads $\eta_B = \frac{\sigma_B}{\dot{\epsilon}}$. For a Newtonian fluid, $\eta_B = 6\eta_S$.

The biaxial extensional energy, E_B , dissipated during the expansion of the sheet can be written as³⁴

$$\begin{aligned} E_B &= \int_0^{t_{\max}} dt \int_V \sigma_B \dot{\epsilon} dV \\ &\approx \eta_B \frac{\pi d_0^3}{6} \int_0^{t_{\max}} \left(\frac{1}{d} \frac{\partial d}{\partial t} \right)^2 dt \\ &\approx \eta_B \frac{\pi d_0^3}{6} t_{\max} \left\langle \left(\frac{\partial \ln(d)}{\partial t} \right)^2 \right\rangle \\ &= \eta_B \frac{\pi v_0 d_0^3}{6} \frac{\ln^2 \left(\frac{d_{\max}}{d_0} \right)}{d_{\max}}, \end{aligned} \quad (9)$$

where $\dot{\epsilon} = \frac{1}{d} \frac{\partial d}{\partial t}$ is the biaxial extensional strain rate.

c. Comparison between shear and biaxial extensional viscous dissipations. In order to assess the respective roles of viscous dissipation due to shear and biaxial extensional deformations during the expansion of a drop, we compare in Fig. 6 the variations of the biaxial extensional viscous energy E_B [Eq. (9)] with the two limits for the shear viscous dissipation energy $E_{S,H}$ [Eq. (6)] [Fig. 6(a)] and $E_{S,\delta}$ [Eq. (8)] [Fig. 6(b)]. The dissipation energies have been normalized by the initial kinetic energy of the drop $E_K = \frac{1}{2} m v_0^2$, with m the mass of the drop, and plotted as a function of the zero-shear rate Ohnesorge

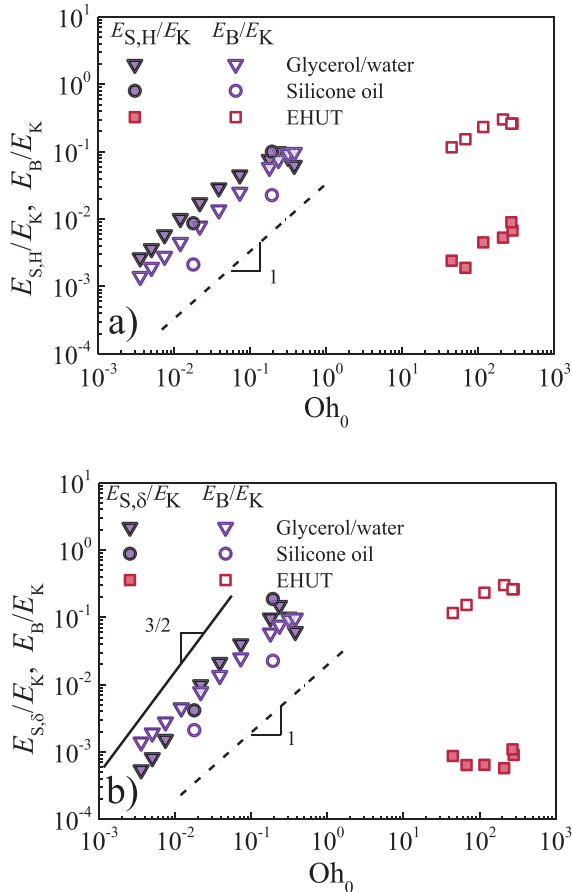


FIG. 6. Variations of the biaxial extensional viscous energy E_B calculated from Eq. (9) and the two limits of the shear viscous dissipation energy, respectively, (a) $E_{S,H}$ from Eq. (6), and (b) $E_{S,\delta}$ from Eq. (8) during the expansion of a drop impacting a small solid target, as a function of the zero-shear rate Ohnesorge number, Oh_0 , for the two classes of Newtonian fluids (purple symbols) and EHUT supramolecular polymer solutions (red squares). The dissipation energies have been normalized by the initial kinetic energy of the drop $E_K = \frac{1}{2}m v_0^2$. The dashed and solid lines indicate a slope of 1 and 1.5, respectively.

number, Oh_0 . We find that $E_{S,H}$ and $E_{S,\delta}$ exhibit power law evolution with the viscosity, which mirrors their explicit dependence with η_0 , $E_{S,H} \sim \eta_0$ [Eq. (6)] and $E_{S,\delta} \sim \eta_0^{3/2}$ [Eq. (8)], reflecting the fact that the dependence of d_{Max} with viscosity is much weaker. This is also the case for E_B , which increases as a power law with η_0 , $E_B \sim \eta_0$ [Eq. (9)], since $\eta_B = 6 \eta_0$ for Newtonian fluids.

Moreover, $E_{S,\delta}$ and $E_{S,H}$ are of the same order of magnitude. Hence, for convenience, we choose the simplest one, $E_{S,H}$ for further discussion on the competition between shear and biaxial extensional viscous dissipation. From Eqs. (6) and (9), we can compute the ratio of the two sources of viscous dissipation energy as

$$\frac{E_B}{E_S} = \frac{64}{3} \left(\frac{d_0}{d_{Max}} \right)^2 \left(\frac{d_0}{d_T} \right)^4 \ln^2 \left(\frac{d_{max}}{d_0} \right). \quad (10)$$

This ratio strongly depends on the drop-to-target size ratio, $\frac{d_0}{d_T}$. It does not depend explicitly on η_0 , but indirectly because of the dependence of the maximal expansion diameter on the sample viscosity. Furthermore, as evidenced by the superposition of $E_{S,H}/E_K$ and E_B/E_K in Fig. 6, $\frac{E_B}{E_{S,H}}$ is close to one and, as expected, depends only weakly on η_0 .

B. Viscoelastic supramolecular polymers

In this section, we present the results for non-Newtonian fluids. In contrast to their Newtonian counterparts, these samples have shear and biaxial extensional viscosities that depend on the applied deformation rate.

1. Viscoelasticity

Figure 7(a) shows the dynamic moduli (G' , G'') as a function of oscillatory frequency (ω) for some representative concentrations. As discussed previously,⁴⁴ these systems behave as Maxwell fluids at low frequencies. This is confirmed by the good agreement between the data and the Maxwell fits [lines in Fig. 7(a)] where $G' = G_0 \frac{\omega^2 \tau_0^2}{1 + \omega^2 \tau_0^2}$ and $G'' = G_0 \frac{\omega \tau_0}{1 + \omega^2 \tau_0^2}$, with G_0 being the elastic modulus and τ_0 the characteristic relaxation time. In Fig. 7(b), we plot the relevant viscoelastic quantities (G_0 , τ_0 , and η_0) for the range of concentrations studied here, extracted from the linear viscoelastic spectra. We find that these quantities follow scaling laws with concentration ($G_0 \sim C^{1.9}$, $\tau_0 \sim C^{0.8}$, and $\eta_0 \sim C^{2.6}$) in agreement with.⁴⁶

Figure 7(c) depicts the complex viscosity, $|\eta^*|$, as a function of frequency, along with the steady shear viscosity, $\eta_S(\dot{\gamma})$, as a function of shear rate. The collapse of the dynamic and steady data (especially above 0.37 g/L) validates the Cox–Merz rule.⁵⁸ We describe the data with a fit by means of the Cross model,⁵⁹ one of many options for empirical models, all giving comparable results:

$$\eta_S(\dot{\gamma}) = \eta_\infty + \frac{\eta_0 - \eta_\infty}{1 + (k\dot{\gamma})^n}. \quad (11)$$

Here, η_∞ is the viscosity at very large shear rate that we set equal to the solvent viscosity ($\eta_\infty = 1.5$ mPa s), η_0 is the zero-shear-rate viscosity [plotted in Fig. 7(b)], n is the shear-thinning exponent, and the parameter k is the inverse of a critical shear rate.⁵⁷ We find that the Cross model provides a good description of the samples' shear-thinning behavior [continuous lines in Fig. 7(c)], except at very large shear rates where some deviation is systematically measured. All data can be fitted with a very similar shear-thinning exponent $n = 0.97 \pm 0.05$.

2. Drop impact experiments

Figure 8 (Multimedia view) depicts snapshots of the drop after its impact for an EHUT solution with $C = 0.37$ g/L at different times. The general phenomenology that has been observed for Newtonian samples (see Figs. 3 and 4) is also found here, and the expansion process does not exhibit any pertinent qualitative differences compared to that of Newtonian samples. This suggests common physical processes driving the expansion dynamics of sheets of different kinds of systems.

In Fig. 9, \tilde{d} is plotted as a function of the zero-shear-rate Ohnesorge number, Oh_0 , for both EHUT solutions (red half plain

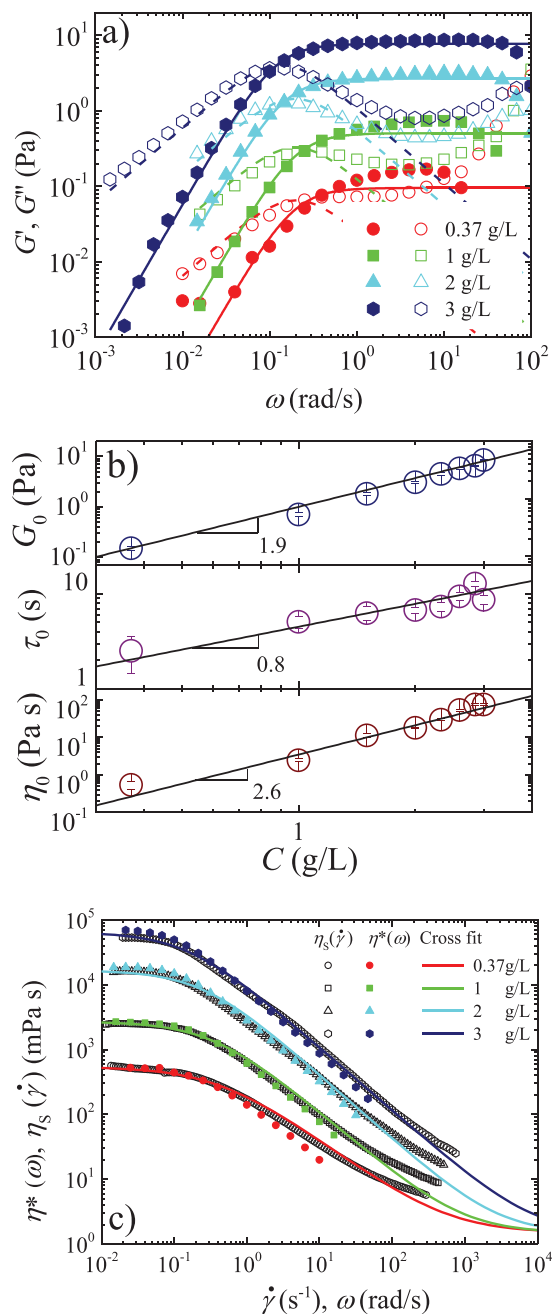


FIG. 7. (a) Frequency dependence of the storage (G' , filled symbols) and loss (G'' , open symbols) moduli of different EHUT supramolecular polymer solutions. The lines (solid for G' , dashed for G'') are Maxwell model fits for samples with different concentrations as indicated in the legend. (b) Evolution of the storage modulus (top), terminal relaxation time (middle), extracted from the Maxwell fits, and zero-shear-rate viscosity (bottom) with sample concentration. The concentration dependence is indicated by the slopes in each figure. (c) Complex viscosity as a function of frequency (closed symbols) and steady shear viscosity as a function of shear rate (open samples), and fits (lines) using the Cross equation [Eq. (11)], for samples with different concentrations as indicated in the legend.

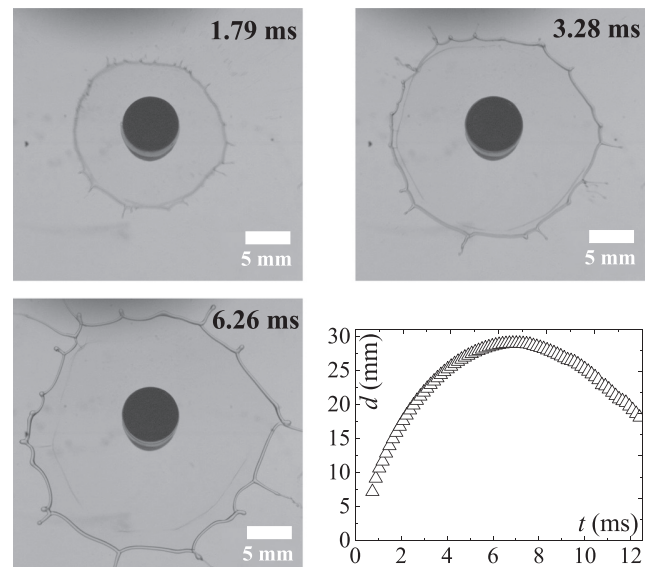


FIG. 8. Snapshots taken at different times (as indicated on each image) during the expansion of a sheet for EHUT sample with concentration $C = 0.37$ g/L. Multimedia view: <https://doi.org/10.1063/5.0057316.3>

squares) and Newtonian samples (green plain triangles) impacted on a small target. We find that for the thinning fluids, the onset of the viscous regime takes place at much higher Oh_0 , hence at much larger η_0 (by factor of 100) as compared to Newtonian samples, a clear indication that the zero-shear-rate viscosity, is not the relevant quantity to characterize the dissipation process for viscoelastic fluids. We first argue that elasticity does not play an important role in the expansion dynamics of the present viscoelastic sheets. Indeed, even if the characteristic relaxation time of the EHUT is always much larger than the

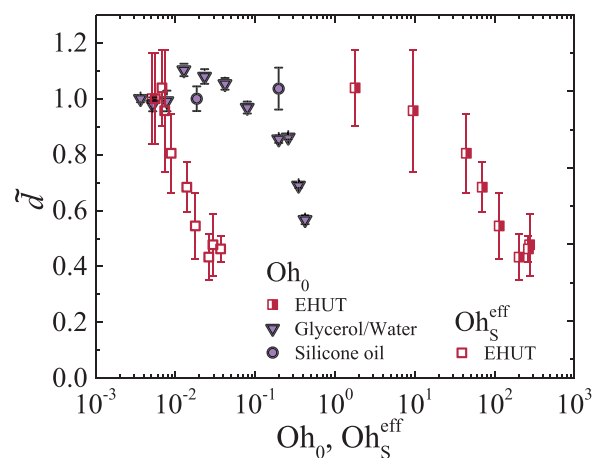


FIG. 9. Normalized maximum expansion factor $\bar{\beta}$ as a function of the zero-shear-rate Ohnesorge number, Oh_0 , for an EHUT supramolecular polymer solutions (closed squares) and for the Newtonian water/glycerol mixtures and silicone oils (purple symbols) and of the effective shear Ohnesorge number, Oh_S^{eff} (see the text), for the EHUT supramolecular polymer solutions (open squares).

characteristic time of the impact experiment [see the regime where storage modulus overwhelms the loss modulus in Fig. 7(a)] so that in principle elasticity should play a role in drop impact experiments, bulk elastic energy contribution is negligible with respect to the capillary contribution if the elastocapillary length, defined as $l_{ec} = \frac{3\Gamma}{G_0}$, is larger than the drop diameter d_0 .²³ Taking $G_0 = 8.5$ Pa, $\Gamma = 25$ mN/m, and $d_0 = 4$ mm, for the most concentrated sample investigated [Figs. 7(a) and 7(b)], one gets $l_{ec}/d_0 = 2.2 > 1$. This ratio is even larger for less concentrated polymer solutions. Therefore, bulk elastic energy contributions can be safely neglected in the present framework. Hence, the contrasted results for Newtonian and non-Newtonian samples must stem from the thinning character of EHUT solutions. Actually, different groups have successfully accounted for the shear-thinning upon impact on a solid surface with a size larger than the expanding maximum sheet diameter.^{8,11,13,32}

In our case, the non-stationary shear rate experienced by the part of the expanding liquid sheet in contact with the target can be analyzed as following. We estimate the spatial average shear rate $\dot{\gamma}(t)$ experienced by the sheet on the target at a given time t . We assume a constant thickness $H(t)$ throughout r at a given time. We define by t^* , the time at which the expanding sheet reaches the edge of the target, that is, $R(t^*) = R_T = \frac{d_T}{2}$.

For $t < t^*$,

$$\dot{\gamma}(t) = \frac{1}{\pi R^2(t)} \int_0^{R(t)} \frac{1}{R(t)H(t)} \frac{dR}{dt} 2\pi r^2 dr = \frac{4R^2(t)}{d_0^3} \frac{dR}{dt}. \quad (12)$$

For $t > t^*$,

$$\dot{\gamma}(t) = \frac{1}{\pi R_T^2} \int_0^{d_T/2} \frac{1}{R(t)H(t)} \frac{dR}{dt} 2\pi r^2 dr = \frac{2d_T R(t)}{d_0^3} \frac{dR}{dt}. \quad (13)$$

Finally, we calculate the time-averaged shear rate experienced by the sheet on the target during the entire expansion process as

$$\langle \dot{\gamma} \rangle = \frac{1}{t_{\max}} \left(\int_0^{t^*} \frac{4R^2}{d_0^3} \frac{dR}{dt} dt + \int_{t^*}^{t_{\max}} \frac{4R_T R}{d_0^3} \frac{dR}{dt} dt \right), \quad (14)$$

$$\langle \dot{\gamma} \rangle = \frac{4}{t_{\max} d_0^3} \left(\frac{d_T^3}{24} + \frac{d_T (d_{\max}^2 - d_T^2)}{16} \right). \quad (15)$$

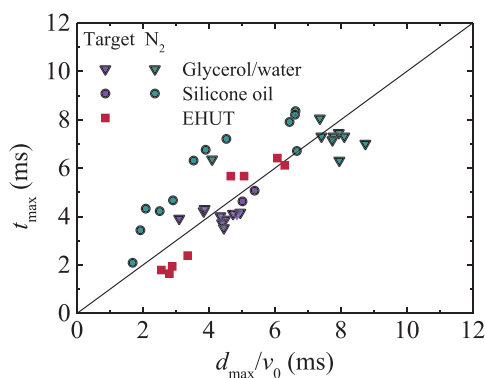


FIG. 10. Time to reach the maximal expansion, t_{\max} , as a function of d_{\max}/v_0 , with d_{\max} the maximal expansion of the sheet and v_0 the impact velocity, for all impact experiments. The line corresponds to $t_{\max} = \frac{d_{\max}}{v_0}$.

A good approximation, well supported by the experimental results (see Fig. 10), is $t_{\max} \approx \frac{d_{\max}}{v_0}$ with v_0 the impact velocity. Moreover, by assuming that $3d_{\max}^2 \gg d_T^2$, the time-averaged shear rate, $\langle \dot{\gamma} \rangle$, reads:

$$\langle \dot{\gamma} \rangle \approx \frac{d_T d_{\max} v_0}{4d_0^3}. \quad (16)$$

Having shown in Fig. 7(c) that the flow curves are well fitted by the Cross model [Eq. (11)], the effective shear viscosities, η_S^{eff} , are evaluated from the Cross fits at the relevant shear rate, $\langle \dot{\gamma} \rangle$. The latter vary from $\langle \dot{\gamma} \rangle = 1420 \text{ s}^{-1}$ to 3220 s^{-1} leading to effective viscosities varying between $\eta_S^{\text{eff}} = 10$ and 2 mPa s .

In Fig. 9, we plot the normalized maximum expansion as a function of an effective Ohnesorge number, Oh_S^{eff} , where η_0 is replaced by η_S^{eff} for the non-Newtonian fluids (open red squares). The plot shows that viscoelastic samples expand much less than one would expect based only on their shear viscosity at the relevant shear rate, when taking as reference the data for Newtonian fluids. Moreover, taking into account the shear-thinning viscosity generates an unrealistic situation where samples with almost the same shear-thinning viscosity exhibit different expansions. Therefore, the shear-thinning viscosity fails to properly describe the maximum expansion of the viscoelastic sheets. Instead, the biaxial extensional viscous dissipation during the expansion in the air must be considered. The deformation field during the sheet expansion upon impacting a small target is essentially biaxial extensional, except on the small target where the sheet experiences both shear and biaxial extensional deformations. Given the very low value of the shear-thinning viscosity, we anticipate that the dissipation is mainly due to the biaxial extensional flow.

3. Viscous dissipation processes

In order to estimate the shear and biaxial extensional dissipation energy of rheo-thinning fluids, one must assess the relevant rate-dependent viscosities involved in these processes.

a. Effective shear viscosity. In order to account for the rate-dependent viscosity in the shear dissipation energy of non-Newtonian fluids, we will consider the effective shear viscosity, η_S^{eff} , resulting from the shear thinning of the EHUT solution and accessible by mean of classical rotational rheometry (see Sec. III B 2).

b. Effective biaxial extensional viscosity. Measuring properly, the biaxial extensional viscosity is a difficult task for viscoelastic fluids of low viscosity such as the present EHUT solutions.^{37,38,60–66} In the framework of the impact drop problem, we have very recently established a successful, yet simple strategy in order to address this challenge.²⁴ Our approach consists of mapping the viscoelastic systems to Newtonian samples impacted under cold Leidenfrost conditions where they experience a purely biaxial extensional deformation. Thus, we attribute to the viscoelastic sample an effective biaxial extensional viscosity equal to the biaxial extensional viscosity of a Newtonian fluid with the same maximum expansion factor. Operationally, we shift horizontally the data of \tilde{d} obtained for the viscoelastic samples so that they overlap the reference data for the Newtonian fluids (Fig. 11). The shift factor yields directly an effective biaxial extensional Ohnesorge

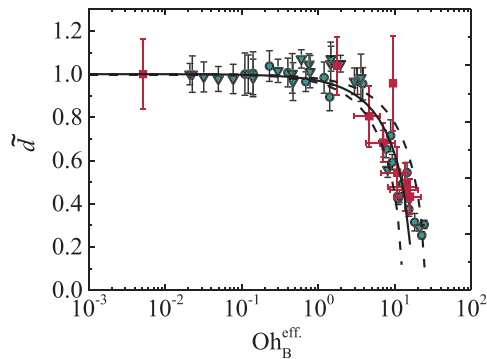


FIG. 11. Normalized maximum expansion factor for drops of Newtonian fluids impacting a surface covered with liquid nitrogen as a function of Ohnesorge number based on η_B^0 (green symbols), together with that of EHUT samples (red squares) impacting a small target as a function of an effective Ohnesorge number based on an effective biaxial extensional viscosity η_B^{eff} chosen to collapse on the two sets of data in the viscous regime. The thin continuous line is the best fit with Eq. (17), and the dash lines show error bars on the fitting parameter β .

number, $Oh_B^{\text{eff}} = \frac{\eta_B^{\text{eff}}}{\sqrt{\rho\Gamma d_0}}$, from which an effective biaxial extensional viscosity η_B^{eff} is derived. η_B^{eff} is different from the biaxial extensional viscosity in the Newtonian limit, $\eta_B^0 = 6\eta_0$. Note that only \tilde{d} data in the viscous regime are shifted for EHUT systems (data in the capillary regime are not subjected to the shift).

In Fig. 11, we show the fit of the in Ref. 24: in

$$\tilde{d} = \sqrt{1 - \beta Oh_B^{\text{eff}}}. \quad (17)$$

Here, $\beta = 0.060 \pm 0.020$ is the only fitting parameter. The model in Eq. (17) is based on an energy conservation balance, assuming that the initial kinetic energy, E_K , is fully converted into surface energy, E_Γ , and biaxial extensional viscous dissipation energy, E_B (the shear viscous dissipation energy, E_S , is neglected).

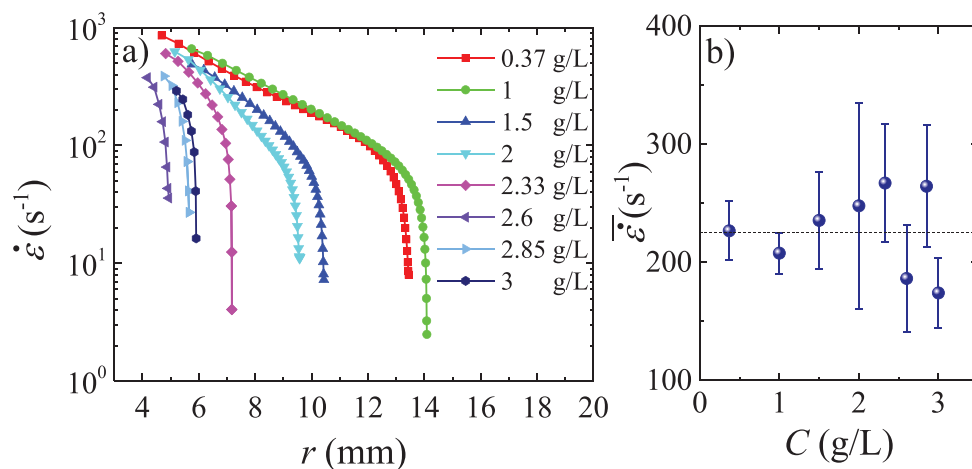


FIG. 12. (a) Evolution of the biaxial extensional strain rate as a function of the radius of the sheet during its expansion for EHUT samples with different concentrations, as indicated in the legend. (b) Average strain rate calculated according to Eq. (18) as a function of concentration. Error bars represent the standard deviation of three different experiments.

In the following, we will verify our assumption that the biaxial extensional dissipation is the relevant source of viscous dissipation in the present experimental conditions. First, we validate the rheological origin of η_B^{eff} . The effective biaxial extensional viscosity, η_B^{eff} , is expected to depend on the strain rate. We use here the same approach as the one developed in Ref. 24 to extract a relevant strain rate for the impact experiment. The time-dependent biaxial extensional strain rate in the expansion regime (Fig. 12) is averaged as

$$\bar{\dot{\epsilon}} = \frac{\int_0^{R_{\text{max}}} r \dot{\epsilon} dr}{\int_0^{R_{\text{max}}} r dr}. \quad (18)$$

Although the average strain rate (Fig. 12) does not vary significantly with sample concentration ($\bar{\dot{\epsilon}}_{\text{Mean}} = 225 \pm 35 \text{ s}^{-1}$), in the following we use the computed average strain rate ($\bar{\dot{\epsilon}}$) for each concentration.

We report in Fig. 13 the variation of the normalized effective biaxial extensional viscosity, $\eta_B^{\text{eff}}/\eta_B^0$, of EHUT supramolecular polymers as a function of the effective Weissenberg number, Wi^{eff} . The latter is defined as $Wi^{\text{eff}} = \tau_0 \bar{\dot{\epsilon}}$, where τ_0 is the relaxation time obtained from linear shear rheology measurements (Fig. 7) and $\bar{\dot{\epsilon}}$ is computed using Eq. (18) (Fig. 12).

On the same plot, we report previous experimental data for normalized biaxial extensional thinning viscosities measured for different viscoelastic fluids using different setups.^{37,38} We also report polyethylene oxide (PEO) solutions data impacted under cold Leidenfrost conditions from our previous work.²⁴ The EHUT experimental data follow remarkably well the experimental results reported in the literature for stationary biaxial extensional deformation flows of different systems (surfactant wormlike micelles in Ref. 37, polystyrene solutions in Ref. 38, and PEO solutions in Ref. 24). At low Weissenberg numbers ($Wi = \dot{\epsilon} \tau_0 < 1$), the biaxial extensional viscosity is rate independent and reaches the Newtonian limit: $\eta_B = \eta_B^0 = 6\eta_0$. By contrast, when $Wi > 1$, the biaxial extensional viscosity decreases with the strain rate as $\eta_B \sim 6\eta_0 (\dot{\epsilon} \tau_0)^{-0.5}$.

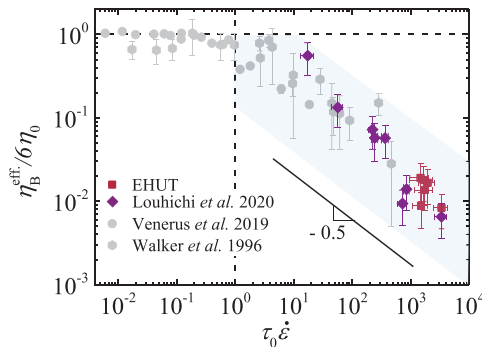


FIG. 13. Effective thinning biaxial extensional viscosity, extracted from the manual shift of the data from Fig. 11 in order to collapse with the data for Newtonian samples, normalized by the plateau biaxial extensional viscosity as a function of the Weissenberg number for the different EHUT solutions studied here (red squares), together with the literature data as indicated in the legend. A unique master biaxial flow curve is obtained with a thinning exponent of -0.5 in agreement with theoretical predictions (see the text). The gray zone is the region of data uncertainties.

with a thinning exponent of -0.5 as validated by theoretical predictions in the framework of the classical tube-based model.⁶⁷

c. Comparison between shear and biaxial extensional viscous dissipation. After assessing η_S^{eff} and validating the rheological origin of η_B^{eff} , we can now compute and compare the two viscous dissipation processes for the supramolecular polymers. In order to account for the rate-dependent viscosity in the shear dissipation energy of non-Newtonian fluids, we have replaced, in Eqs. (6) and (8), η_S by η_S^{eff} . On the other hand, we replaced, in Eq. (9), η_B by η_B^{eff} , to evaluate the biaxial extensional viscous energy.

Results are reported in Fig. 6. The dissipation energies have been normalized by the initial kinetic energy of the drop $E_K = \frac{1}{2}mv_0^2$ and plotted as a function of the zero-shear-rate Ohnesorge number. We observe that the biaxial extensional viscous dissipation energy is larger by two orders of magnitude than the shear dissipation energy (for both limits in the calculation of the shear dissipation energy) despite the fact that the zero-shear viscosity of the less concentrated complex fluid sample (about 10 Pa s) is two orders of magnitude larger than the more viscous Newtonian samples we have investigated (about 0.2 Pa s). Note that in the same experimental conditions, a Newtonian viscous sample with a viscosity of 10 Pa s will not expand outside of the target after impact.

IV. CONCLUSIONS

Drop impact experiments on a small solid target have been performed with Newtonian fluids and solutions of entangled supramolecular polymers as rheo-thinning viscoelastic fluids. Upon impact on the surface, a drop expands into a sheet. A part of the expanding sheet is always at intimate contact with the target, while the rest of the sheet freely expands in the air. We have measured the maximum expansion of sheets for the two classes of fluids. We have quantitatively assessed the energy dissipation due to shear and biaxial extensional deformations, and have highlighted the distinctive roles of shear and biaxial extensional viscosities. We have shown that the expansion process is controlled by a combination of shear (on the target) and biaxial extensional (in the air) deformations. For Newtonian fluids, the two sources of dissipation remain of the same order of magnitude. In sharp

contrast to the findings for Newtonian fluids, for the rheo-thinning viscoelastic fluids, the dominant source of viscous dissipation is the biaxial extensional deformation during the sheet expansion, and consequently, the biaxial thinning extensional viscosity is found to control the maximum expansion of the sheets. The physical reason is that the thinning behavior of the fluid strongly depends on the flow type, since nonlinear viscosities scale differently with the relevant deformation rate. In other words, polymeric fluids exhibit a different thinning behavior in shear and in biaxial extension, justifying the distinction we made between the two viscous dissipation modes. On the contrary, for Newtonian fluids, both viscosities are proportional to each other, and thus, the distinction of the nature of the viscous dissipation is less important. We have also shown that the ratio between the two dissipation modes strongly depends on the size of the target. It would therefore be interesting to study the contribution of the shear dissipation at different drops to target ratios. This will be the task of future work.

AUTHORS' CONTRIBUTIONS

A.L. and C.-A.C. contributed equally to this work.

ACKNOWLEDGMENTS

This work was financially supported by the EU (Marie Skłodowska Curie) ITN Supolen No. 607937, the labex NUMEV (No. ANR-10-LAB-20), and the H2020 Program (Marie Curie Actions) of the European Commission's Innovative Training Networks (ITN) (No. H2020-MSCA-ITN-2017) under DoDyNet REA Grant Agreement (GA) No. 765811.

DATA AVAILABILITY

The data that support the findings of this study are available from the corresponding author upon reasonable request.

REFERENCES

- 1C. Josserand and S. T. Thoroddsen, "Drop impact on a solid surface," *Annu. Rev. Fluid Mech.* **48**, 365–391 (2016).
- 2W. Wirth, S. Storp, and W. Jacobsen, "Mechanisms controlling leaf retention of agricultural spray solutions," *Pest Manage. Sci.* **33**, 411–420 (1991).
- 3B. de Gans, P. C. Duineveld, and U. S. Schubert, "Inkjet printing of polymers: State of the art and future developments," *Adv. Mater.* **16**, 203–213 (2004).
- 4R. Crooks and D. V. Boger, "Influence of fluid elasticity on drops impacting on dry surfaces," *J. Rheol.* **44**, 973–996 (2000).
- 5D. C. D. Roux and J. J. Cooper-White, "Dynamics of water spreading on a glass surface," *J. Colloid Interface Sci.* **277**, 424–436 (2004).
- 6C. Ukiwe and D. Y. Kwok, "On the maximum spreading diameter of impacting droplets on well-prepared solid surfaces," *Langmuir* **21**, 666–673 (2005).
- 7S. T. Thoroddsen, T. G. Etoh, and K. Takehara, "High-speed imaging of drops and bubbles," *Annu. Rev. Fluid Mech.* **40**, 257–285 (2008).
- 8G. German and V. Bertola, "Impact of shear-thinning and yield-stress drops on solid substrates," *J. Phys.: Condens. Matter* **21**, 375111 (2009).
- 9D. Izbassarov and M. Muradoglu, "Effects of viscoelasticity on drop impact and spreading on a solid surface," *Phys. Rev. Fluids* **1**, 23302 (2016).
- 10J. J. Cooper-White, R. C. Crooks, and D. V. Boger, "A drop impact study of worm-like viscoelastic surfactant solutions," *Colloids Surf., A* **210**, 105–123 (2002).
- 11S. M. An and S. Y. Lee, "Maximum spreading of a shear-thinning liquid drop impacting on dry solid surfaces," *Exp. Therm. Fluid Sci.* **38**, 140–148 (2012).
- 12N. Laan, K. G. de Bruin, D. Bartolo, C. Josserand, and D. Bonn, "Maximum diameter of impacting liquid droplets," *Phys. Rev. Appl.* **2**, 44018 (2014).

- ¹³R. Andrade, O. Skurtys, and F. Osorio, "Development of a new method to predict the maximum spread factor for shear thinning drops," *J. Food Eng.* **157**, 70–76 (2015).
- ¹⁴F. Boyer, E. Sandoval-Nava, J. H. Snoeijer, J. F. Dijksman, and D. Lohse, "Drop impact of shear thickening liquids," *Phys. Rev. Fluids* **1**, 13901 (2016).
- ¹⁵V. Bergeron, D. Bonn, J. Y. Martin, and L. Vovelle, "Controlling droplet deposition with polymer additives," *Nature* **405**, 772–775 (2000).
- ¹⁶D. Richard, C. Clanet, and D. Quéré, "Contact time of a bouncing drop," *Nature* **417**, 811 (2002).
- ¹⁷J. C. Bird, R. Dhiman, H.-M. Kwon, and K. K. Varanasi, "Reducing the contact time of a bouncing drop," *Nature* **503**, 385–388 (2013).
- ¹⁸D. Khojasteh, M. Kazerouni, S. Salarian, and R. Kamali, "Droplet impact on superhydrophobic surfaces: A review of recent developments," *J. Ind. Eng. Chem.* **42**, 1–14 (2016).
- ¹⁹G. Martouzet, C. Lee, C. Pirat, C. Ybert, and A.-L. Biance, "Drag reduction on drop during impact on multiscale superhydrophobic surfaces," *J. Fluid Mech.* **892**, R2–12 (2020).
- ²⁰L. Wachters, L. Smulders, J. R. Vermeulen, and H. C. Kleiweg, "The heat transfer from a hot wall to impinging mist droplets in the spheroidal state," *Chem. Eng. Sci.* **21**, 1231–1238 (1966).
- ²¹A.-L. Biance, C. Pirat, and C. Ybert, "Drop fragmentation due to hole formation during Leidenfrost impact," *Phys. Fluids* **23**, 022104 (2011).
- ²²C. Antonini, I. Bernagozzi, S. Jung, D. Poulikakos, and M. Marengo, "Water drops dancing on ice: How sublimation leads to drop rebound," *Phys. Rev. Lett.* **111**, 14501 (2013).
- ²³S. Arora, J.-M. Fromental, S. Mora, T. Phou, L. Ramos, and C. Ligoure, "Impact of beads and drops on a repellent solid surface: A unified description," *Phys. Rev. Lett.* **120**, 148003 (2018).
- ²⁴A. Louhichi, C.-A. Charles, T. Phou, D. Vlassopoulos, L. Ramos, and C. Ligoure, "Biaxial extensional viscous dissipation in sheets expansion formed by impact of drops of Newtonian and non-Newtonian fluids," *Phys. Rev. Fluids* **5**, 053602 (2020).
- ²⁵C.-A. Charles, A. Louhichi, L. Ramos, and C. Ligoure, "Viscoelasticity and elastocapillarity effects in the impact of drops on a repellent surface," *Soft Matter* **17**, 5829–5837 (2021).
- ²⁶A. Rozhkov, B. Prunet-Foch, and M. Vignes-Adler, "Impact of water drops on small targets," *Phys. Fluids* **14**, 3485–3501 (2002).
- ²⁷A. Rozhkov, B. Prunet-Foch, and M. Vignes-Adler, "Impact of drops of polymer solutions on small targets," *Phys. Fluids* **15**, 2006–2019 (2003).
- ²⁸A. Rozhkov, B. Prunet-Foch, and M. Vignes-Adler, "Dynamics of a liquid lamella resulting from the impact of a water drop on a small target," *Proc. R. Soc. London, Ser. A* **460**, 2681–2704 (2004).
- ²⁹A. Rozhkov, B. Prunet-Foch, and M. Vignes-Adler, "Dynamics and disintegration of drops of polymeric liquids," *J. Non-Newtonian Fluid Mech.* **134**, 44–55 (2006).
- ³⁰E. Villermaux and B. Bossa, "Drop fragmentation on impact," *J. Fluid Mech.* **668**, 412–435 (2011).
- ³¹C. Vernay, L. Ramos, and C. Ligoure, "Free radially expanding liquid sheet in air: Time- and space-resolved measurement of the thickness field," *J. Fluid Mech.* **764**, 428–444 (2015).
- ³²S. Arora, C. Ligoure, and L. Ramos, "Interplay between viscosity and elasticity in freely expanding liquid sheets," *Phys. Rev. Fluids* **1**, 83302 (2016).
- ³³B. Keshavarz, E. C. Houze, J. R. Moore, M. R. Koerner, and G. H. McKinley, "Ligament mediated fragmentation of viscoelastic liquids," *Phys. Rev. Lett.* **117**, 129–126 (2016).
- ³⁴Y. Wang and L. Bourouiba, "Unsteady sheet fragmentation: Droplet sizes and speeds," *J. Fluid Mech.* **848**, 946–967 (2018).
- ³⁵M. Arogeti, E. Sher, and T. Bar-Kohany, "Drop impact on small targets with different target-to-drop diameters ratio," *Chem. Eng. Sci.* **193**, 89–101 (2019).
- ³⁶P. S. Raux, A. Troger, P. Jop, and A. Sauret, "Spreading and fragmentation of particle-laden liquid sheets," *Phys. Rev. Fluids* **5**, 044004 (2020).
- ³⁷L. M. Walker, P. Moldenaers, and J.-F. Berret, "Macroscopic response of worm-like micelles to elongational flow," *Langmuir* **12**, 6309–6314 (1996).
- ³⁸D. C. Venerus, R. M. Mick, and T. Kashyap, "Equibiaxial elongational rheology of entangled polystyrene melts," *J. Rheol.* **63**, 157–165 (2019).
- ³⁹A. Crisp, E. de Juan, and J. Tiedeman, "Effect of silicone oil viscosity on emulsification," *Arch. Ophthalmol.* **105**, 546–550 (1987).
- ⁴⁰Glycerine Producers' Association, *Physical Properties of Glycerine and Its Solutions* (Glycerine Producers' Association, 1963).
- ⁴¹B. Isare, S. Pensec, M. Raynal, and L. Bouteiller, "Bisurea-based supramolecular polymers: From structure to properties," *C. R. Chim.* **19**, 148–156 (2016).
- ⁴²F. Lortie, S. Boileau, L. Bouteiller, C. Chassenieux, B. Demé, G. Ducouret, M. Jalabert, F. Lauprêtre, and P. Terech, "Structural and rheological study of a bis-urea based reversible polymer in an apolar solvent," *Langmuir* **18**, 7218–7222 (2002).
- ⁴³L. Bouteiller, O. Colombani, F. Lortie, and P. Terech, "Thickness transition of a rigid supramolecular polymer," *J. Am. Chem. Soc.* **127**, 8893–8898 (2005).
- ⁴⁴G. Ducouret, C. Chassenieux, S. Martins, F. Lequeux, and L. Bouteiller, "Rheological characterisation of bis-urea based viscoelastic solutions in an apolar solvent," *J. Colloid Interface Sci.* **310**, 624–629 (2007).
- ⁴⁵T. Shikata, T. Nishida, B. Isare, M. Linares, R. Lazzaroni, and L. Bouteiller, "Structure and dynamics of a bisurea-based supramolecular polymer in n-dodecane," *J. Phys. Chem. B* **112**, 8459–8465 (2008).
- ⁴⁶A. Louhichi, "Supramolecular assemblies and networks: Interactions, viscoelasticity and flow," Ph.D. thesis (University of Crete, 2017).
- ⁴⁷N. Burger, A. Mavromanolakis, G. Meier, P. Brocurens, R. Lazzaroni, L. Bouteiller, B. Loppinet, and D. Vlassopoulos, "Stabilization of supramolecular polymer phase at high pressures," *ACS Macro Lett.* **10**, 321–326 (2021).
- ⁴⁸A. Louhichi, A. R. Jacob, L. Bouteiller, and D. Vlassopoulos, "Humidity affects the viscoelastic properties of supramolecular living polymers," *J. Rheol.* **61**, 1173–1182 (2017).
- ⁴⁹N. J. Van Zee, B. Adelizzi, M. F. J. Mabesoone, X. Meng, A. Aloï, R. H. Zha, M. Lutz, I. A. W. Filot, A. R. A. Palmans, and E. W. Meijer, "Potential enthalpic energy of water in oils exploited to control supramolecular structure," *Nature* **558**, 100–103 (2018).
- ⁵⁰Y. Wang and L. Bourouiba, "Drop impact on small surfaces: Thickness and velocity profiles of the expanding sheet in the air," *J. Fluid Mech.* **814**, 510–534 (2017).
- ⁵¹S. Chen and V. Bertola, "The impact of viscoplastic drops on a heated surface in the Leidenfrost regime," *Soft Matter* **12**, 7624–7631 (2016).
- ⁵²L.-H. Luu and Y. Forterre, "Giant drag reduction in complex fluid drops on rough hydrophobic surfaces," *Phys. Rev. Lett.* **110**, 184501 (2013).
- ⁵³J. Madejski, "Solidification of droplets on a cold surface," *Int. J. Heat Mass Transfer* **19**, 1009–1013 (1976).
- ⁵⁴P. Attané, F. Girard, and V. Morin, "An energy balance approach of the dynamics of drop impact on a solid surface," *Phys. Fluids* **19**, 012101 (2007).
- ⁵⁵I. V. Roisman, "Inertia dominated drop collisions. II. An analytical solution of the Navier–Stokes equations for a spreading viscous film," *Phys. Fluids* **21**, 052104 (2009).
- ⁵⁶C. Clanet and E. Villermaux, "Life of a smooth liquid sheet," *J. Fluid Mech.* **462**, 307–340 (2002).
- ⁵⁷C. W. Macosko, *Rheology: Principles, Measurements, and Applications*, Advances in Interfacial Engineering Series (Wiley, 1994).
- ⁵⁸W. P. Cox and E. H. Merz, "Correlation of dynamic and steady flow viscosities," *J. Polym. Sci.* **28**, 619–622 (1958).
- ⁵⁹M. M. Cross, "Rheology of non-Newtonian fluids: A new flow equation for pseudoplastic systems," *J. Colloid Interface Sci.* **20**, 417–437 (1965).
- ⁶⁰D. D. Joye, G. W. Poehlein, and C. D. Denson, "A bubble inflation technique for the measurement of viscoelastic properties in equal biaxial extensional flow," *Trans. Soc. Rheol.* **16**, 421–445 (1972).
- ⁶¹D. C. Venerus, T.-Y. Shiu, T. Kashyap, and J. Hostettler, "Continuous lubricated squeezing flow: A novel technique for equibiaxial elongational viscosity measurements on polymer melts," *J. Rheol.* **54**, 1083–1095 (2010).
- ⁶²M. Johnson, N. Murphy, R. Ekins, J. Hanley, and S. Jerrams, "Equi-biaxial fatigue testing of EPM utilising bubble inflation," *Polym. Test.* **53**, 122–131 (2016).
- ⁶³H. Huang and J. L. Kokini, "Measurement of biaxial extensional viscosity of wheat flour doughs," *J. Rheol.* **37**, 879–891 (1993).
- ⁶⁴P. Hachmann and J. Meissner, "Rheometer for equibiaxial and planar elongations of polymer melts," *J. Rheol.* **47**, 989–1010 (2003).
- ⁶⁵C. A. Cathey and G. G. Fuller, "Uniaxial and biaxial extensional viscosity measurements of dilute and semi-dilute solutions of rigid rod polymers," *J. Non-Newtonian Fluid Mech.* **30**, 303–316 (1988).
- ⁶⁶J. M. Maerker and W. R. Schowalter, "Biaxial extension of an elastic liquid," *Rheol. Acta* **13**, 627–638 (1974).
- ⁶⁷G. Marrucci and G. Ianniruberto, "Interchain pressure effect in extensional flows of entangled polymer melts," *Macromolecules* **37**, 3934–3942 (2004).

5.3 Effect of the target size on maximal expansion

5.3.1 Newtonian fluids

As shown in equations 6 and 8 of the paper in section 5.2, the shear dissipation, which affects the expansion of the sheet, is expected to be target-size dependent. In this section, this effect is experimentally investigated by impacting drops on targets of different sizes in the regime $d_T > d_0$ with d_T the diameter of the target and d_0 the drop diameter. Note that Arogeti et al. experimentally studied the opposite regime, with target to drop ratios $\frac{d_T}{d_0}$ ranging from 0.3 to 0.9 [Arogeti 2019].

We use home-made translucent targets, enabling the measurement of the sheet expansion before it reaches out of the target. The target diameter varies from 5 to 30 mm (See section 2.1.3.1), yielding $\frac{d_T}{d_0}$ in the range 1.25 to 4.25.

Snapshots of sheets produced by the impact of a glycerol and water mixture (22% w/w glycerol, $\eta_S = 1.5$ mPa s) at maximal expansion on targets of different sizes and for an impact velocity $v_0 = 3.7$ m/s are presented in Figure 5.1. The maximal expansion of the sheet decreases (from 21.2 mm to 17.2 mm) when d_T increases. Additionally, we observe that the amount of secondary droplet ejections and the size of filaments expanding from the rim decreases as the size of the target increases. Yet, the number of filaments increases with the size of the target.

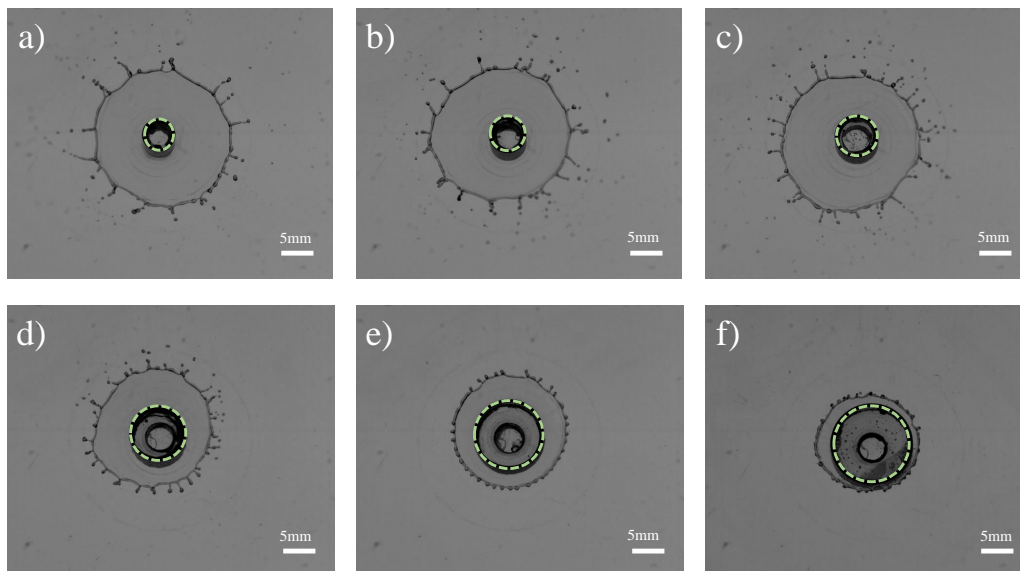


Figure 5.1: Snapshots of sheets of glycerol/water (22/78 w/w, $\eta_S = 1.5$ mPa s) mixture at maximal expansion after impact at an impact velocity $v_0 = 3.7$ m/s on targets with diameter a) 5 mm b) 6 mm c) 7 mm d) 9 mm e) 11 mm f) 13 mm. Scale bars are 5 mm. The dotted green lines highlight the target.

In Figure 5.2, we report the maximal stretching ratio, $\beta_{\max} = \frac{d_{\max}}{d_0}$ as a function of the target diameter for glycerol/water mixtures of different shear viscosity ($\eta = 1$ to 309 mPa s) performed at several impact velocities ($v_0 = 1.5$ to 4.7 m/s). The maximal stretching ratio, β_{\max} , decreases from a first plateau until reaching a second plateau when the size of the target increases. The sharpness of this decrease is more important for the samples with intermediate viscosity as the samples with the highest and lowest viscosity tend to expand similarly on each target (See inset of Figure 5.2).

The dashed line in Figure 5.2 corresponds to $d_T = d_{\max}$. The data points above this line result from the impacts for which the sheet expanded outside of the target. The drops were impacted on targets from smallest to largest until reaching the target size at which the sheet did not expand outside, explaining that most data points lie above the dashed line. Additional impacts were performed on the largest target ($d_T = 30$ mm) as a reference on a plane surface.

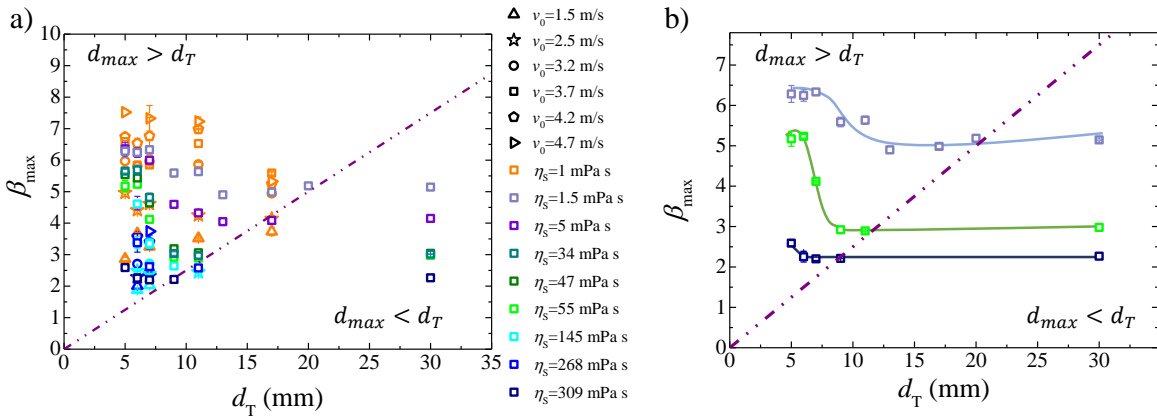


Figure 5.2: a) Maximal stretching ratio, β_{\max} , as a function of the target diameter for all glycerol and water mixtures of different viscosity impacted at different impact velocity, v_0 , as indicated in the legend. b) Results for low (1.5 mPa s), intermediate (55 mPa s) and high (309 mPa s) viscosity samples impacted at $v_0 = 3.7$ m/s. The lines are guides for the eyes. The error bars represent the standard deviation for three separate experiments. In some cases, the error bars are smaller than the symbol size. In a,b) the dash dotted lines delineate two regimes: $d_{\max} > d_T$ and $d_{\max} < d_T$.

To quantitatively explain the dependence of the maximal stretching ratio with the target size, we rationalize the maximal expansion with energy balance arguments (Equation 5.1) and assess the dissipation involved in the dynamic of expansion of the sheets. Energy conservation reads:

$$E_K = E_\gamma + E_{\text{diss}} \quad (5.1)$$

with E_K , the kinetic energy at impact and E_γ , the surface energy and E_{diss} the

dissipated energy at maximal expansion. For E_{diss} , we distinguish two sources: the shear and the biaxial extensional viscous dissipation energies, respectively E_S and E_B .

We write the viscous shear energy dissipated during sheet expansion (from section 5.2) as

$$E_S \approx \int_0^{t_{\text{max}}} \int_{V_{\text{shear}}} \sigma_S \dot{\gamma} dV_{\text{shear}} dt \quad (5.2)$$

with V_{shear} , the sheared volume, $\dot{\gamma}$, the shear rate, σ_S , the shear stress and t_{max} , the time at maximal expansion. As explained in section 5.2, the evaluation of the sheared volume is not trivial since a viscous boundary layer develops with time from the solid surface of the target and defines the sheared portion of the sheet (See Figure 5.3 a)) until propagating to the entire sheet thickness at $t = t^*$. For times larger than t^* , the sheared volume is the total thickness of the sheet, $H(t)$, times the area of the layer in contact with the target (See Figure 5.3 b)). Figure 5.3 shows a representation of the sheared volume (hatches) to consider at different times. The thickness of the boundary layer, $\delta(t) \approx \sqrt{\frac{\eta_S t}{\rho}}$ (with η_S , the shear viscosity), evolves with time as $t^{1/2}$ while the thickness of the sheet, $H(t) = \frac{2d_0^3}{3v_0^2 t^2}$, as calculated by volume conservation assuming that the sheet is a pancake of uniform thickness, decreases as t^{-2} . We define t^* as the time at which $\delta = H$. Thus $t^* = \left(\frac{2d_0^3}{3v_0^2} \sqrt{\frac{\rho}{\eta_S}}\right)^{2/3}$. The sheared volume, V_{shear} , is given by:

$$\begin{cases} t > t^* & V_{\text{shear}} = \frac{\pi d_T^2 H(t)}{4} \\ t \leq t^* & V_{\text{shear}} = \frac{\pi d_T^2 \delta(t)}{4} \end{cases} \quad (5.3)$$

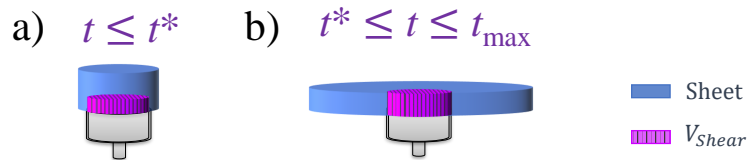


Figure 5.3: Schematic representation of the expanding sheet (blue) and the sheared Volume (purple) at a) $t \leq t^*$ and b) $t^* \leq t \leq t_{\text{max}}$.

We have evaluated t^* and plotted t^* against t_{max} , the time to reach the maximal expansion, in Figure 5.4 along with a line representing $t^* = t_{\text{max}}$. For samples which lay above this line, the thickness to consider to estimate the sheared volume is $\delta(t)$ at early times and becomes $H(t)$ after t^* . In the other hand, for samples below $t^* = t_{\text{max}}$, the relevant thickness is always $\delta(t)$. We find that in most case, $t^* \geq t_{\text{max}}$. Samples with $t^* < t_{\text{max}}$ have very low viscosity, $\eta_S = 1$ and 1.5 mPa s, and the dissipated energy during their impact is negligible since they are in the capillary regime. This statement is verified in Figure 5.5 where the ratio of the dissipated energy to the kinetic energy, $\frac{E_{\text{diss}}}{E_K}$ is plotted as a function of the target size. We here find that for the samples with $t^* < t_{\text{max}}$,

$\frac{E_{\text{diss}}}{E_K}$ is at most 11 %. Because the dissipation is negligible, using $H(t)$ instead of $\delta(t)$ to evaluate the sheared volume in the samples of low viscosity does not lead to significant error.

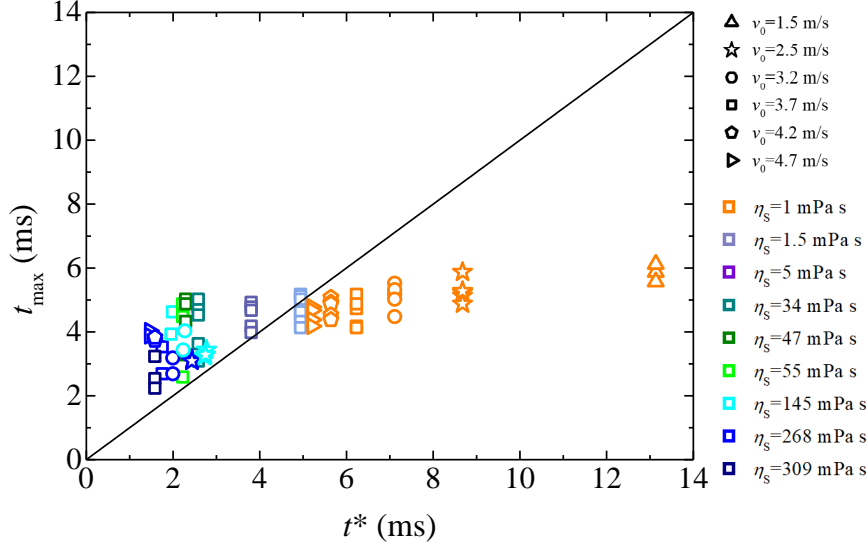


Figure 5.4: Comparison between t_{max} and t^* for glycerol/water mixtures of different viscosities (as indicated in the legend) impacted on targets of different sizes. The different symbols correspond to different impact velocities, v_0 , as indicated in the legend. At a given t^* , the different data points correspond to different target sizes. The line represents $t_{\text{max}} = t^*$.

We thus consider $H(t)$ as the relevant thickness at all times for the sheared volume when estimating the shear dissipation energy (Equation 6 of section 5.2).

$$E_S \approx \frac{3\pi\eta_S d_T^4 v_0}{64d_0^3} d_{\text{max}} \quad (5.4)$$

Note that in section 5.2, the two expressions for the shear dissipation energy evaluated by considering either δ or H are found to be of the same order of magnitude.

On the other hand, the shear dissipation energy is compared to the biaxial extensional viscous dissipation energy (Equation 9 of section 5.2)

$$E_B \approx \eta_B \frac{\pi v_0 d_0^3}{6d_{\text{max}}} \ln^2 \left(\frac{d_{\text{max}}}{d_0} \right) \quad (5.5)$$

The ratio E_B/E_S reads

$$\frac{E_B}{E_S} = \frac{\eta_B}{\eta_S} \frac{32}{9} \left(\frac{d_0}{d_T} \right)^4 \left(\frac{d_0}{d_{\text{max}}} \right)^2 \ln^2 \left(\frac{d_{\text{max}}}{d_0} \right) \quad (5.6)$$

For Newtonian fluids, $\eta_B = 6\eta_S$ so equation 5.6 reads

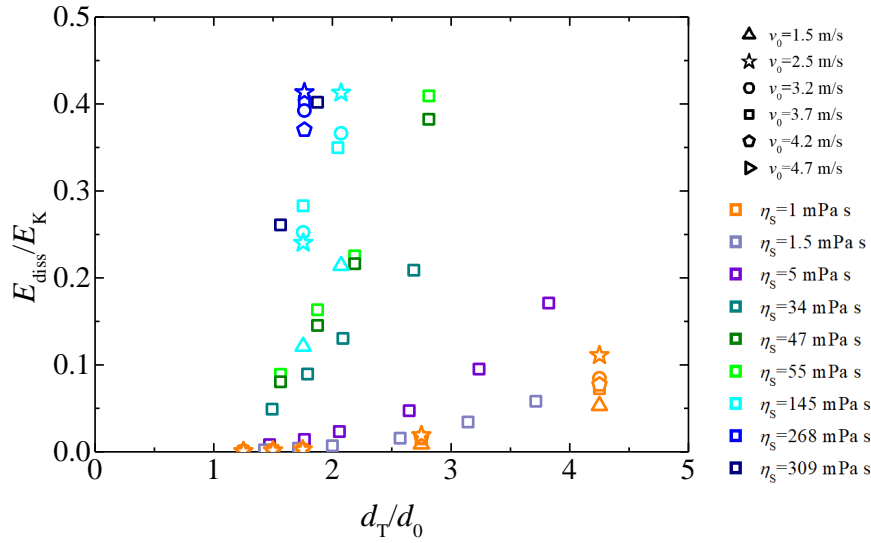


Figure 5.5: The ratio of the dissipated energy at maximal expansion, E_{diss} , over the initial kinetic energy, E_K , as a function of the normalized target ratio, d_T/d_0 .

$$\frac{E_B}{E_S} = \frac{64}{3} \left(\frac{d_0}{d_T} \right)^4 \left(\frac{d_0}{d_{\text{max}}} \right)^2 \ln^2 \left(\frac{d_{\text{max}}}{d_0} \right) \quad (5.7)$$

In that case, the ratio E_B/E_S does not depend directly on the viscosity and the only sample dependent quantity is d_{max} which weakly decreases with viscosity. Experimental data for the ratio E_B/E_S (given by equation 5.6) as a function of the normalized target size, d_T/d_0 , are shown in Figure 5.6. We essentially find a dependence with d_T with a -4 power law. At a fixed target to drop ratio, the experimental values for E_B/E_S in Figure 5.6 increases weakly with the viscosity as expected from the dependence with d_{max} (equation 5.7).

Additionally, E_B/E_S is close to 1 for small target to drop ratio and strongly decreases at larger target to drop ratio showing a dominance of the shear viscous dissipation in the expansion dynamics of sheets formed by the impact of Newtonian fluids as the size of the targets increases.

We will now rationalize the maximal expansion with energy balance conservation arguments. From Figures 5.5 and 5.6, we prove that the biaxial extensional viscous dissipation is negligible with respect to the shear viscous dissipation. Indeed, even in the case when $E_B \approx E_S$ we are in a regime where viscous dissipation energy is negligible compared to surface tension energy (see Figure 5.5) and one can write $E_B + E_S \ll E_\gamma$. Hence, in both cases, it is reasonable to write an energy balance equation for the sheet expansion dynamic omitting the biaxial extensional dissipation energy.

$$E_K = E_\gamma + E_S \quad (5.8)$$

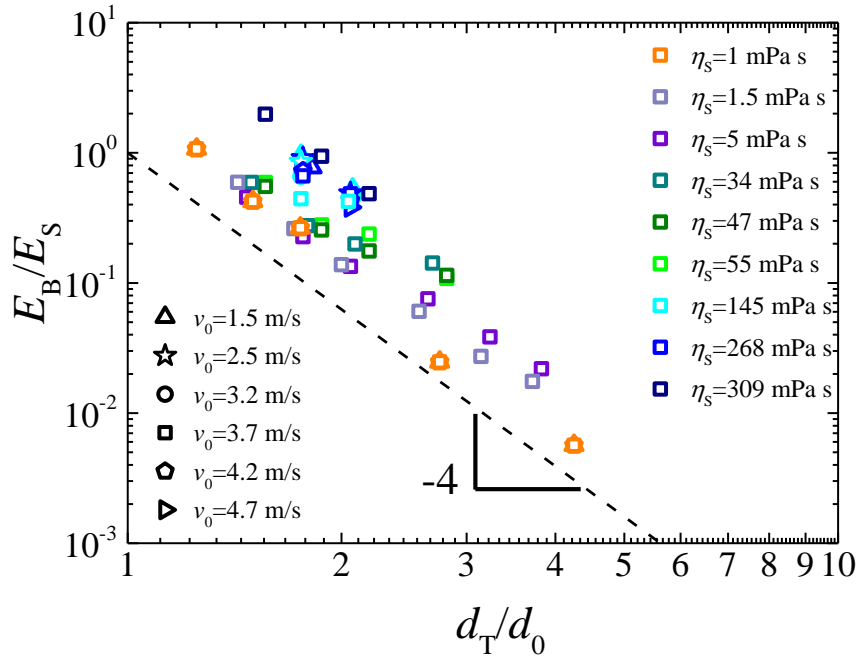


Figure 5.6: Ratio E_B/E_S as a function of the normalized target size, d_T/d_0 , for glycerol/water mixtures impacted with different impact velocity, v_0 , as indicated in the legend.

with $E_K = \frac{mv_0^2}{2}$, the kinetic energy of the drop of mass m , $E_\gamma = \frac{1}{2}\pi\gamma d_{\max}^2$, the surface energy. In the case of an inviscid fluid, viscous dissipation is negligible and Equation 5.8 reads

$$E_K = \frac{1}{2}\pi\gamma d_{\max,inv}^2 \quad (5.9)$$

with $d_{\max,inv}$ the maximal expansion of an inviscid fluid.

The ratio of equations 5.8 and 5.9 gives:

$$\tilde{d}^2 + \frac{3}{32}\sqrt{6} \text{Oh}_0 \left(\frac{d_T}{d_0}\right)^4 \tilde{d} - 1 = 0 \quad (5.10)$$

where $\tilde{d} = \frac{d_{\max}}{d_{\max,inv}}$ and $\text{Oh}_0 = \frac{\eta_S}{\sqrt{\rho}\gamma d_0}$. Equation 5.10 shows a dependence of the maximal expansion with the zero-shear rate Ohnesorge number times the normalized target size to the power 4. To verify this dependence, we first estimate \tilde{d} as $\frac{d_{\max}}{d_{\max,water}} \frac{\gamma_{water}}{\gamma_{gly/water}}$. We then plot \tilde{d} as a function of $\text{Oh} \left(\frac{d_T}{d_0}\right)^4$ along with Equation 5.10 in Figure 5.7. $\frac{\gamma_{water}}{\gamma_{gly/water}}$ is a correction to account for the difference in surface tension between water ($\gamma_{water} = 72$ mN/m) and the glycerol/water mixtures ($\gamma_{gly/water}$ ranges between 71.5 and 64 mN/m). The experimental data collapse quite well on the curve given by the analytic equation 5.10 without adjustable parameters. The residuals to the curve are plotted in the inset of

Figure 5.7 and lay between +9 % and -25 %.

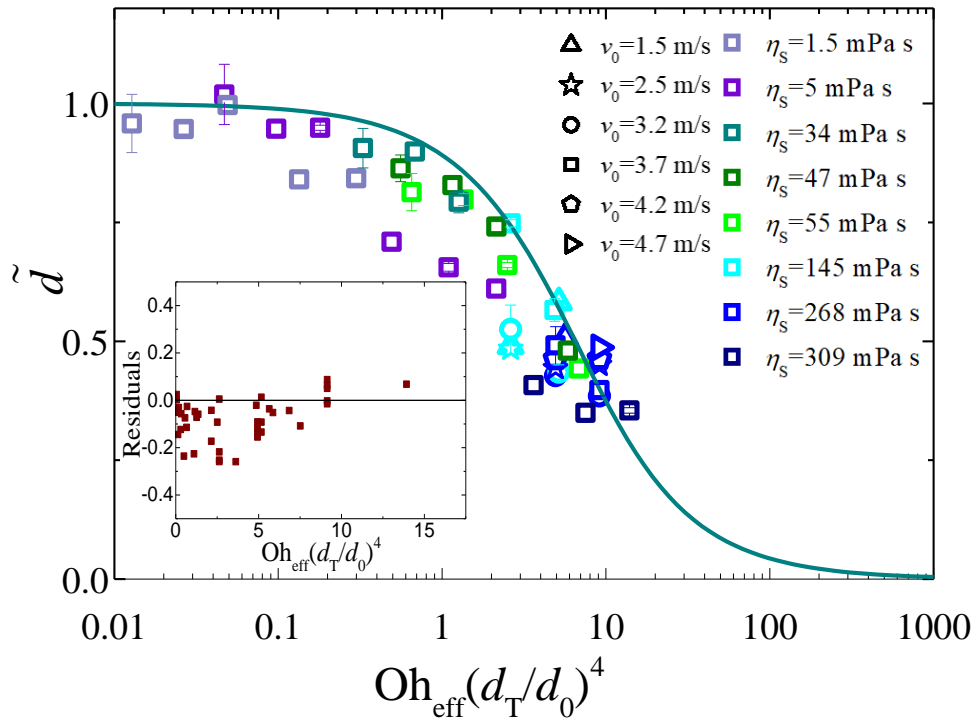


Figure 5.7: Maximum spreading factor normalized by the maximum spreading factor of water and corrected for γ for glycerol/water mixtures on targets of various sizes as a function of $Oh \left(\frac{d_T}{d_0}\right)^4$. The line is the theoretical equation 5.10. The inset is the residuals of the data to the curve.

The model describes well the dependence of the maximal expansion with the target-to-drop diameters ratio times the Ohnesorge number. Moreover, the good quantitative agreement shows that, in the case of Newtonian fluids of different viscosities impacted at different velocities, the biaxial extensional component of the viscous dissipation can be reasonably neglected.

5.3.2 PEO solutions

PEO solutions, which are rheo-thinning fluids, are also impacted on the different targets. We use a PEO with a molecular weight of 8000 kg/mol. The dilute to semi-dilute transition occurs at $C^* = 0.27\%$. The concentrations are chosen in order to have two samples in the dilute regime ($C = 0.02\%$ and $C = 0.2\%$) and two samples in the semi-dilute regime ($C = 0.5\%$ and $C = 1\%$) (See Figure 2.33). The zero-shear rate viscosities

of the investigated samples range from $\eta_0 = 1.5$ to 6530 mPa s. Figure 5.8 shows sheets at maximal expansion resulting from those impacts. The maximal expansion decreases with the target size for the sample in the dilute regime and, seems to be independent of the target size in the semi-dilute regime. The maximal expansion on the small target for the sample at $C = 0.02\%$ is larger than for the sample at $C = 1\%$ and tends to be the same as the target size increases. Moreover, for the sample at $C = 0.02\%$, the number of instabilities seems to increase with the target size while the size of the filament decreases, as it was observed for the Glycerol/water mixture in Figure 5.1. No instabilities were observed for the sample at $C = 1\%$.

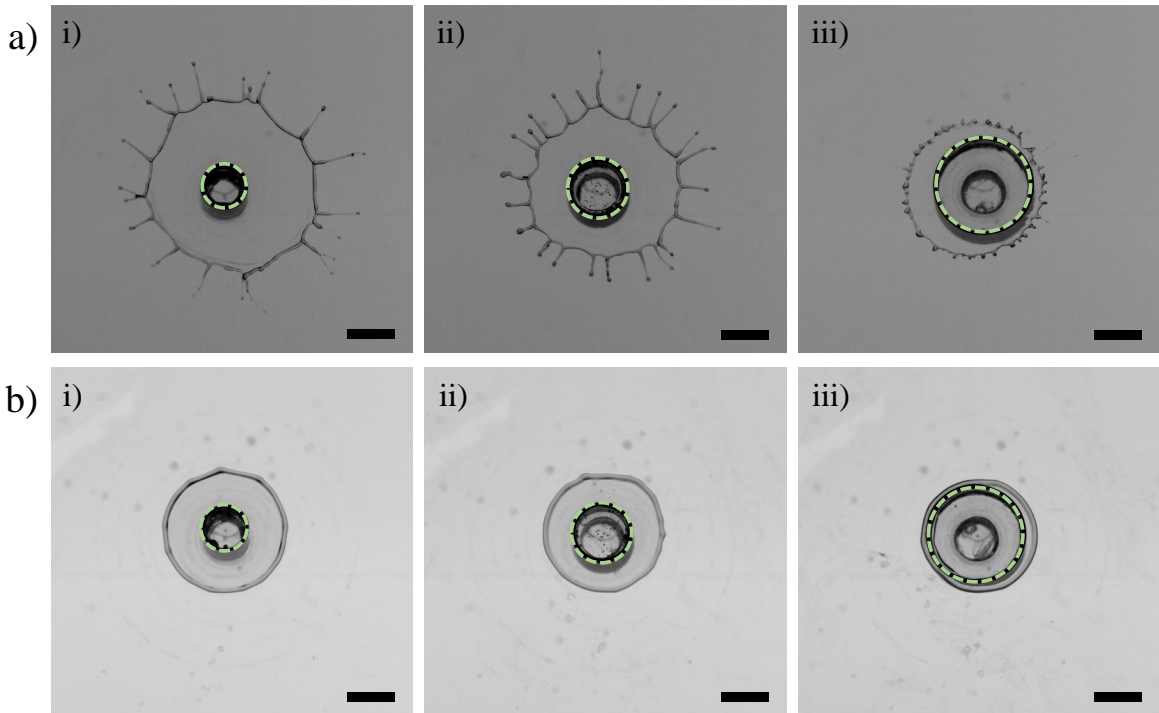


Figure 5.8: Snapshots of sheets of PEO solutions of concentrations a) $C = 0.02\%$ and b) $C = 1\%$ at maximal expansion after impact at an impact velocity $v_0 = 3.7\text{m/s}$ on targets with diameter i) 5 mm ii) 7 mm iii) 11 mm. Scale bars are 5 mm. The dotted green lines highlight the target.

The maximum spreading factors are shown in Figure 5.9 along with the previous results for Newtonian samples (gray symbols). The data points above the dashed line indicate impacts for which the sheet expands outside of the target. We observe a decrease of β_{\max} with increasing target size for PEO solutions below C^* and no effect of the target size on the expansion of semi-dilute PEO solutions ($C > C^*$).

We first discuss the relative contribution of viscous dissipation. In the case of PEO

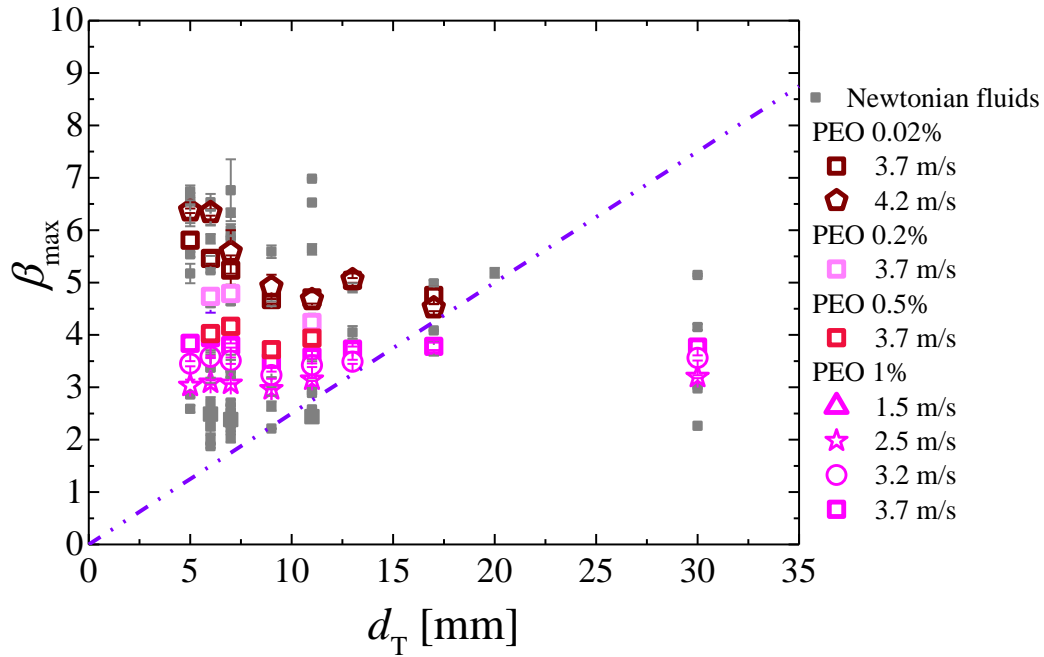


Figure 5.9: Maximum spreading factor for glycerol/water mixtures (gray symbols) and PEO solutions impacted on targets of various sizes. Gray symbols are Newtonian fluids from section 5.3.1.

solutions, the thinning behaviors in shear and in biaxial extension are different. Thus, one must evaluate the relevant quantities for η_B and η_S to calculate the ratio E_B/E_S . We do not have access to η_B experimentally, and we cannot evaluate it as done in section 5.2 with the set of data collected for the PEO samples. Indeed, as we increase the size of the target, and thus the portion of energy dissipated via viscous shear dissipation, we cannot discriminate between the two modes of dissipation when shifting the data as in section 5.2. Not knowing the value of E_B/E_S , we must in principle include the two types of dissipation in the energy balance. Nevertheless, this equation would also include η_B and is complicated. For the sake of simplicity, we decide to neglect biaxial extensional viscous dissipation, which is expected to be more important for impacts on the small targets. Therefore, to rationalize the maximal expansion, we use the equation 5.10 developed from an energy balance including E_S but neglecting E_B . The assumption $\eta_S = \eta_0$ is used to evaluate E_S as we have done for Newtonian fluids. Note that in this manner, we neglect the non-Newtonian behavior of the PEO solutions. We plot on Figure 5.10, $\tilde{d} = \frac{d_{\max, \text{PEO}}}{d_{\max, \text{water}}} \frac{\gamma_{\text{water}}}{\gamma_{\text{PEO}}}$, as a function of $\text{Oh}_0 \left(\frac{d_T}{d_0} \right)^4$ along with the results from Figure 5.7 for the glycerol/water mixtures (gray symbols). The theoretical prediction given by Equation 5.10 and represented by the line in Figure 5.10 largely underestimates the maximal expansion of the sheets of PEO in the semi-dilute regime.

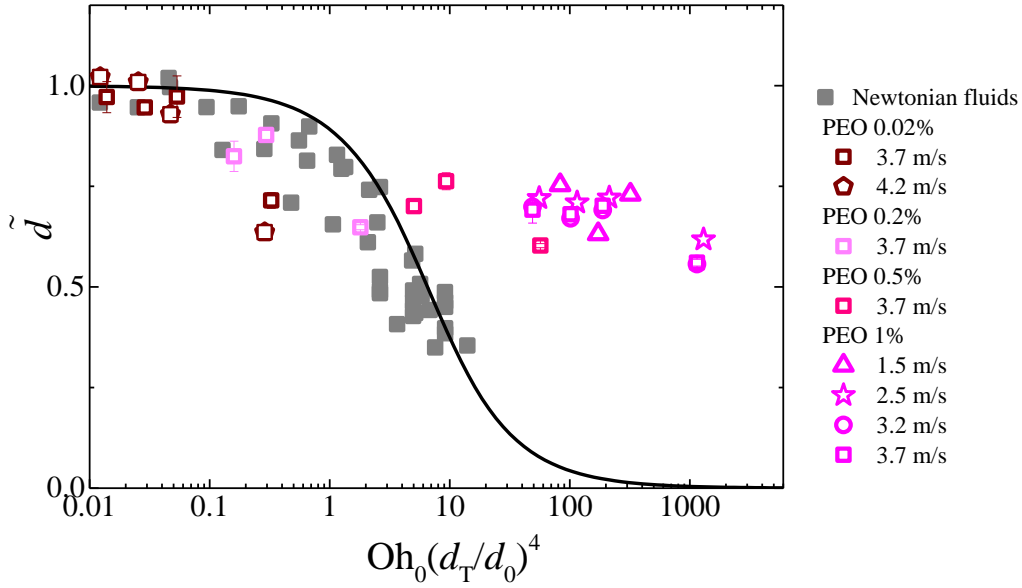


Figure 5.10: Maximum spreading factor normalized by the maximum spreading factor of water and corrected for γ for glycerol/water mixtures (gray symbols) and PEO solutions on targets of various sizes as a function of $Oh_0 \left(\frac{d_T}{d_0} \right)^4$. The line is the theoretical prediction (equation 5.10).

The underestimation of \tilde{d} comes very likely from the fact that in the case of rheo-thinning fluids, using the zero-shear-rate viscosity, η_0 , to estimate the dissipation results in an overestimation of the latter. Indeed, as shown in Figure 5.11, the viscosity of the PEO solutions in the semi-dilute regime decreases with the sollicitation rate. The effective shear viscosity, $\eta_{S,eff}$, is obtained by evaluating the shear viscosity at the relevant shear rate. We calculate the mean shear rate undergone by the sheet from the first time of impact to maximal expansion, $\langle \dot{\gamma} \rangle \approx \frac{d_T d_{max} v_0}{4d_0^3}$ which, for an impact velocity of 3.7 m/s, ranges between 1800 s^{-1} on the target of 6 mm and 3300 s^{-1} on the target of 11 mm for PEO 0.5% and between 1300 s^{-1} on the target of 5 mm and 3500 s^{-1} on the target of 13 mm for PEO 1%. The effective shear viscosity, $\eta_{S,eff} = \eta_S(\langle \dot{\gamma} \rangle)$, thus ranges between 9 and 7 mPa s for PEO 0.5% and between 34 and 15 mPa s for PEO 1% as compared to $\eta_0 = 270 \text{ mPa s}$ for PEO 0.5% and $\eta_0 = 6500 \text{ mPa s}$ for PEO 1%.

Figure 5.12 represents the experimental data for \tilde{d} as a function of $Oh_{eff} \left(\frac{d_T}{d_0} \right)^4$ with $Oh_{eff} = \frac{\eta_{eff}}{\sqrt{\rho \gamma d_0}}$. η_{eff} is η_S for Newtonian, η_0 for unentangled PEO solutions and $\eta_S(\langle \dot{\gamma} \rangle)$ for PEO solutions in the semi-dilute regime. The results in Figure 5.12 shows that \tilde{d} is better described by equation 5.10 when considering the effective viscosity of the sample during

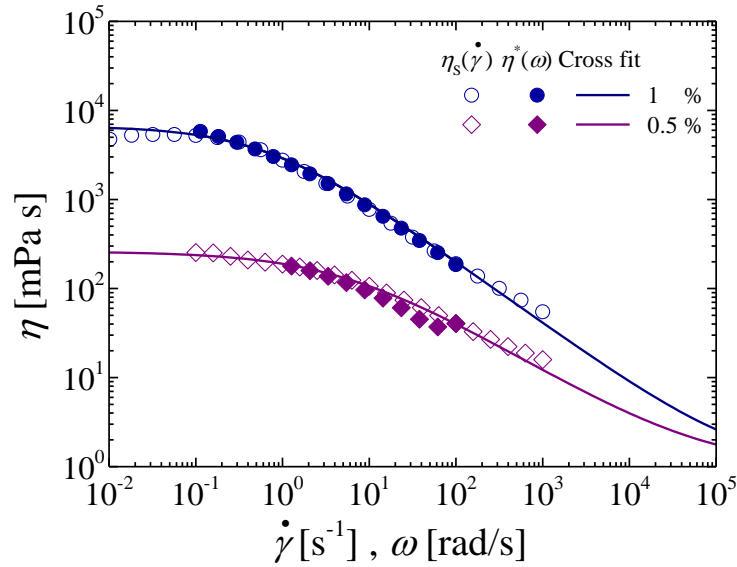


Figure 5.11: Complex viscosity as a function of the oscillation frequency, $\eta^*(\omega)$ (closed symbols), steady shear viscosity as a function of the shear rate, $\eta_S(\dot{\gamma})$ (open symbols) and fits (continuous lines) using the Cross equation (Eq 2.15).

expansion instead of the zero shear viscosity.

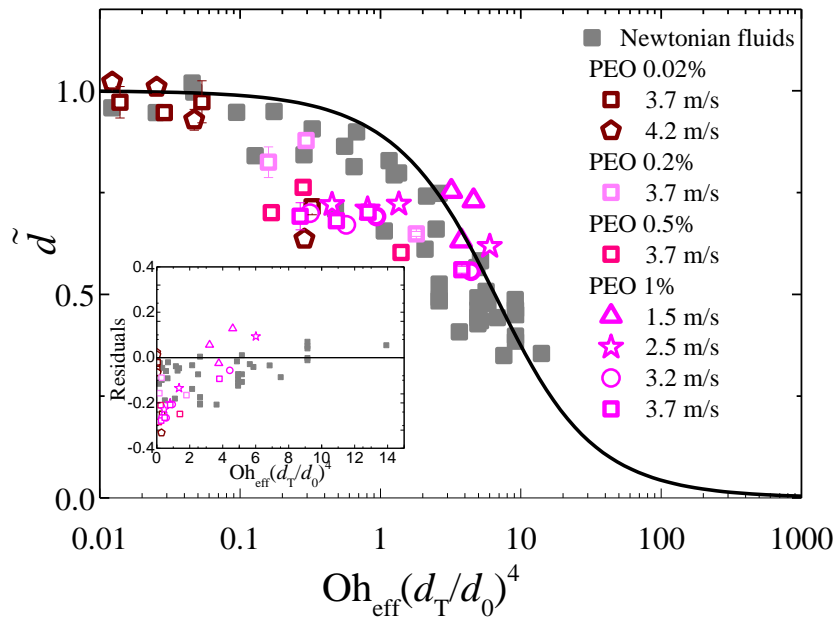


Figure 5.12: Maximum spreading factor normalized by its value at low viscosity for PEO solutions on targets of various sizes as a function of $Oh_{\text{eff}} \left(\frac{d_T}{d_0} \right)^4$. The line is the theoretical equation 5.10. The inset is the residuals of the data to the curve.

Nevertheless, the quantitative agreement is not as good as for the Newtonian fluids as it can be seen from the residuals to the curve in the inset of Figure 5.12. The residuals range between +13 % and -33 %. The poorer agreement with the theoretical expectation (Eq. 5.10) might come from the non-negligible contribution from the effective biaxial extensional viscous dissipation energy, which was overlooked in our model. As expected, the agreement is worse for the semi-dilute samples impacted on the small targets, for which E_B is probably greater than E_S , and becomes better at larger target to drop diameter ratios.

5.4 Conclusion

Drops impacted on a target of comparable size are subjected to both shear and biaxial extensional viscous dissipation due to the intimate contact of part of the sheet with the target while the rest of the sheet is freely expanding in the air. We have demonstrated that for the EHUT solutions, which are strongly shear-thinning, the dominant source of viscous dissipation after impact is caused by the biaxial extensional deformation of the sheet. For Newtonian fluids, however, the two sources of dissipation on the target are of the same order of magnitude. The competition between shear and biaxial extensional viscous dissipation is quantitatively assessed, and the expression for the shear viscous dissipation energy shows a dependence with the size of the target to the power of four.

We have explored the impact of the target size on the shear viscous dissipation by producing targets of various sizes for impact of Newtonian fluids and PEO solutions. We have found an analytical prediction for the maximal expansion of the sheets, based on an energy balance including, as viscous dissipation, the shear dissipation and showed that the maximal expansion depends on $\text{Oh}_{\text{eff}} \left(\frac{d_T}{d_0} \right)^4$. Here Oh_{eff} is the effective Ohnesorge number defined by $\frac{\eta_S}{\sqrt{\rho\gamma d_0}}$ for Newtonian, $\frac{\eta_0}{\sqrt{\rho\gamma d_0}}$ for PEO solutions in the unentangled regime and $\frac{\eta_S(\langle\bar{\dot{\gamma}}\rangle)}{\sqrt{\rho\gamma d_0}}$ for PEO solutions in the semi-dilute regime. $\eta_S(\langle\bar{\dot{\gamma}}\rangle)$ is obtained from evaluating the steady shear viscosity at the relevant shear rate experienced by the expanding sheet, thus accounting for the shear-thinning nature of the samples. The expansion of Newtonian samples has been quantitatively well described by this analytical expression, showing that the biaxial extensional viscous dissipation can be reasonably neglected during the expansion on a target. However, the prediction is less good for the PEO solutions as the contribution from the biaxial extensional viscous dissipation is expected to be more important than for Newtonian samples.

A close look at the rim of viscous sheets

Contents

6.1	Introduction	127
6.2	Thickness fields	128
6.3	Experimental analysis of the rim	133
6.3.1	Emergence of the rim	134
6.3.2	Thickness of the lamella at the foot of the rim	135
6.3.3	Shape of the rim	135
6.4	Theoretical considerations	142
6.4.1	Filling velocity of the rim	142
6.4.2	Filling rate of the rim	147
6.4.3	Emergence of the rim	147
6.5	Conclusion	149

6.1 Introduction

In this chapter, we provide an analysis of the rim bounding a liquid sheet freely expanding on a repellent surface. When a drop of Newtonian fluid expands after impact, a rim appears at the edge of the sheet and propagates toward the center because of the capillary forces in the sheet frame of reference. Studying the dynamics of the rim is of great interest to those who want to characterize the ejection of secondary droplets arising from the destabilization of the rim after the impact of a drop of fluid, and this is the focus of several previous studies [Roisman 2006, Villermaux 2011, Wang 2018]. However, few studies focus on the growth dynamics of a rim during the expansion of a liquid sheet especially from an experimental point of view. Noticeable works include [Roux 2004, de Ruiter 2010, Eggers 2010, Ogawa 2018]. Very recently, Wang measured the volume of the rim of a dyed water drop impacting a small target and undergoing unsteady fragmentation [Wang 2021b]. They assumed the rim cross-section to be circular and found good agreements with predictions for the rate of volume injection into the rim as well as the cumulative volume fraction entering the rim that they obtained using the

radius of the sheet and its thickness at the rim entrance. However, as the shape of the rim is not measured and only assumed, it is difficult to assess the relevance of their results.

The emergence and growth of a rim is not only observed for liquid sheet expansion. This phenomenon was studied extensively in the context of film bursting [Taylor 1959, Culick 1960, McEntee 1969, Petit 2015, Vernay 2015b]. Indeed, when a film is perforated, the fluid accumulates in the rim outside the undisturbed film, collecting all the disappearing material during the opening of the hole. The motion of this rim has been initially studied by Taylor [Taylor 1959] and Culick [Culick 1960] and is closely related to the rim motion and growth in drop impact dynamics [Roisman 2002, Eggers 2010, Villiermaux 2011, Ogawa 2018, Wang 2021b]. Some works in the field of film bursting looked into the cross-section shape adopted by this growing rim, and in some situations observed shapes diverging from the expected circular one. The first observation comes from McEntee and Mysels who evidenced the presence of a thickened film, which they called "aureole", spreading ahead of the expected narrow rim during the bursting of a soap film [McEntee 1969]. The emergence of this aureole was attributed to the presence of surfactants in the film [Frankel 1969] and was also reported in later studies [Florence 1972, Liang 1996, Lhuissier 2009, Petit 2015].

In this chapter, we first describe the thickness profiles as measured for the entire sheets and then focus on the geometrical characteristics of the rim (its real shape and volume). In the rest of this chapter, we focus on momentum and mass conservation arguments to access the velocity at which the rim is fed by the fluid in the expanding sheet and compare this velocity to theoretical predictions. We also consider the filling rate of the rim and define a criterion for the time of emergence of the rim.

6.2 Thickness fields

We perform analysis on sheets of glycerol/water mixtures with viscosity ranging from 60 to 813 mPa s. We did not analyze Newtonian fluids with lower viscosities as they induce significant secondary droplet ejections and form a crown (see section 2.1.4.2). A dye, nigrosin (1.19 g/L), is added to the glycerol/water mixtures to enhance the contrast and quantitatively measure the thickness of the sheets. The impact velocity is fixed at $v_0 = 4.2$ m/s. Drops of initial diameter $d_0 = 4.5$ mm are impacted on liquid nitrogen (cold Leidenfrost conditions). Snapshots of the sheets at maximal expansion are shown in Figure 6.1. In each image, one can observe a darker area at the edges of the liquid sheets, which corresponds to a thicker part of the sheet. The difference between this darker area and the rest of the sheet is more defined for low viscosity samples (Figure 6.1 a) and b)) and seems to fade in more as the viscosity increases. Short fingers as well as some droplet ejections are also observed around the sheets of lower viscosity (Figure 6.1 a) and b)). Green circles, with the same diameters as the effective diameters measured from the

sheets area, have been added on the snapshots to help in the appreciation of the sheets circularity. We observe that, as viscosity increases, the sheet tends to be a perfect circle at maximal expansion (Figure 6.1 f). Nevertheless, even for the samples of the lowest viscosity, the deviation from the circular shape is small, which justifies the azimuthal average we perform while measuring the thickness field of such sheets.

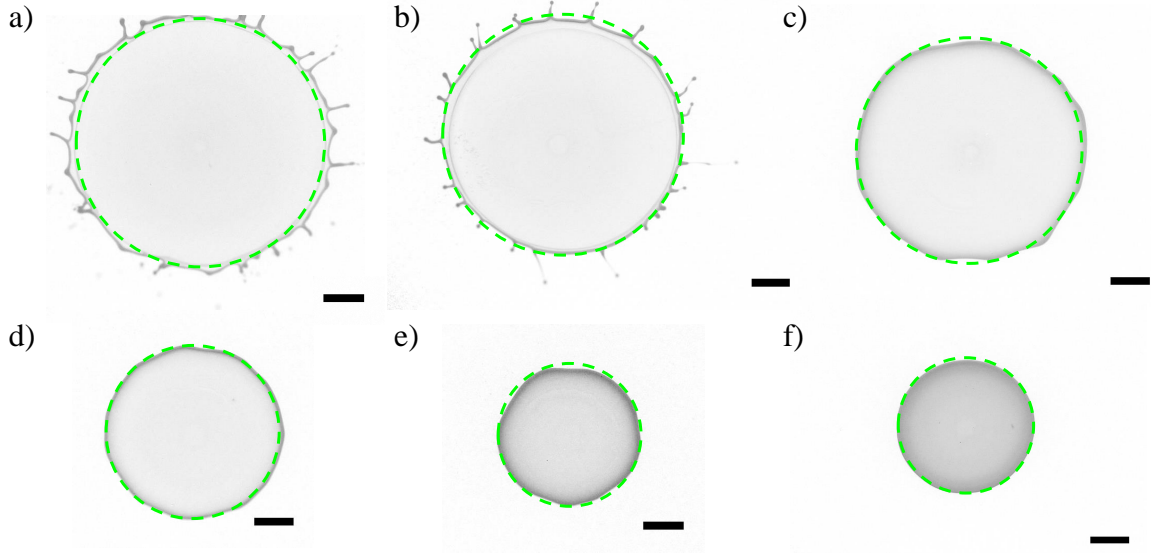


Figure 6.1: Snapshots of sheets of glycerol/water mixtures with viscosity a) 60 mPa s b) 76 mPa s c) 270 mPa s d) 365 mPa s e) 530 mPa s and f) 813 mPa s. Snapshots are taken at maximal expansion, for an impact velocity $v_0 = 4.2$ m/s. The scale bars are 5 mm. The dashed green circles are added to appreciate the deviation of the sheets from circularity and their diameters corresponds to the diameters calculated from the area of the sheet.

The thickness profiles of the sheets during expansion are measured, as explained in section 2.1.4.3, by transmittance. They are averaged along the azimuthal coordinate with an angular step of 1° . In Figure 6.2, we present the thickness profiles as a function of r , the radial axis, at different times for three representative Newtonian samples (80 wt%, 93 wt% and 97.5 wt% of glycerol in water) giving low ($\eta = 60$ mPa s), intermediate ($\eta = 365$ mPa s) and high ($\eta = 813$ mPa s) shear viscosities. For samples of lower viscosity, the thickness at the center of the sheet, h_C , decreases more rapidly during the expansion and follows a power-law decay with exponent -1.5 versus -1.2 for samples of high viscosity (Figure 6.3). This power-law decay of the central lamella thickness has been previously observed and predicted by a power-law decay with a similar exponent for ethanol drops in Leidenfrost conditions [Lastakowski 2014]. Note that the first profiles shown are at $t = 1.79$ ms because of technical issues encountered when measuring the profiles as explained in section 2.1.4.3. The times at which the profiles are accepted are taken when the volume of a given sheet, as calculated by equation 6.1, is roughly constant (Figure 6.6). On Figure 6.2, one can observe the apparition of a bulge at the extremity of the sheet thickness

profile. This bulge is called a rim and is often assimilated to a torus of revolution in the literature. Here, we measure the thickness profile of the sheet and thus have access to the profile of the rim, which allows us to evaluate its shape but also how rims evolve with time. The rim moves on the radial axis, following the sheet expansion, and becomes more pronounced with time. The maximum height of the rim, $h(R_{\text{peak}})$, increases with time.

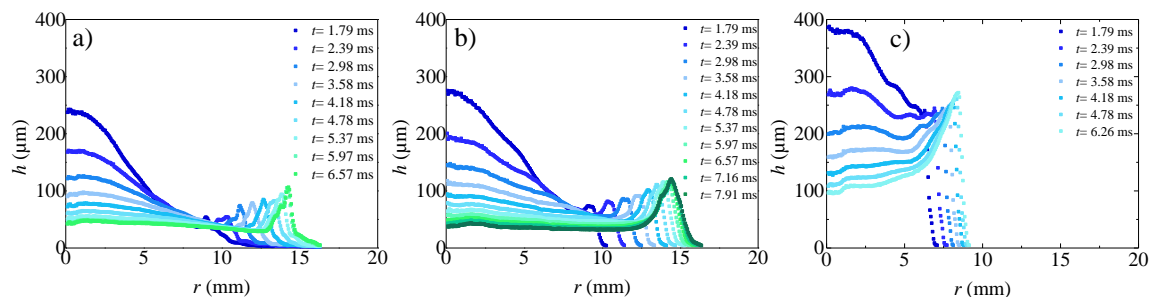


Figure 6.2: Thickness profiles of the sheets as a function of the radius, r , as averaged azimuthally, at different times as indicated in the legend for glycerol/water mixtures with different shear viscosities a) 60 mPa s b) 365 mPa s and c) 813 mPa s. The impact velocity is $v_0 = 4.2$ m/s. The last time shown in each panel corresponds to the time at maximal expansion.

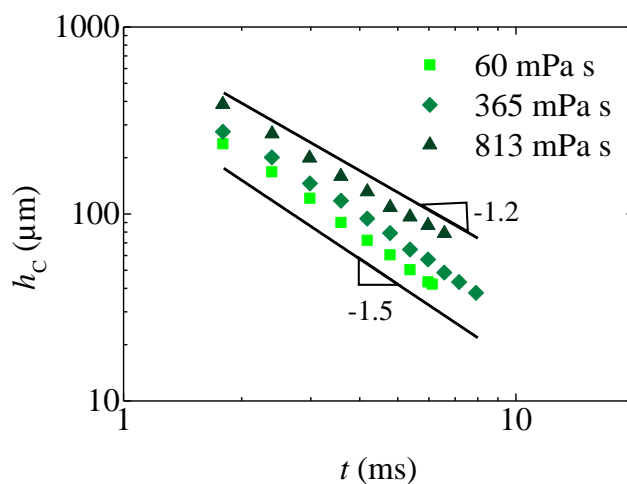


Figure 6.3: Time evolution of the thickness of the sheet at $r = 0$ for glycerol/water mixtures with different shear viscosity as indicated in the legend.

We discuss here, the standard deviation caused by the azimuthal fluctuations of the thickness when averaging h over the azimuthal coordinates. In Figure 6.4 a), we show the thickness field of the sheet at maximal expansion for the samples of lowest ($\eta = 60$ mPa s) and highest ($\eta = 813$ mPa s) viscosity along with the error bars resulting from

the fluctuations of the thickness around the azimuthal coordinates. Far from the rim, the fluctuations are quite low, as it was observed by [Vernay 2015a], and of the order of 10 % for both low and high viscous sheets. On the contrary, at the rim, the standard deviation differs from low (80 % at the peak of the rim) to high (10 % at the peak of the rim) viscosity. The standard deviation resulting from the azimuthal average at the peak of the rim for the different samples at t_{\max} is shown as a function of the shear viscosity in Figure 6.4 b) and decreases linearly with viscosity from $\sim 80\%$ down to 10% as η increases. These much higher fluctuations for samples of low viscosity are believed to result from the presence of fingers and instabilities at the rim. Though these standard deviations are quite high, it does not bring error on R_{in} , R_{peak} and R_{out} or the volume because we obtain the latter by revolution of the mean value of h .

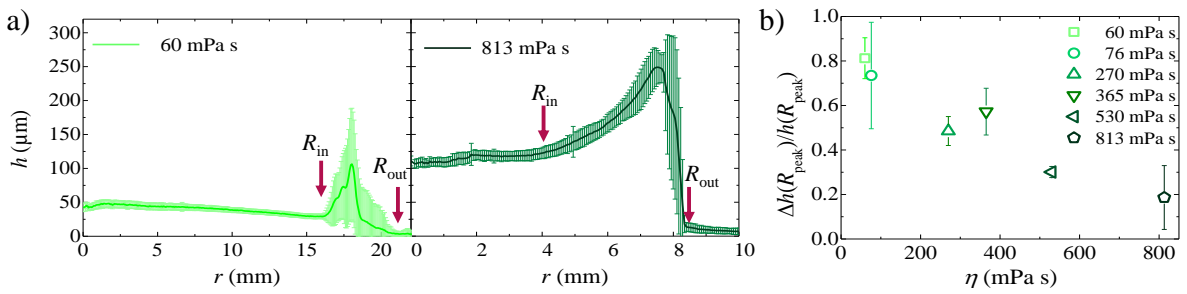


Figure 6.4: a) Thickness profiles of the sheet as a function of the radius, r , as averaged azimuthally, at maximal expansion for two glycerol/water mixtures with shear viscosity 60 mPa s and 813 mPa s. The impact velocity is $v_0 = 4.2$ m/s. The error bars result from the azimuthal average. The arrows indicate the positions of R_{in} and R_{out} . b) Fluctuations for h at $R_{\text{peak}}(t_{\max})$ caused by the azimuthal average of the sheet thickness as a function of the sample shear viscosity.

Figure 6.5 shows the time evolution of $2R_{\text{peak}}$ (symbols) along with the effective diameter, d , measured according to the method in section 2.1.4.1, which gives $d = \sqrt{\frac{4A}{\pi}}$, for different glycerol/water mixtures. We explain how we retrieve the radius at which the rim is the highest, R_{peak} , in section 2.1.4.3: $\frac{\partial h(R_{\text{peak}})}{\partial r} = 0$. The position of the peak of the rim coincide with the measure for the apparent diameter showing that following the highest point of the rim, R_{peak} , is another method to measure the time evolution of the sheet expansion. Moreover, this result confirms the accuracy of our thickness field analysis.

Figure 6.6 shows the volume of the sheet, V_{sheet} , normalized by the volume of the initial drop, V_0 as a function of time. V_{sheet} is obtained from the thickness field, $h(r, t)$, using the equation

$$V_{\text{sheet}}(t) = \int_0^{R_{\text{out}}(t)} 2\pi r h(r, t) dr \quad (6.1)$$

With $R_{\text{out}}(t)$ the radius of the sheet at time t , as obtained from the thickness profile.

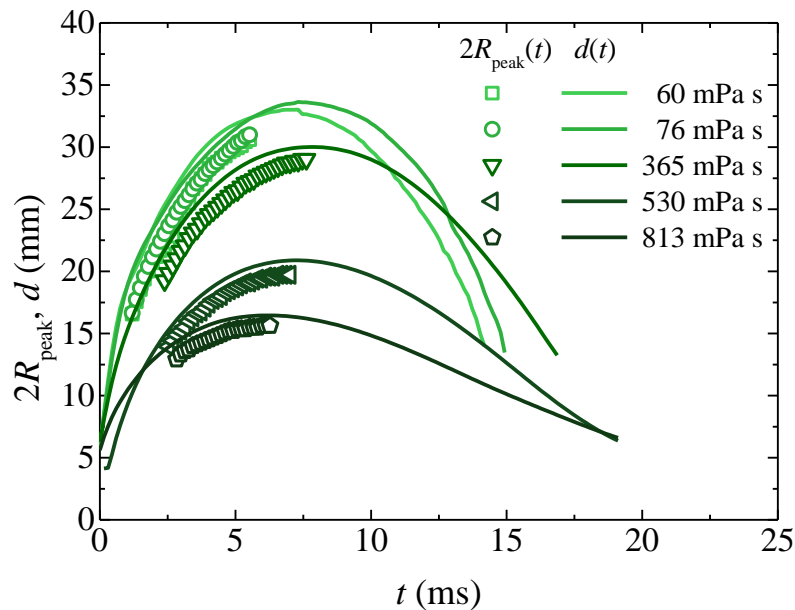


Figure 6.5: Comparison of the effective diameter, d , as measured in section 2.1.4.1 with the position of the peak of the rim, R_{peak} , identified following the method in section 2.1.4.3.

We find that V_{sheet}/V_0 is constant for the more viscous samples and increases before reaching a plateau for samples of lower viscosity. This increase suggests that we do not evaluate properly the volume of the sheet at short times. For this reason, we do not consider times shorter than 1.79 ms for which the volume increases. In the inset of Figure 6.6, we show the time averaged V_{sheet}/V_0 as a function of viscosity. Because this value is equal to or lower than one, in the remaining of this chapter, the volume of the rim will be normalized by V_{sheet} .

Figure 6.7 shows the profiles at maximal expansion for glycerol/water mixtures of different viscosity. This profile is built by reflecting, across the ordinate axis, the thickness field which was previously averaged over the azimuthal coordinates (See section 2.1.4.3). The overall thickness of the sheet is larger for higher viscosity samples (around 100 μm for the center part of the sheet and 250 μm for the rim versus 50 μm and 100 μm for the less viscous fluids) which is not surprising as these samples expand less upon impact.

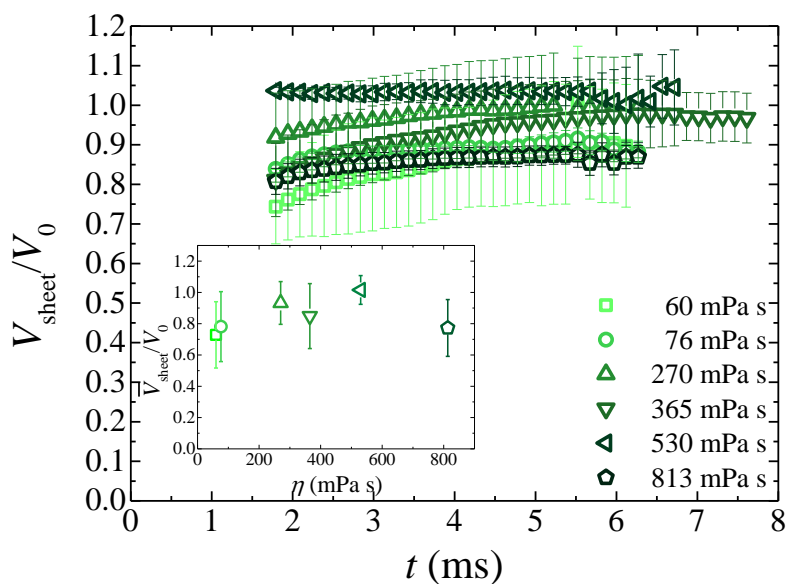


Figure 6.6: Volume of the sheet V_{sheet} , as calculated from equation 6.1, normalized by V_0 , the volume of the drop, as a function of time. The error bars come from the average over three distinct experiments. The inset represents V_{sheet}/V_0 averaged over time as a function of the shear viscosity.

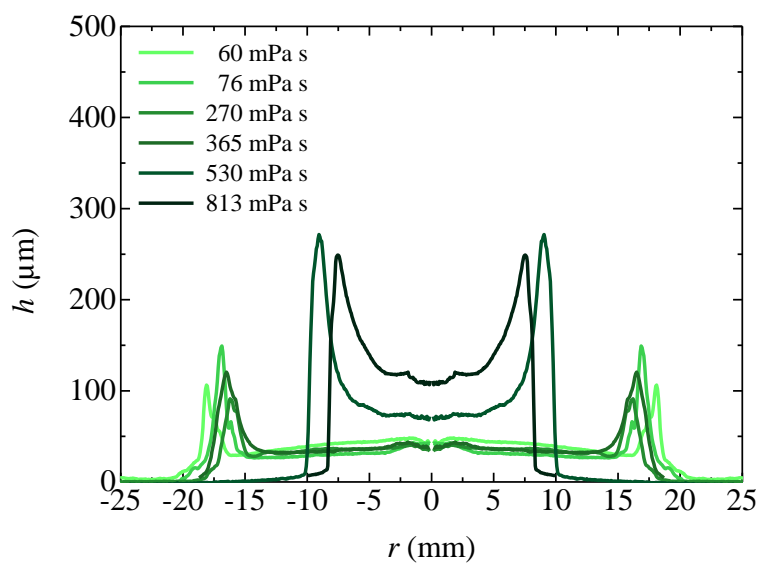


Figure 6.7: Thickness profiles at maximal expansion built by reflection across the ordinate axis for glycerol/water mixtures with different viscosities as indicated in the legend.

6.3 Experimental analysis of the rim

The rim profile is obtained using the method described in 2.1.4.3 which identifies the radii of the inner, $R_{\text{in}}(t)$, and outer, $R_{\text{out}}(t)$, sides of the rim. In Figure 6.8, we show the

thickness field of the sheet at maximal expansion for the samples of lowest ($\eta = 60$ mPa s) and highest ($\eta = 813$ mPa s) viscosity. The outer radius of the rim, R_{out} , is defined as the first non-null value after removing the noise from the thickness profiles. The radius of the inner part of the rim, R_{in} , is easy to define at low viscosity (Figure 6.8 a)) as the thickness profile, at the transition from the rest of the sheet to the rim, has a minimum that can easily be detected. On the contrary, for viscous fluids, the transition from the rest of the sheet to the rim is broad, and the minimum is more difficult to identify (Figure 6.8 b)). We defined a criterion which allows to identify R_{in} for all samples whatever their viscosity:

$$\left. \frac{1}{h(r)} \frac{\partial h}{\partial r} \right|_{R_{\text{in}}} = 0.15 \quad (6.2)$$

This criterion is somewhat arbitrary. For this reason, the analysis for which the value of R_{in} has an impact were performed using $\frac{h'}{h}(R_{\text{in}}) = 0.1, 0.15$ and 0.2 and showed no significant qualitative and quantitative discrepancy. Arrows on the graphs (Figure 6.8) show the positions of R_{in} and R_{out} as found by using our method. On Figure 6.8 a), R_{out} is further from the peak as compared to Figure 6.8 b). Indeed, the profile in Figure 6.8 a) is for a sheet of low viscosity and has instabilities, which we take into account.

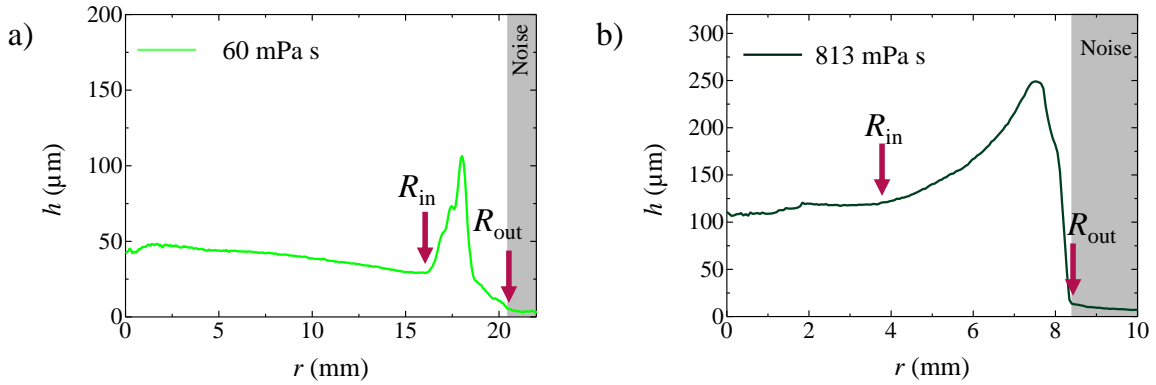


Figure 6.8: Thickness profiles of the sheet as a function of the radius, r , as averaged azimuthally, at maximal expansion for two glycerol/water mixtures with shear viscosity a) 60 mPa s and b) 813 mPa s. The impact velocity is $v_0 = 4.2$ m/s. The arrows indicate the positions of R_{in} and R_{out} .

6.3.1 Emergence of the rim

At short times, it might not be possible to find R_{in} which is defined as the radius before R_{peak} at which h'/h is closest to 0.15 (see section 2.1.4.3). We can define an apparition time for the rim, t_{rim} . t_{rim} is represented as a function of the viscosity in Figure 6.9. t_{rim} is measured to increase with sample viscosity, from ≈ 1 ms for $\eta = 60$ mPa s to ≈ 3 ms for $\eta = 813$ mPa s.

The rim, for the more viscous sheets, appears at longer times around $t_{\text{rim}} = 3$ ms for sample with $\eta = 813$ mPa s as compared to 1 ms for the less viscous samples.

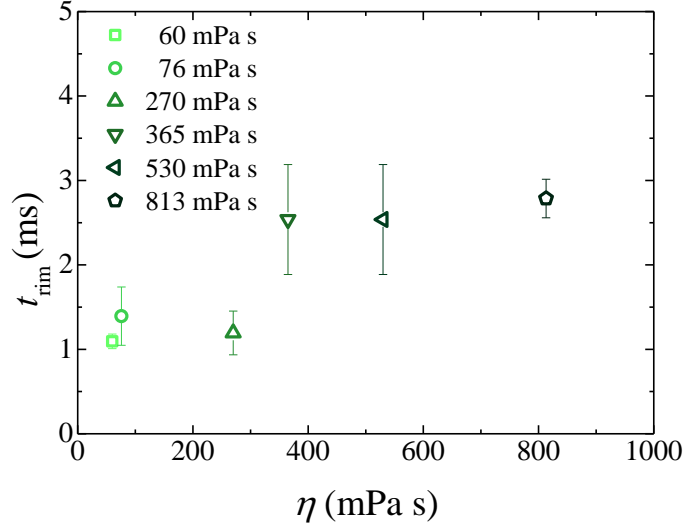


Figure 6.9: Apparition time for the rim, t_{rim} , as a function of the sample viscosity. The error bars come from the average over three distinct experiments.

6.3.2 Thickness of the lamella at the foot of the rim

The thickness at $R_{\text{in}}(t)$ corresponds to the thickness at the entrance of the rim, $e = h(R_{\text{in}})$. This is a useful parameter for the quantitative modeling of the rim dynamics, as detailed below. The time evolution of e for all samples is represented in Figure 6.10. This quantity is constant for samples of low viscosity and follows a sharp decrease with time before reaching a plateau for samples of higher viscosity.

6.3.3 Shape of the rim

Our experiments provide a unique opportunity to measure the actual profile of the rim. The profiles of the rim are shown in Figure 6.11 for sheets at their maximal expansion. To obtain a cross-section at t_{max} of the envelope of the rim in a plane containing the revolution axis, we plot, in Figure 6.12, $h_1 = \frac{h(r, t_{\text{max}})}{2}$ and $h_2 = \frac{-h(r, t_{\text{max}})}{2}$ as a function of r , assuming that the sheet is symmetric with respect to the horizontal axis. To have a realistic shape of the cross-section, we use the same scale for the horizontal and vertical axis. Furthermore, to compare the different samples, we only show the external part of the sheet last 5 mm from the edge of the cross-section. Note that the envelopes do not

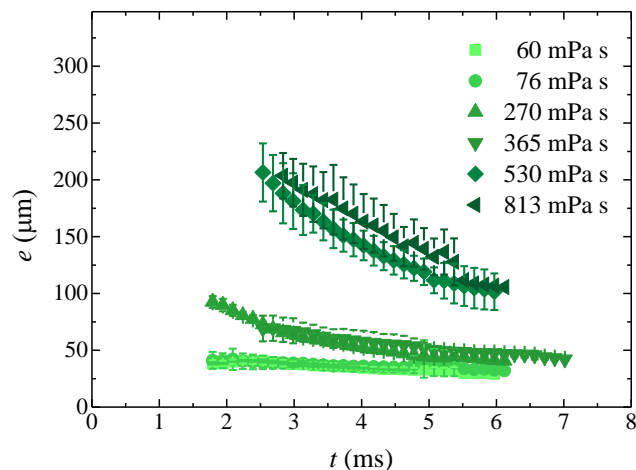


Figure 6.10: Thickness at the entrance of the rim, e , as a function of time. The error bars come from the average of three distinct experiments.

close as we do not go below 5 μm , which is the amplitude of the noise.

In Figure 6.11, the rim is delimited on the left by R_{in} and on the right by R_{out} . We can clearly see that the shape of the rim cross-section differs from the circular one, which is the shape usually assumed to model the rim [Yarin 2017, Wang 2018]. The rim is rather a toroid of revolution with a cross-section close to an oblate ellipse. Figure 6.13 shows the eccentricity, $Ecc = (R_{\text{out}} - R_{\text{in}})/h(R_{\text{peak}})$, of the ellipse containing the rim cross-section at maximal expansion as a function of the shear viscosity. The shape of the profile we measure seems to correspond to the aureole initially observed by [McEntee 1969] and measured experimentally by [Florence 1972] when looking at punctured soap films. But we could not make quantitative comparison because there is, to our best knowledge, no data showing the shape of the rim in the literature. The emergence of an aureole was attributed to surface tension gradients caused by the presence of surfactants in solution [McEntee 1969, Petit 2015, Bico 2015]. Though, in our situation, the surface tension is a constant, thus the aureole shape we obtain for the rim cannot be attributed to surface tension gradients. Interestingly, [Vernay 2015b] studied the bursting of dilute oil-in-water emulsion-based liquid sheets ($\eta = 1 \text{ mPa s}$) in presence of surfactants but looking at the thickness profiles provided in their paper, we do not observed a large eccentricity ($Ecc \approx 1$) of the shape of the rim at the nucleating holes caused by Marangoni effect. Nor did we observe large eccentricity ($Ecc \approx 1$) of the rim bounding an expanding sheet of water impacted on a small target by Vernay et al. [Vernay 2015a]. However, Lagubeau et al. obtained thickness profiles of a drop of glycerol/water ($\eta = 6 \text{ mPa s}$) expanding on a hydrophobic substrate and one can notice on these profiles, rims with width 10 times larger than the maximum height, i.e. $Ecc \approx 10$, which is of the same order as what we observe here [Lagubeau 2012]. As it is, it is not clear if this eccentricity is related to the surface or to the viscosity. Either way, it is obvious in our situation that the cross-section

is far from being circular.

Additionally, the whole shape of the cross-section depends strongly on the viscosity. The rim is thicker for samples of higher viscosities and the rim spans a larger section of the sheet. [Frankel 1969] showed that, in the case of a punctured film, the viscosity of the fluid leads to a thicker part which extends further toward the undisturbed sheet if the viscosity is larger. This hydrodynamic analysis corroborates our measurements where the rim extends further away from the rim for higher viscosities. The asymmetry of the rim at maximal expansion for the sample of the highest viscosity ($\eta = 813 \text{ mPa s}$), which does not have instabilities, is equal to $As = 3$. With $As = \frac{R_{\text{peak}} - R_{\text{in}}}{R_{\text{out}} - R_{\text{peak}}}$.

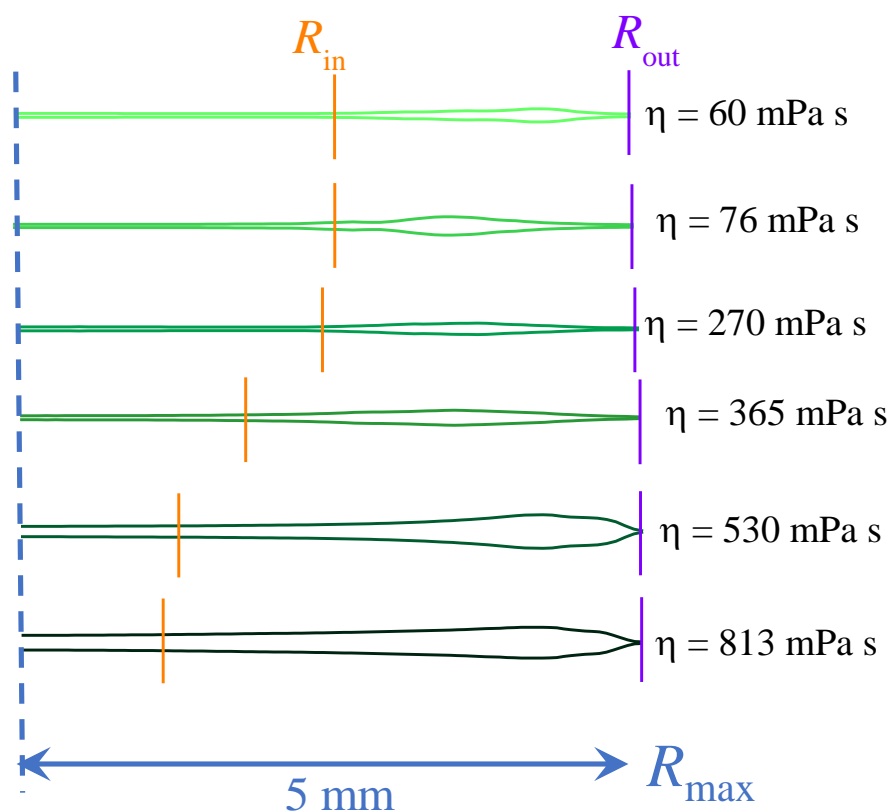


Figure 6.11: Shape of the external part of the sheet (the last 5 mm) for the different samples at maximal expansion represented by plotting, on the vertical axis, $h(r, t_{\text{max}})/2$ and $-h(r, t_{\text{max}})/2$ with a same scale for the x and y-axis, so the shape is not deformed, as a function of r . The rim is delimited by R_{in} and R_{out} .

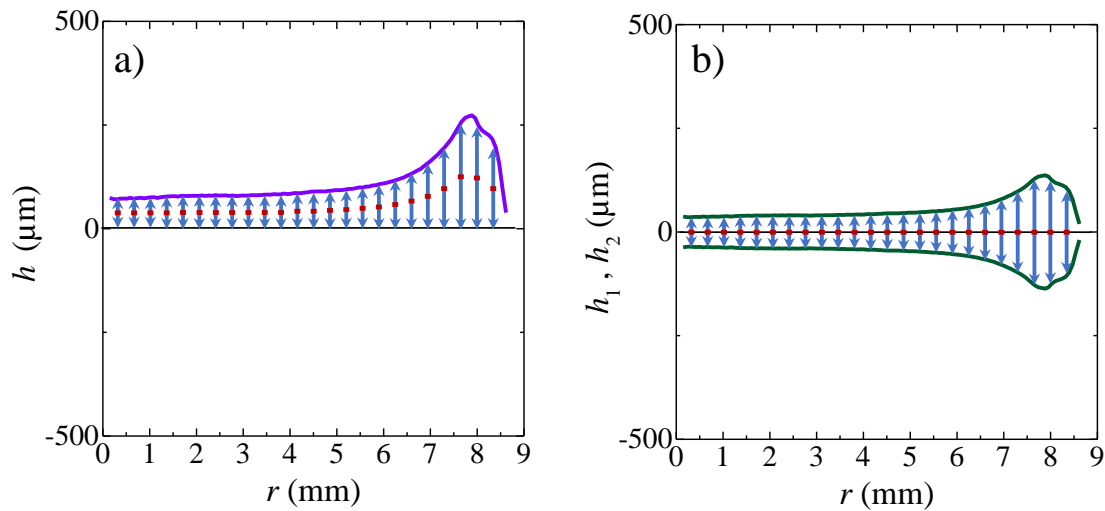


Figure 6.12: Schematic representation of the technique followed to obtain the cross-section of the rim in Figure 6.11. a) The thickness profile, $h(t)$, as measured by transmission. b) The real shape of the profile obtained by reflection with respect to the horizontal axis of $h(t)/2$.

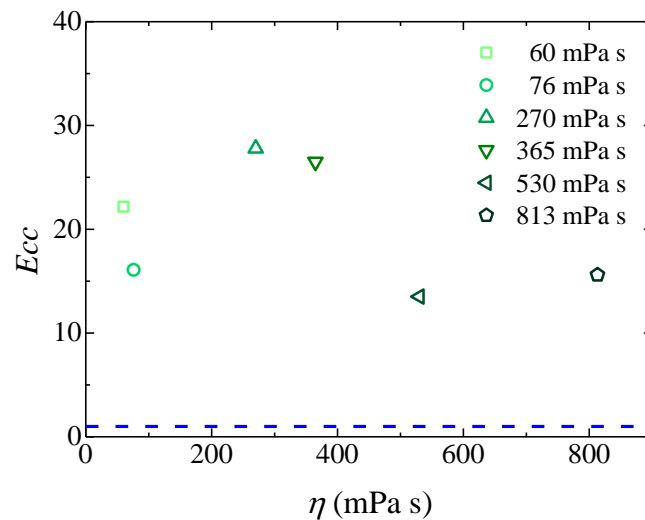


Figure 6.13: Eccentricity, $Ecc = (R_{\text{out}} - R_{\text{in}})/h(R_{\text{peak}})$, of the profiles shown in Figure 6.2 as a function of the shear viscosity, η . The dashed line marks the expectation for a circular cross-section.

Here, we are interested in the time evolution of the volume of the rim. We consider the volume of the fluid accumulating in the rim, thus, we take into account the ligaments and small instabilities.

An important side of our analysis is that we have access to a more accurate measurement

of the rim volume since we measure the thickness profile and there is no need to assimilate the rim to a torus of revolution. The volume of the rim reads

$$V_{\text{rim}}(t) = \int_{R_{\text{in}}(t)}^{R_{\text{out}}(t)} 2\pi r h(r, t) dr \quad (6.3)$$

where R_{in} , the radius of the inner side of the rim, and R_{out} , the radius of the outer side of the rim, are both determined according to section 2.1.4.3. Doing so, we assume that the rim is a toroid of revolution (and not a torus). This assumption is fully justified by the good circularity of the shape of the sheets (see figure 6.1).

Figure 6.14 shows the volume of the rim, V_{rim} , normalized by the volume of the sheet, V_{sheet} (Eq. 6.1) as a function of time normalized by the collision time, $t_{\text{col}} = \frac{d_0}{v_0}$. The volume increases linearly with time. Interestingly, the intercept that would result from the prolongation of the data to $t/t_{\text{col}} = 0$ following a straight line (shown in the inset of Figure 6.14) seems to differ for the samples of high viscosity ($\eta > 365$ mPa s). Note that, for the very viscous samples, the rim tends to appear at larger times explaining why there is no data at $t/t_{\text{col}} < 3$. The slope, b , is the dimensionless filling rate of the rim, which is reported in Figure 6.15 for all samples as a function of the biaxial extensional Ohnesorge number, $\text{Oh}_B = \frac{\eta_B}{\sqrt{\rho\gamma d_0}}$.

The slope, b , corresponds to the non-dimensional filling rate of the rim. This filling rate is constant with time for each sample and depends weakly on the viscosity. This observation is confirmed by the weak slope of the regression line fitting the data for the non-dimensional filling rate, b , as a function of Oh_B represented by a blue line in Figure 6.15. Note that, to make sure that this result is reliable, the same analysis was also done with $h'/h = 0.1$ and 0.2 as criterion to find R_{in} . The slopes, b , obtained using the different criteria, are very similar at low viscosity. They are slightly more sensitive to the criterion at high viscosity, as evidenced by the large error bars. Nevertheless, the values for the linear fit of $b(\text{Oh}_B)$ round up to the same values with the three criteria. This confirms that the arbitrary criterion of $h'/h = 0.15$ does not affect our conclusions. b , the non-dimensional filling rate, varies linearly with Oh_B :

$$b = \frac{1}{V_{\text{sheet}}} \frac{dV_{\text{rim}}}{dt} t_{\text{col}} = C_1 + C_2 \text{Oh}_B \quad (6.4)$$

with t_{col} , the collision time. From the fit (Figure 6.15), $C_1 = 0.06 \pm 0.004$ and $C_2 = 0.006 \pm 0.0008$. There is a very weak dependence of the filling rate with Oh_B . Oh_B varies by a factor 10 while the filling rate varies by a factor 2.

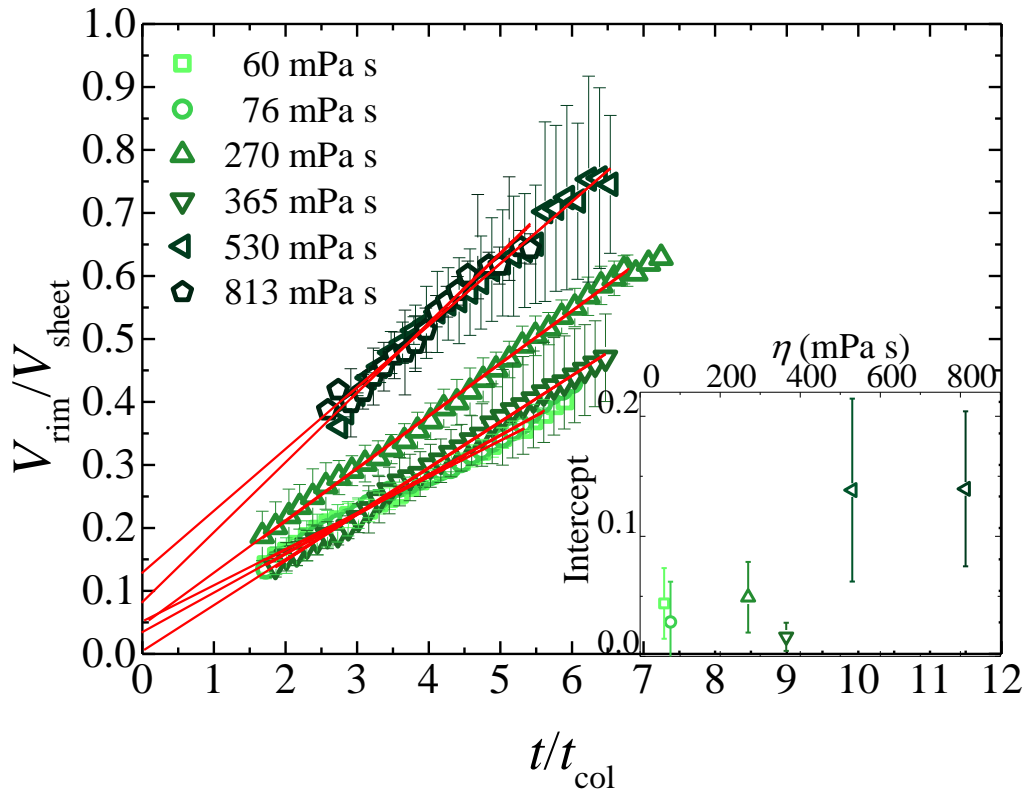


Figure 6.14: Volume of the rim, V_{rim} , normalized by the sheet volume, V_{sheet} , as a function of the normalized time t/t_{col} . The red lines are the linear fits. The inset shows the intercept of the linear fit as a function of the shear viscosity. Error bars come from the average for three distinct impact experiments.

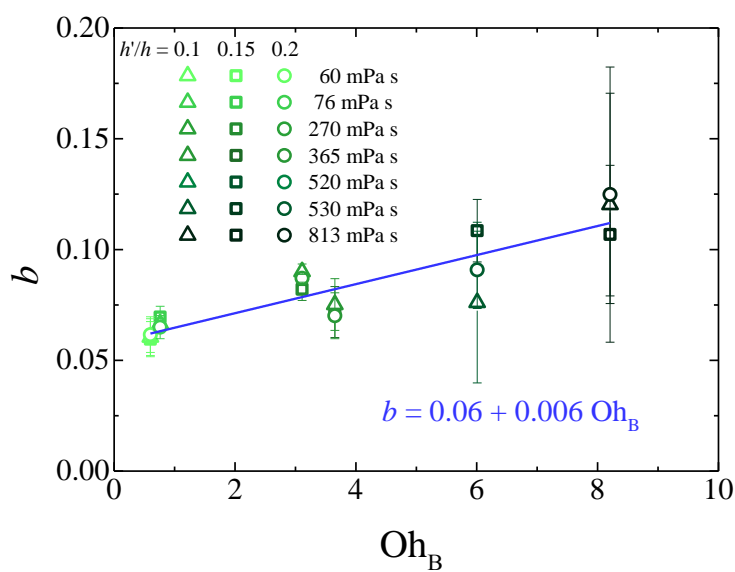


Figure 6.15: Slope of the evolution of the normalized rim volume, $V_{\text{rim}}/V_{\text{sheet}}$, with the reduced time, t/t_{col} , as a function of the biaxial extensional Ohnesorge number, Oh_B . Error bars come from the average for three distinct impact experiments. The blue line is the best linear fit of the experimental data.

6.4 Theoretical considerations

In this section, we build a theoretical model for the filling velocity of the rim based on momentum conservation and access the experimental filling velocity of the rim using mass conservation arguments. We compare the filling rate to what we have found experimentally. We, moreover, find a criterion for the time of emergence of a rim.

6.4.1 Filling velocity of the rim

From our experimental observations, we consider, at a time t , a part of the rim assimilated to a toroid of revolution with a cross-section, S_{rim} , connected to the liquid sheet of radius R as represented in Figure 6.16. The thickness of the sheet at the entrance of the rim is e . The liquid in the sheet feeds the rim with a local velocity, v_{fill} .

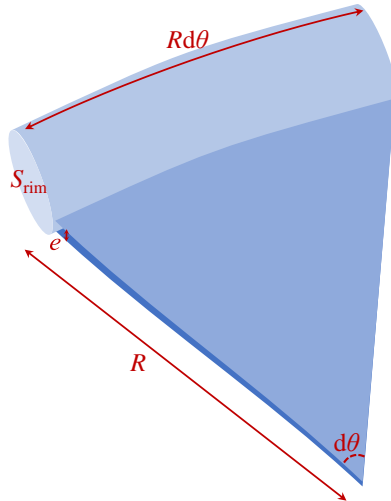


Figure 6.16: Schematic representation of a portion of the sheet with its rim of cross-section S_{rim} .

We write the stress tensor in the sheet

$$\begin{cases} \sigma_{rr} = -p + 2\eta \frac{R\dot{R}}{r^2} \\ \sigma_{\theta\theta} = -p + 2\eta \frac{R\dot{R}}{r^2} \\ \sigma_{zz} = -p - 4\eta \frac{R\dot{R}}{r^2} \end{cases}$$

With η , the shear viscosity, r , the radial position in the sheet plane R the radius of the sheet and p , the pressure in the film, which is equal to $-4\eta \frac{R\dot{R}}{r^2}$ due to the absence of axial stress at the film surface. Hence

$$\begin{cases} \sigma_{rr} = 6\eta \frac{R\dot{R}}{r^2} \\ \sigma_{\theta\theta} = 6\eta \frac{R\dot{R}}{r^2} \\ \sigma_{zz} = 0 \end{cases}$$

We consider the momentum balance in the Galilean reference frame of the laboratory for the portion of the rim.

$$\frac{d(m\dot{R})}{dt} = \dot{R}\dot{m} + m\ddot{R} = \dot{m}u - 2\gamma R d\theta + R d\theta e \sigma_{rr}(R) \quad (6.5)$$

With $m = \rho S_{\text{rim}} R d\theta$, the mass of the portion of the rim, u , the Eulerian radial velocity of the liquid in the sheet at $R(t)$ and \dot{R} , the expansion velocity of the sheet. The left hand-side of Equation 6.5 is the rate of change of the rim momentum and the right hand-side regroups the forces acting on the rim: the first being the inertial forces of the fluid, the second being caused by surface tension and the third by the viscous forces. Using the local mass conservation, $\dot{m} = e(u - \dot{R}) \rho R d\theta$, and $\sigma_{rr}(R) = 6\eta \frac{\dot{R}}{R}$ equation 6.5 reads

$$\dot{R}e(u - \dot{R}) \rho R d\theta + \rho S_{\text{rim}} R d\theta \ddot{R} = \rho e R d\theta (u - \dot{R})u - 2\gamma R d\theta + 6R d\theta e \eta \frac{\dot{R}}{R} \quad (6.6)$$

Equation 6.6 simplifies as

$$e\rho(u - \dot{R})\dot{R} - e\rho(u - \dot{R})u = -2\gamma + 6e\eta \frac{\dot{R}}{R} - \rho S_{\text{rim}} \ddot{R} \quad (6.7)$$

Which, after some simple mathematical operations, reads

$$v_{\text{fill}} = \sqrt{\frac{2\gamma}{e\rho} - \frac{6\eta}{\rho} \frac{\dot{R}}{R} + \frac{V_{\text{rim}}}{2e\pi R} \ddot{R}} \quad (6.8)$$

With $V_{\text{rim}} = 2\pi S_{\text{rim}} R$ and $v_{\text{fill}} = u - \dot{R}$, the filling velocity of the rim. We thus obtain a theoretical expression for the filling velocity at a time t . In this expression, the effects of capillarity, viscosity and inertia are decoupled.

Interestingly, when the effects of viscosity and inertia are negligible, we obtain the well known classical Culick velocity, $v_{\text{Culick}} = \sqrt{\frac{2\gamma}{\rho e}}$, usually used to describe the formation of a propagating growing rim at the edge of an opening surface by balancing the capillary force applied to the rim with the inertial force of the flow entering the rim [Taylor 1959, Culick 1960, Yarin 2017].

Equation 6.8 depends on R , \dot{R} and \ddot{R} . These three quantities are plotted for the sample of viscosity $\eta = 270$ mPa s in Figure 6.17 as a function of time. The acceleration of the sheet, \ddot{R} , is a negative quantity whose value is between -20 and -80 time the gravity.

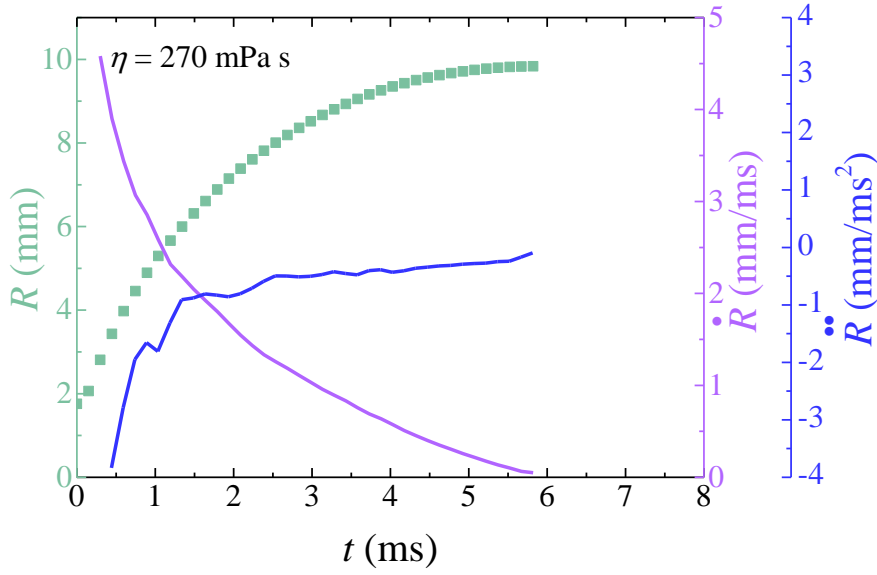


Figure 6.17: Time evolution of R , \dot{R} and \ddot{R} for sample of high viscosity ($\eta = 270$ mPa s).

Because \ddot{R} is negative while R and \dot{R} are strictly positive, v_{fill} defined by Equation 6.8 only exists when the absolute value of the first term, $|2\gamma/e\rho|$, is larger than the absolute value of the sum of the second and third terms, $-\frac{6\eta}{\rho}\frac{\dot{R}}{R}$ and $\frac{V_{\text{rim}}}{2e\pi R}\ddot{R}$. These terms which are respectively the contributions from capillarity, viscosity and inertia to v_{fill} are represented in Figure 6.18 as a function of time. We can see that in our situation, the effect of the viscous forces on the filling velocity is negligible at higher times. The contributions from the viscous forces are plotted for all samples in Figure 6.19. This contribution is larger for viscous samples as compared to samples of low viscosity at short times but this contribution decreases with time and vanishes at larger times for all samples. The inertial forces, however, are important contrarily to what is usually claimed in the literature [Villermaux 2011]. The contribution from the inertial forces is always smaller than the contribution from capillarity but both are, nevertheless, of the same order of magnitude.

To experimentally measure the filling velocity, we have to provide a relationship with experimentally accessible quantities. We write the mass conservation at times t and $t + dt$.

$$R(t)\rho v_{\text{fill}}(t)e(t)d\theta dt = [R(t + dt)S_{\text{rim}}(t + dt) - R(t)S_{\text{rim}}(t)]\rho d\theta \quad (6.9)$$

Neglecting the second order term in dt , the filling velocity then reads

$$v_{\text{fill}}(t) \approx \frac{1}{e(t)} \left[\dot{S}_{\text{rim}}(t) + \frac{\dot{R}(t)}{R(t)} S_{\text{rim}}(t) \right] \quad (6.10)$$

Using the time variation of the torus volume, $\frac{dV_{\text{rim}}(t)}{dt} = 2\pi \left(\dot{S}_{\text{rim}}(t)R(t) + S_{\text{rim}}(t)\dot{R}(t) \right)$, the filling velocity of the rim, $v_{\text{fill}}(t)$, can be reformulated as

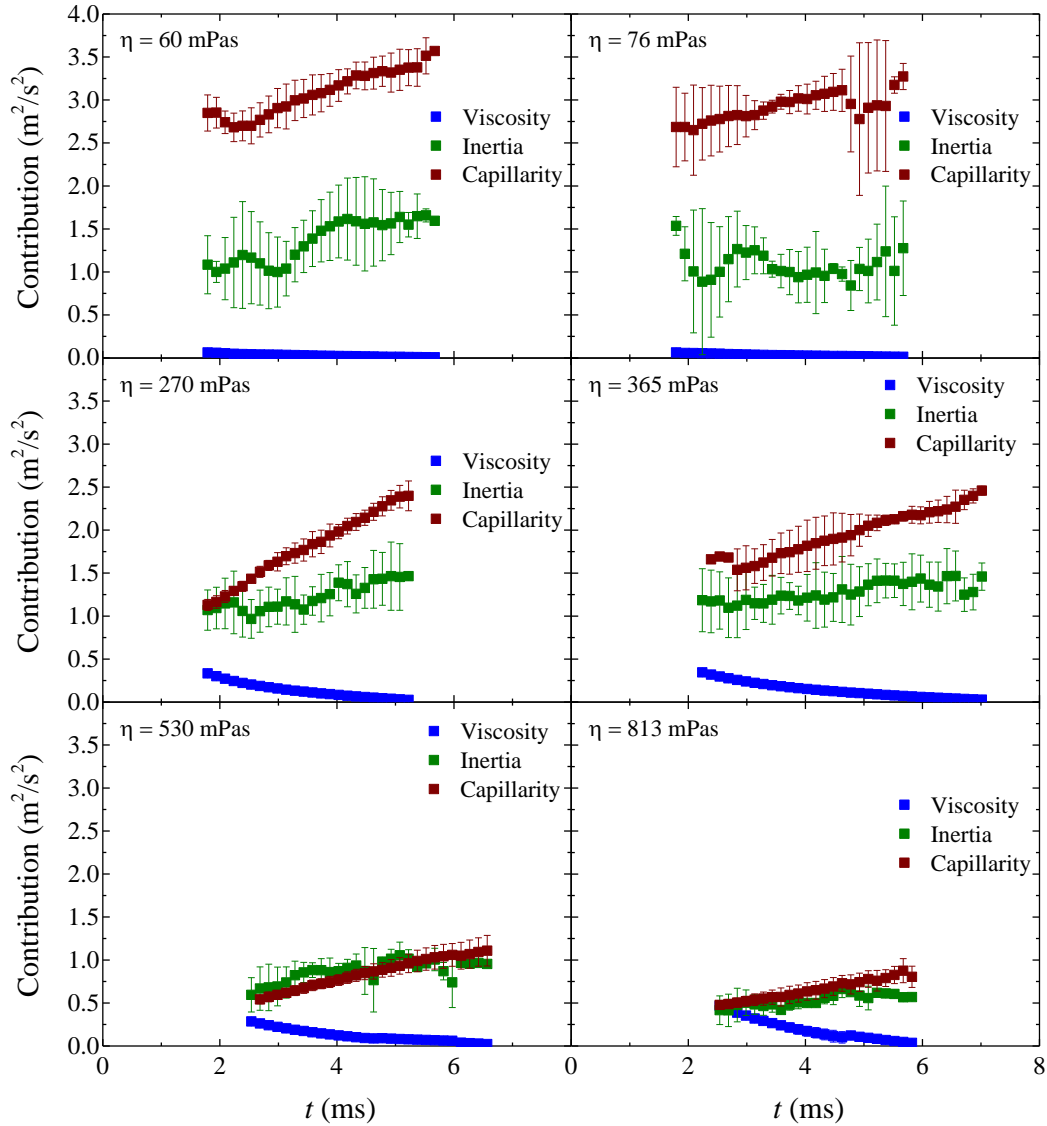


Figure 6.18: Contributions from capillarity, $|2\gamma/e\rho|$, viscosity, $|\frac{6\eta}{\rho}\frac{\dot{R}}{R}|$, and inertia, $|\frac{V_{\text{rim}}}{2e\pi R}\ddot{R}|$, to v_{fill} as a function of time for glycerol/water samples of different viscosity as indicated on the graphs. The error bars result from the average of three distinct experiments.

$$v_{\text{fill}}(t) = \frac{1}{2e(t)\pi R(t)} \frac{dV_{\text{rim}}(t)}{dt} \quad (6.11)$$

v_{fill} can thus be experimentally evaluated. In Figure 6.20, we compare the experimental values for v_{fill} , as measured using Equation 6.11 and averaged over time, to the theoretical expectations and Culick's velocity, v_{Culick} as a function of the viscosity.

$v_{\text{fill,exp}}$ is clearly weaker than Culick's velocity to which it is often approximated. This discrepancy is not due to the viscous forces as it is clear from Figure 6.18 that their

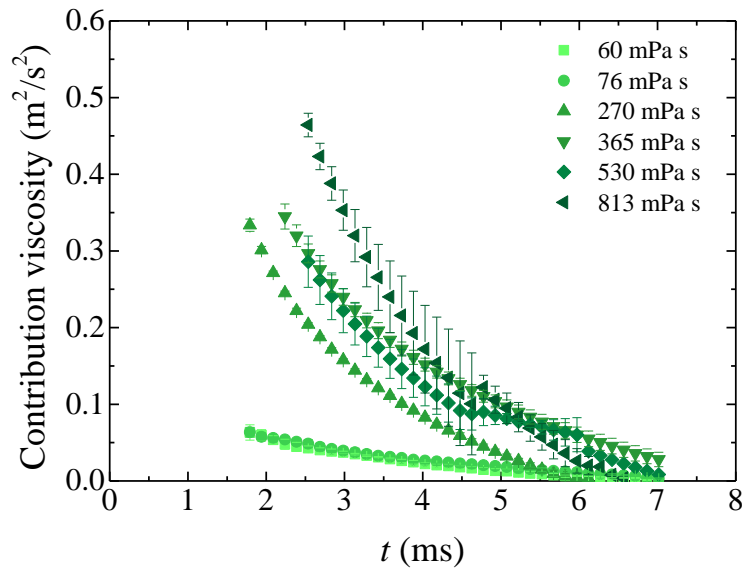


Figure 6.19: Contribution from viscosity, $|\frac{6\eta}{\rho} \frac{\dot{R}}{R}|$ to v_{fill} as a function of time for glycerol/water samples of different viscosity. The error bars result from the average of three distinct experiments.

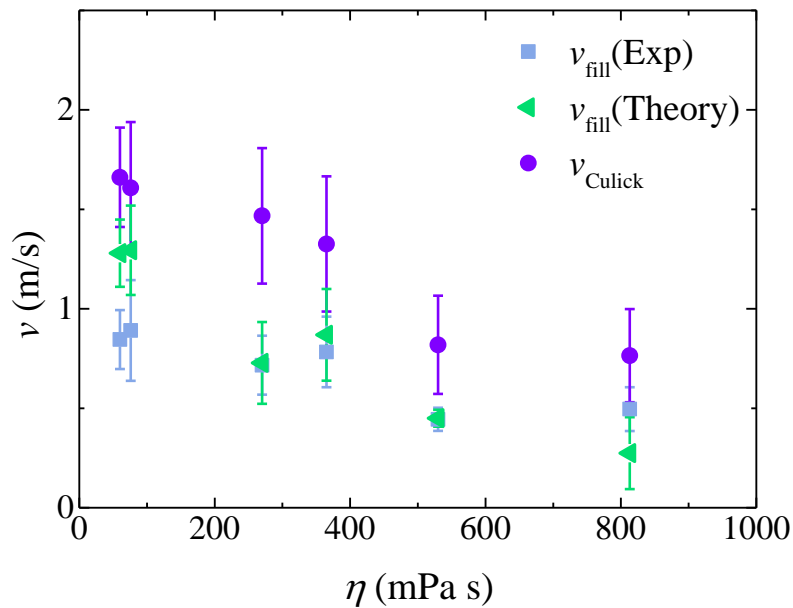


Figure 6.20: $v_{\text{fill,exp}}$, v_{fill} , and v_{Culick} as a function of viscosity. The error bars come from the average of three distinct experiments.

effect is negligible. The effect of viscosity on a growing rim was already considered by [Debrégeas 1995] who found that the hole after bursting of a very viscous suspended liquid film in the absence of any surfactant grows without forming a rim. However, these films

are also viscoelastic. Debregeas et al. believed this viscoelasticity to be responsible for the "instantaneous" uniform thickening of the film after bursting, which prevents the emergence of a rim. The effect of inertia which is often neglected, on the other hand, is not negligible for our experimental conditions. Indeed, the velocity predicted by equation 6.8 is in much better quantitative agreement with the experimental values, $v_{\text{fill,exp}}$. Thus, the slowing down of the sheet expansion as a non-negligible effect on the rim growth. Eventually, the different velocities decrease for increasing viscosity. [McEntee 1969] Found that the rim velocity decreases with increasing film thickness. This could explain why the filling velocity is lower for samples of higher viscosity as their e is larger.

6.4.2 Filling rate of the rim

In Figure 6.15, we show the filling rate of the rim as a function of viscosity. This latter does not have a very strong effect. Here, we want to quantitatively rationalize the effect of viscosity using the findings in section 6.4.1.

Thanks to the good agreement between experience and theory for the filling rate

$$\frac{1}{2e\pi R(t)} \frac{dV_{\text{rim}}(t)}{dt} \approx v_{\text{fill}} \quad (6.12)$$

At t_{max} , Equation 6.12 reads

$$\frac{1}{V_{\text{sheet}}} \frac{dV_{\text{rim}}(t_{\text{max}})}{dt} \approx \frac{2v_{\text{fill}}}{R_{\text{max}}} \quad (6.13)$$

with $V_{\text{sheet}} \approx \pi R_{\text{max}}^2 e(t_{\text{max}})$ and $R_{\text{max}} = R_{\text{max,inv}} \sqrt{1 - \alpha \text{Oh}_B}$ with $\alpha = 0.025 \pm 0.015$ for Newtonian fluids (cf. Chapter 3). Equation 6.13 then reads

$$\frac{1}{V_{\text{sheet}}} \frac{dV_{\text{rim}}(t)}{dt} \approx \frac{1}{t_{\text{col}}} \left(\frac{2v_{\text{fill}}d_0}{R_{\text{max,inv}}v_0} + \alpha \frac{v_{\text{fill}}d_0}{R_{\text{max,inv}}v_0} \text{Oh}_B \right) \quad (6.14)$$

where $C_1 = \frac{2v_{\text{fill}}d_0}{R_{\text{max,inv}}v_0}$ and $C_2 = \alpha \frac{v_{\text{fill}}d_0}{R_{\text{max,inv}}v_0}$. For the values of v_{fill} in Figure 6.20, we find $C_1 = 0.10 \pm 0.056$ and $C_2 = 0.001 \pm 6.10^{-4}$ which have the same order of magnitude as the values obtained experimentally in Figure 6.15 ($C_1 = 0.06$ and $C_2 = 0.006$).

The good agreement between the theoretical and experimental values of C_1 and C_2 confirms by another approach that our prediction for the filling velocity are in good quantitative agreement with the experiments. The filling rate is constant with time as the volume of the rim varies linearly with time and depend slightly on the viscosity. This dependence on viscosity of the filling rate even though we have seen that the filling velocity is not affected by viscosity is explained by the dependence of R_{max} on viscosity in the viscous regime.

6.4.3 Emergence of the rim

Before the rim appears, $V_{\text{rim}} = 0$. In that case, the filling velocity becomes

$$v_{\text{fill}} = \sqrt{\frac{2\gamma}{e\rho} - \frac{6\eta}{\rho} \frac{\dot{R}}{R}} \quad (6.15)$$

which rewrites

$$v_{\text{fill}} = v_{\text{Culick}} \sqrt{1 - 3\dot{\epsilon}t_\eta} \quad (6.16)$$

with $\dot{\epsilon} = \frac{\dot{R}}{R}$ the extensional rate and $t_\eta = \frac{e\eta}{\gamma}$ the viscous time. We thus obtain a first criterion for the apparition of the rim

$$3\dot{\epsilon}t_\eta < 1 \quad (6.17)$$

Indeed, for $3\dot{\epsilon}t_\eta > 1$, v_{fill} cannot exist and so does the rim. The apparition of the rim is also limited by the collision time, $t_{\text{col}} = \frac{d_0}{v_0}$, which corresponds to the time for a drop of initial diameter, d_0 , to travel its own distance when impacted at a velocity, v_0 . Thus, the second criterion is

$$t > t_{\text{col}} \quad (6.18)$$

On Figure 6.21, we plotted $3\dot{\epsilon}t_\eta$ as a function of time for three experiments for each glycerol/water mixtures. The symbols in red are $3\dot{\epsilon}t_\eta$ at times when there is not yet a rim. The experimental observations for the appearance of the rim respect quantitatively the criterion given by equation 6.17. Although the viscous forces do not play an important role in the filling velocity once the rim is formed, they are the ones which dictate when the rim will appear through the viscous time.

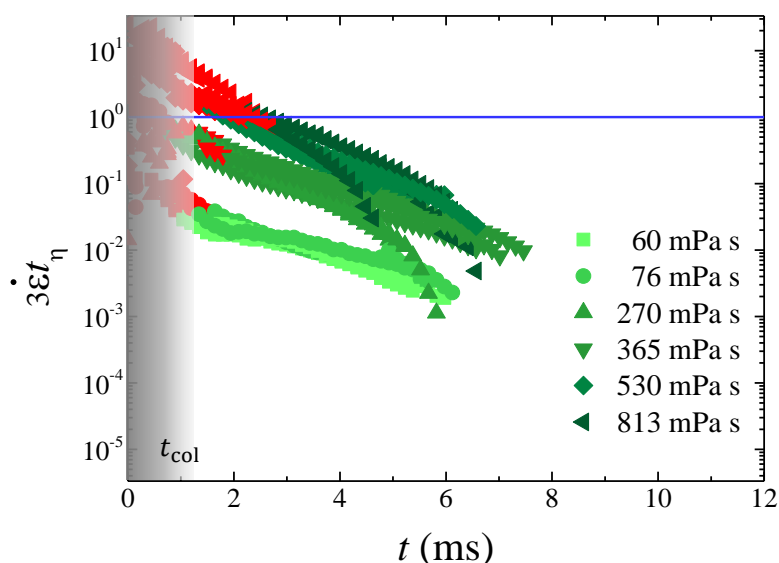


Figure 6.21: $3\dot{\varepsilon}t_\eta$ as a function of time for glycerol/water mixtures of different viscosity. Three distinct experiments are represented for each viscosity. Symbols in red are data before the detection of a rim and the gray area delimits the collision time.

6.5 Conclusion

In this chapter, we have measured the thickness field of expanding sheets of Newtonian fluids on a repellent surface and have quantitatively characterized the rim bounding the sheet. For the first time, to the best of our knowledge, we provide direct observation of the shape of the rim bounding an expanding sheet. We show that the shape of the rim cross-section is very far from the circular one usually assumed. We measure the filling rate and velocity and find intriguing results that were not expected based on previous works from the literature. We show clearly that the filling velocity of the rim is significantly lower than Culick's velocity, which is generally used to describe the growth of a rim bordering a free liquid sheet. The difference between these two velocities takes its origin in the effect of the inertial forces, which are neglected in the standard Culick-like approach. We include the deceleration of the sheet in our prediction and obtain good quantitative agreements with the experimentally measured filling velocity. As soon as there is a rim, the contribution of viscosity is negligible. Nevertheless, the rim was observed to appear later for fluids of higher viscosity. In good agreement with our findings, we found a criterion dictating the apparition of the rim, which depends on the viscous time. Finally, we have been able to measure and rationalize the filling rate of the rim of viscous sheets.

Spinning elastic beads: a route for simultaneous measurements of the shear modulus and the interfacial energy of soft materials

In this chapter, we report the paper *Spinning elastic beads: a route for simultaneous measurements of the shear modulus and the interfacial energy of soft materials*, A. Carbonaro*, K.-N. Chagua-Encarnacion*, C.-A. Charles*, T. Phou, C. Ligoure, S. Mora and D. Truzolillo, *Soft Matter*, 16 (36), 8412-8421, 2020, where the bulk elastic response and the contribution from the surface tension to the deformation of an elastic beads under rotation in a spinning drop tensiometer are fully decoupled and predicted. In this paper, we also show that the surface tension and surface stress are the same in the case of soft hydrogels.

* These three authors have contributed equally to this work.



Cite this: *Soft Matter*, 2020,
16, 8412

Spinning elastic beads: a route for simultaneous measurements of the shear modulus and the interfacial energy of soft materials

Alessandro Carbonaro,^{†a} Kennedy-Nexon Chagua-Encarnacion,^{†a}
Carole-Ann Charles,^{†a} Ty Phou,^a Christian Ligoure,^{id}*^a Serge Mora^{id}*^b and
Domenico Truzzolillo^{id}*^a

Large deformations of soft elastic beads spinning at high angular velocity in a denser background fluid are investigated theoretically, numerically, and experimentally using millimeter-size polyacrylamide hydrogel particles introduced in a spinning drop tensiometer. We determine the equilibrium shapes of the beads from the competition between the centrifugal force and the restoring elastic and surface forces. Considering the beads as neo-Hookean up to large deformations, we show that their elastic modulus and interfacial energy constant can be simultaneously deduced from their equilibrium shape. Also, our results provide further support to the scenario in which interfacial energy and interfacial tension coincide for amorphous polymer gels.

Received 2nd June 2020,
Accepted 5th August 2020

DOI: 10.1039/d0sm01024c

rsc.li/soft-matter-journal

1 Introduction

When subjected to external loads, elastic bodies change their shape due to the interplay between the applied load and the restoring forces of the material the body is made of.^{1,2} Below the elastic limit, these are the bulk elastic forces following the material-specific stress–strain relation, and the surface forces dictated by the interfacial free energy that characterizes the interaction with the surrounding medium. Since the subtle balance between these forces stays relevant even beyond the elastic limit and determines, together with the onset of plastic events, the occurrence of material failure and permanent deformation,³ bulk and surface stresses turn out to drive the behavior of soft materials under many circumstances.^{1–3} For this reason understanding the importance of these two contributions to material response is of paramount importance.

The impact of interfacial stresses on the equilibrium shape of elastic materials can be readily quantified by the elasto-capillary length ℓ , defined as the ratio of the interfacial energy per unit area Γ to the shear modulus G_0 of the body under consideration. When ℓ is comparable with or larger than other characteristic lengths of the system^{4–6} interfacial stresses must

be taken into account to compute stationary material shapes and to predict possibly the onset of instabilities.^{7–9} This is the case for soft elastic samples with small geometric features. For example, for a hydrogel with shear modulus $G_0 \sim 30$ Pa and interfacial tension $\Gamma \sim 30$ mN m⁻¹, the elasto-capillary length is $\ell = 1$ mm. Therefore, the equilibrium shapes of millimetric and submillimetric elastic particles must be necessarily affected by the interfacial contribution to their total energy.

Despite of this general and well-grounded consideration, many important questions concerning the interplay between bulk and interfacial stresses^{10,11} and the very nature of the latter in amorphous solids^{12,13} remain unanswered. For a generic material immersed in a background medium interfacial energy is the energy required to create a unit area of new surface by a division process, whereas interfacial tension is the surface stress associated with its deformation. For Newtonian liquids, interfacial tension and interfacial energy are two strictly equal quantities since, when a liquid interface is deformed, the distances between the molecules at the interface are not affected by the imposed deformation as molecules can move freely from the bulk to the liquid boundaries. It is generally not so for a solid, for which interfacial energy may depend on the surface area, as first pointed out by Shuttleworth¹⁴ in his pioneering work. Since a solid surface consists of a constant number of atoms, the work done to alter the separation distance between atoms at their surface is expected to depend on this distance itself.^{14–16} As a result, the work required to deform a material is not necessarily the same as the thermodynamic work required to create a new surface. For crystals the problem has been solved^{16,17} since their

^a Laboratoire Charles Coulomb, Université de Montpellier and CNRS,
F-34095 Montpellier, France. E-mail: christian.ligoure@umontpellier.fr,
domenico.truzzolillo@umontpellier.fr

^b Laboratoire de Mécanique et Génie Civil, Université de Montpellier and CNRS,
F-34090 Montpellier, France. E-mail: serge.mora@umontpellier.fr

[†] These three authors contributed equally.

Paper

surface free energy is a function of the surface area itself and hence it is expected to be different from the surface tension. However, for amorphous materials, like cross-linked elastomers, the issue remains unresolved because the molecules have local mobility allowing them, at least in principle, to show liquid-like behavior: the surface reforms in response to external stimuli.^{18,19} While this liquid-like scenario has been recently confirmed for Polydimethylsiloxane (PDMS) elastomers,¹² other experimental works pointed out that for specific soft gels^{13,20,21} the interfacial energy does depend on the surface area, or equivalently on the imposed compressive strain parallel to the surface, and, as a consequence, interfacial free energy and interfacial stress are expected to differ.^{14,20,21}

Moreover, for most solid materials the accurate measurement of the interfacial energy is experimentally challenging, since the intimate coupling between the contributions of interfacial and bulk energies hampers the detection of effects solely due to interfacial stresses. For instance instability thresholds^{5,22} and the shapes taken by softened wedges^{23–25} or ripple deformations²⁶ involve the coupling between surface stress and bulk elasticity through the elasto-capillary length, making impossible to determine separately the two parameters (G_0 and Γ). Even if one of the two parameters, *e.g.* the shear modulus, were determined elsewhere, a measurement relying on a single experiment is of limited accuracy. To solve this problem, indentation tests, standard rheometry or stretching tests, based on a gradual variation of an external load could in principle be used. However, these methods involve the presence of solid–solid contact forces^{27,28} that typically affect the measurement and give rise to issues like slip and edge fracture. Furthermore, in the case of ultrasoft gels the measurement of the elastic modulus through these techniques is even more troublesome since one would be confronted with issues related to insufficient instrumental accuracy.

For these reasons, unveiling effects of surface energy in soft solids remains arduous and it has not been possible to converge to any conclusive result. This motivates investigations of phenomena that originate from a non-negligible contribution of interfacial free energy in the absence of solid–solid contacts over a wide range of strains, while, at the same time, engineering strategies to fully decouple interfacial and bulk stresses would be highly desirable.

In this paper, we tackle this challenging task and report on a theoretical and numerical study of the deformation of soft neo-Hookean beads when they are immersed and spun in a denser background fluid. Strikingly we found that, if the interfacial energy of the beads does not depend on their deformation, the elastic and the interfacial contributions determining the bead shape can be decoupled when the strong deformation limit is reached, namely when the ratio between the two principal axis of the deformed particles is $d_{\max}/d_{\min} \gtrsim 2$. To check further the reliability of our results we have investigated the deformation of soft polyacrylamide beads immersed in a denser immiscible fluid and spun in the capillary of a commercial spinning drop tensiometer (SDT).

Though an SDT is usually employed to measure low liquid–liquid interfacial free energies,^{29–31} recently it has been used

also for purposes ranging from the study of the relaxation dynamics of liquid drops³² and the presence of an effective interfacial tension in miscible fluids,^{32–35} to the characterization of the mechanical properties of thin elastic capsules³⁶ and viscoelastic properties of polymer melts.^{37,38}

Unlike the aforementioned works, here we use an SDT to investigate the equilibrium shapes of full elastic beads with a radius of the order of one millimeter and shear modulus of the order of 10 Pa,¹⁰ for which we expect important elasto-capillary effects. The analysis proposed in this work has been developed specifically for homogeneous beads and is far different from previous attempts to adapt spinning drop tensiometry measurements to elastic and viscoelastic bodies.^{36–38}

When the SDT capillary is spun around its axis at a prescribed angular velocity, and once a steady state is reached, the beads spin solidly with the background fluid and the capillary itself. Since the surrounding fluid is denser than the bead, the centrifugal forces center and stretch the bead on the axis of rotation (Fig. 1). In this geometry, the sample bead is entirely surrounded by a liquid without any contact with other solid bodies. This is an important benefit of this geometry as the only interfacial free energy to be considered is the solid–liquid one. In addition, the external load (*i.e.* the centrifugal forces) can be finely tuned up to values generating large deformations ($\gtrsim 500\%$) of the bead.

The remainder of this paper is organized as follows. Assuming an interfacial energy independent from the deformation, the base equations governing the equilibrium of a spinning elastic bead surrounded by a liquid spinning at the same angular velocity are derived in Section IIA. These equations are first solved by assuming a homogeneous (biaxial) deformation of the bead (Section IIB). It is shown that, within this approximation, the effects on the deformation due to the contributions of the interfacial free energy and bulk elasticity can be decoupled at high centrifugal forcing. A full resolution of the base equations is made in Section IIC using the Finite Element method, showing the limitation of the biaxial approximation for a quantitative analysis. Interestingly, the behaviour emerging from the approximation still holds, providing a way to access to both the elastic

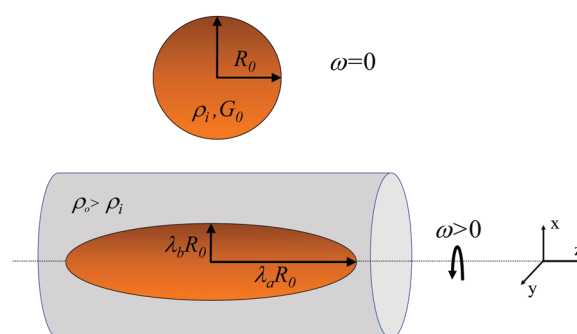


Fig. 1 Sketch of a spherical elastic bead immersed in a liquid of higher mass density and deformed by centrifugal forcing. (a) Initial configuration of the bead at rest ($\omega = 0$). (b) The elastic bead is spun solidly ($\omega > 0$) with a denser fluid, both being contained in a cylindrical capillary. Centrifugal forces give rise to the reversible deformation of the bead and stabilize its position on the capillary axis.

modulus and the interfacial free energy constant of the beads. In Section III we report on experiments carried out with a commercial spinning drop tensiometer and soft polyacrylamide beads. A discussion of the main results and a comparison with the expected values for G_0 and Γ follows. Our experimental results point out that, for acrylamide gels, the interfacial energy is strain-independent and hence that the Shuttleworth effect is absent.¹⁴ Such a conclusion has been further tested by comparing the interfacial energy of the beads and the interfacial tension measured between the background fluid and a non-crosslinked liquid polyacrylamide solution. The agreement between these two values further corroborates a scenario in which bulk elasticity does not contribute significantly to interfacial stresses. Finally, in Section IV we make some concluding remarks and summarize the key results of this work.

II Theory

A. Equilibrium equations at finite strains

The non-linear equations governing the equilibrium (steady) configuration of a rotating elastic sphere are derived considering a positive constant interfacial energy and an isotropic and incompressible neo-Hookean constitutive law. The latter is known to describe well the mechanical properties of soft polyacrylamide gels for strains up to several hundred percent.^{39–41}

Let us consider an elastic bead of radius R_0 , shear modulus G_0 and density ρ_i immersed in an infinite Newtonian background fluid of density $\rho_o > \rho_i$. As the sphere is spun at angular velocity ω around one diameter (aligned along axis z), the bead deforms, stretching along the rotation axis to minimize its rotational energy. In the co-rotating frame the elastic force, the surface force and the centrifugal force are conservative. The equilibrium can therefore be derived from the condition that the total potential energy is minimum. The position \mathbf{R} of a material point in the deformed configuration is given as a map $\mathbf{R}(\mathbf{r})$ in terms of the position \mathbf{r} in the undeformed configuration. For an isotropic and incompressible neo-Hookean solid, the strain energy density is:

$$W_{el} = \frac{G_0}{2} \text{tr}(\mathbf{F}^T \cdot \mathbf{F} - \mathbf{1}), \quad (1)$$

where $\mathbf{F} = \partial \mathbf{R} / \partial \mathbf{r}$ is the deformation gradient and $\mathbf{1}$ the unit matrix. The equilibrium is governed by the minimization of the free energy

$$\mathcal{E} = \Gamma A + \int_{\Omega_0} W_{el} dV_0 + \int_{\Omega_0} \frac{1}{2} \Delta \rho \omega^2 R^2 dV_0, \quad (2)$$

where R is the radial distance from the z -axis in the deformed configuration ($R = \mathbf{R} \cdot \mathbf{R} - \mathbf{R} \cdot \mathbf{e}_z$), dV_0 is a volume element in the reference configuration, Ω_0 is the volume occupied by the bead, A is the area of the deformed boundary and $\Delta \rho = \rho_o - \rho_i$ is the mass density contrast. It's worth stressing that we assume Γ independent of the deformation and the first term on the right hand side of eqn (2), $\mathcal{E}_T = \Gamma A$, represents the total interfacial energy of the system. This assumption, consistent with previous findings on elastic capsules^{42,43} and equivalent to the absence of a

Shuttleworth effect,¹⁴ will be discussed in the light of the results reported in Section III. The second and the third terms are respectively the elastic and the centrifugal energies,⁴⁴ called later \mathcal{E}_e and \mathcal{E}_ω . The equilibrium is governed by the minimization of the free energy, taking into account incompressibility of the elastic material which amounts to impose that the Jacobian of the transformation is equal to one:

$$\det \mathbf{F} = 1. \quad (3)$$

B. Biaxial approximation

1. General equations within the biaxial approximation.

To a first approximation, the problem is simplified by assuming a homogeneous and biaxial deformation of the bead. In the Cartesian coordinate system (x, y, z) , the applied centrifugal forcing gives rise to a prolate ellipsoid with axes $X = \lambda_b x$, $Y = \lambda_b y$ and $Z = \lambda_a z$. The stretch ratios λ_a and λ_b are two strictly positive constants with $\lambda_b < 1$ and $\lambda_a > 1$. This is sketched in Fig. 1. Eqn (3) further imposes $\lambda_a \lambda_b^2 = 1$. For a neo-Hookean material, the strain energy density is $W_{el} = \frac{1}{2} G_0 (\lambda_a^2 + 2\lambda_b^2 - 3)$ and the elastic energy defined in eqn (2) reads:

$$\mathcal{E}_e = \frac{4}{3} \pi R_0^3 \frac{1}{2} G_0 (\lambda_a^2 + 2\lambda_b^2 - 3). \quad (4)$$

The total interfacial energy defined in eqn (2), is:

$$\mathcal{E}_T = \Gamma A = \Gamma \left[2\pi \lambda_b^2 R_0^2 + \frac{2\pi \lambda_a \lambda_b R_0^2}{e} \arcsin(e) \right], \quad (5)$$

where $e = \frac{\sqrt{\lambda_a^2 - \lambda_b^2}}{\lambda_a}$ is the eccentricity of the ellipsoid of revolution. Finally the centrifugal energy, also defined in eqn (2) is given by:

$$\mathcal{E}_\omega = \frac{1}{2} \int \Delta \rho (x^2 + y^2) \omega^2 dV_0 = \frac{4\pi}{15} \Delta \rho \omega^2 \lambda_b^2 R_0^5. \quad (6)$$

Using volume conservation, eqn (4)–(6) allow us writing the total reduced energy density, defined as $\varepsilon = \mathcal{E} / (G_0 V_0)$ with V_0 the volume of the bead, as:

$$\varepsilon = \frac{\alpha}{5} \lambda_a^{-1} + \frac{1}{2} (\lambda_a^2 + 2\lambda_a^{-1} - 3) + \frac{3\beta}{2} \left(\lambda_a^{-1} + \frac{\lambda_a^2}{\sqrt{\lambda_a^3 - 1}} \arcsin \sqrt{\frac{\lambda_a^3 - 1}{\lambda_a^3}} \right), \quad (7)$$

with

$$\alpha = \frac{\Delta \rho R_0^2 \omega^2}{G_0} \quad (8)$$

and

$$\beta = \frac{\Gamma}{G_0 R_0} \quad (9)$$

being two characteristic dimensionless numbers. In particular, α is the Cauchy number and results from the balance between

Paper

inertia and elastic energy, while β is the ratio of the elasto-capillary length to the bead radius.

For a given set (α, β) , the equilibrium shape is given by the minimization of ε with respect to λ_a , *i.e.* by the solution of the nonlinear algebraic equation $\frac{d\varepsilon}{d\lambda_a} = 0$, which can be obtained numerically. The deformation parameter defined as the ratio of the length (d_{\max}) to the width (d_{\min}) of the deformed shape, or equivalently $\lambda_a^{3/2}$, obtained numerically by minimizing eqn (7), is plotted in Fig. 2. Hereafter we derive the analytical expression for the deformation parameter $\lambda_a^{3/2}$ in the two limiting cases of small and large deformations and we show that when the latter are attained a simultaneous measurement of the elastic modulus and the interfacial free energy is feasible.

2. Small deformation limit. Let us first elucidate the behavior of the stretch ratio λ_a in the weak deformation limit, corresponding to Cauchy numbers $\alpha \ll 1$. In this case we can safely write $\lambda_a = 1 + \xi$, with $0 < \xi \ll 1$ and approximate the reduced energy density as follows:

$$\varepsilon \simeq \frac{1}{5}\alpha + 3\beta - \frac{1}{5}\xi\alpha + \xi^2 \left(\frac{1}{5}\alpha + \frac{3}{2} + \frac{6}{5}\beta \right). \quad (10)$$

Minimizing with respect to ξ brings to the following equilibrium deformation with respect to the bead at rest:

$$\lambda_a^{3/2} - 1 \simeq \left[\frac{\alpha}{10 + 8\beta} \right]. \quad (11)$$

Eqn (11) cannot be used to determine separately G_0 and Γ from a single measurement of $\lambda_a^{3/2}$ as a function of ω , since the deformation cannot be expressed as the sum of two (or more) terms each containing only α or β separately.

3. Large deformation limit. For $\alpha \gg 1$ and $\lambda_a \gg 1$, eqn (7) can be approximated by the algebraic sum of three terms:

$$\varepsilon \simeq \frac{1}{2}\lambda_a^2 + \frac{3\pi}{4}\beta\lambda_a^{1/2} + \frac{\alpha}{5}\lambda_a^{-1}. \quad (12)$$

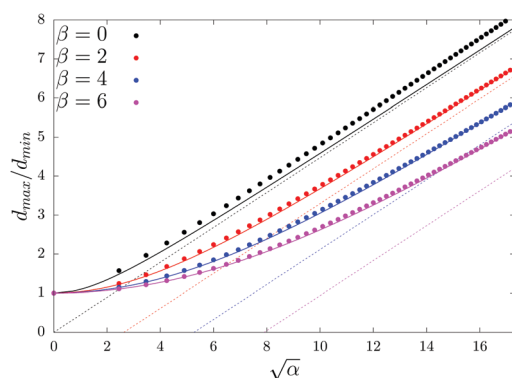


Fig. 2 Length-to-width ratio d_{\max}/d_{\min} of a deformed bead as a function of $\sqrt{\alpha}$ for different values of β (color coded). Solid lines are predictions from the biaxial approximation (minimization of eqn (7)). Asymptotes in the large α limit (eqn (14)) are plotted with dashed lines. Filled circles are the results of FE calculations discussed in Section II.C.

The minimization with respect to λ_a brings to:

$$d_{\max}/d_{\min} = \lambda_a^{3/2} = \frac{1}{2} \left[-\frac{3}{8}\pi\beta + \sqrt{\frac{9}{64}\pi^2\beta^2 + \frac{4}{5}\alpha} \right]. \quad (13)$$

Further expanding eqn (13) for $\alpha \gg 1$, we obtain:

$$d_{\max}/d_{\min} = \sqrt{\frac{\alpha}{5}} - \frac{3}{16}\pi\beta. \quad (14)$$

These asymptotes are plotted together with the complete expressions of d_{\max}/d_{\min} in Fig. 2 for different values of β . Note that due to the limited range of α , chosen accordingly with experiments introduced in Section III, the differences between the complete expression and the asymptotes remain significant and increases for increasing values of β . Quite interestingly eqn (14) decouples α and β , *i.e.* the effects of elasticity and interfacial energy on the bead deformation. In other words, for large centrifugal forcing, the deformation parameter $\lambda_a^{3/2}$ of a bead is proportional to the rotation speed with a proportionality constant equal to $R_0\sqrt{\frac{\Delta\rho}{G_0}}$. R_0 and $\Delta\rho$ being easily known a priori, G_0 can then be determined by considering the slope of $\lambda_a^{3/2}$ versus ω ; next, the evaluation of a (virtual) intercept equal to $-\frac{3\pi\Gamma}{16G_0R_0}$ brings to the measurement of Γ .

G_0 and Γ can then be recovered by considering the large deformation limit with the biaxial approximation. In the following, we show that the approximation is not accurate enough to get precise values of these two quantities. Notwithstanding this, the main result stays valid: it is possible to determine both G_0 and Γ by considering the large deformation limit of a spinning bead.

C. Resolution using the finite element method

This section is devoted to the minimization of eqn (2) with the incompressibility condition (eqn (3)), using the Finite Element (FE) method.

We seek the displacement $\mathbf{u} = \mathbf{R} - \mathbf{r}$ by minimizing the augmented energy (eqn (2)) with the constraint $\det\mathbf{F} = 1$. This last condition is ensured by adding to eqn (2) the supplementary term

$$\int_{\Omega_0} p(\det\mathbf{F} - 1)dV_0, \quad (15)$$

where p is a Lagrange multiplier to be computed together with \mathbf{u} . Because the solution is expected to be axially symmetric, the displacement vector is expressed in a cylindrical coordinate system as $\mathbf{u} = u_r(r,z)\mathbf{e}_r + u_z(r,z)\mathbf{e}_z$. For this two-dimensional problem in terms of r and z , the domain D we consider in the simulation is a disk of radius R_0 defined as $r^2 + z^2 < R_0^2$.

The FE formulation, implemented numerically using the FEniCS finite element library,⁴⁵ is here based on the research of the stationary points of the total energy functional given by eqn (2) with eqn (15). The displacement vector \mathbf{u} and the Lagrange multiplier p are discretized using Lagrange FEs on a

triangular mesh. The nonlinear problem in the (\mathbf{u}, p) variables is solved using a Newton algorithm based on a direct parallel solver (MUMPS,⁴⁶) by setting $G_0 = 1, R_0 = 1, \Gamma = \beta$ and $\Delta\rho\omega^2 = \alpha$.

Quasi-static simulations are computed by progressively increasing the interfacial free energy β up to the desired dimensionless value, then by progressively incrementing the load parameter α , recording the displacement field and the Lagrange multiplier, and reaching convergence at each step. The equilibrium shape of the deformed body are obtained for a large range of parameters α, β (see Fig. 2 and 3).

Fig. 3 shows that the strain energy density is inhomogeneous in the sample, whereas it was assumed to be homogeneous within the biaxial in Section II.B. In Fig. 2, the values of d_{\max}/d_{\min} calculated from the FE method and the biaxial approximation are compared. The biaxial approximation reproduces only qualitatively the deformation behaviour for small to moderate β (see Fig. 2 for $\beta = 0, 2$), converging quantitatively to the FE results only for larger values of β (e.g. $\beta = 4, 6$). Indeed, the biaxial approximation considers only the average deformation in the material instead of considering the local deformation, hence the observed discrepancies. This said, even if a quantitative analysis requires the use of the more precise FE calculation, the biaxial approximation provides a rigorous basis to understand bead deformation and the role played by interfacial stresses when elastic objects get deformed.

Inspired by the results obtained in the framework of the biaxial approximation (Section II.B), we focus on the large deformation limit. Our simulations still suggest that d_{\max}/d_{\min} behaves as

$$d_{\max}/d_{\min} \sim a\sqrt{\alpha} + b \quad (16)$$

in the large deformation limit for any tested value of β (Fig. 4), where a and b are two fitting parameters. Interestingly, the variations of b as a function of β are far more pronounced than

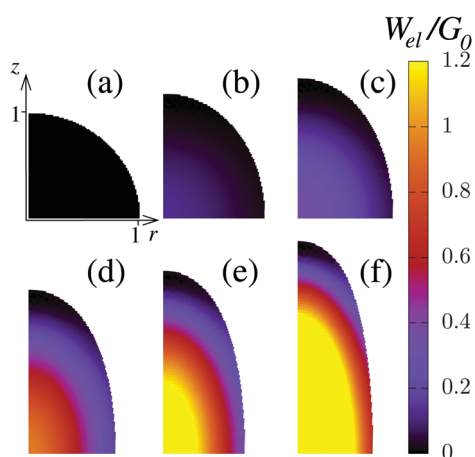


Fig. 3 Maps of the reduced strain energy density W_{el}/G_0 computed for $\beta = 1$ and different loads: $\alpha = 0$ (a), $\alpha = 5$ (b), $\alpha = 10$ (c), $\alpha = 20$ (d), $\alpha = 30$ (e) and $\alpha = 50$ (f). The corresponding values of d_{\max}/d_{\min} are respectively equal to 1 (a), 1.3 (b), 1.6 (c), 2.0 (d), 2.4 (e), 3.0 (f). Unit-length is chosen so that initial configuration (a) is a disk of radius $R_0 = 1$. By symmetry, a quarter of the system is enough to completely characterize the deformed configurations of the bead.

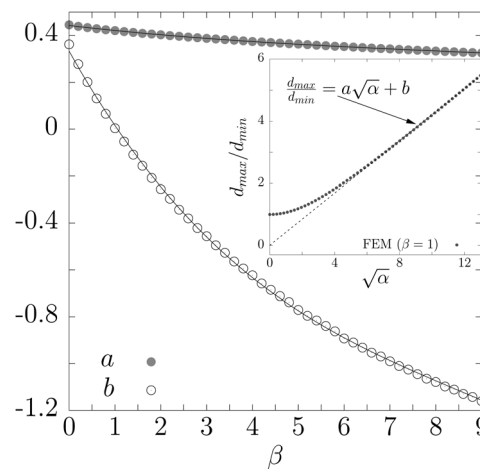


Fig. 4 $a(\beta)$ and $b(\beta)$ resulting from the fits of the large deformation limit of function $a\sqrt{\alpha} + b$ on d_{\max}/d_{\min} . The range for the fits is $d_{\max}/d_{\min} \in [2.5, 6]$, in accordance with the domain explored in experiments detailed in Section III. Solid lines result from fourth order polynomial fits for $a(\beta)$ and $b(\beta)$ (see Table 1). Inset: d_{\max}/d_{\min} calculated by the FE simulations as a function of $\sqrt{\alpha}$ for $\beta = 1$. d_{\max}/d_{\min} is well approximated by the linear equation $d_{\max}/d_{\min} = a\sqrt{\alpha} + b$ in the large deformations limit.

the variations of a , a result reminiscent with what was obtained in Section II.B (see eqn (14)).

Let us consider now experiments in which d_{\max}/d_{\min} has been measured as a function of ω . In the regime of large deformations, we expect from eqn (16) the deformed shape of the spinning bead to follow $d_{\max}/d_{\min} \sim A\omega + B$. This is indeed observed for our polyacrylamide millimetric particles (see Fig. 7 and Section III for more details). Hence A and B can be, in principle, experimentally determined. In the other hand, we know from the results of the FE simulations that:

$$d_{\max}/d_{\min} \sim a(\beta)\sqrt{\alpha} + b(\beta) = a(\beta)\sqrt{\frac{\Delta\rho}{G_0}}R_0\omega + b(\beta). \quad (17)$$

By identifying A and B within eqn (17), we obtain:

$$\begin{cases} A = a(\beta)R_0\sqrt{\frac{\Delta\rho}{G_0}} \\ B = b(\beta). \end{cases} \quad (18)$$

Once the dependence of b on β is obtained from the FE solution, β can be determined. Then, from the first equation in (18), one can determine G_0 by performing a linear fit of the experimental data (d_{\max}/d_{\min} versus ω) in the large deformation limit, and finally, the interfacial free energy can be calculated as $\Gamma = \beta R_0 G_0$. Once more, this shows that both the interfacial free energy Γ and the shear modulus G_0 of the bead can be extracted by fitting the bead deformation as a function of ω . To elucidate better the validity of eqn (16), d_{\max}/d_{\min} is plotted as a function of $a(\beta)\sqrt{\alpha} + b(\beta)$ for different values of β (Fig. 5). $a(\beta)$ and $b(\beta)$ have been determined by considering deformations d_{\max}/d_{\min} in the range $[2.5, 6]$, accordingly with the domain explored in experiments discussed in Section III. Even if the asymptotic regime is never strictly reached in this range for any β , the linear approximation of d_{\max}/d_{\min} as function of $\sqrt{\alpha}$ remains

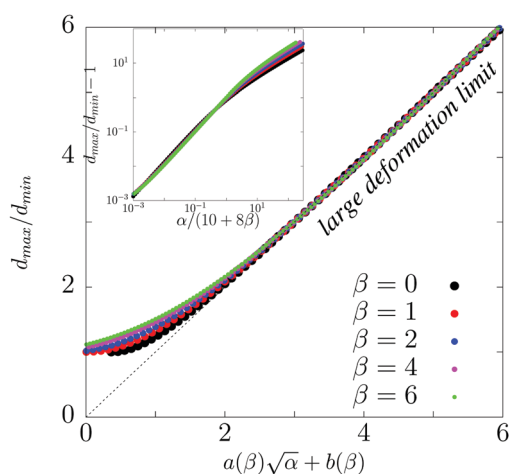


Fig. 5 d_{\max}/d_{\min} computed from the FE simulations as a function of $a\sqrt{\alpha} + b$ where a and b are determined as a function of β (see Fig. 4). Inset: $d_{\max}/d_{\min} - 1$ as a function of $\alpha/(10 + 8\beta)$.

Table 1 Coefficients K_i giving the best cubic polynomial fit of $a(\beta)$ and $b(\beta)$ shown in Fig. 4 and discussed in the main text

	K_1	K_2	K_3	K_4
$a(\beta)$	0.4422	-0.02848	1.69×10^{-3}	-6.65×10^{-5}
$b(\beta)$	0.3327	-0.3467	3.12×10^{-2}	-1.23×10^{-3}

very good. To make our results readily exploitable for future measurements, we have fitted separately $a(\beta)$ and $b(\beta)$ with a cubic function, namely $K_1 + K_2\beta + K_3\beta^2 + K_4\beta^3$. We report all values for the coefficients K_i in Table 1 and the result of the fit is shown in Fig. 4. The collapse of all curves in Fig. 5 confirms that the approximation $d_{\max}/d_{\min} \simeq a(\beta)\sqrt{\alpha} + b(\beta)$ is relevant for d_{\max}/d_{\min} in the experimental range.^{2,6}

Finally it's worth noting that in the case $\alpha \ll 1$ (small deformation limit), the expression obtained from the biaxial approximation seems to hold well in the framework of the FE calculation (see inset of Fig. 5): all the deformations calculated for different β -values *via* FE method collapse on the bisector of the first quadrant when plotted *versus* the deformation obtained under biaxial approximation (eqn (11)). Indeed, matching the effective local deformation with the overall deformation of the bead is here relevant, because the material behaviour can be linearized within the limit of the small deformations.

III Experiments

A. Materials and methods

Polyacrylamide beads are prepared by copolymerization of acrylamide and *N,N*-methylenebisacrylamide in the presence of tetramethylethylenediamine (TEMED) and sodium persulfate as initiators, in water. Prior to mixing the constituents, all the solutions are saturated with nitrogen gas, to ensure the near insufficiency of oxygen. A given volume of the liquid mixture, corresponding to the radius of the bead, is transferred to an

Eppendorf tube filled with the fluorinated oil in which all beads are solidly spun in our experiments. The aqueous droplets are small enough so that interfacial free energy ($\approx 33 \pm 3 \text{ mN m}^{-1}$ measured by SDT in absence of crosslinker) made them spherical in oil. The polymerization and interchain crosslinking stopped after approximately 2 hours. The crosslinker and the acrylamide monomer concentrations were fixed respectively to $0.00119 \pm 0.0006 \text{ mol l}^{-1}$ and $0.45 \pm 0.01 \text{ mol l}^{-1}$ for all preparations. The same preparation protocol has been previously employed in our group to synthesize beads in silicon oil with shear modulus ranging from 13 Pa to 29 Pa.¹⁰ Hence hereafter we will not consider any crosslinker and/or monomer density variation in the beads, whose effects will be possibly investigated in a future publication.

However, although the beads have been produced with the same protocol, we expect to find differences in their properties due to small uncontrolled variations affecting the preparation protocol and concerning the crosslinker/monomer molar ratio, the crosslinker and monomer concentrations, the presence of oxygen during the synthesis and the purity of the components. Since we consider beads characterized by low mass fractions of acrylamide, their mass density can be considered equal to the density of water at $T = 25 \text{ }^\circ\text{C}$, $\rho_i = 0.997 \text{ g cm}^{-3}$.

All experiments were performed with a Krüss spinning drop tensiometer (SDT). Rates of rotation were accurate to 1%. The outer liquid, Fomblin Y oil [linear formula $\text{CF}_3\text{O}[-\text{CF}(\text{CF}_3)-\text{CF}_2\text{O}]_x(-\text{CF}_2\text{O})_y\text{CF}_3$] of mass density $\rho_o = 1.9 \text{ g cm}^{-3}$ was purchased from Sigma-Aldrich and used without further purification at $25.0 \text{ }^\circ\text{C}$. The temperature of the setup was always set to $25.0 \pm 0.5 \text{ }^\circ\text{C}$ and kept constant using a flow of temperature-controlled air.

All beads were illuminated by a blue Light Emitting Diode (LED) with a dominant emission wavelength of 469 nm. Measurements were performed using a cylindrical capillary with internal diameter $2R_c = 3.25 \text{ mm}$. Video recording has been performed by using a CCD camera attached to the SDT with a field of view $6 \text{ mm} \times 4.5 \text{ mm}$ and resolution $2.3 \text{ } \mu\text{m}$. Different tests were performed with rotation rates ranging from 6000 rpm to 15 000 rpm. For our beads/oil system the displacement of the drop off the rotation axis due to buoyancy was smaller than $7 \text{ } \mu\text{m}$ for $\omega > 800 \text{ rad s}^{-1}$, as calculated following ref. 47. Such unavoidable deviation due to buoyancy is therefore much smaller than the bead size and of the same order of magnitude of the resolution of the camera used for the visual inspection the equilibrium shapes of the beads. The effect of buoyancy can thus be neglected and the measured deformation for $\omega > 800 \text{ rad s}^{-1}$ can be considered as only originated from the balance between the external forcing and the response of the material.

Being the refractive index of the background fluid ($n_b = 1.299$) close to that of water, fluorescent labelling was needed to ensure sufficient optical contrast and track the bead deformation. Under the illumination of the blue LED light, fluorescein-rich beads appear as bright green-yellow regions, since the fluorescein adsorption and emission spectra (in polar solvents) are peaked at $\lambda \approx 485 \text{ nm}$ and $\lambda \approx 511 \text{ nm}$,^{32,48,49} respectively.

B. Analysis

Four beads (coded as B1, B2, B3, B4) have been tested in the SDT in the large deformation limit ($d_{\max}/d_{\min} > 2$). Fig. 6 shows one fluoresceinated bead (B1) under different forcing (from 6000 rpm to 15 000 rpm). For all beads we have extracted the parameter A and B from the relation $d_{\max}/d_{\min} = A\omega + B$ in the large deformation regime (see Fig. 7), and then, G_0 and Γ have been deduced following the procedure detailed in Section II.C (see Table 2).

To check further the validity of our approach for largely deformed beads, we have rescaled our experimental data with the same procedure already adopted for the theoretical values of d_{\max}/d_{\min} (Fig. 8). Fig. 8 shows all values of d_{\max}/d_{\min} obtained for different synthesis of polyacrylamide beads in function of the rescaled forcing $A\omega + B$. All data collapse on a master curve, showing that the large deformation limit is indeed reached in all cases. The accuracy of our model in describing the data shows that the interfacial energy does not depend on the surface area of the bead, excluding the presence of a Shuttleworth effect.¹⁴

The values of the interfacial free energy are found to be similar among the beads, with a weighted average of $\Gamma = 28.1 \pm 3.0 \text{ mN m}^{-1}$ (see Table 2). Error bars could be reduced by exploring larger values of ω , which was not possible with our SDT. Since our gels are in water, we compare the interfacial

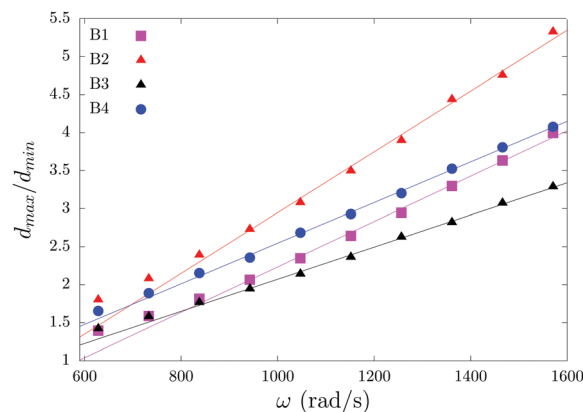


Fig. 7 d_{\max}/d_{\min} as a function of ω for four polyacrylamide beads with different radius R_0 and/or different shear modulus G_0 . Solid lines are the results of linear fit $d_{\max}/d_{\min} = A\omega + B$ carried out for $\omega > 800 \text{ rad s}^{-1}$ (see Table 2).

energies of the elastic beads and that of a droplet containing a non-crosslinked polyacrylamide solution at the same acrylamide molar concentration of the beads. Interestingly, we found $\Gamma_{\text{liq}} = 33 \pm 3 \text{ mN m}^{-1}$ for the liquid droplet. Our measurements are therefore compatible with a negligible contribution of the polymer network to the interfacial energy.

As a final remark, we stress that the polymerization reaction used to synthesize the beads occurred into the background fluorinated oil used subsequently in SDT experiments. On the one hand, this ensures that the beads are not subject to a possible contamination that may arise from the synthesis in other immiscible media and that may affect subsequently the measurement performed in the SDT, notably the measured interfacial energy. On the other hand this oil inevitably alters the polymerization process, hence modifying the value of the gel modulus with respect to other similar synthesis already performed in our group.¹⁰ This deviation, which can be significant for gels with low elastic modulus, is more pronounced as the contact surface between the aqueous solution and oil is larger. For this reason, we could not perform different types of synthesis like those carried out to produce macroscopic polyacrylamide gels,^{10,50} whose modulus can be determined *via* other methods.^{10,41} This hampered a direct cross-check of the values obtained for the shear modulus of our beads. Further research activity is being carried on in our group to develop a synthesis protocol enabling to crosscheck the measurement of elastic moduli obtained *via* a SDT. Despite of that, the values obtained with the SDT method seem relevant as they are in excellent agreement with those found *via* impact experiments¹⁰ for similar polyacrylamide beads, suggesting that the bead deformation method under centrifugal forcing may serve as an ideal strategy to measure accurately both the elastic moduli and the surface energies of soft elastic materials.

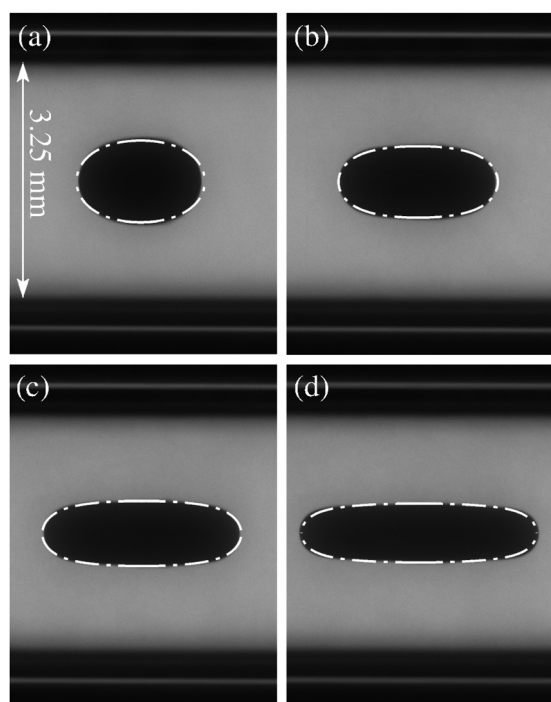


Fig. 6 Snapshots of sample B1 (details are given in Table 2) spinning with angular velocities 6000 rpm (a), 9000 rpm (b), 12 000 rpm (c) and 15 000 rpm (d). The observed deformation is correctly captured by the one obtained minimizing the total energy using the FE method (Section II.C), whose result is represented by the white dash-dotted lines. The corresponding values of the load are $\alpha = 27$ (a), 60 (b), 107 (c) and 167 (d). The global deformations d_{\max}/d_{\min} are 1.6 (a), 2.2 (b), 3.0 (c) and 3.9 (d).

4 Conclusions

Due to the interplay between bulk and surface forces acting simultaneously, isolating the effects of the solid-liquid

Table 2 Data obtained from the analysis of the measurements of d_{\max}/d_{\min} as a function of ω for the four tested samples. The reported uncertainties are the fit errors obtained using the nonlinear least-squares Marquardt–Levenberg algorithm, and according to the method described in Section II

Sample	R_0 , mm	A , s	B	β	G_0 , Pa	Γ , mN m ⁻¹
B1	0.73 ± 0.01	$2.99 \times 10^{-3} \pm 0.07 \times 10^{-3}$	-0.75 ± 0.09	4.9 ± 0.6	7.1 ± 0.3	25.6 ± 4.4
B2	0.89 ± 0.01	$4.00 \times 10^{-3} \pm 0.01 \times 10^{-3}$	-1.05 ± 0.14	7.8 ± 1.6	5.1 ± 0.3	35.3 ± 8.9
B3	0.89 ± 0.01	$2.11 \times 10^{-3} \pm 0.04 \times 10^{-3}$	-0.042 ± 0.050	1.2 ± 0.2	27.8 ± 1.0	28.9 ± 5.0
B4	0.965 ± 0.010	$2.67 \times 10^{-3} \pm 0.04 \times 10^{-3}$	-0.13 ± 0.05	1.5 ± 0.2	16.4 ± 4.0	29.3 ± 10.0

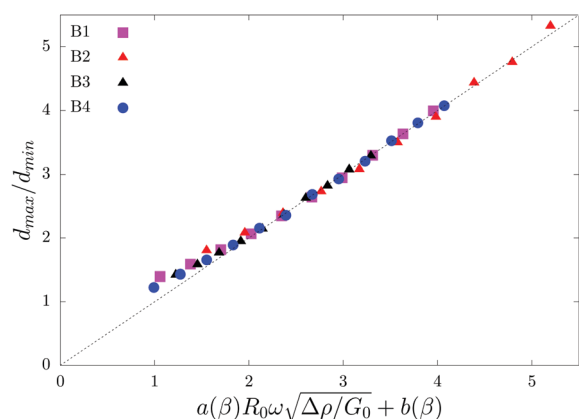


Fig. 8 d_{\max}/d_{\min} as a function of the rescaled angular velocity, for polyacrylamide beads with different radius and/or elastic modulus.

interfacial free energy constant of a soft solid is challenging. While for materials with large shear moduli the contribution of interfacial stresses to deformation can generally be safely neglected, the equilibrium shapes and the stability of soft solids under external drives are altered significantly by their ability to store and/or release interfacial energy. For such systems, measuring the shear modulus is also a difficult task since standard rheometric techniques are often confronted with experimental issues, like wall slip, edge fracture and instrumental resolution, hampering the accurate measurement of the material moduli. For this reason, a robust method able to measure unambiguously both the shear modulus and the interfacial free energy is highly desirable. In this paper we have shown that simultaneous measurements of the shear modulus and the interfacial free energy of elastic materials can be achieved without contact with a solid surface by analysing the shape of spinning soft beads. These measurements are based on a gradual variation of the load, *i.e.* of the angular velocity of the bead. This method requires the prior knowledge of the constitutive equation of the material. Here, in particular, we have investigated the case the isochoric neo-Hookean model, valid for polyacrylamide gels. We have shown that the deformation d_{\max}/d_{\min} of polyacrylamide beads is well approximated by a linear function of the angular speed for large deformations, supporting the validity of our model and the absence of any Shuttleworth effect.¹⁴ We have measured the solid–liquid interfacial free energy for solid particles undergoing large deformations, and we have shown that, for these systems, the interfacial free energy is similar to the liquid–liquid interfacial tension measured in absence of elastic bulk forces. Our results

corroborate a scenario where the deformation of soft amorphous polymer materials under an external load can be described considering one single interfacial free energy parameter independent on the deformation. Though it has been applied to one experimental system, our analysis suggests a much more general behavior of the interfaces between soft gels and newtonian fluids or gases, in line with previous results.^{9,51,52} For materials following another known constitutive law (like the Gent model⁵³ or Mooney–Rivlin model⁵⁴), the method described here also applies provided that this elastic law is accounted for in the simulations so that the functions $a(\beta)$ and $b(\beta)$ are properly determined. We hope that our work motivates further research both to improve and adapt SDT apparatus to the measurement of the elastic modulus of soft materials and to generalize our results to different elastic and viscoelastic systems.

Conflicts of interest

The authors state that there are no conflicts to declare.

Acknowledgements

CL and C-AC acknowledge partial financial support of the H2020 Program (Marie Curie Actions) of the European Commission's Innovative Training Networks (ITN) (H2020-MSCA-ITN-2017) under DoDyNet REA Grant Agreement (GA) No. 765811. The authors are most grateful to Jean Marc Fromental for providing technical help.

References

- 1 R. Style, A. Jagota, C. Hui and E. Dufresne, Elastocapillarity: surface tension and the mechanics of soft solids, *Annu. Rev. Condens. Matter Phys.*, 2017, **8**, 99–118.
- 2 J. Bico, E. Reyssat and B. Roman, Elastocapillarity: When surface tension deforms elastic solids, *Annu. Rev. Fluid Mech.*, 2018, **50**, 629–659.
- 3 C. Creton and M. Ciccotti, Fracture and adhesion of soft materials: a review, *Rep. Prog. Phys.*, 2016, **79**(4), 046601.
- 4 M. Nicolson, Surface tension in ionic crystals, *Proc. R. Soc. A*, 1955, **228**, 490–510.
- 5 S. Mora, T. Phou, J. M. Fromental, L. M. Pismen and Y. Pomeau, Capillarity driven instability of a soft solid, *Phys. Rev. Lett.*, 2010, **105**, 214301.
- 6 R. Style, C. Hyland, R. Boltynskiy, J. Wettlaufer and E. Dufresne, Surface tension and contact with soft elastic solids, *Nat. Commun.*, 2013, **4**, 2728.

- 7 B. Andreotti, A. Marchand, S. Das and J. H. Snoeijer, Elastocapillary instability under partial wetting conditions: Bending versus buckling, *Phys. Rev. E: Stat., Nonlinear, Soft Matter Phys.*, 2011, **84**(6), 061601.
- 8 A. A. Evans, S. E. Spagnolie, D. Bartolo and E. Lauga, Elastocapillary self-folding: buckling, wrinkling, and collapse of floating filaments, *Soft Matter*, 2013, **9**(5), 1711–1720.
- 9 A. Chakrabarti and M. K. Chaudhury, Direct Measurement of the Surface Tension of a Soft Elastic Hydrogel: Exploration of Elastocapillary Instability in Adhesion, *Langmuir*, 2013, **29**(23), 6926–6935.
- 10 S. Arora, J. Fromental, S. Mora, T. Phou and C. Ligoure, Impact of beads and drops on a repellent solid surface: a unified description, *Phys. Rev. Lett.*, 2018, **120**, 148003.
- 11 M. Zhao, F. Lequeux, T. Narita, M. Roché and L. Limat, Growth and relaxation of a ridge on a soft poroelastic substrate, *Soft Matter*, 2018, **14**, 61–72.
- 12 S. Mondal, M. Phukan and A. Ghatak, Estimation of solid-liquid interfacial tension using curved surface of a soft solid, *Proc. Natl. Acad. Sci. U. S. A.*, 2015, **112**(41), 12563–12568.
- 13 B. Andreotti and J. Snoeijer, Soft wetting and the shuttleworth effect, at the crossroads between thermodynamics and mechanics, *EPL*, 2016, **113**, 66001.
- 14 R. Shuttleworth, The surface tension of solids, *Proc. Phys. Soc.*, 1950, **63**, 444–457.
- 15 P. Muller, Elastic effects on surface physics, *Surf. Sci. Rep.*, 2004, **54**(5–8), 157–258.
- 16 E. Orowan, Surface energy and surface tension in solids and liquids, *Proc. R. Soc. A*, 1970, **316**(1527), 473–491.
- 17 T. V. Savina, A. A. Golovin, S. H. Davis, A. A. Nepomnyashchy and P. W. Voorhees, Faceting of a growing crystal surface by surface diffusion, *Phys. Rev. E: Stat., Nonlinear, Soft Matter Phys.*, 2003, **67**(2), 021606.
- 18 A. Vaidya and M. K. Chaudhury, Synthesis and Surface Properties of Environmentally Responsive Segmented Polyurethanes, *J. Colloid Interface Sci.*, 2002, **249**(1), 235–245.
- 19 H. Hillborg, N. Tomczak, A. Olh, H. Schnherr and G. J. Vancso, Nanoscale Hydrophobic Recovery: A Chemical Force Microscopy Study of UV/Ozone-Treated Cross-Linked Poly(dimethylsiloxane), *Langmuir*, 2004, **20**(3), 785–794.
- 20 R. W. Style, A. Jagota, C.-Y. Hui and E. R. Dufresne, Elastocapillarity: Surface Tension and the Mechanics of Soft Solids, *Annu. Rev. Condens. Matter Phys.*, 2017, **8**(1), 99–118.
- 21 B. Andreotti and J. H. Snoeijer, Statics and Dynamics of Soft Wetting, *Annu. Rev. Fluid Mech.*, 2020, **52**(1), 285–308.
- 22 S. Mora, M. Abkarian, H. Tabuteau and Y. Pomeau, Surface instability of soft solids under strain, *Soft Matter*, 2011, **7**, 10612–10619.
- 23 C. Hui, A. Jagota, Y. Lin and E. Kramer, Constraints on microcontact printing imposed by stamp deformation, *Langmuir*, 2002, **18**, 1394–1407.
- 24 S. Mora, C. Maurini, T. Phou, J. M. Fromental, B. Audoly and Y. Pomeau, Solid drops: Large capillary deformations of immersed elastic rods, *Phys. Rev. Lett.*, 2013, **111**, 114301.
- 25 S. Mora and Y. Pomeau, Softening of edges of solids by surface tension, *J. Phys.: Condens. Matter*, 2015, **27**, 194112.
- 26 D. Paretkar, X. Xu, C. Y. Hui and A. Jagota, Flattening of a patterned compliant solid by surface stress, *Soft Matter*, 2014, **10**, 4084–4090.
- 27 A. Chakrabarti, M. K. Chaudhury, S. Mora and Y. Pomeau, Elastobuoyant heavy spheres: A unique way to study non-linear elasticity, *Phys. Rev. X*, 2016, **6**, 041066.
- 28 J. Delavoipiere, Y. Tran, E. Verneuil and A. Chateauminois, Poroelastic indentation of mechanically confined hydrogel layers, *Soft Matter*, 2016, **12**, 8049.
- 29 B. Vonnegut, Rotating Bubble Method for the Determination of Surface and Interfacial Tensions, *Rev. Sci. Instrum.*, 1942, **13**(1), 6–9.
- 30 S. Bamberger, G. V. Seaman, K. Sharp and D. E. Brooks, The effects of salts on the interfacial tension of aqueous dextran poly(ethylene glycol) phase systems, *J. Colloid Interface Sci.*, 1984, **99**(1), 194–200.
- 31 Y. Liu, R. Lipowsky and R. Dimova, Concentration Dependence of the Interfacial Tension for Aqueous Two-Phase Polymer Solutions of Dextran and Polyethylene Glycol, *Langmuir*, 2012, **28**(8), 3831–3839.
- 32 A. Carbonaro, L. Cipelletti and D. Truzzolillo, Spinning Drop Dynamics in Miscible and Immiscible Environments, *Langmuir*, 2019, **35**(35), 11330–11339.
- 33 A. Carbonaro, L. Cipelletti and D. Truzzolillo, Ultralow effective interfacial tension between miscible molecular fluids, *Phys. Rev. Fluids*, 2020, **5**, 074001.
- 34 B. Zoltowski, Y. Chekanov, J. Masere, J. A. Pojman and V. Volpert, Evidence for the Existence of an Effective Interfacial Tension between Miscible Fluids. 2. Dodecyl Acrylate-Poly(dodecyl acrylate) in a Spinning Drop Tensiometer, *Langmuir*, 2007, **23**(10), 5522–5531.
- 35 J. A. Pojman, C. Whitmore, M. L. Turco Liveri, R. Lombardo, J. Marszalek, R. Parker and B. Zoltowski, Evidence for the Existence of an Effective Interfacial Tension between Miscible Fluids: Isobutyric Acid-Water and 1-Butanol-Water in a Spinning-Drop Tensiometer, *Langmuir*, 2006, **22**(6), 2569–2577.
- 36 G. Pieper, H. Rehage and D. Barth-Biesel, Deformation of a Capsule in a Spinning Drop Apparatus, *J. Colloid Interface Sci.*, 1998, **202**(2), 293–300.
- 37 D. D. Joseph, M. S. Arney, G. Gillberg, H. Hu, D. Hultman, C. Verdier and T. M. Vinagre, A spinning drop tensioextensometer, *J. Rheol.*, 1992, **36**(4), 621–662.
- 38 H. T. Patterson, K. H. Hu and T. H. Grindstaff, Measurement of interfacial and surface tensions in polymer systems, *J. Polym. Sci., Polym. Symp.*, 2007, **34**(1), 31–43.
- 39 R. Ogden, *Non-Linear Elastic Deformations*, Ellis Horwood Limited, Chichester, 1984.
- 40 J. Li, Y. Hu, J. Vlassak and Z. Suo, Experimental determination of equations of state for ideal elastomeric gels, *Soft Matter*, 2012, **8**, 8121.
- 41 S. Mora, E. Ando, J. Fromental, T. Phou and Y. Pomeau, The shape of hanging cylinders, *Soft Matter*, 2020, **15**, 5464–5473.
- 42 J. Hegemann, H.-H. Boltz and J. Kierfeld, Elastic capsules at liquid-liquid interfaces, *Soft Matter*, 2018, **14**(27), 5665–5685.

- 43 C. Wischniewski, E. Zwar, H. Rehage and J. Kierfeld, Strong Deformation of Ferrofluid-Filled Elastic Alginate Capsules in Inhomogenous Magnetic Fields, *Langmuir*, 2018, **34**, 13534–13543.
- 44 F. Richard, A. Chakrabarti, B. Audoly, Y. Pomeau and S. Mora, Buckling of a spinning elastic cylinder: linear, weakly nonlinear and post-buckling analyses, *Proc. R. Soc. A*, 2018, **474**, 20180242.
- 45 A. Logg, K. Mardal and G. Wells, *Automated Solution of Differential Equations by the Finite Element Method*, Springer, 2012.
- 46 P. Amestoy, I. Duff, J. L'Excellent and J. Koster, A fully asynchronous multifrontal solver using distributed dynamic scheduling, *SIAM J. Matrix Anal. Appl.*, 2001, **23**, 15–41.
- 47 P. Currie and J. Van Nieuwkoop, Buoyancy effects in the spinning-drop interfacial tensiometer, *J. Colloid Interface Sci.*, 1982, **87**(2), 301–316.
- 48 J. Panchompoo, L. Aldous, M. Baker, M. I. Wallace and R. G. Compton, One-step synthesis of fluorescein modified nano-carbon for Pd(ii) detection *via* fluorescence quenching, *Analyst*, 2012, **137**(9), 2054.
- 49 L. Szalay and E. Tombacz, Effect of the solvent on the fluorescence spectrum of tryptaflavine and fluorescein, *Acta Phys. Acad. Sci. Hung.*, 1964, **16**(4), 367–371.
- 50 A. Chakrabarti, A. Porat, E. Raphaël, T. Salez and M. K. Chaudhury, Elastowetting of Soft Hydrogel Spheres, *Langmuir*, 2018, **34**(13), 3894–3900.
- 51 X. Shao, J. R. Saylor and J. B. Bostwick, Extracting the surface tension of soft gels from elastocapillary wave behavior, *Soft Matter*, 2018, **14**(36), 7347–7353.
- 52 X. Shao, S. A. Fredericks, J. R. Saylor and J. B. Bostwick, A method for determining surface tension, viscosity, and elasticity of gels via ultrasonic levitation of gel drops, *J. Acoust. Soc. Am.*, 2020, **147**, 2488–2498.
- 53 A. Gent, A new constitutive relation for rubber, *Rubber Chem. Technol.*, 1996, **69**, 59–61.
- 54 M. Mooney, A theory of large elastic deformation, *J. Appl. Phys.*, 1940, **11**, 582–592.

General conclusions and perspectives

The aim of this thesis was to study the expansion dynamics of viscoelastic liquid sheets after impact in order to better understand and evaluate the roles of bulk elasticity, surface tension and viscosity as well as the different modes of dissipation during the entire process. Additionally, the evolution of the rim present at the edge of the expanding sheet and the deformation of elastic beads under rotation were investigated.

The impacts of Newtonian, shear-thinning polymer solutions and model viscoelastic fluids, which behave as Maxwell fluids, are investigated taking advantage of the simplified dissipation process provided by the cold Leidenfrost effect. The sheet expansion takes place in non-wetting and slip conditions, where two regimes were identified for its maximal expansion. A capillary regime where the maximal expansion does not depend on the viscosity and is controlled by the surface tension forces, and a viscous regime where the viscous forces overtake the capillary forces, resulting in a reduced expansion. The reduced expansion is the result of biaxial extensional viscous dissipation occurring during the impact process. This dissipation may be characterized by the biaxial extensional viscosity, which is, for the Newtonian fluids, $\eta_B = 6\eta$ with η , the shear viscosity. For the polymer solutions, we observed a strong enhancement of the maximal expansion, which was explained by accounting for their thinning behavior. Our strategy has been to define an effective biaxial extensional thinning viscosity, η_B^{shift} , obtained by taking the value of η_B of a Newtonian fluid which yields the same expansion factor as the polymer solution of interest.

We have investigated Maxwell fluids characterized by low elastic moduli and relaxation times spanning over almost two orders of magnitude. For these fluids, no simple correlation could be made between the experimental results for d_{max} , the maximum diameter reached by the sheet, and the time for it to be reached, t_{max} , and the viscosity, bulk elasticity or relaxation times of the samples. To rationalize these results, we developed a theoretical model based on energy conservation arguments, which allows a simplified description of the sheet deformation mechanism using a non-linear damped harmonic oscillator model. In the model, the damping coefficient changes with time and is proportional to an effective biaxial extensional viscosity, which, for the viscoelastic samples, accounts for the dynamics of the expansion by considering the viscous part of the complex modulus at an average extensional rate. The undamped angular frequency of the oscillator in this model is a combination of the surface tension and the effective modulus, which is calculated by evaluating the elastic part of the complex modulus for the average extensional rate. The numerical predictions for d_{max} and t_{max} obtained when using this model, with no adjustable parameter, are in good agreement with the experimental data.

Impacts on a small target leads to a deformation mode, which combines shear and biaxial deformation. We evaluate the competition between the different modes of dissipation

in the mixed flow resulting from the impact on, first, a small target of size comparable to that of the drop and, subsequently, on targets of increasing sizes. When a drop is impacted on a target, part of the expanding sheet remains in close contact with the target while the rest of the sheet expands in the air. On the small target, the two sources of dissipation are of the same order of magnitude for the Newtonian fluids, which was not the case for the strongly rheo-thinning solutions considered based on supramolecular polymer (EHUT). For the EHUT solutions, the dominant mode of dissipation originates from biaxial extensional viscous dissipation. Therefore, the biaxial thinning extensional viscosity is found to control the maximum expansion of the strongly shear-thinning viscoelastic sheets made of EHUT solutions on the small target. Quantitatively assessing the competition between shear and biaxial extensional viscous dissipations, we show a dependence of the shear dissipation energy with the size of the target to the power of four. We investigate this dependence in a second part of this chapter, by increasing progressively the size of the target. As the size of the target increases, the contribution of biaxial extension to the dissipation is increasingly dominated by the shear contribution. The maximal diameter reached by the Newtonian sheets is satisfyingly described by an analytical equation based on an energy balance neglecting the biaxial extensional dissipation, which goes from comparable to negligible for increasing target size. This same prediction was used to rationalize experimental results from the impact of polymer solutions. However, even when accounting for the thinning behavior of the viscoelastic polymer solutions, the agreement between experimental results and theory is not as satisfactory as for Newtonian fluids due to a larger contribution of biaxial extension to dissipation.

Additionally, we provide thickness field measurements of Newtonian liquid sheets of various viscosities expanding on a nitrogen vapor layer. For the first time, to the best of our knowledge, the shape of the rim cross-section is unveiled. We have demonstrated a cross-section different from the circular shape usually assumed. The filling rate and filling velocity of the rim were measured. Comparison with theoretical predictions showed that the inertial forces, which are commonly neglected, must be accounted for to properly model the rim dynamics. Additionally, we show that, even though viscosity does not affect the rim growth after its emergence, the time at which the rim appears is governed by viscosity a viscous time that depends on viscosity and surface tension.

We have deviated from the study of drop impact to look into the biaxial deformation of elastic beads under rotation in a denser fluid. We showed that in the limit of strong deformation, the effect of bulk elasticity can be decoupled from the one of the interfacial energy. We obtained simultaneous measurements of both the interfacial tension and elastic modulus of soft elastic beads, for which elasto-capillary effects prevent to overlook one over the other. This work constitutes a first step toward the study of the deformation of elastic and viscoelastic systems under rotation and the use of spinning drop tensiometer apparatus to measure the elastic modulus of soft materials. Preliminary experiments were performed with drops of micro-emulsions and wormlike micelles. The extension and

relaxation of the drops after a sudden increase or decrease of the rotational velocity was measured. The time evolution of the drop length following the increase (decrease) of the rotational speed showed a rapid increase (decrease), which continued to evolve after more than thousands of seconds, hinting to a first rapid dynamic followed by an extremely slow dynamic. This behavior is yet to be understood and will be the subject of complementary efforts.

Overall, this work has permitted to establish the mechanism of dissipation in liquid sheets expanding freely on a liquid nitrogen vapor cushion or on targets of different sizes. We demonstrate the biaxial extensional dissipation to be the relevant dissipation mechanism for a free liquid sheet expanding on a repellent surface. Finer analysis of the dissipation processes in an expanding liquid sheet could be done by looking into the different mechanisms of dissipation which were overlooked in the frame of this thesis such as the edge effects, the compression of the gas or the dissipation caused by fluid recirculation in the rim.

A very promising instrumental aspect of the work presented here is the prospect of a new type of biaxial extensional rheometer which can measure the rheological values of viscoelastic samples under pure biaxial extensional deformation but also under mixed flow fields. The latter, which is more relevant to real life situations, is obtained by gradually introducing shear thanks to increasing target sizes. Measuring the response under biaxial extensional deformation of viscoelastic fluids is still very problematic, especially in the case of fluids of low viscosity. Furthermore, this new type of rheometer using drop impact would give access to large biaxial extensional deformations and shear rates which cannot be reached by traditional rheometry but which are relevant in industrial processes. To develop experimental set-ups toward this goal, we could implement a pressure sensor to measure the stress.

The rim bounding a sheet has been well described for Newtonian fluids. Generalizing our model to viscoelastic fluids using the same experimental tools would allow one to evaluate how and if viscoelasticity affects the existence and dynamics of the rim. Figure A shows a sheet of PEO solution at maximal expansion next to a Newtonian sheet of the same zero-shear viscosity. These two snapshots let us presuppose different results for viscoelastic samples. This suggests that elasticity is expected to play a role on the rim dynamics and instabilities.

Moreover, studying the effect of viscoelasticity on instabilities is yet to be explored. Instabilities occurring during expansion of Newtonian liquid sheets have been extensively studied, which is not the case of instabilities of sheets produced from viscoelastic fluids. Though, nucleation and growth of holes during the biaxial extension of viscoelastic sheets is an important problem for polymer processing. We observed this anomaly for sheets of wormlike micelles and micro-emulsions of high elasticity impacting on liquid nitrogen (see Figure B). The experimental conditions considered here provide a favorable setting

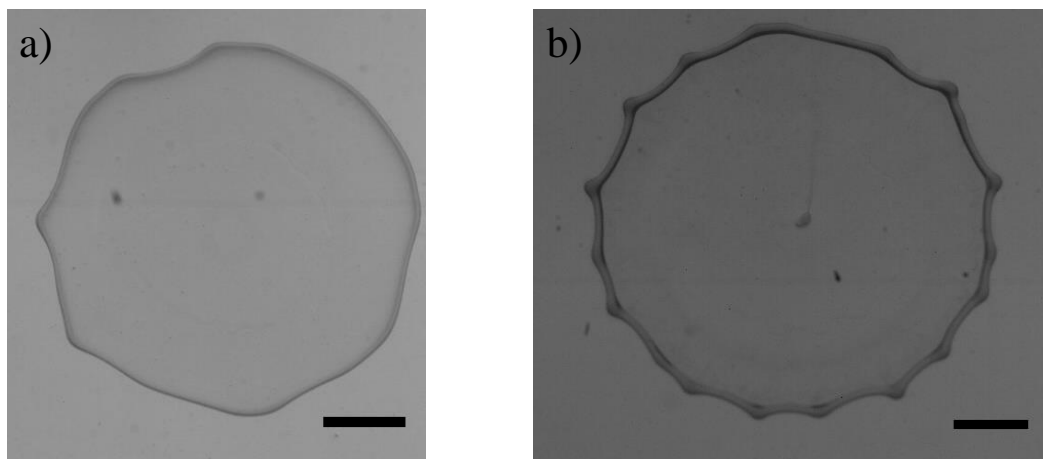


Figure A: Sheets at maximal expansion of a) glycerol/water mixture and b) PEO solution of same zero shear viscosity ($\eta_0 = 270$ mPa s). The scale bars are 5 mm.

to observe the nucleation and growth of holes in viscoelastic liquid sheets thanks to the transparency of the substrate. Moreover, the problem is simplified by the fact that the instabilities observed in this situation are resulting from the biaxial extensional deformation, the shear being ruled out of the equation.

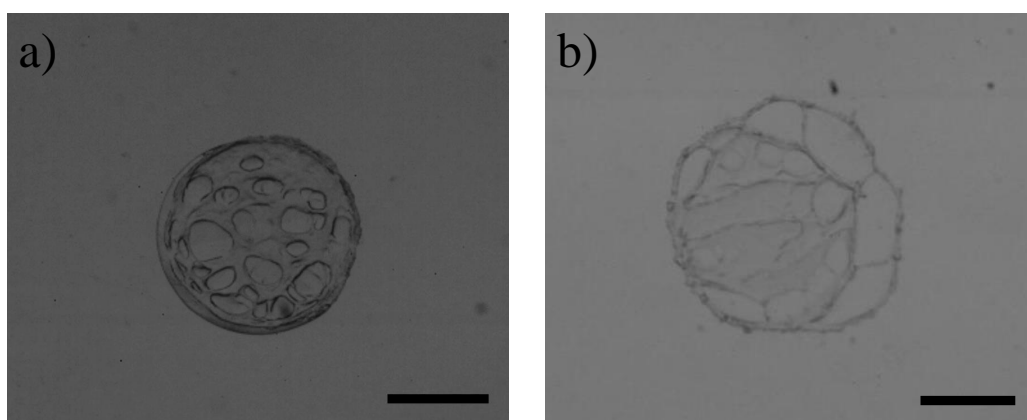


Figure B: Sheets of a) wormlike micelles with $\phi = 6\%$ and $\alpha = 0.048\%$ b) bridged micro-emulsions with C18, $\phi = 3\%$ and $r = 8$. The scale bars are 5 mm.

Another type of destabilization worth studying, particularly in these times when the question of airborne transmitted diseases is on everyone's lips, is the ejection of secondary droplets or spray after the impact of a saliva drop. Saliva is a viscoelastic fluid composed of water, ions and proteins. Preliminary experiments were performed with saliva with the aim of understanding and predicting its destabilization after impact on a small target. Figure C shows a snapshot of a sheet, in the retraction phase, produced by the impact of a drop of saliva at high velocity ($v_0 = 6$ m/s) on a small target. Very long filaments are

connected to the lamella but no ejection of droplets is observed. Modifications could be made to the experimental set-up to increase the impact velocity in the hope of observing the destabilization of the sheet into a spray.

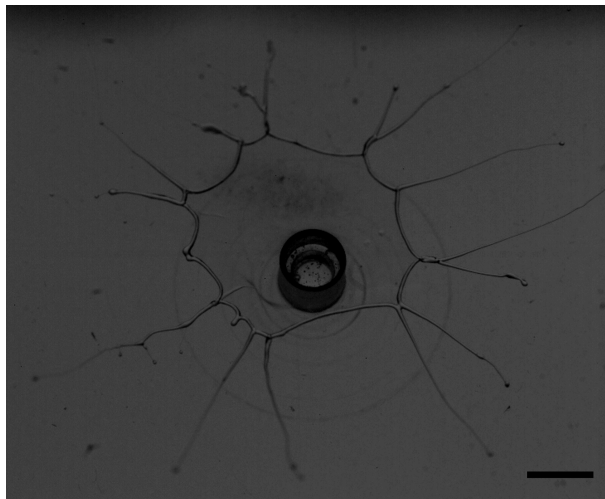


Figure C: A sheet of saliva drop impacted at $v_0 = 6$ m/s on a target with $d_T = 5$ mm. The scale bar is 5 mm.

To conclude, the work presented in this thesis and the remaining open questions proves once again that the interest for drop impact, and more generally their deformation, spans from drawings of Leonardo da Vinci to contemporary concerns.

Bibliography

- [An 2012] Sang Mo An and Sang Yong Lee. *Maximum spreading of a shear-thinning liquid drop impacting on dry solid surfaces*. *Exp. Therm. Fluid Sci.*, vol. 38, no. C, pages 140–148, 2012. (Cited on page 18.)
- [Antonini 2012] Carlo Antonini, Alidad Amirfazli and Marco Marengo. *Drop impact and wettability: From hydrophilic to superhydrophobic surfaces*. *Phys. Fluids*, vol. 24, no. 10, 2012. (Cited on page 10.)
- [Antonini 2013] C Antonini, I Bernagozzi, S Jung, D Poulikakos and M Marengo. *Water drops dancing on ice: how sublimation leads to drop rebound*. *Phys. Rev. Lett.*, vol. 111, no. 1, page 14501, 2013. (Cited on pages 13, 14, 15, 16 and 45.)
- [Arogeti 2019] M. Arogeti, E. Sher and T. Bar-Kohany. *Drop impact on small targets with different target-to-drop diameters ratio*. *Chem. Eng. Sci.*, vol. 193, no. 2019, pages 89–101, 2019. (Cited on pages 4, 8, 9 and 114.)
- [Arora 2016] Srishti Arora, Christian Liguore and Laurence Ramos. *Interplay between viscosity and elasticity in freely expanding liquid sheets*. *Phys. Rev. Fluids*, vol. 1, no. 8, pages 1–15, 2016. (Cited on pages 4, 8, 20 and 21.)
- [Arora 2018] S. Arora, J. M. Fromental, S. Mora, Ty Phou, L. Ramos and C. Liguore. *Impact of Beads and Drops on a Repellent Solid Surface: A Unified Description*. *Phys. Rev. Lett.*, vol. 120, no. 14, page 148003, 2018. (Cited on pages 4, 14, 20, 21, 25, 45, 47 and 48.)
- [Attané 2007] P Attané, F Girard and V Morin. *An energy balance approach of the dynamics of drop impact on a solid surface*. *Phys. Fluids*, vol. 19, page 012101, 2007. (Cited on page 24.)
- [Bakshi 2007] Shamit Bakshi, Ilia V. Roisman and Cam Tropea. *Investigations on the impact of a drop onto a small spherical target*. *Phys. Fluids*, vol. 19, no. 3, 2007. (Cited on page 7.)
- [Bamberger 1984] Stephan Bamberger, Geoffrey V.F. Seaman, K. A. Sharp and Donald E. Brooks. *The effects of salts on the interfacial tension of aqueous dextran poly(ethylene glycol) phase systems*. *J. Colloid Interface Sci.*, vol. 99, no. 1, pages 194–200, 1984. (Cited on page 37.)
- [Bartolo 2007] Denis Bartolo, Arezki Boudaoud, Grégoire Narcy and Daniel Bonn. *Dynamics of non-newtonian droplets*. *Phys. Rev. Lett.*, vol. 99, no. 17, pages 1–4, 2007. (Cited on page 18.)

- [Bergeron 2000] Vance Bergeron, Daniel Bonn, Jean Yves Martin and Louis Vovelle. *Controlling droplet deposition with polymer additives*. Nature, vol. 405, pages 772–775, 2000. (Cited on page 17.)
- [Bergman 2011] T L Bergman, A S Lavine and F P Incropera. Fundamentals of Heat and Mass Transfer, 7th Edition. John Wiley & Sons, Incorporated, 2011. (Cited on pages 48 and 49.)
- [Berry 2015] Joseph D. Berry, Michael J. Neeson, Raymond R. Dagastine, Derek Y.C. Chan and Rico F. Tabor. *Measurement of surface and interfacial tension using pendant drop tensiometry*. J. Colloid Interface Sci., vol. 454, pages 226–237, 2015. (Cited on page 34.)
- [Bertola 2009] V. Bertola. *An experimental study of bouncing Leidenfrost drops: Comparison between Newtonian and viscoelastic liquids*. Int. J. Heat Mass Transf., vol. 52, no. 7-8, pages 1786–1793, 2009. (Cited on page 17.)
- [Bertola 2012] V. Bertola and M. Marengo. *Single drop impacts of complex fluids: a review*. Drops Bubbles Contact with Solid Surfaces, pages 267–298, 2012. (Cited on page 17.)
- [Bertola 2015] Volfango Bertola and Mark D. Haw. *Impact of concentrated colloidal suspension drops on solid surfaces*. Powder Technol., vol. 270, no. PB, pages 412–417, 2015. (Cited on page 19.)
- [Biance 2006] Anne-Laure Laure Biance, Frédéric Chevy, Christophe Clanet, Guillaume Lagubeau and David Quéré. *On the elasticity of an inertial liquid shock*. J. Fluid Mech., vol. 554, pages 47–66, 2006. (Cited on pages 21 and 25.)
- [Biance 2011] Anne Laure Biance, Christophe Pirat and Christophe Ybert. *Drop fragmentation due to hole formation during Leidenfrost impact*. Phys. Fluids, vol. 23, no. 2, pages 1–7, 2011. (Cited on pages 12 and 13.)
- [Bico 2015] J. Bico. *Cracks in bursting soap films*. J. Fluid Mech., vol. 778, pages 1–4, 2015. (Cited on page 136.)
- [Bouteiller 2005] Laurent Bouteiller, Olivier Colombani, Frédéric Lortie and Pierre Terech. *Thickness transition of a rigid supramolecular polymer*. J. Am. Chem. Soc., vol. 127, no. 24, pages 8893–8898, 2005. (Cited on page 68.)
- [Boyer 2016] François Boyer, Enrique Sandoval-Nava, Jacco H. Snoeijer, J. Frits Dijksman and Detlef Lohse. *Drop impact of shear thickening liquids*. Phys. Rev. Fluids, vol. 1, no. 1, pages 13901–13909, 2016. (Cited on pages 4 and 19.)
- [Cates 1987] M. E. Cates. *Reptation of Living Polymers: Dynamics of Entangled Polymers in the Presence of Reversible Chain-Scission Reactions*. Macromolecules, vol. 20, no. 9, pages 2289–2296, 1987. (Cited on page 64.)

- [Cathey 1988] Cheryl A. Cathey and Gerald G. Fuller. *Uniaxial and biaxial extensional viscosity measurements of dilute and semi-dilute solutions of rigid rod polymers*. J. Nonnewton. Fluid Mech., vol. 30, no. 2-3, pages 303–316, 1988. (Cited on page 31.)
- [Çengel 2001] Yunus A. Çengel and Michael A. Boles. *Thermodynamics: An Engineering Approach*. McGraw-Hill Education, Boston, 8th editio édition, 2001. (Cited on page 48.)
- [Çengel 2002] Yunus A. Çengel. *Heat Transfer: A Practical Approach*. McGraw-Hill Education, New York, 2nd editio édition, 2002. (Cited on pages 47 and 48.)
- [Chen 1979] Betty Chen and Andreas Chrambach. *Estimation of polymerization efficiency in the formation of polyacrylamide gel, using continuous optical scanning during polymerization*. J. Biochem. Biophys. Methods, vol. 1, pages 105–116, 1979. (Cited on page 70.)
- [Chen 2016] Simeng Chen and Volfango Bertola. *The impact of viscoplastic drops on a heated surface in the Leidenfrost regime*. Soft Matter, vol. 12, no. 36, pages 7624–7631, 2016. (Cited on page 19.)
- [Cheng 1977] Lung Cheng. *Dynamic Spreading of Drops Impacting onto a Solid Surface*. Ind. Eng. Chem., Process Des. Dev, vol. 16, pages 192–197, 1977. (Cited on page 23.)
- [Clanet 2002] Christophe Clanet and Emmanuel Villermaux. *Life of a smooth liquid sheet*. J. Fluid Mech., vol. 462, pages 307–340, 2002. (Cited on page 8.)
- [Cox 1958] W. P. Cox and E. H. Merz. *Correlation of Dynamic and Steady Flow Viscosities The*. J. Polym. Sci., vol. XXVIII, no. 118, pages 619–622, 1958. (Cited on pages 66 and 69.)
- [Crisp 1987] Angela Crisp, Dejuan E, James Tiedeman, Eugene de Juan and James Tiedeman. *Effect of silicone oil viscosity on emulsification*. Arch. Ophthalmol., vol. 105, no. 4, pages 546–550, 1987. (Cited on page 57.)
- [Crooks 2000] Regan Crooks and David V Boger. *Influence of fluid elasticity on drops impacting on dry surfaces*. J. Rheol. (N. Y. N. Y)., vol. 44, no. 4, pages 973–996, 2000. (Cited on pages 4 and 17.)
- [Crooks 2001] Regan Crooks, Justin Cooper-White and David V. Boger. *The role of dynamic surface tension and elasticity on the dynamics of drop impact*. Chem. Eng. Sci., vol. 56, no. 19, pages 5575–5592, 2001. (Cited on page 17.)
- [Cross 1965] M M Cross. *Rheology of non-Newtonian fluids: a new flow equation for pseudoplastic systems*. J. Colloid Sci., vol. 30, pages 417–437, 1965. (Cited on pages 40 and 66.)

- [Culick 1960] F. E. C. Culick. *Comments on a Ruptured Soap Film*. J. Appl. Phys. 31,, vol. 31, page 1128, 1960. (Cited on pages 128 and 143.)
- [De Gennes 1971] P. G. De Gennes. *Reptation of a polymer chain in the presence of fixed obstacles*. J. Chem. Phys., vol. 55, no. 2, pages 572–579, 1971. (Cited on page 64.)
- [de Gennes 2004] Pierre-Gilles de Gennes, Françoise Brochard-Wyart and David Quéré. *Capillarity and Wetting Phenomena: Drops, Bubbles, Pearls, Waves*. Springer, New York, NY, 1 édition, 2004. (Cited on page 10.)
- [De Goede 2018] T. C. De Goede, N. Laan, K. G. De Bruin and D. Bonn. *Effect of Wetting on Drop Splashing of Newtonian Fluids and Blood*. Langmuir, vol. 34, no. 18, pages 5163–5168, 2018. (Cited on page 18.)
- [de Ruiter 2010] Jolet de Ruiter, Rachel E. Pepper and Howard A. Stone. *Thickness of the rim of an expanding lamella near the splash threshold*. Phys. Fluids, vol. 22, no. 2, pages 1–9, 2010. (Cited on pages 28 and 127.)
- [Debrégeas 1995] G. Debrégeas, P. Martin and F. Brochard-Wyart. *Viscous bursting of suspended films*. Phys. Rev. Lett., vol. 75, no. 21, pages 3886–3889, 1995. (Cited on page 146.)
- [Eggers 2010] Jens Eggers, Marco A. Fontelos, Christophe Josserand and Stéphane Zaleski. *Drop dynamics after impact on a solid wall: Theory and simulations*. Phys. Fluids, vol. 22, no. 6, pages 1–13, 2010. (Cited on pages 16, 23, 26, 29, 127 and 128.)
- [Filali 1999] Mohammed Filali, Raymond Aznar, Mattias Svenson, Grégoire Porte and Jacqueline Appell. *Swollen micelles plus hydrophobically modified hydrosoluble polymers in aqueous solutions: Decoration versus bridging. A small angle neutron scattering study*. J. Phys. Chem. B, vol. 103, no. 34, pages 7293–7301, 1999. (Cited on pages 58 and 59.)
- [Filali 2001] Mohammed Filali, Mohamed Jamil Ouazzani, Eric Michel, Raymond Aznar, Grégoire Porte and Jacqueline Appell. *Robust phase behavior of model transient networks*. J. Phys. Chem. B, vol. 105, no. 43, pages 10528–10535, 2001. (Cited on pages 59 and 60.)
- [Fischer 1997] Peter Fischer and Heinz Rehage. *Rheological master curves of viscoelastic surfactant solutions by varying the solvent viscosity and temperature*. Langmuir, vol. 13, no. 26, pages 7012–7020, 1997. (Cited on page 65.)
- [Florence 1972] A. T. Florence and G. Frens. *Aureole profile in bursting soap films. Surface tension and surface relaxation in rapidly compressed monolayers*. J. Phys. Chem., vol. 76, no. 21, pages 3024–3029, 1972. (Cited on pages 128 and 136.)

- [Frankel 1969] Stanley Frankel and Karol J. Mysels. *The bursting of soap films. II. Theoretical considerations*. J. Phys. Chem., vol. 73, no. 9, pages 3028–3038, 1969. (Cited on pages 128 and 137.)
- [Gilet 2015] T. Gilet and L. Bourouiba. *Fluid fragmentation shapes rain-induced foliar disease transmission*. J. R. Soc. Interface, vol. 12, no. 104, 2015. (Cited on page 27.)
- [Girard 2019] Henri Louis Girard, Dan Soto and Kripa K. Varanasi. *Waterbowls: Reducing Impacting Droplet Interactions by Momentum Redirection*. ACS Nano, vol. 13, no. 7, pages 7729–7735, 2019. (Cited on page 8.)
- [GmbH-Internetagentur 2020] Deutscher Tele Markt GmbH-Internetagentur. *Bubble pressure method for measuring the surface tension*, May 2020. (Cited on page 36.)
- [Gordillo 2018] Leonardo Gordillo, Ting Pi Sun and Xiang Cheng. *Dynamics of drop impact on solid surfaces: Evolution of impact force and self-similar spreading*. J. Fluid Mech., vol. 840, pages 190–214, 2018. (Cited on page 4.)
- [Hendricks 1971] R. C. Hendricks and K. J. Baumeister. *Liquid or solid on liquid in Leidenfrost film boiling*. Adv. Cryog. Eng., vol. 16, pages 456–466, 1971. (Cited on page 49.)
- [Huang 1993] Hsimin Huang and Jozef L. Kokini. *Measurement of biaxial extensional viscosity of wheat flour doughs*. J. Rheol. (N. Y. N. Y)., vol. 37, no. 5, pages 879–891, 1993. (Cited on page 31.)
- [Jha 2020] Aditya Jha, Pierre Chantelot, Christophe Clanet and David Quéré. *Viscous bouncing*. Soft Matter, vol. 16, no. 31, pages 7270–7273, 2020. (Cited on page 25.)
- [Johnson 2016] Mark Johnson, Niall Murphy, Ray Ekins, John Hanley and Stephen Jerrams. *Equi-biaxial fatigue testing of EPM utilising bubble inflation*. Polym. Test., vol. 53, pages 122–131, 2016. (Cited on page 31.)
- [Joseph 1992] D. D. Joseph, M. S. Arney, G. Gillberg, H. Hu, D. Hultman, C. Verdier and T. M. Vinagre. *A spinning drop tensioextensometer*, volume 36. 1992. (Cited on pages 31 and 37.)
- [Josserand 2016] C. Josserand and S.T. Thoroddsen. *Drop Impact on a Solid Surface*. Annu. Rev. Fluid Mech., vol. 48, no. 1, pages 365–391, 2016. (Cited on pages 3, 4, 6, 22, 23, 24 and 101.)
- [Joye 1972] Donald D. Joye, Gary W. Poehlein and Costel D. Denson. *Bubble Inflation Technique for the Measurement of Viscoelastic Properties in Equal Biaxial Extensional Flow - 2*. Trans Soc Rheol, vol. 16, no. 3, pages 421–44.5, 1972. (Cited on page 31.)

- [Khojasteh 2016] Danial Khojasteh, Moradi Kazerooni, Sahba Salarian and Reza Kamali. *Droplet impact on superhydrophobic surfaces: A review of recent developments*. J. Ind. Eng. Chem., vol. 42, pages 1–14, 2016. (Cited on page 10.)
- [Kim 2011] Heetae Kim, Young Hee Lee and Hoonyoung Cho. *Levitation time measurement of water drops on the surface of liquid nitrogen*. J. Korean Phys. Soc., vol. 58, no. 6, pages 1628–1632, 2011. (Cited on page 49.)
- [Krechetnikov 2010] R Krechetnikov. *Stability of liquid sheet edges*. Phys. Fluids, vol. 22, page 092101, 2010. (Cited on page 27.)
- [Laan 2015] Nick Laan, Karla G. De Bruin, Denise Slenter, Julie Wilhelm, Mark Jermy and Daniel Bonn. *Bloodstain Pattern Analysis: Implementation of a fluid dynamic model for position determination of victims*. Sci. Rep., vol. 5, pages 1–8, 2015. (Cited on page 3.)
- [Lagubeau 2012] Guillaume Lagubeau, Marco A. Fontelos, Christophe Josserand, Agnès Maurel, Vincent Pagneux and Philippe Petitjeans. *Spreading dynamics of drop impacts*. J. Fluid Mech., vol. 713, pages 50–60, 2012. (Cited on pages 26 and 136.)
- [Lastakowski 2014] H. Lastakowski, F. Boyer, A. L. Biance, C. Pirat and C. Ybert. *Bridging local to global dynamics of drop impact onto solid substrates*. J. Fluid Mech., vol. 747, no. 4, pages 103–118, 2014. (Cited on pages 26, 51 and 129.)
- [Lee 2010] Minhee Lee, Young Soo Chang and Ho-Young Kim. *Drop impact on microwetting patterned surfaces*. Phys. Fluids, vol. 22, no. 7, pages 72101–72108, 2010. (Cited on page 4.)
- [Lee 2012] Ji San Lee, Byung Mook Weon, Jung Ho Je and Kamel Fezzaa. *How does an air film evolve into a bubble during drop impact?* Phys. Rev. Lett., vol. 109, no. 20, pages 1–5, 2012. (Cited on page 5.)
- [Leidenfrost 1756] Joan Gottlob Leidenfrost. AQVÆ COMMVNIS. 1756. (Cited on page 11.)
- [Lejeune 2018] S. Lejeune, T. Gilet and L. Bourouiba. *Edge effect: Liquid sheet and droplets formed by drop impact close to an edge*. Phys. Rev. Fluids, vol. 3, no. 8, pages 1–32, 2018. (Cited on page 7.)
- [Lhuissier 2009] Henri Lhuissier and Emmanuel Villermaux. *Soap films burst like flapping flags*. Phys. Rev. Lett., vol. 103, no. 5, pages 1–4, 2009. (Cited on page 128.)
- [Liang 1996] N. Y. Liang, C. K. Chan and H. J. Choi. *Dynamics of the formation of an aureole in the bursting of soap films*. Phys. Rev. E, vol. 54, no. 4, pages R3117–R3120, 1996. (Cited on page 128.)

- [Liu 2012] Yonggang Liu, Reinhard Lipowsky and Rumiana Dimova. *Concentration dependence of the interfacial tension for aqueous two-phase polymer solutions of dextran and polyethylene glycol*. Langmuir, vol. 28, no. 8, pages 3831–3839, 2012. (Cited on page 37.)
- [Lortie 2002] Frédéric Lortie, Sylvie Boileau, Laurent Bouteiller, Christophe Chassenieux, Bruno Demé, Guylaine Ducouret, Matthieu Jalabert, Françoise Lauprêtre and Pierre Terech. *Structural and rheological study of a bis-urea based reversible polymer in an apolar solvent*. Langmuir, vol. 18, no. 19, pages 7218–7222, 2002. (Cited on page 67.)
- [Louhichi 2020] Ameer Louhichi, Carole-Ann Charles, Ty Phou, Dimitris Vlassopoulos, Laurence Ramos and Christian Ligoure. *Biaxial extensional viscous dissipation in sheets expansion formed by impact of drops of Newtonian and non-Newtonian fluids*. Phys. Rev. Fluids, vol. 5, no. 5, page 053602, 2020. (Cited on pages 50 and 65.)
- [Luu 2009] Li-Hua Hua Luu and Yoël Forterre. *Drop impact of yield-stress fluids*. J. Fluid Mech., vol. 632, pages 301–327, 2009. (Cited on pages 19 and 20.)
- [Luu 2013] Li Hua Luu and Yoël Forterre. *Giant drag reduction in complex fluid drops on rough hydrophobic surfaces*. Phys. Rev. Lett., vol. 110, no. 18, pages 1–5, 2013. (Cited on page 19.)
- [Lv 2016] Cunjing Lv, Pengfei Hao, Xiwen Zhang and Feng He. *Drop impact upon superhydrophobic surfaces with regular and hierarchical roughness*. Appl. Phys. Lett., vol. 108, no. 14, 2016. (Cited on pages 10 and 11.)
- [Macosko 1994] C W Macosko. Rheology: Principles, Measurements and Applications. Wiley-VCH, 1994. (Cited on pages 38 and 40.)
- [Maerker 1974] J. M. Maerker and W. R. Schowalter. *Biaxial extension of an elastic liquid*. Rheol. Acta, vol. 13, pages 627–638, 1974. (Cited on page 31.)
- [Marston 2013] J. O. Marston, M. M. Mansoor and S. T. Thoroddsen. *Impact of granular drops*. Phys. Rev. E - Stat. Nonlinear, Soft Matter Phys., vol. 88, no. 1, pages 1–4, 2013. (Cited on page 4.)
- [Massiera 2002a] Gladys Massiera. *Micelles géantes décorées de copolymères amphiphiles : propriétés structurales et dynamiques*. PhD thesis, Université de Montpellier, 2002. (Cited on page 63.)
- [Massiera 2002b] Gladys Massiera, Laurence Ramos and Christian Ligoure. *Hairy worm-like micelles: Structure and interactions*. Langmuir, vol. 18, no. 15, pages 5687–5694, 2002. (Cited on page 62.)

- [McEntee 1969] Winnie R. McEntee and Karol J. Mysels. *The bursting of soap films. I. An Experimental Study*. J. Phys. Chem., vol. 73, no. 9, pages 3018–3028, 1969. (Cited on pages 128, 136 and 147.)
- [Menter 2000] Paul Menter. *Acrylamide Polymerization—A Practical Approach*. Tech-Note 1156, Bio-Rad Laboratories, 2000. (Cited on page 70.)
- [Moreira 2010] A. L.N. Moreira, A. S. Moita and M. R. Panão. *Advances and challenges in explaining fuel spray impingement: How much of single droplet impact research is useful?* Prog. Energy Combust. Sci., vol. 36, no. 5, pages 554–580, 2010. (Cited on page 12.)
- [Nasto 2019] Alice Nasto, P. T. Brun and A. E. Hosoi. *Drop impact on hairy surfaces*. Phys. Rev. Fluids, vol. 4, no. 6, pages 1–7, 2019. (Cited on pages 11 and 12.)
- [Ogawa 2018] M. Ogawa, A. B. Aljedaani, E. Q. Li, S. T. Thoroddsen and A. L. Yarin. *Evolution of toroidal free-rim perturbations on an expanding circular liquid sheet*. Exp. Fluids, vol. 59, no. 0, page 148, 2018. (Cited on pages 8, 29, 127 and 128.)
- [Okumura 2003] K. Okumura, F. Chevy, D. Richard, D. Quéré and C. Clanet. *Water spring: A model for bouncing drops*. Europhys. Lett., vol. 62, no. 2, pages 237–243, 2003. (Cited on page 25.)
- [Padmanathan 2019] Arul Mozhi Devan Padmanathan, Apoorva Sneha Ravi, Hema Choudhary, Subramanyan Namboodiri Varanakkottu and Sameer V. Dalvi. *Predictive Framework for the Spreading of Liquid Drops and the Formation of Liquid Marbles on Hydrophobic Particle Bed*. Langmuir, vol. 35, no. 20, pages 6657–6668, 2019. (Cited on page 24.)
- [Pasandideh-Fard 1996] M. Pasandideh-Fard, Y. M. Qiao, S. Chandra and J. Mostaghimi. *Capillary effects during droplet impact on a solid surface*. Phys. Fluids, vol. 8, no. 3, pages 650–659, 1996. (Cited on pages 16 and 23.)
- [Pasandideh-Fard 2002] M. Pasandideh-Fard, V. Pershin, S. Chandra and J. Mostaghimi. *Splat shapes in a thermal spray coating process: Simulations and experiments*. J. Therm. Spray Technol., vol. 11, no. 2, pages 206–217, 2002. (Cited on page 3.)
- [Patterson 2007] H. T. Patterson, K. H. Hu and T. H. Grindstaff. *Measurement of interfacial and surface tensions in polymer systems*. J. Polym. Sci. Part C Polym. Symp., vol. 34, no. 1, pages 31–43, 2007. (Cited on page 37.)
- [Petit 2015] P. C. Petit, M. Le Merrer and A. L. Biance. *Holes and cracks in rigid foam films*. J. Fluid Mech., vol. 774, 2015. (Cited on pages 128 and 136.)
- [Pieper 1998] G. Pieper, H. Rehage and D. Barthès-Biesel. *Deformation of a capsule in a spinning drop apparatus*. J. Colloid Interface Sci., vol. 202, no. 2, pages 293–300, 1998. (Cited on pages 31 and 37.)

- [Quéré 2013] David Quéré. *Leidenfrost Dynamics*. *Annu. Rev. Fluid Mech.*, vol. 45, no. 1, pages 197–215, 2013. (Cited on page 11.)
- [Rahimi 2011] Shai Rahimi and Daniel Weihs. *Gelled fuel simulant droplet impact onto a solid surface*. *Propellants, Explos. Pyrotech.*, vol. 36, no. 3, pages 273–281, 2011. (Cited on page 18.)
- [Raux 2020] Pascal S. Raux, Anthony Troger, Pierre Jop and Alban Sauret. *Spreading and fragmentation of particle-laden liquid sheets*. *Phys. Rev. Fluids*, vol. 5, no. 4, page 44004, 2020. (Cited on page 4.)
- [Rehage 1988] H. Rehage and H. Hoffmann. *Rheological Properties of Viscoelastic Surfactant Systems*. *J. Phys. Chem.*, vol. 92, no. 16, pages 4712–4719, 1988. (Cited on page 62.)
- [Rehage 1991] H. Rehage and H. Hoffmann. *Viscoelastic surfactant solutions: model systems for rheological research*. *Mol. Phys.*, vol. 74, no. 5, pages 933–973, 1991. (Cited on page 62.)
- [Rein 2002] Martin Rein. *Interactions between Drops and Hot Surfaces*. In Rein M. *Drop-Surface Interact.*, volume 456, pages 535–546. Springer, Vienna, cism inter édition, 2002. (Cited on page 13.)
- [Richard 2002] Denis Richard, Christophe Clanet and David Quéré. *Contact time of a bouncing drop*. *Nature*, vol. 417, page 811, 2002. (Cited on pages 12 and 24.)
- [Rioboo 2001] R. Rioboo and C. Tropea. *Outcomes from a drop impact on solid surfaces*. vol. 11, pages 155–165, 2001. (Cited on pages 4, 5, 6 and 43.)
- [Rioboo 2002] R. Rioboo, M. Marengo and C. Tropea. *Time evolution of liquid drop impact onto solid, dry surfaces*. *Exp. Fluids*, vol. 33, no. 1, pages 112–124, 2002. (Cited on page 4.)
- [Roisman 2002] Ilia V. Roisman, Romain Rioboo and Cameron Tropea. *Normal impact of a liquid drop on a dry surface: Model for spreading and receding*. *Proc. R. Soc. A Math. Phys. Eng. Sci.*, vol. 458, no. 2022, pages 1411–1430, 2002. (Cited on pages 23 and 128.)
- [Roisman 2006] Ilia V. Roisman, Kristijan Horvat and Cam Tropea. *Spray impact: Rim transverse instability initiating fingering and splash, and description of a secondary spray*. *Phys. Fluids*, vol. 18, no. 10, 2006. (Cited on page 127.)
- [Roisman 2009] Ilia V. Roisman. *Inertia dominated drop collisions. II. An analytical solution of the Navier-Stokes equations for a spreading viscous film*. *Phys. Fluids*, vol. 21, no. 5, 2009. (Cited on pages 23, 24 and 26.)

- [Roux 2004] D C D Roux and J J Cooper-White. *Dynamics of water spreading on a glass surface*. J. Colloid Interface Sci., vol. 277, no. 2, pages 424–436, 2004. (Cited on pages 28 and 127.)
- [Rozhkov 2002] A. Rozhkov, B. Prunet-Foch and M. Vignes-Adler. *Impact of water drops on small targets*. Phys. Fluids, vol. 14, no. 10, pages 3485–3501, 2002. (Cited on pages 4, 7, 8, 43 and 101.)
- [Rozhkov 2003] A. Rozhkov, B. Prunet-Foch and M. Vignes-Adler. *Impact of drops of polymer solutions on small targets*. Phys. Fluids, vol. 15, no. 7, pages 2006–2019, 2003. (Cited on pages 8 and 18.)
- [Rozhkov 2004] A Rozhkov, B Prunet-Foch and M Vignes-Adler. *Dynamics of a liquid lamella resulting from the impact of a water drop on a small target*. Proc. R. Soc. Lond., vol. 460, no. 2049, pages 2681–2704, 2004. (Cited on pages 8 and 27.)
- [Rubinstein 2003] Michael Rubinstein and R. H. Colby. Polymer Physics. Oxford university press New York, 2003. (Cited on page 66.)
- [Sen 2021] Samya Sen, Anthony G. Morales and Randy H. Ewoldt. *Thixotropy in viscoplastic drop impact on thin films*. Phys. Rev. fluids, vol. 6, page 043301, 2021. (Cited on page 19.)
- [Steffe 1996] James F. Steffe. Rheological methods in food process engineering. East Lansing, MI : Freeman Press, 1996. (Cited on pages 40 and 42.)
- [Takamura 2012] Koichi Takamura, Herbert Fischer and Norman R Morrow. *Physical properties of aqueous glycerol solutions*. J. Pet. Sci. Eng., vol. 98-99, pages 50–60, 2012. (Cited on page 57.)
- [Tanaka 2003] Yoshimi Tanaka, Yoshihiro Yamazaki and Ko Okumura. *Bouncing gel balls: Impact of soft gels onto rigid surface*. EPL (Europhysics Lett., vol. 63, no. 1, page 146, 2003. (Cited on pages 4, 21 and 25.)
- [Tanaka 2005] Y. Tanaka. *Impact of gel balls beyond the Hertzian regime*. Eur. Phys. J. E, vol. 18, no. 1, pages 95–103, 2005. (Cited on pages 4, 21 and 25.)
- [Taylor 1959] Sir Geoffrey Taylor. *The dynamics of thin sheets of fluid. III. Disintegration of fluid sheets*. Proc. R. Soc. London. Ser. A. Math. Phys. Sci., vol. 253, no. 1274, pages 313–321, 1959. (Cited on pages 128 and 143.)
- [Thoroddsen 2008] S T Thoroddsen, T G Etoh and K Takehara. *High-Speed Imaging of Drops and Bubbles*. Annu. Rev. Fluid Mech., vol. 40, no. 1, pages 257–285, 2008. (Cited on page 3.)

- [Venerus 2010] D. C. Venerus, T.-Y. Shiu, T. Kashyap and J. Hosttetter. *Continuous lubricated squeezing flow: A novel technique for equibiaxial elongational viscosity measurements on polymer melts*. J. Rheol. (N. Y. N. Y)., vol. 54, no. 5, pages 1083–1095, 2010. (Cited on page 31.)
- [Venerus 2019] David C Venerus, Rebecca M Mick and Teresita Kashyap. *Equibiaxial elongational rheology of entangled polystyrene melts*. J. Rheol. (N. Y. N. Y)., vol. 63, no. 1, pages 157–165, 2019. (Cited on page 31.)
- [Vernay 2015a] C Vernay, L Ramos and C Ligoure. *Free radially expanding liquid sheet in air: time-and space-resolved measurement of the thickness field*. J. Fluid Mech., vol. 764, pages 428–444, 2015. (Cited on pages 8, 27, 44, 51, 131 and 136.)
- [Vernay 2015b] Clara Vernay, Laurence Ramos and Christian Ligoure. *Bursting of Dilute Emulsion-Based Liquid Sheets Driven by a Marangoni Effect*. Phys. Rev. Lett., vol. 115, no. 19, pages 2–6, 2015. (Cited on pages 128 and 136.)
- [Vernay 2016] Clara Vernay. *Destabilization of liquid sheets of dilute emulsions*. PhD thesis, Université de Montpellier, 2016. (Cited on page 43.)
- [Villermaux 2011] E Villermaux and B BOSSA. *Drop fragmentation on impact*. J. Fluid Mech., vol. 668, pages 412–435, 2011. (Cited on pages 8, 27, 28, 44, 127, 128 and 144.)
- [Visser 2015] Claas Willem Visser, Philipp Erhard Frommhold, Sander Wildeman, Robert Mettin, Detlef Lohse and Chao Sun. *Dynamics of high-speed micro-drop impact: Numerical simulations and experiments at frame-to-frame times below 100 ns*. Soft Matter, vol. 11, no. 9, pages 1708–1722, 2015. (Cited on page 5.)
- [Vonnegut 1942] B Vonnegut. *Rotating bubble method for the determination of surface and interfacial tensions*. Rev. Sci. Instrum., vol. 13, no. 1, pages 6–9, 1942. (Cited on page 37.)
- [Walker 1996] L M Walker, P Moldenaers and J F Berret. *Macroscopic response of wormlike micelles to elongational flow*. Langmuir, vol. 12, no. 26, pages 6309–6314, 1996. (Cited on page 31.)
- [Wang 2000] A. B. Wang and C. C. Chen. *Splashing impact of a single drop onto very thin liquid films*. Phys. Fluids, vol. 12, no. 9, pages 2155–2158, 2000. (Cited on page 15.)
- [Wang 2017] Y. Wang and L. Bourouiba. *Drop impact on small surfaces: thickness and velocity profiles of the expanding sheet in the air*. J. Fluid Mech., vol. 814, pages 510–534, 2017. (Cited on pages 4, 8, 27 and 51.)

- [Wang 2018] Y. Wang, R. Dandekar, N. Bustos, S. Poulain and L. Bourouiba. *Universal Rim Thickness in Unsteady Sheet Fragmentation*. Phys. Rev. Lett., vol. 120, no. 20, pages 1–6, 2018. (Cited on pages 28, 29, 127 and 136.)
- [Wang 2019] Yi Bo Wang, Xiao Dong Wang, Yan Ru Yang and Min Chen. *The Maximum Spreading Factor for Polymer Nanodroplets Impacting a Hydrophobic Solid Surface*. J. Phys. Chem. C, vol. 123, pages 12841–12850, 2019. (Cited on page 22.)
- [Wang 2020a] Xin Wang, Dian Ji Lin, Yi Bo Wang, Shu Rong Gao, Yan Ru Yang and Xiao Dong Wang. *Rebound dynamics of two droplets simultaneously impacting a flat superhydrophobic surface*. AIChE J., vol. 66, page e16647, 2020. (Cited on page 22.)
- [Wang 2020b] Yi Bo Wang, Yi Feng Wang, Shu Rong Gao, Yan Ru Yang, Xiao Dong Wang and Min Chen. *Universal Model for the Maximum Spreading Factor of Impacting Nanodroplets: From Hydrophilic to Hydrophobic Surfaces*. Langmuir, vol. 36, pages 9306–9316, 2020. (Cited on page 22.)
- [Wang 2021a] Y. Wang and L. Bourouiba. *Growth and breakup of ligaments in unsteady fragmentation*. J. Fluid Mech., vol. 910, page A39, 2021. (Cited on page 28.)
- [Wang 2021b] Yongji Wang. *Fundamentals in unsteady fluid fragmentation from drop impact*. PhD thesis, Massachusetts Institute of Technology, 2021. (Cited on pages 29, 30, 127 and 128.)
- [Wijshoff 2018] Herman Wijshoff. *Drop dynamics in the inkjet printing process*. Curr. Opin. Colloid Interface Sci., vol. 36, pages 20–27, 2018. (Cited on page 3.)
- [Wildeman 2016] Sander Wildeman, Claas Willem Visser, Chao Sun and Detlef Lohse. *On the spreading of impacting drops*. J. Fluid Mech., vol. 805, pages 636–655, 2016. (Cited on page 24.)
- [Wirth 1991] Wolfgang Wirth, Siegfried Storp and Wolfgang Jacobsen. *Mechanisms controlling leaf retention of agricultural spray solutions*. Pestic. Sci., vol. 33, pages 411–420, 1991. (Cited on page 3.)
- [Worthington 1877] A M Worthington. *On the forms assumed by drops of liquids falling vertically on a horizontal plate*. Proc. R. Soc. London, vol. 25, pages 261–272, 1877. (Cited on page 3.)
- [Worthington 1895] Arthur Mason Worthington. *The splash of a drop*. Soc. Promot. Christ. Knowl., pages 7–76, 1895. (Cited on pages 3 and 4.)
- [Xi Yuan Hua 1988] Xi Yuan Hua and Milton J. Rosen. *Dynamic surface tension of aqueous surfactant solutions. I. Basic parameters*. J. Colloid Interface Sci., vol. 124, no. 2, pages 652–659, 1988. (Cited on page 35.)

- [Xie 2017] Kaili Xie, Clément De Loubens, Frédéric Dubreuil, Deniz Z. Gunes, Marc Jaeger and Marc Léonetti. *Interfacial rheological properties of self-assembling biopolymer microcapsules*. *Soft Matter*, vol. 13, no. 36, pages 6208–6217, 2017. (Cited on page 31.)
- [Yarin 2017] Alexander L. Yarin, Ilia V. Roisman and Cameron Tropea. *Collision Phenomena in Liquids and Solids*. 2017. (Cited on pages 4, 12, 23, 24, 27, 136 and 143.)
- [Zhang 1997] Xiaoguang Zhang and Osman A. Basaran. *Dynamic surface tension effects in impact of a drop with a solid surface*. *J. Colloid Interface Sci.*, vol. 187, no. 1, pages 166–178, 1997. (Cited on page 35.)

Gouttes et billes sous grande déformation biaxiale : le rôle de la viscosité et de l'élasticité.

Résumé: La compréhension des phénomènes de déformation de gouttes après impact constitue un enjeu considérable pour des secteurs industriels tels que l'impression par jet d'encre, l'application de pesticides, le revêtement par pulvérisation, etc. Poussés par ces motivations, nous étudions les déformations subies par des gouttes de fluides Newtoniens, rhéo-fluidifiants, et de gels transitoires après impact, et de billes élastiques molles dans une autre configuration expérimentale.

Dans un premier temps, les gouttes sont impactées sur une surface couverte d'une fine couche d'azote liquide qui en s'évaporant fournit les conditions idéales pour étudier la déformation de nappes liquides grâce à un effet Leidenfrost froid. Dans ces conditions, deux régimes sont identifiés : un régime capillaire pour lequel le diamètre maximal de la nappe ne dépend pas de la viscosité du fluide et un régime visqueux pour lequel celui-ci décroît lorsque la viscosité augmente. Cette décroissance est due à la dissipation visqueuse lors de l'extension de la nappe et est contrôlée par la viscosité extensionnelle biaxiale. Pour des solutions polymériques, nous montrons que cette viscosité prend en compte le caractère rhéo-fluidifiant du fluide. Dans ces conditions, nous avons impacté des fluides plus complexes qui se comportent comme des fluides de Maxwell. Un modèle d'oscillateur harmonique amorti non linéaire prédit le diamètre maximal de la nappe, d_{\max} , ainsi que le temps, t_{\max} , nécessaire pour atteindre d_{\max} . Un bon accord quantitatif entre expérience et théorie est obtenu pour des fluides Newtoniens jusqu'à des viscosités élevées et des fluides de Maxwell dont le temps de relaxation caractéristique est plus grand, plus petit ou comparable au temps caractéristique de l'expérience, t_{\max} .

Dans une deuxième partie, les gouttes sont impactées sur de petites surfaces solides, appelées cibles, complexifiant le champ d'écoulement auquel les gouttes sont soumises. En effet, la portion de la nappe se trouvant en contact avec la cible est soumise à un cisaillement qui engendre une dissipation visqueuse de cisaillement et la portion s'étendant hors de la cible est uniquement sujette à la dissipation extensionnelle biaxiale. Nous prédisons l'expansion maximale de la nappe en fonction de la viscosité pertinente identifiée en évaluant quantitativement les dissipations dues au cisaillement et à l'extension biaxiale. Nous montrons, finalement, une corrélation entre le diamètre maximal de la nappe et le diamètre de la cible. A nouveau, l'importance de considérer le caractère rhéo-fluidifiant des solutions de polymères, pour rationaliser les résultats expérimentaux, est démontrée.

Nous nous intéressons ensuite à l'émergence et à la dynamique du bourrelet entourant une nappe visqueuse en expansion. Nous présentons des mesures directes du champ d'épaisseur de la nappe qui permettent de mesurer les évolutions temporelles de la forme et du volume du bourrelet. Un modèle analytique est développé pour prédire la vitesse et le taux de remplissage du bourrelet. Nous identifions et comparons les importances relatives des contributions de la tension de surface, des forces d'inertie et de la viscosité à la vitesse de remplissage. Nous montrons que la contribution des forces d'inertie ne peut être négligée. Un très bon accord est trouvé entre valeurs théoriques et expérimentales.

Finalement, nous utilisons un tensiomètre à bille tournante pour étudier la déformation biaxiale de billes élastiques molles. Ce dispositif permet de déformer une bille élastique immergée dans un fluide plus dense par la mise en rotation autour de son axe d'un capillaire qui les contient. Avec l'hypothèse d'une déformation homogène de la bille, nous parvenons à découpler théoriquement la mesure du module élastique de celle de la tension de surface. Ces mesures sont confrontées avec succès aux mesures expérimentales.

Mots clés: impact de gouttes, nappe liquide, viscoélasticité, déformation biaxiale, mécanismes de dissipation

Drops and beads under large biaxial deformation: the role of viscosity and elasticity.

Abstract: Comprehending the deformation of drops upon impact constitutes a major challenge for industrial sectors such as ink-jet printing, pesticide application, spray coating, etc. For this reason, we study the biaxial deformation of drops of Newtonian, rheo-thinning and Maxwell fluids following their impact, and of soft elastic beads using another experimental configuration.

First, viscous drops are impacted on a surface covered by a thin layer of liquid nitrogen, which by its evaporation creates the ideal non-wetting and slip conditions provided by the cold Leidenfrost effect. In these experimental conditions, we identify two regimes: a capillary regime where the maximal diameter reached by the sheet, d_{\max} , does not depend on the viscosity of the fluid and a viscous regime where d_{\max} decreases as the viscosity increases. This decrease is due to the viscous dissipation taking place during the sheet extension. The dissipation is governed by the biaxial extensional viscosity. For polymer solutions, the biaxial extensional viscosity takes into account the rheo-thinning nature of the fluid. In the same experimental conditions, we also impact viscoelastic Maxwell fluids. A non-linear damped harmonic oscillator model predicts the maximal diameter, d_{\max} , reached by the sheet as well as the time, t_{\max} , needed to reach d_{\max} . Good quantitative agreement is found between experiments and theory for Newtonian fluids of various viscosities and Maxwell fluids with characteristic relaxation times smaller, larger or comparable to the characteristic time of the experiment, t_{\max} .

In a second part of this work, the drops are impacted on small solid surfaces, named targets, complicating the flow field undergone by the sheet. The part of the sheet in contact with the target is subjected to shear, and shear viscous dissipation develops. On the other hand, the part expanding freely outside of the target only suffers dissipation caused by the biaxial extensional deformation of the sheet. We predict the maximum expansion factor of the sheet as a function of the relevant viscosity by evaluating quantitatively the viscous dissipation due to shear and biaxial extensional deformations. We finally show a correlation between the maximal diameter reached by the sheet and the target size. Once again, the importance of considering the rheo-thinning behavior of the polymer solutions to rationalize the experimental results is emphasized.

We then investigate the emergence and dynamics of the rim formed at the free edge of an expanding viscous sheet. We provide direct measurements of the sheet thickness field, allowing the measurement of the time evolution of the shape and volume of the rim. We develop an analytical model, which predicts the filling rate and velocity of the rim. We identify and compare the relative importance of the contributions due to surface tension, inertial forces, and viscosity to the filling velocity. We show that the contribution of the inertial forces cannot be neglected. We find a good quantitative agreement between the experimental and theoretical values for the filling rate and velocity.

Finally, we use a spinning drop tensiometer to measure the biaxial deformation of soft elastic beads. The set-up allows the deformation of a soft elastic bead immersed in a denser fluid by putting in rotation along its axis a capillary containing the bead and fluid. Under the assumption of homogeneous deformation of the bead, we obtain a theoretical decoupling of the measurement of surface tension and elastic modulus, which was confirmed by a confrontation with the experimental values.

Keywords: drop impact, liquid sheet, viscoelasticity, biaxial deformation, dissipation mechanisms
